Functional characterization of sequence variants in leucine-rich repeat kinase 2 (*LRRK2*) and its possible interaction with the translocase of outer mitochondrial membrane (TOM) protein complex

by

Annika Neethling

Dissertation presented for the degree of Doctor of Philosophy in Science (Human Genetics) in the Faculty of Medicine and Health Sciences at Stellenbosch University

Supervisor: Prof. Soraya Bardien

Co-supervisor: Dr. Monique Williams

March 2017

Declaration

By submitting this thesis electronically, I declare that the entirety of the work contained therein is my own, original work, that I am the sole author thereof (save to the extent explicitly otherwise stated), that reproduction and publication thereof by Stellenbosch University will not infringe any third party rights and that I have not previously in its entirety or in part submitted it for obtaining any qualification.

Signature: …….. Date: ……March 2017.....

Abstract

Parkinson's disease (PD) is an incurable neurodegenerative disorder, characterized by the progressive loss of dopaminergic neurons in the midbrain of affected individuals. Both environmental and genetic factors contribute to the aetiology of PD, with more than a dozen genes implicated in disease development. Yet, the exact mechanisms by which each gene (and mutation) contribute to the pathophysiology of PD remain to be elucidated. Mitochondrial dysfunction is a recurring theme associated with neurodegeneration and recently the translocase of outer mitochondrial membrane (TOM) complex, which plays a role in the maintenance of healthy mitochondria, has been implicated in PD pathogenesis. The TOM complex, consisting primarily of TOM20, TOM22, TOM40 and TOM70, is involved in the translocation of nuclear-encoded proteins into the mitochondria where they are needed for normal mitochondrial function. Mutations in the leucine-rich repeat kinase 2 (*LRRK2*) gene are the most common cause of autosomal dominant PD and the LRRK2 protein has been associated with numerous cellular functions including mitochondrial homeostasis, the autophagy/lysosomal pathway, cell signalling and synaptic vesicle trafficking. The most common PD-causing mutation, G2019S, is located in the kinase domain of LRRK2 and has consistently been shown by various researchers to increase kinase activity. Recently, members of our group identified a novel variant (Q2089R) in *LRRK2*. This variant is also located in the kinase domain of LRRK2 and requires further investigation to determine its pathogenicity. The aim of the present study was to functionally characterize wild type (WT) and mutant *LRRK2* (G2019S and Q2089R) under basal and stress [Carbonyl cyanide m-chlorophenyl hydrazone (CCCP)] conditions and also to determine whether WT LRRK2 interacts with the TOM complex.

The frequency of *LRRK2* Q2089R in South African PD patients and controls was determined using a custom Taqman™ SNP genotyping assay. *In silico* analysis of the effect of the amino acid substitution from Glutamine (Q) to Arginine (R) was performed using various prediction tools. Two cellular models of PD including (1) HEK293 cells transfected with WT and mutant LRRK2 constructs and (2) patient-derived dermal fibroblasts were used for the functional studies. LRRK2 mutant constructs were generated using site-directed mutagenesis in pcDNA-DEST53, a mammalian expression vector. We obtained skin biopsies from individuals harbouring G2019S, Q2089R or WT LRRK2 and cultured dermal fibroblasts as an *ex vivo* model of the disorder. We investigated the kinase activity of LRRK2 using autophosphorylation of Serine 1292 and Western blot analysis. Metabolic activity was measured using a 3-(4,5-Dimethylthiazol-2-yl)-2,5-Diphenyltetrazolium Bromide (MTT) assay and mitochondrial membrane potential (MMP) was measured using the JC-1 fluorochrome and flow cytometric analysis. Mitochondrial and glycolytic respiration experiments were performed using the Seahorse XF Analyzer and mitochondrial DNA copy number was determined by quantitative real-time PCR (qRT-PCR). Autophagic markers, LC3 II and P62, were detected using Western blot analysis. Co-localization experiments of WT LRRK2 and the TOM complex was performed using confocal and super resolution structured illumination microscopy (SR-SIM), while protein interactions were investigated using co-immunoprecipitation and Western blot analysis.

The frequency of Q2089R was found to be 0.2% (1/493) in PD patients and 0.1% (1/776) in controls. Multiple *in silico* tools predicted the Q to R substitution to possibly be pathogenic ['deleterious' (CADD score=24.1, 'possibly damaging' (Polyphen) and 'disease causing' (Mutation Taster)]. The LRRK2 constructs were successfully generated and fibroblasts were successfully cultured. Notably, in HEK293 cells, we found that Q2089R *almost completely abolished* autophosphorylation activity of LRRK2 ($p=0.026$). Q2089R-carrying cells also exhibited a decrease in metabolic activity in HEK293 cells ($p=0.016$) and fibroblasts ($p<0.05$). In addition, in both cell types a significantly decreased MMP was observed [$p=0.043$ and $p=0.009$ for HEK293 cells and fibroblasts (under stress), respectively]. Furthermore, Q2089R-carrying fibroblasts showed an increase in basal respiration ($p=0.012$), proton leak respiration ($p=0.0001$),

maximal respiration ($p<0.0001$) and spare respiratory capacity ($p<0.0001$), while ATP-coupling efficiency ($p=0.0014$), glycolytic reserve ($p=0.006$) and glycolytic capacity ($p=0.007$) was significantly reduced. In both models, Q2089R cells exhibited an increase in autophagosome pool size ($p<0.05$ for LC3 II and $p<0.05$ for P62).

In the case of G2019S, a marked increase in autophosphorylation activity ($p=0.019$) was observed in HEK293 cells, which is in accordance with many previous studies. Decreased metabolic activity ($p=0.021$) and MMP ($p=0.038$) were also observed in these cells. G2019S-carrying fibroblasts displayed reduced metabolic activity ($p<0.05$) and increased basal respiration ($p=0.029$), ATP-linked respiration ($p=0.029$), glycolysis ($p=0.001$) and autophagosome pool size ($p=0.022$ for LC3 II). The MMP of these fibroblasts showed a non-significant trend for a decrease under stress conditions ($p=0.057$).

Interestingly, WT LRRK2 was shown to co-localize and co-immunoprecipitate with a protein complex containing subunits TOM22, TOM40 and TOM70 but not TOM20 under basal conditions. Under stress conditions, an association between LRRK2 and TOM20 was observed while the association between LRRK2 and the complex containing TOM22 and TOM70 increased. Finally, from our findings and the published literature, we propose a model for the involvement of LRRK2 (WT and Q2089R) in cellular functioning and cell death. This involves the loss of kinase activity and association with the TOM complex, which ultimately links LRRK2 with mitochondrial (dys)function, mitochondrial biogenesis and the autophagy/lysosomal pathway.

In conclusion, we characterized a functional variant in the kinase domain of LRRK2 and propose additional functions for this large multi-domain protein. This study also provides evidence for a novel association between LRRK2 and the TOM complex. Interestingly, our findings challenge the notion that it is only increased LRRK2 kinase activity that is implicated in PD pathogenesis. We acknowledge, however, that our findings are preliminary and that further validation studies are necessary to validate our results and hypothesis. Future targeted experiments on LRRK2 are needed in order to unravel the complex pathobiology and to decipher the sequence of events that lead to development of PD in susceptible individuals.

Opsomming

Parkinson se siekte (PS) is ‘n ongeneesbare neurodegeneratiewe versteuring wat gekenmerk word deur die progressiewe verlies van dopaminergiese neurone in die brein van geaffekteerde individue. Beide omgewings- en genetiese faktore dra by tot die etiologie van PS, met meer as ‘n dosyn gene wat geïmpliseer word by die ontwikkeling van hierdie siektetoestand. Desondanks moet die presiese meganisme waardeur elke geen (en mutasie) bydra tot die patofisiologie van PS nog uitgeklaar word. Mitochondriale disfunksie is ‘n herhalende tema wat verband hou met neurodegenerasie en die translokase van die buitenste mitochondriale membranekompleks (TOM), wat onlangs geïdetifiseer is as ‘n belangrike rol-speler in die instandhouding van gesonde mitochondria. Die TOM kompleks wat hoofsaaklik bestaan uit TOM20, TOM22, TOM40 en TOM70 is betrokke by die vervoer van kern-geënkodeerde proteïene tot binne in die mitochondria waar dit benodig word vir normale mitochondriale funksionering. Mutasies in die *LRRK2* geen is die mees algeneme oorsaak van outosomale dominante PS en die LRRK2 proteïen word geassosieer met talle sellulêre funksies insluitend mitochondriale homeostase, die autophagy/lisosomale pad weg, sellulêre seine en sinaptiese vesikulêre vervoer. Die mees algemene PS-veroorsaakende mutasie, G2019S, is geleë in die kinase domein en verhoog kinase aktiwiteit van LRRK2. Lede van hierdie navorsingsgroep het onlangs ‘n nuwe variant (Q2089R) geïdentifiseer in LRRK2. Hierdie variant is ook geleë in die kinase domein van LRRK2 en vereis verdere ondersoek ten einde vas te stel of dit wel patogenies is. Die doel van die huidige studie was om funksionele kenmerke van wilde tipe (WT) en gemuteerde LRRK2 (G2019S en Q2089R) te ondersoek onder normale asook stremmings [Carbonyl cyanide m-chlorophenyl hydrazone (CCCP)] kondisies en ook om te bepaal of WT LRRK2 interaksie toon met die subeenhede van die TOM kompleks.

Die frekwensie van LRRK2 Q2089R is vasgestel in Suid-Afrikaanse PS pasiënte en kontroles deur die gebruik van n Taqman™ SNP genotipeerings toets. *In silico* analise van die aminosuur verandering van Glutamien (Q) tot Arginien (R) is uitgevoer met behulp van verskeie voorspellings algoritmes. Twee sellulêre modelle van PS, insluitend (1) HEK293 selle wat getransfekteer is met WT en gemuteerde LRRK2 vektore sowel as (2) pasiënt dermale fibroblaste, is gebruik vir fuksionele studies. LRRK2 mutante vektore was gegenereer deur gebruik te maak van plek-gerigte mutagenese in pcDNA-DEST53, ‘n soogdier uitdrukkings vektor. Velbiopsies van individue wat die G2019S, Q2089R of WT LRRK2 dra is gebruik om fibroblaste te kweek en te gebruik as ‘n *ex vivo* model vir die siekte. Die kinase aktiwiteit van LRRK2 is ondersoek deur gebruik te maak van outofosforilasie van Serien 1292 en Westerse klad analise. Sel-metaboliese aktiwiteit is gemeet met behulp van ‘n 3-(4,5-Dimethylthiazol-2-yl)-2,5-Diphenyltetrazolium Bromied (MTT) toets en die mitochondriale membraan potentiaal (MMP) is gemeet deur die JC-1 fluorochroom en vloei-sitometrise ontleding. Mitochondriale en glikolitiese respirasie eksperimente was uitgevoer met behulp van die Seahorse XF Analyzer en die mitochondriale DNA kopiegetal is bepaal deur kwantitatiewe “real-time PCR (qRT-PCR)”. Merkers van autophagy, LC3 II en P62, is opgespoor met behulp van Westerse klad analise. Co-lokaliserings eksperimente van LRRK2 en die TOM kompleks is uitgevoer met behulp van konfokale en super resolusie gestruktureerde verligtings mikroskopie (SR-SIM), terwyl proteïen interaksies ondersoek is met behulp van mede-immunopresipitasie en Westerse klad analise.

Die frekwensie van Q2089R was 0.2% (1/493) in PS pasiënte en 0.1% (1/776) in kontrole individue. Verskeie *in silico* toetse het voorspel dat die Q na R vervanging moontlik patogenies sal wees [‘nadelig’ (CADD telling=24.1), ‘moontlik skadelik’ (PolyPhen) en ‘siekte-veroorsakend’ (Mutation Taster)]. Die LRRK2 vektore was suksesvol gegenereer en die fibroblaste is suksesvol gekweek. In HEK293 selle is bevind dat Q2089R *byna heeltemal die outofosforilasie aktiwiteit van LRRK2 afgeskaf* het (p=0.026). Q2089R-draende selle het ook ‘n afname in sel-metaboliese aktiwiteit getoon in HEK293 selle (p=0.016) en fibroblaste (p<0.05). Verder, in beide seltipes het die MMP aansienlik afgeneem [(p=0.043 en p=0.009 vir

HEK293 selle en fibroblaste (onder stres), onderskeidelik)]. In Q2089R-fibroblaste was n toename in basale respirasie ($p=0.012$), proton lek respirasie ($p=0.0001$), maksimale respirasie ($p<0.0001$) en vrye respiratoriese kapasiteit ($p<0.0001$) waargeneem, terwyl ATP-koppelings doeltreffendheid ($p=0.0014$), glikolitiese reserwe ($p=0.006$) en glikolitiese kapasiteit ($p=0.007$) aansienlik verminder is. In beide modelle van Q2089R is die autophagosoom poel grootte verhoog ($p<0.05$ vir LC3 II en $p<0.05$ vir P62).

In die geval van G2019S, in ooreenstemming met veskeie vorige studies, is n verhoging in outofosforilasie aktiwiteit waargeneem in HEK293 selle. Verminderde sel lewensvatbaarheid ($p=0.021$) en MMP ($p=0038$) is ook opgemerk in hierdie selle. G2019S-draende fibroblaste het n afname getoon in selproliferasie terwyl basale respirasie ($p=0.029$), ATP-gekoppelde respirasie ($p=0.029$), glikoliese ($p=0.001$) en autophagosoom poel grootte ($p=0.022$ vir LC3 II) toegeneem het. Die MMP van hierdie fibroblaste het 'n nie-beduidende tendens van afname onder stremming getoon ($p=0.057$).

Interessant genoeg is dit bevind dat WT LRRK2 co-lokaliseer en mede-immunopresipiteer met ‘n proteïen kompleks wat TOM22, TOM40 en TOM70 maar nie TOM20 bevat onder normale toestande nie. Onder stremming is 'n assosiasie tussen LRRK2 en TOM20 waargeneem terwyl die assosiasie tussen LRRK2 en die kompleks wat TOM22 en TOM70 bevat toegeneem het. Laastens, uit ons bevindinge en vanuit die gepubliseerde literatuur, stel ons 'n model voor vir die betrokkenheid van LRRK2 (WT en Q2089R) in sel funksionering en seldood. Dit behels die verlies van kinase aktiwiteit en assosiasie met die TOM kompleks, wat uiteindelik LRRK2 heg met mitochondriale (dis)funksie, mitochondriale biogenese en die autophagy/lisosomale pad weg.

Ten slotte is daar ‘n funksionele variant in die kinase domein van LRRK2 gekarakteriseer en bykomende funksies vir hierdie groot multi-domein proteïen voorgestel. Hierdie studie bied ook bewyse van 'n nuwe assosiasie tussen LRRK2 en die TOM kompleks. Daarenteen bevraagteken hierdie studie die idee dat dit net verhoogde LRRK2 kinase aktiwiteit is wat betrokke is by PS ontwikkeling. Die navorsers van hierdie studie erken egter dat die bevindinge voorlopig is en dat verdere verifiering studies nodig is om die resultate asook hipotese te bevestig. Toekomstige geteikende eksperimente op LRRK2 is nodig om die komplekse patobiologie te ontrafel en om die volgorde van gebeure te ontsyfer wat aanleiding gee tot die ontwikkeling van PS in vatbare individue.

Acknowledgements

I would like to express my sincerest gratitude towards the following individuals who have actively contributed to this thesis and who have supported me throughout this degree.

To my supervisor, Prof Soraya Bardien. Thank you for your support, expert supervision and encouragement. Not only were you a dedicated and kind mentor, but without your assistance and knowledgeable input this thesis would not have been possible. You motivated me to persevere and I truly appreciate the positive guidance over the past three years.

To my co-supervisor, Dr. Monique Williams. Thank you for all the effort and intellectual (and technical) input you contributed towards this thesis.

Dr. Olga Corti and Fiona Bonello (and others) at the ICM Brain and Spine Institute, Paris, France. Thank you for hosting me for three months and helping me with the initial co-localization expeiments. You kept me busy and made my time away from home very productive.

Thank you to Prof Francois van der Westhuizen and Ms Hayley van Dyk from North West University for hosting me and assisting with the Seahorse experiments and data analysis.

I would also like to thank Mrs Lize van der Merwe, Ms Rozanne Adams (Central Analytical Facility, Stellenbosch University) and Dr. Ben Loos (Department of Physiology, Stellenbosch University) for their assistance with the confocal microscope, flow cytometry and data interpretation. Thank you to Dr. Glynis Johnson for your help with protein modeling. A special thank you to Dr. Craig Kinnear for always being willing to assist with experiments and data interpretation. I appreciate the imput you contributed towards this degree.

Thank you to Stellenbosch University, the Department of Biomedical Sciences and Prof Paul van Helden for the use of their facilities. Also to the National Research Foundation (NRF), Harry Crossley Foundation, Ernst and Ethel Eriksen Trust and the Boehringer Ingelheim Fonds for financial support.

To the PD-group, my co-workers in the MAGIC lab and the department (especially Juanelle du Plessis and Brigitte Glanzmann). Thank you for your infinite support over the years (seven to be exact!). You were always there to listen and give advice on an intellectual, but more importantly, a personal level. Without you this degree (and the previous ones) would certainly have been much more challenging.

To my loving parents, Junita and Kobus, and sisters, Heloïse and Amor. You are precious and irreplaceable people in my life and I thank you for your devoted and caring support over the years.

My fiancé, Briaan Cooper. Thank you for your endless love and encouragement. You always supported me and made me believe in myself. I couldn't have done this without you.

Finally, I would like to thank God for giving me the strength to persevere.

Table of contents **Page**

List of Abbreviations

2-DG	2-deoxy-glucose
3'	Three-prime
3D	Three-dimensional
5'	Five-prime
6-OHDA	6-hydroxydopamine
A	Adenine
α	Alpha
AAO	Age at onset
Aβ	Amyloid-β
AD	Alzheimer's disease
ADP	Adenosine diphosphate
ANOVA	Analysis of Variance
AR	Autosomal recessive
ATP	Adenosine triphosphate
AV	Autophagic vacuole
BafA1	Bafilomycin A1
BBB	Blood-brain barrier
Bp	Base pair
BSA	Bovine serum albumin
C	Cytosine
CAF	Central Analytical Facility
CCCP	Carbonyl cyanide m-chlorophenyl hydrazone
CMA	chaperone-mediated autophagy
Co-IP	Co-immunoprecipitation
CRISPR	Clustered regularly interspaced short palindromic repeats
C-terminal	Carboxyl-terminal
ddH2O	Distilled deionized water
DJ-1	Daisuke-junko-1
DBS	Deep Brain Stimulation
DMEM	Dulbecco's Modified Eagle Medium
DMSO	Dimethyl sulfoxide
DNAJC	DNAJ- Homolog Subfamily C
Drp1	Dynamin-related protein 1
e'	Electron
ECAR	Extracellular Acidification Rate
EIF4G1	Eukaryotic translation initiation factor 4G1
EOPD	Early onset Parkinson's disease
ETC	Electron transport chain
F	Phenylalenine
FADH2	Reduced flavin adenine dinucleotide
FBOX7	F-box only protein 7
FBS	Fetal bovine sSerum
FCCP	Carbonyl cyanide p-trifluoromethoxyphenyl hydrazon
FITC	Fluorescein isothiocyanate
G	Guanine
GBA	Glucocerebrosidase
gDNA	Genomic DNA
H+	Proton
Hsp70	Heat shock protein 70
Hsp90	Heat shock protein 90

IMM	Inner mitochondrial membrane
IMS	Inter membrane space
iPSCs	Induced pluripotent stem cells
JC-1	5,5',6,6' tetrachloro – 1,1,3,3' tetraethylbenzimidazol-carbocyanine iodide
JNK	Jun N-terminal kinase
K	Lysine
kb	Kilobase
kDa	Kilodalon
L	Liter
LB	Luria-Bertani
LC3 II	Microtubule-associated protein 1 light chain 3
LOPD	Late onset Parkinson's disease
LRRK1	Leucine-rich repeat kinase 1
LRRK2	Leucine-rich repeat kinase 2
MAO-B	Monamine-oxidase B
MAPT	Microtubule-associated protein tau
MBP	Myelin basic protein
MEFs	Mouse embryonic fibroblasts
Mfn1	Mitofusin 1
Mfn2	Mitofusin 2
mg	Milligram
ml	Milliliter
mM	Millimolar
mm	Millimeter
MMP	Mitochondrial membrane potential
MPP+	1-methyl-4-pyridinium
MPTP	1-methyl-4-phenyl-1,2,3,6-tetrahydropyridine
mTOR	Mammalian target of rapamycin
mtDNA	Mitochondrial DNA
MTT	3-(4,5-dimethylthiazol-2-yl)-2,5-diphenyltetrazolium bromide
NADH	Reduced nicotinamide adenine dinucleotide
ng	Nanogram
NGS	Next generation sequencing
nM	Nanomolar
nm	Nanometer
N-terminal	Amino-terminal
OCR	Oxygen consumption rate
OMM	Outer mitochondrial membrane
OPA1	Optic atrophy protein 1
ORF	Open reading frame
PBS	Phosphate buffered saline
PCD	Programmed cell death
PCR	Polymerase chain reaction
PD	Parkinson's disease
PE	Phosphatidylethanolamine
PE	Phycoerythrin
Pi	Inorganic phosphate
PINK1	PTEN-induced putative kinase 1
PTP	Permeability transition pore
qPCR	Quantitative PCR
R	Arginine
ROS	Reactive oxygen species
SAP	Shrimp alkaline phosphatase

SB	Sodium tetraborate
siRNA	Small interfering RNA
SNc	Substantia nigra pars compacta
SNCA	α-synuclein
SNP	Single nucleotide polymorphism
T	Thymine (base in DNA)
T	Threonine (amino acid in protein)
Ta	Annealing temperature
TBST	Tris Buffered Saline with Tween 20
Tm	Melting temperature
TOM	Translocase of outer mitochondrial membrane
TPR	Tetratricopeptide repeat
uMtCK	Ubiquitous mitochondrial creatine kinase
UPS	Ubiquitin proteasome system
VPS35	Vacuolar protein sorting 35
WES	Whole exome sequencing
WT	Wild type
Y	Tyrosine
µg	Microgram
µl	Microliter
µM	Micromolar
µm	Micrometer
°C	Degrees Celsius

List of figures

Chapter 1

Chapter 2

Chapter 3

Chapter 4

List of tables

Chapter 1

Chapter 2

Chapter 3

Chapter 4

Chapter 1: Introduction

Contents

1.1 Introduction to Parkinson's disease

Parkinson's disease (PD) is a common, incurable neurodegenerative disorder of the central nervous system affecting approximately 1% of individuals over the age of 60 and up to 5% of individuals aged over 85 years (Reeve *et al.*, 2014). Clinically, PD is characterized by the pronounced loss of dopaminergic neurons in the substantia nigra pars compacta in the midbrain (Figure 1.1) which ultimately causes impairment of the individual's motor skills. These motor symptoms include resting tremor, rigidity and slowness of movement (bradykinesia). The reduction in neurotransmitter dopamine levels at the nerve terminals lead to the dysregulation of motor circuits. In addition to affecting an individual's movement, motor circuit dysregulation disrupts the psychiatric and cognitive states of PD patients, and these are referred to as the non-motor symptoms (Cookson and Bandmann, 2010).

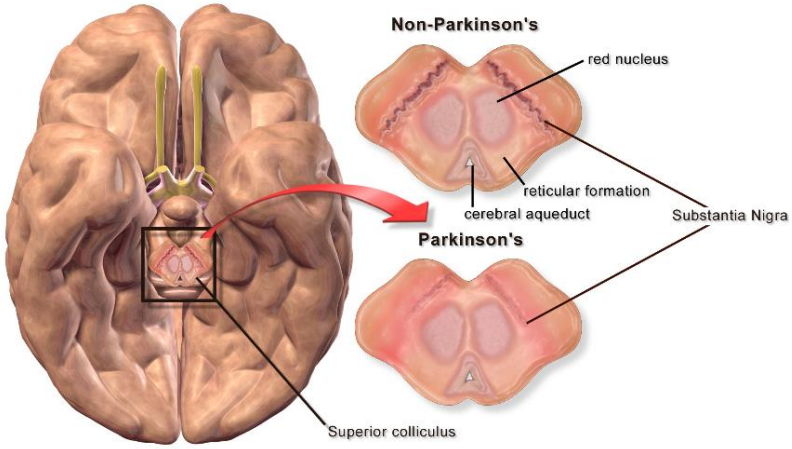

Figure 1.1 A diagram of the midbrain and region affected by Parkinson's disease. The cross-section images of the midbrain showing the diminished pigmentation of the dopamine-producing neurons in the substantia nigra of Parkinson's disease affected individuals (bottom right) compared to the dark pigmented neurons of healthy individuals (top right). Taken with permission from http://www.braintrainuk.com/other-conditions-that-neurofeedback-supports/neurofeedback-for-parkinsons/

Even though previous research provided significant insight into neurodegenerative disorders, currently no treatment is available to prevent neurodegeneration progression in PD (Xiong *et al.*, 2009). One of the major difficulties with this disorder is that 50-60% of nigral neurons and up to 80-85% of dopamine have been depleted when individuals first present with symptoms (Marsden, 1982; Isacson, 2002). These neurons never regenerate and thus highlights the importance for the identification of biomarkers for earlier disease detection and diagnosis. Therefore, more research is necessary to improve our

understanding of the molecular basis of the processes involved in PD. This knowledge is critical in order to facilitate development of effective neuroprotective strategies or even a cure for the disease.

The global prevalence of PD has been estimated to be between 41 and 1,903 per 100,000 individuals between 40 and 80 years of age (Pringsheim *et al.*, 2014). The incidence rate is reported to range from 3 to 105 per 100 000 individuals of a population that is between 40 and 80 years of age (Hirsch *et al.*, 2016). However, much lower prevalence and incidence rates are reported for countries in Sub-Saharan Africa (SSA) (Dotchin *et al.*, 2008). These lower figures are thought to be underestimates due to the fact that patients are either misdiagnosed with diseases other than PD, or remain undiagnosed (Okubadejo *et al.*, 2006; Akinyemi, 2012). It could also be attributed to under-reporting where individuals diagnosed with PD do not declare their disease status in the fear of being stigmatized (Silberberg and Katabira, 2006; Kaddumukasa *et al.*, 2015) or that patients living in rural areas will seek help from traditional healers instead of visiting medical facilities (Dotchin *et al.*, 2008). Furthermore, the lack of appropriate medical and scientific equipment, the relatively poor medical infrastructure, and the low number of neurologists and movement disorder specialists, contribute to the limited knowledge on PD in SSA countries (Okubadejo *et al.*, 2006; Dotchin *et al.*, 2008). The lower frequency of PD in SSA could also be ascribed to the differences in age-distribution in these populations (Akinyemi, 2012). Another important reason for region/country specific prevalence differences could be due to different methodologies used for the studies. The genetic causes of PD in SSA, specifically in South African populations including the black and Afrikaner populations, has not yet been established (Merwe *et al.*, 2012; Blanckenberg *et al.*, 2013; Carr and Coller, 2014). This indicates that SSA populations carry unique mutations that remain to be identified.

As increased age is a significant risk factor for PD, the prevalence of this disorder is set to increase significantly worldwide. It has been projected that the number of individuals with PD in five of Western Europe's most populated nations (Germany, France, United Kingdom, Italy and Spain) will double by the year 2030 (from 4.6 million to approximately 9.3 million individuals) (Dorsey *et al.*, 2007). More recently the rise in PD prevalence was predicted for both developed (in Europe and North America) and developing (Tanzania) countries with an estimated increase of 92% and 184%, respectively by the year 2050 (Bach *et al.*, 2011; Dotchin *et al.*, 2012). This alarmingly high increase in Tanzania, is in line with the rapidly changing population demographics in SSA, where the numbers of individuals aged 60 years and older in SSA countries are predicted to double by the year 2030 (and again by 2050) thus surpassing the numbers projected for many other regions including North America (Okubadejo *et al.*, 2006; Velkoff and Kowal, 2006).

PD was previously thought to be the archetypal environmental disorder and has been associated with various factors such as well-water drinking and exposure to pesticides (Preux *et al.*, 2000; Adler, 2009). However, it has since been recognized that both genetic and environmental factors contribute to development of the disease (Sherer *et al.*, 2002; Dawson, 2003). This, in conjunction with evidence of substantial phenotypic diversity between PD patients, led researchers to postulate that several different genes and various pathways could be involved in PD pathogenesis (Moore *et al.*, 2005; Wirdefeldt *et al.*, 2011). To date, mitochondrial dysfunction, oxidative stress, autophagy, protein aggregation and misfolding and impaired drug and toxin management have all been implicated in neurodegeneration and PD development (Cookson and Bandmann, 2010; Wallings *et al.*, 2015).

1.2 Genes implicated in Parkinson's disease

Over the past two decades, several PD-causing genes have been identified (Table 1.1). Although these genes have been the focus of many studies, the function of proteins such as P5 Subfamily of ATPase (ATP13A2) and Leucine rich repeat kinase 2 (LRRK2) has not yet been fully elucidated. Without a comprehensive understanding of PD-causing mutations and their functions, development of appropriate and effective therapeutic intervention will not be possible. Therefore, further investigation into these proteins and their corresponding functions are of upmost importance. The present study will focus on LRRK2 and will involve an investigation into its possible functions in cellular models of PD.

1.2.1 LRRK2: discovery, domain structure and functions

LRRK2, is located at the PARK8 locus on chromosome 12p11.2-q13.1 and encodes a large multi-domain protein comprising 2,527 amino acids (Funayama *et al.*, 2002; Guo *et al.*, 2006). Mutations in *LRRK2* were first implicated in autosomal dominant (AD) late-onset PD using high-resolution recombination mapping and candidate gene sequencing (Paisán-Ruíz *et al.*, 2004; Zimprich *et al.*, 2004; Funayama *et al.*, 2005). One of the first mutations, I2020T, was reported in a family from Germany (Zimprich *et al.*, 2004)and later it was found in the original PARK8-linked Japanese family (Funayama *et al.*, 2002, 2005). Later, several other families across different populations with AD late-onset PD was identified to carry mutations in *LRRK2*.

The protein product of *LRRK2*, which mainly localizes to the cytoplasm and the outer mitochondrial membrane, contains several potential protein-protein interaction sites surrounding the core region (Biskup *et al.*, 2006; Cookson, 2010). LRRK2 also consists of several functional domains which include an armadillo repeats (ARM) region, an ankyrin repeats (ANK) region, the leucine-rich repeat (LRR) domain, a

ROC GTPase domain, a C-terminal of Roc (COR) domain, a protein kinase catalytic domain (KIN) and a WD40 domain (Figure 1.2) (Smith *et al.*, 2005; Lobbestael *et al.*, 2013).

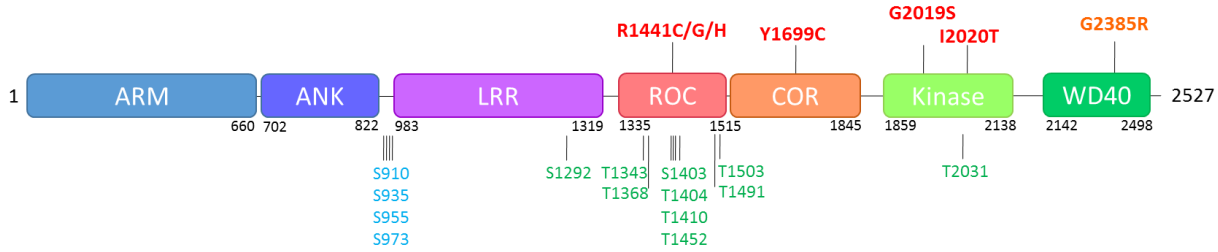

Figure 1.2 Schematic diagram of LRRK2. The most extensively studied pathogenic mutations are illustrated on top (red). G2385R (orange) is an established susceptibility allele for PD. *In vitro* autophosphorylation sites are shown in green and cellular phosphorylation sites are indicated in blue at the bottom of the image. Modified from (Lobbestael *et al.*, 2013; Steger *et al.*, 2016).

The ROC and COR domains are connected and function as a single unit (Bosgraaf and Van Haastert, 2003). These domains have GTPase activity, which hydrolyses GTP to GDP to donate a phosphate group to other proteins/pathways and act as molecular switches, regulates various processes including vesicular transport and cytoskeletal reorganization (Guo *et al.*, 2006). Additionally, the ROC and COR domains are typically preceded by a LRR domain which serves as a protein recognition site and is involved in protein-protein interactions (Kobe and Kajava, 2001). Similarly, the ARM domain, the ANK domain (both at the N-terminal) and the WD40 domain (at the C-terminal) have also been shown to be involved in protein-protein interactions (Sedgwick and Smerdon, 1999; Guo *et al.*, 2006; Gilsbach and Kortholt, 2014). The kinase domain, which follows the COR domain, is responsible for phosphorylation of various proteins and plays an important role in signal transduction within the cell (Gilsbach and Kortholt, 2014).

LRRK2, and its homolog LRRK1, form part of the ROCO protein family and are believed to be the only members of this family to harbor a GTPase and a kinase domain within the same protein (Biskup *et al.*, 2006). LRRK1 and LRRK2 are known to form heterodimers. Although, LRRK1 has not been directly implicated in PD, it has been shown that a missense mutation in LRRK1 (L416M) resulted in a younger age of PD onset in a large LRRK2 G2019S Tunisian population consisting of familial and sporadic PD individuals (Dachsel *et al.*, 2010). Additionally, several novel non-synonymous variants were identified in *LRRK1* through exome sequencing of affected individuals from a family with late-onset PD (Schulte *et al.*, 2014). Although these variants did not affect cell viability and subcellular localization, the results suggest a role for *LRRK1*, in combination with *LRRK2*, as a possible disease-modifier.

Table 1.1 Genes that have been implicated in Parkinsonism

Gene symbol	Gene/ Protein name	Inheritance	Proposed or known function	Reference(s)
SNCA	Alpha synuclein	AD	Regulation of dopamine release and transport	(Polymeropoulos *et al.*, 1997)
PARK2 (*Parkin*)	Parkin	AR	Removal of abnormal or damaged proteins and mitochondria (mitophagy)	(Kitada *et al.*, 1998)
SCA2	Spinocerebellar ataxia type 2 protein	AD	Epidermal Growth Factor Receptor (EGFR) trafficking	(Gwinn-Hardy *et al.*, 2000)
SCA3	Spinocerebellar ataxia type 3 protein	AD	Protein homeostasis and degradation of misfolded chaperone substrates	(Gwinn-Hardy *et al.*, 2001)
DJ-1	Oncogene DJ-1	AR	Protects cells against oxidative stress and cell death	(Bonifati *et al.*, 2003)
GBA	Glucocerebrosidase	-	Provides instructions for making beta-*glucocerebrosidase* which is active in lysosomes	(Tayebi *et al.*, 2003)
LRRK2	Leucine rich repeat kinase 2	AD	Phosphorylation of proteins, cell signaling and protein interactions	(Paisán-Ruíz *et al.*, 2004; Zimprich *et al.*, 2004)
PINK1	PTEN putative induced kinase	AR	Protects against mitochondrial dysfunction during cellular stress and involved in mitophagy	(Valente *et al.*, 2004)
ATP13A2	P5 Subfamily of ATPase	AD	Intracellular cation homeostasis and the maintenance of neuronal integrity	(Ramirez *et al.*, 2006)
FBXO7	F-Box Protein 7	AR	Phosphorylation-dependent ubiquitination and regulation of hematopoiesis	(Di Fonzo et al. 2009; Shojaee et al. 2008)
PLA2G6	Phospholipase A2 Group 6	AR	Involved in apoptosis and in regulating transmembrane ion flux	(Paisan-Ruiz *et al.*, 2009)
VPS35	Vacuolar sorting protein 35	AD	Transport of proteins from endosome to trans-Golgi network	(Vilariño-Güell *et al.*, 2011)
EIF4GI	Eukaryotic translation Initiation Factor 4 Gamma 1	AD	Recruitment of mRNA to the ribosome	(Chartier-Harlin *et al.*, 2011)
DNAJC6	DnaJ heat shock protein family (Hsp40) member C6	AR	Regulate molecular chaperone activity by stimulating ATPase activity	(Edvardson *et al.*, 2012)
SYNJ1	Synaptojanin 1	AR	Synaptic transmission and membrane trafficking	(Krebs *et al.*, 2013; Quadri *et al.*, 2013)
DNAJC13	DnaJ heat shock protein family (Hsp40) Member C13	AD	Involved in membrane trafficking through early endosomes and plays a role in clathrin-mediated endocytosis	(Vilariño-Güell *et al.*, 2014)
CHCHD2	Coiled-coil-helix-coiled-coil-helix 2	AD	Possible role in oxidative phosphorylation	(Funayama *et al.*, 2015)
TMEM230	Transmembrane protein 230	AD	Involved in synaptic vesicle trafficking	(Deng *et al.*, 2016)

Abbreviations: AD, autosomal dominant; AR, autosomal recessive;

In terms of the physiological processes in which LRRK2 is involved, the recurring cellular themes are vesicle cycling, autophagy, mitochondrial stress response (fission/fusion), miRNA processing and cytoskeletal regulation (Figure 1.3) (Sanna *et al.*, 2012; Wallings *et al.*, 2015). These processes are also highlighted in the Parkinson's Disease Map (PDMap) (http://minerva.uni.lu/MapViewer/). Although it is not clear if these represent independent roles for LRRK2, it is certainly possible that LRRK2 might have important roles in a number of cellular processes given its multiple domain structure (Lazarou et al. 2012; Paisán-Ruiz et al. 2013).

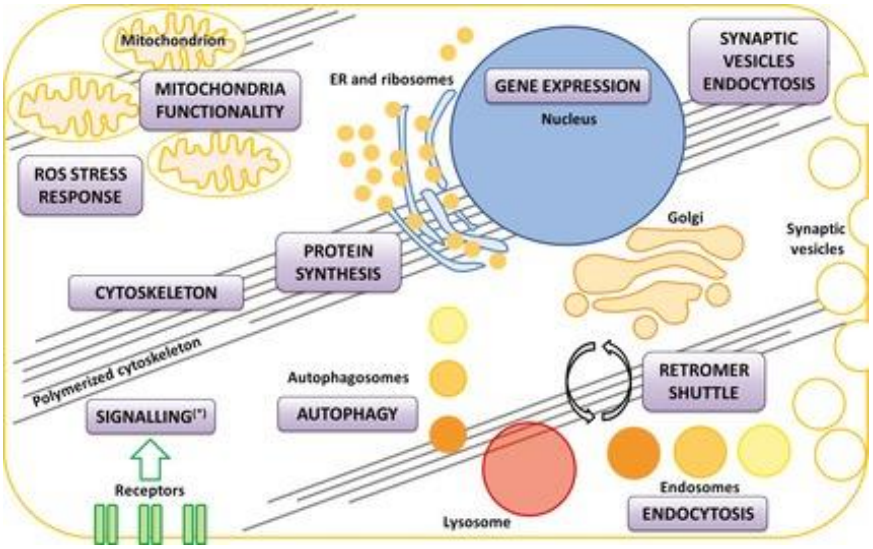

Figure 1.3 Schematic representation of LRRK2's cellular functions. The diagram shows the cellular processes that have been associated with LRRK2 function in physiology and/or disease including mitochondrial functional, reactive oxygen species (ROS) stress response and autophagy. Reproduced with permission from (Wallings *et al.*, 2015).

A domain in LRRK2 that is of interest to the present study, especially with regards to PD pathogenesis, is the protein kinase domain. Protein kinases phosphorylate proteins on their serine (Ser), threonine (Thr), tyrosine (Tyr) or histidine (His) residues. Kinases are enzymes that transfer phosphate groups from donor molecules to specific substrates, and are used to transmit cellular signals to control inter-cellular and intra-cellular processes. Phosphorylation is a reversible process and has been shown to modulate protein activity, regulate localization of proteins to a specific cellular compartment, stabilize proteins or target them for degradation (Cohen, 2001). Additionally, it has also been shown to affect protein-protein interactions by initiating or disrupting such interactions.

1.2.2 PD-causing mutations of LRRK2

Mutations in *LRRK2* are the most common cause of PD worldwide (Paisán-Ruíz *et al.*, 2004; Zimprich *et al.*, 2004; Wirdefeldt *et al.*, 2011), accounting for approximately 10% of AD PD and 4% of sporadic

PD cases in several European and US populations (Lesage and Brice, 2009). These mutations are typically associated with late-onset familial AD or sporadic forms of PD. Interestingly, only a few of these variants are considered to be pathogenic mutations (Figure 1.2).

LRRK2 has 51 exons, however mutation screening studies mainly focus on exons 19, 24, 31, 35, 38 and 41 since most of the PD-causing mutations reside in these particular exons (Foroud, 2005; Klein and Westenberger, 2012). Well-established pathogenic mutations include R1441C (exon 31) (Zimprich *et al.*, 2004), R1441G (exon 31) (Paisán-Ruíz *et al.*, 2004) and R1441H (exon 31) (Mata *et al.*, 2005) (Roc GTPase domain), Y1699C (exon 35) (Paisán-Ruíz *et al.*, 2004) (COR domain), G2019S (exon 41) (Di Fonzo et al. 2005) and I2020T (exon 41) (Zimprich *et al.*, 2004; Funayama *et al.*, 2005) (kinase domain) and the susceptibility allele, G2385R (exon 48) (WD40 domain) (Figure 1.2). Very recently, Mata and co-workers discovered another mutation, R1441S, in the Roc domain of LRRK2 (Mata *et al.*, 2016). Numerous other mutations have also been identified including R1628P, N1437H, S1761R and E1874Stop, although it is unclear at this stage whether these mutations are truly pathogenic or not (Doggett *et al.*, 2012; Lorenzo-Betancor *et al.*, 2012; Mata *et al.*, 2013; Li *et al.*, 2014). Generally, the mutations in the Roc and COR domains, decrease GTPase activity, whereas mutations in the kinase domain e.g. G2019S increase kinase activity (Greggio *et al.*, 2006; Guo *et al.*, 2007; Lewis *et al.*, 2007). However, the exact mechanism by which *LRRK2* mutations result in disease remains unclear. The increased kinase activity observed with the G2019S mutation suggest a gain-of-function mechanism of *LRRK2*-linked disease, with a central role for kinase activity in PD development. However, other studies have reported variable findings for the I2020T mutation also located in the kinase domain; showing either increased kinase activity (Gloeckner *et al.*, 2006; Ray *et al.*, 2014; Ho *et al.*, 2016), no change in kinase activity (Anand *et al.*, 2009) or even a decrease in kinase activity (Jaleel *et al.*, 2007a; Reynolds *et al.*, 2014).

Both the G2019S and R1441C mutations have been shown to play a role in post-synaptic calcium (Ca^{2+}) imbalance, which lead to the excessive clearing of mitochondria from dendrites through a specialized form of autophagy known as mitophagy (Cherra *et al.*, 2013). More recently it was shown that mutations in the ROC-COR domain of LRRK2 disrupts axonal transport *in vitro* and *in vivo* (Godena *et al.*, 2014). These mutants induce locomotor deficits through the binding of de-acetylated microtubules. When microtubule acetylation increases the axonal transport and locomotor deficits are restored, identifying a possible therapeutic mechanism for PD.

The frequency of the most common *LRRK2* PD-causing mutation, G2019S, fluctuates across populations and is found to be most common in North African Arabs (30-40%) and Ashkenazi Jewish

populations (10-30%) primarily due to founder effects, and rare in Asian populations (0.4% in Japan) (Lesage *et al.*, 2010; Alcalay *et al.*, 2013; Trinh *et al.*, 2014).

1.2.3 LRRK2's kinase domain and possible substrates

Proteins with kinase activity assist in phosphorylation of target molecules, which is an essential step in turning on and off many cellular activities, whereas the GTPase activity in proteins may be involved in proliferation and differentiation (Scheffzek and Ahmadian, 2005). When LRRK2 was first implicated in PD pathogenesis, a great deal of focus was aimed towards the kinase domain of this protein. As mentioned, numerous studies have found that G2019S exhibits an increased kinase activity however this is not the case for all of the other PD-causing mutations, and further studies on the kinase activity are therefore warranted. Cellular phosphorylation and autophosphorylation assays on LRRK2 confirmed kinase activity of endogenous as well as overexpressed forms of the protein (West *et al.*, 2005; Gloeckner *et al.*, 2006; Smith *et al.*, 2006; Sen *et al.*, 2009). LRRK2's kinase activity is dependent on its ability to form homodimers and is regulated by its GTPase activity (Gloeckner *et al.*, 2006; West *et al.*, 2007; Sen *et al.*, 2009; Webber *et al.*, 2011). Numerous cellular phosphorylation sites have been identified in LRRK2 including Ser^{910}, Ser^{935}, Ser^{955} and Ser^{973} (Dzamko *et al.*, 2010; Doggett *et al.*, 2012). However, these are not LRRK2 autophosphorylation sites per se, but are believed to be regulated by LRRK2's kinase activity, and have previously been used as an indirect measure of kinase activity. This was possible since the phosphorylation status of these cellular phosphorylation sites are linked to pathogenic *LRRK2* mutations (Zhao *et al.*, 2012; Reynolds *et al.*, 2014).

Recently, Ser^{1292} was identified as an autophosphorylation site *in vitro* and *in vivo* (Sheng *et al.*, 2012). Autophosphorylation of Ser^{1292} has been used as an indirect measure of LRRK2's kinase activity and it has been suggested that autophosphorylation could potentially be a useful tool to determine the degree of kinase activity in experimental and pathological conditions (Sheng *et al.*, 2012; Reynolds *et al.*, 2014). The development of phospho-specific antibodies, such as anti-LRRK2 phospho-Ser^{1292}, serves as a convenient method for the detection of autophosphorylation *in vitro*, and analysis of autophosphorylation mutants could aid in elucidating the role of each domain in the regulation of LRRK2's functions (Sheng *et al.*, 2012; Reynolds *et al.*, 2014).

A variety of physiological kinase substrates have been proposed for LRRK2 with the consensus phosphorylation sequence for LRRK2 being F/Y-x-T-x-R/K (Pungaliya *et al.*, 2010). LRRK2 was shown to phosphorylate threonine 558 in moesin (a protein responsible for anchoring the actin cytoskeleton to the plasma membrane), the peptide LRRKtide (a synthetic substrate of LRRK2) as well as myelin basic protein (MBP) which is responsible for myelination of nerves (West *et al.*, 2005; Jaleel *et al.*, 2007a). G2019S mutant LRRK2 has since been shown to also phosphorylate and bind to Beclin-2 (Bcl-2) at the

threonine at position 56 (Su *et al.*, 2015). Results from this study show that the expression of Bcl-2 phosphor mutant (Bcl-2 T56A) abolishes mitochondrial depolarization and autophagy induced by G2019S mutants in an overexpression model. Furthermore, Ho and colleagues showed that LRRK2 also phosphorylates the threonine at positions 304 and 377 in p53, a tumor suppressor (Ho *et al.*, 2015). Additionally, the ribosomal protein s15 was also shown to be a pathogenic substrate of LRRK2, indicated by the significant increase in phosphorylation by mutant *LRRK2* (G2019S and I2020T) in a *Drosophila melanogaster* model (from now on referred to as *Drosophila*) as well as in a human neuronal model of PD (Martin *et al.*, 2014). The G2019S mutant-induced dopamine neuronal degeneration and neurite loss could be rescued by the substitution of the threonine at position 136 in s15 with an alanine. It was subsequently postulated that elevated mutant *LRRK2* phosphorylation of substrates, such as s15, could contribute to LRRK2-mediated toxicity.

Recently, phosphoproteomics, genetics, and pharmacology was used to identify additional substrates of LRRK2 (Steger *et al.*, 2016). It was shown that LRRK2 is able to phosphorylate a subset of Rab GTPases namely Rab3a, Rab7a, Rab8a, Rab10 and Rab12 on conserved residues both *in vivo* and *in vitro*, recognizing them as true physiological substrates of LRRK2. Thus, identifying additional functions of LRRK2 in protein cycling between the cytosol and membrane compartments and Rab homeostasis.

1.3 Parkinson's disease and mitochondrial dysfunction

Substantial evidence exists for a key role of mitochondrial dysfunction in PD. Mitochondria are highly dynamic organelles that perform a variety of essential physiological functions in all eukaryotic cells (Chan, 2006; Perier and Vila, 2012). This includes the control of apoptosis in response to both intracellular and extracellular events, Ca^{2+} homeostasis, importing of mitochondrial proteins and the production of energy in the form of ATP via oxidative phosphorylation (Perier and Vila, 2012; Dudek *et al.*, 2013; Abeliovich and Dengjel, 2016). ATP is produced as a result of the transfer of electrons from NADH (reduced nicotinamide adenine dinucleotide) or $FADH_2$ (reduced flavin adenine dinucleotide) to oxygen (O_2) in the inner mitochondrial membrane (IMM) through a selection of complexes (complex I-V) (Berg *et al.*, 2002).

Some of the earliest evidence for the involvement of mitochondrial dysfunction in PD, came from the observation of Parkinsonism in heroin abusers who were accidentally exposed to 1-methyl-4-phenyl-1,2,3,4-tetrahydropyridine (MPTP) (Langston *et al.*, 1983). This inhibitor of complex I of the mitochondrial electron transport chain (ETC) can cross the blood-brain barrier and cause substantia nigra dopaminergic neuronal cell death which results in irreversible features of Parkinsonism. Following oxidation of MPTP to MPP^+, MPP^+ accumulates in mitochondria and thus inhibits NADH

ubiquinone oxidoreductase (complex I). Exposure to environmental toxins, such as pesticides, that inhibit mitochondrial respiration and promotes the production of reactive oxygen species (ROS) is another mechanism implicated in PD development (Greenamyre and Hastings, 2004; Dias *et al.*, 2013). The increased production of ROS is a general by-product of mitochondrial impairment, which could explain the oxidative damaged lipids, DNA and proteins and the decrease in complex I activity detected in the brains of PD patients (Dias *et al.*, 2013; Hwang, 2013). The inhibition of mitochondrial complex I has also been implicated in ubiquitin proteasome system (UPS) dysregulation by producing a toxic build-up of oxidatively damaged proteins (Shamoto-Nagai *et al.*, 2003).

Notably, a number of PD-causing genes are known to be involved in the maintenance of healthy mitochondria including *PARK2* (hereafter referred to as *Parkin*), *PINK1*, *DJ-1* and *SNCA*. Also, mitochondrial dysfunction including respiration deficits, oxidative stress and Ca^{2+} homeostasis, have been observed in almost all genetic models of PD including *PINK1*, *Parkin*, *DJ-1* and *LRRK2* mutant or deficient models (Zhu and Chu, 2010). These models range from invertebrates such as *Caenorhabditis elegans* (C. elegans), *Drosophila* and zebrafish to vertebrates such as dog, monkey, mouse as well as patient-derived cell lines (fibroblasts or induced pluripotent stem cells - iPSCs).

DJ-1 mutant studies in animal models have revealed decreased mitochondrial membrane potential (MMP), decreased mitochondrial complex activities and increased ROS (Wang *et al.*, 2012a). The role of DJ-1 in mitophagy is still unclear although it has been suggested that a decrease in MMP results in the translocation of DJ-1 to the OMM, where mitophagy would be initiated through as-yet-unknown processes. In wild type (WT) form, the DJ-1 protein protects the cell against oxidative stress (Bonifati *et al.*, 2003). However, when PD-causing mutations are present in *DJ-1*, the DJ-1 protein is not able to function normally thus eliminating its protective effect against oxidative stress. Furthermore, defective α-synuclein (*SNCA*) has also been shown to be associated with mitochondrial dysfunction and endoplasmic reticulum (ER) stress (Cooper *et al.*, 2006; Martin *et al.*, 2006; Schapira, 2008). Previous studies have shown that the complete knockout of *PINK1* in a mouse model caused a decrease in dopamine release that leads to major mitochondrial defects within striatal neurons of the animals (Exner *et al.*, 2007; Lutz *et al.*, 2009; Malkus *et al.*, 2009). Furthermore, mutant *PINK1* resulted in dysregulation of mitochondrial Ca^{2+} homeostasis giving rise to the increased production of ROS.

Parkin and PINK1 are known to work together in a pathway known as the PINK1/Parkin pathway. PINK1 levels are strictly controlled in healthy mitochondria by the continuous turnover of PINK1 with the assistance of mitochondrial membrane potential-dependent presenilin-associated rhomboid-like protein (PARL) cleavage (Jin *et al.*, 2010; Narendra *et al.*, 2010). PINK1 starts off as a 63kDa precursor protein in the cytosol and later becomes a 52kDa mature protein as it is translocated and imported

into the mitochondria. Following the import into mitochondria under normal physiological conditions, PINK1 is rapidly degraded and therefore confirms that these mitochondria are healthy (Figure 1.4 A).

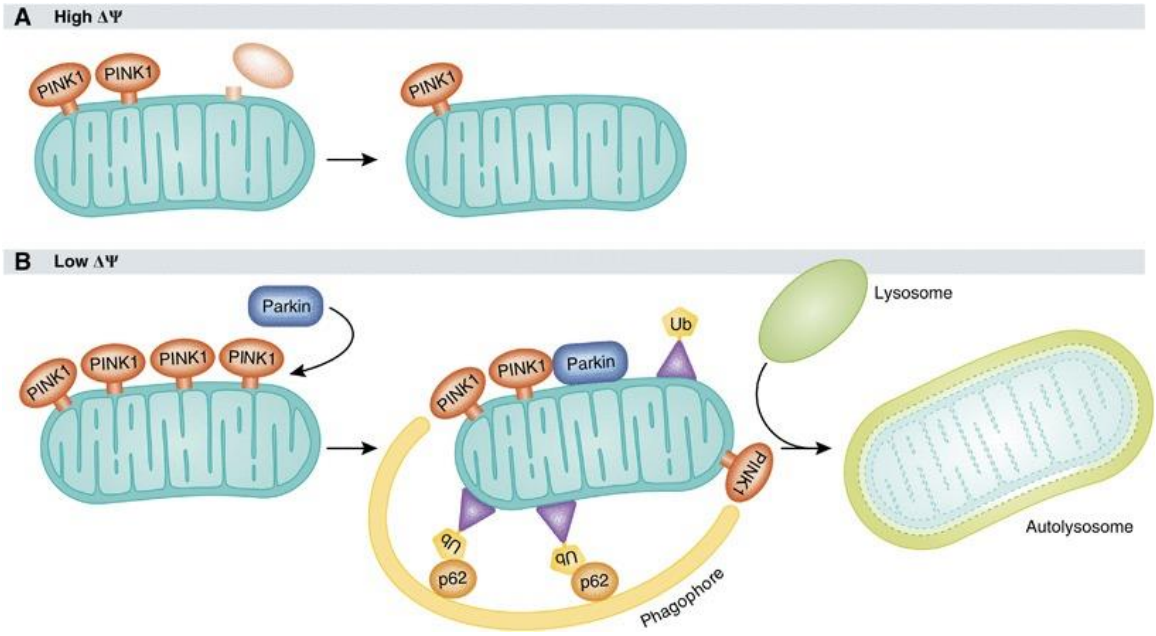

Figure 1.4 A representation of the PINK1/Parkin-mediated mitophagy. A) Under normal physiological conditions, when the mitochondrial membrane potential is high, PTEN-induced putative kinase 1 (PINK1) is imported into the mitochondria and degraded to maintain low levels of endogenous PINK1 in healthy mitochondria. **B)** When the mitochondrial membrane potential decreases under pathological conditions, PINK1 accumulates on the outer mitochondrial membrane recruiting Parkin through the cytoplasm to mitochondria. Parkin is responsible for ubiquitinating (Ub) several outer mitochondrial membrane proteins which are then recognized by autophagy protein, p62. These adaptor proteins link the ubquitinated cargo to the autophagosome. Damaged mitochondria are engulfed and upon fusion with lysosomes the content of the autolysosome is degraded. Abbreviations: P62, Sequestosome 1; ΔΨ mitochondrial membrane potential. Reproduced with permission from EMBO.(Exner *et al.*, 2012).

However, when mitochondria are stressed and the MMP is lost due to the treatment of cells with uncouplers such as the protonophore carbonyl cyanide m-chlorophenyl hydrazone (CCCP), or other external or internal stressors, the import of PINK1 is impaired causing it to accumulate on the OMM. This accumulation serves as a warning signal and recruits cytosolic Parkin to the OMM (Figure 1.4 B). Upon activation of selected stress-signaling pathways or blockade of the mitochondrial protein import, Parkin's E3 ubiquitin ligase activity is activated by the kinase activity of PINK1 which recruits cytosolic Parkin to stressed mitochondria (Bertolin et al. 2013). Parkin is subsequently responsible for the ubiquitination of several OMM proteins such as Porins, Mitofusin, and Miro proteins, which targets dysfunctional mitochondria for degradation (Chan *et al.*, 2011; Narendra *et al.*, 2012; Sarraf *et al.*, 2013). This process involves the degradation of OMM proteins and autophagy-dependent removal

of mitochondrial fragments, known as mitophagy (Lemasters, 2005; Park *et al.*, 2006; Narendra *et al.*, 2008, 2012).

Drosophila PD models also revealed that PINK1 and Parkin function to maintain mitochondrial dynamics, protecting the cell against oxidative stress and to maintain mitochondrial integrity (Clark *et al.*, 2006a; Park *et al.*, 2006; Pridgeon *et al.*, 2007; McLelland *et al.*, 2014; Li and Hu, 2015). This supports studies suggesting that mitochondrial dysfunction may be an important contributing factor in PD development (Schapira and Jenner, 2011; Lazarou *et al.*, 2012).

1.4 Role of the TOM complex and mitophagy in Parkinson's disease

In order for mitochondria to function properly, mitochondrial proteins, of which almost all are nuclear encoded and synthesized in the cytosol, are imported into the mitochondria through the Translocase of Outer Mitochondrial Membrane (TOM) complex (Figure 1.5). It has been shown that the import of precursor proteins into mitochondria generally occurs in a post-translational manner, and that cytosolic ribosomes responsible for translating mRNAs for mitochondrial precursor proteins are associated with the OMM (Eliyahu *et al.*, 2010; Dudek *et al.*, 2013). The mitochondrial targeting sequence (MTS) is in the precursor protein, often in the form of a cleavable N-terminal presequence and consists of 10-80 basic and hydrophobic amino acids (Roise and Schatz, 1988; Pfanner and Chacinska, 2002). Mitochondrial presequences form α-helices at the N-terminals and contain specific information that directs proteins to the mitochondria. In yeast the recruitment of mRNAs to the OMM is dependent on the outer membrane precursor protein receptors tom20 and tom70, two subunits of the TOM complex (Eliyahu *et al.*, 2010; Gadir *et al.*, 2011).

The TOM complex, consisting of TOM5, TOM6, TOM7, TOM20, TOM22, TOM40 and TOM70 (in humans), is responsible for mediating the import of nearly all mitochondrial proteins. This system is essential for mitochondrial function and it relies on a negative MMP (Chacinska *et al.*, 2009; Dudek *et al.*, 2013; Sokol *et al.*, 2014). The central part of the TOM complex is TOM40, an integral membrane protein with a β-barrel structure that forms the channel for precursor protein translocation across the OMM (Figure 1.5).

TOM20 serves as the first recognition site for presequence-containing proteins and thereafter they are transferred to TOM22 (the central receptor). Alternatively, TOM70 functions as the initial docking site for precursor proteins of Inner Mitochondrial Membrane (IMM) metabolite carriers after which they are also transferred to TOM22. Following successful recognition, the pre-proteins are inserted into the TOM40 channel and imported into the mitochondria (Figure 1.5). The targeting, import and

sorting of precursor proteins are dependent on specific import signals with the most common signal being the N-terminal extension known as the presequence. Both TOM20 and TOM70 function as quality control proteins, serving as initial docking sites for precursor proteins and they only allow proteins with the appropriate identification (target signal) to enter the mitochondria.

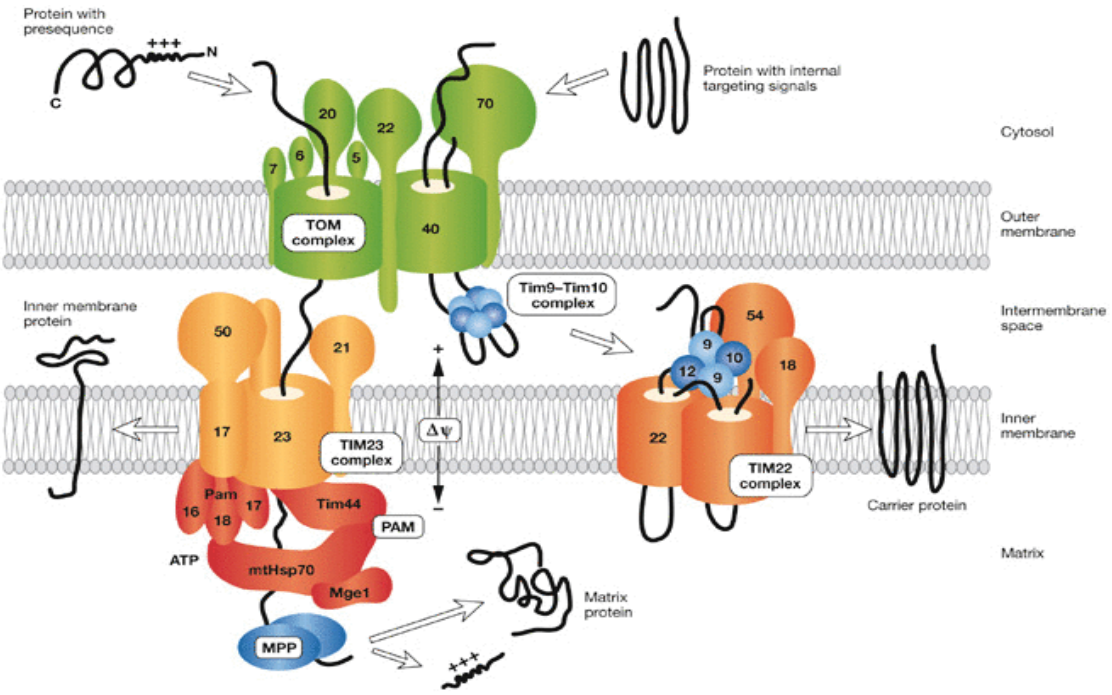

Figure 1.5 Schematic representation of mitochondrial protein import. Proteins containing pre-sequences are directed through the TOM complex, TIM23 complex and PAM to reach the mitochondrial matrix via TOM20 and TOM22. Proteins containing internal target sequences are recognized by TOM70 and translocated to TOM22 and through TOM40, the pore subunit of the TOM complex. Abbreviations: MtHsp70, matrix heat shock protein 70; PAM, presequence translocase-associated motor; TIM, translocase of the inner membrane; TOM, translocase of the outer membrane; ΔΨ, mitochondrial membrane potential. Reproduced with permission from EMBO (Bolender *et al.*, 2008).

Protein import into mitochondria through the TOM complex is essential for organelle biogenesis, and subsequent survival of the entire cell. Recent evidence has implicated the TOM complex in PD pathogenesis (Bender *et al.*, 2013). Also, when PINK1 accumulates at the OMM of dysfunctional mitochondria, it does so at the TOM machinery and recruits Parkin specifically to this complex (Lazarou *et al.*, 2012). Therefore, this suggest that the TOM machinery is a *key molecular switch* in the maintenance of healthy mitochondria via the PINK1/Parkin pathway and is of particular interest in the search for PD-causing pathways and possible therapeutic targets.

Although the role of the TOM complex and its individual subunits in the import of PINK1 is well-established due to studies showing the complex formation between PINK1 and the TOM subunits, the

exact import pathway of PINK1 remains to be elucidated (Lazarou *et al.*, 2012; Bertolin *et al.*, 2013; Kato *et al.*, 2013). Also, whether TOM activity is a deliberate decision in the activation of mitophagy is unclear (Sokol *et al.*, 2014). It has been postulated that when mitochondria becomes repolarized, the accumulated PINK1 on the OMM could be imported into mitochondria and thus rescue the organelle from mitophagy (Lazarou *et al.*, 2012). This import is believed to be initiated by the association between PINK1 and the TOM complex.

Impaired mitochondrial import through the TOM machinery was previously proposed to play a crucial role in the activation of the PINK1/Parkin-dependent mitochondrial clearance pathway. The core subunit of this complex, TOM40, is down regulated in PD patients midbrain samples and PD mouse models (Greene *et al.*, 2012; Bender *et al.*, 2013; Bertolin *et al.*, 2013). Bertolin and colleagues confirmed that PINK1 accumulates at the TOM complex when mitochondrial import is blocked and that Parkin is in close proximity to this complex; showing a strong positive Förster resonance energy transfer (FRET) signal with TOM70 (Bertolin *et al.*, 2013). This study also showed that PD-causing mutations in Parkin results in a weakened and disrupted interaction between Parkin and both TOM40 and TOM70 (Bertolin *et al.*, 2013). Subsequently, it was hypothesized that the weakened interaction between mutant Parkin and specific subunits of the TOM complex will lead to defective mitochondria not being cleared, thus acting as the primary pathogenic mechanism in autosomal recessive PD.

Importantly, LRRK2 is also known to interact with Parkin (Smith *et al.*, 2005). This interaction is confined to the cytosol and was identified for both WT and mutant forms of *LRRK2* using co-immunoprecipitation analysis. Smith and colleagues also observed an increase in cytoplasmic protein aggregation containing LRRK2 and enhanced Parkin-dependent ubiquitination of these protein aggregates when co-expressing Parkin and LRRK2 in cells (Smith *et al.*, 2005). Furthermore, the effect of Parkin on the ubiquitination of these protein aggregates could possibly be ascribed to the stimulation of Parkin's ubiquitin ligase activity via LRRK2 interaction; thus possibly linking LRRK2 to mitochondrial maintenance via a Parkin pathway. However, subsequent studies could not confirm a direct link between LRRK2 and Parkin (Dächsel *et al.*, 2006). These differences could possibly be due to inadequate biological tools such as non-specific antibodies or techniques with low sensitivity that were used in early studies.

The remaining sections of this Chapter will focus on evidence for LRRK2 playing an integral role in maintenance of healthy mitochondria, which forms the basis of this doctoral thesis.

1.5 Localization of LRRK2 to the mitochondria

LRRK2 is located predominantly in the cytoplasm of cells and has been shown to aggregate upon overexpression in mammalian cells (Smith *et al.*, 2005; Greggio *et al.*, 2006; MacLeod *et al.*, 2006) (Figure 1.6). Subsequent studies found LRRK2 to be associated with the mitochondria primarily in the OMM thus providing evidence for mitochondrial involvement for this protein (Biskup et al. 2006; West et al. 2005). Overexpression of LRRK2 in cultured cells also showed an associated with the OMM (West et al. 2005) and was subsequently confirmed when investigating endogenous LRRK2 in mammalian brain tissue (Biskup *et al.*, 2006).

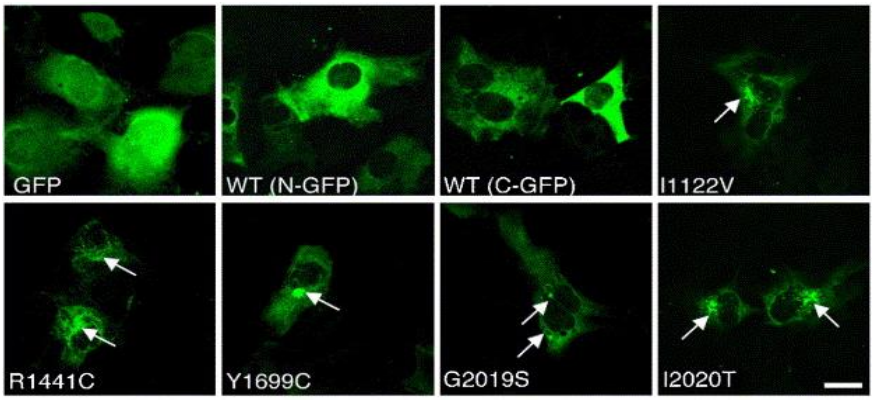

Figure 1.6 Cytoplasmic localization of overexpressed LRRK2. COS7 cells were transfected with LRRK2 (WT and mutant) that were either N-terminally (N-GFP) or C-terminally (C-GFP) tagged to GFP. GFP alone (top row, left) was located in the cytosol and nucleus whereas GFP-LRRK2 (top row, second and third panel) is localized mainly in the cytoplasm. Protein aggregates are observed upon overexpression of mutant LRRK2 (white arrows). Reprinted from (Greggio *et al.*, 2006) with permission from Elserivier.

Gloeckner and co-workers also found LRRK2 to be significantly associated with the OMM (Gloeckner *et al.*, 2006) when it was overexpressed in human embryonic kidney (HEK293) cells and subcellular fractionation and fluorescence microscopy was used to determine its exact localization. Fractionation results showed that LRRK2 was exclusively detected in the membranous fractions which were enriched in mitochondria and in microsomal membranes, suggesting that LRRK2 is strongly associated with or possibly attached to these organelles or structures in the cytoplasm. Fluorescence microscopy further showed that LRRK2 co-localizes with mitochondria, (when using TOM20 immunostaining as a mitochondrial marker) (Figure 1.7), the ER, the Golgi apparatus and the microtubular cytoskeleton.

Figure 1.7 LRRK2 co-localizes to the mitochondria. Immunofluorescence microscopy show that overexpressed GFP-tagged LRRK2 (green) co-localizes to mitochondria (red) in HEK293 cells. TOM20 (red) was used as the mitochondrial marker. Reproduced from (Gloeckner *et al.*, 2006) by permission of Oxford University Press.

1.6 LRRK2's involvement in mitochondrial dynamics

Although a variety of pathways have been suggested for the development of PD, the pathogenesis of this debilitating disease appears to concentrate on a small number of overlapping mechanisms including mitochondrial dysfunction and oxidative stress (Greenamyre and Hastings, 2004). The maintenance of mitochondria, including the continuous biogenesis and removal of damaged mitochondrial pools, are of upmost importance to normal cellular health and function. Failure to maintain healthy mitochondrial homeostasis has been implicated in development of PD, and is thought to be one of the hallmarks of neurodegeneration (Beal 1998; Chan 2006; Schon and Przedborski 2011; Narendra, Walker, and Youle 2012; Exner et al. 2012).

Mitochondrial function is highly dependent on the health of the mitochondrial pool. This is controlled by the continuous fission and fusion of mitochondria which is reliant on a variety of proteins including mitochondrial fission protein 1 (Fis1) and dynamin-like protein (DRP1), (responsible for fission), and mitochondrial dynamin-like GTPase 1 (OPA1), mitofusion 1 (Mfn1) and mitofusion 2 (Mfn2), (responsible for fusion dynamics) (Chan, 2006) (Figure 1.8). Mitochondrial fusion may play a protective role in neurons, whereas fission is likely to aid in enhancing the general dispersion of mitochondria throughout high energy dependent cells such as neurons (Chen and Chan, 2009).

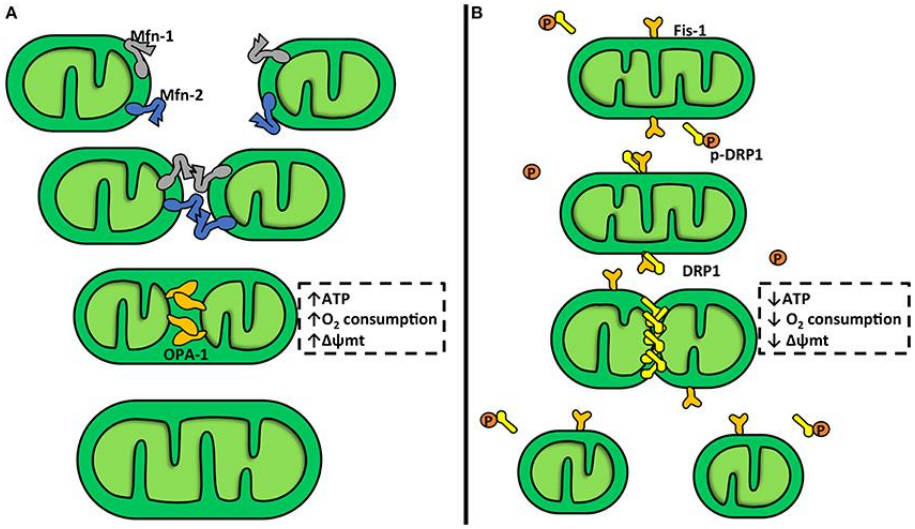

Figure 1.8: Illustration of mitochondrial dynamics. **A) Mitochondrial fusion**. Mitofusion-1 and 2 (Mfn1 and Mfn2) are transmembrane GTPases in the outer mitochondrial membrane (OMM). The C-terminals of these proteins are responsible for binding adjacent mitochondria to promote OMM fusion. Optic atrophy protein-1 (OPA-1) is a dynamin-related protein in the inner mitochondrial membrane (IMM). OPA-1 mediates the attachment and fusion of the IMM. Mitochondrial fusion is associated with an increase in the mitochondrial potential (ΔΨ), oxygen consumption, and ATP production. **B) Mitochondrial fission**. Two proteins, dynamin-related protein-1 (DRP1) and fission protein-1 (Fis1), are responsible for fission. DRP1 is a large cytosolic GTPase. Mitochondrial fission is associated with a decrease in ΔΨ, oxygen consumption, and ATP production. Reproduced with permission from (Chiong *et al.*, 2014).

Upon mitochondrial fusion, the outer and inner membranes of two organelles fuse together. This is followed by mixing of the mitochondrial matrix content, including the mixing of mitochondrial DNA (mtDNA) gene products within mitochondria. In mammalian cells, two GTPases located on the OMM known as mitofusins, Mfn1 and Mfn2, and one IMM dynamin family GTPase protein, OPA1, are essential for mitochondrial fusion. On the other hand, when mitochondria enter the process of fission (where mitochondria divide), a single dynamin family member, DRP1 (a mitochondrial fission regulator protein), is required (Smirnova *et al.*, 2001). It has been shown that mitochondrial fragmentation is caused by the increased recruitment of DRP1 (Labrousse *et al.*, 1999; Wang *et al.*, 2008b). DRP1 is largely a cytosolic GTPase which is recruited and localized to specific locations on the OMM; and binds to adaptor proteins such as Fis1 (Chan, 2006; Bliek *et al.*, 2013).

Interestingly, protein interactions between WT LRRK2 and the four main regulators of mitochondrial dynamics (DRP1, Mfn1, Mfn2 and OPA1) have been verified *in vitro* (Stafa *et al.*, 2014). LRRK2 has been linked to regulation of mitochondrial dynamics through a direct interaction with mitochondrial DRP1 (Wang *et al.*, 2012b). A study investigating the mitochondrial fragmentation caused by the expression of WT and G2019S *LRRK2* (Niu *et al.*, 2012) demonstrated specific interactions between both WT and mutant LRRK2 and DRP1 using co-immunoprecipitation analysis. Therefore, LRRK2 was responsible for

the recruitment of DRP1 to the OMM through cytosolic translocation, regulating mitochondrial dynamics (Niu *et al.*, 2012; Wang *et al.*, 2012b). These interactions were however independent of DRP1 activity, since LRRK2 was able to interact with the dominant-negative mutant form of DRP1 (K38A) (Wang *et al.*, 2012b).

Subsequently, the overexpression of both LRRK2 and DRP1 was shown to lead to the recruitment of DRP1 from the cytoplasm exclusively to the mitochondrial membrane (Niu *et al.*, 2012), and caused either rapid clearance of mitochondria, or the accumulation of mitochondria around the nuclei of cervical cancer (HeLa) cells. The co-dependence of LRRK2 and DRP1 on mitochondrial fragmentation was also interrogated using a knockdown model of DRP1 in HeLa cells (Wang *et al.*, 2012b). Surprisingly, when DRP1 expression was reduced mitochondrial fragmentation also declined, indicating that LRRK2-induced mitochondrial fragmentation is dependent on DRP1 expression.

To explain how LRRK2 activates DRP1 recruitment, researchers investigated the interactions between different forms of LRRK2 (including LRRK2 WT, LRRK2 G2019S and a kinase dead LRRK2 D1994A) and DRP1. DRP1 interacted with of both *LRRK2* WT and G2019S (Wang *et al.*, 2011; Niu *et al.*, 2012). However, the interaction was abolished when cells expressed *LRRK2* D1994A, indicating that the LRRK2-mediated DRP1 recruitment is dependent on the kinase activity of LRRK2. Therefore, the increase in LRRK2 kinase activity results in increased mitochondrial fission and decreased mitochondrial fusion.

Interestingly, transmitochondrial cytoplasmic hybrid cell lines (cybrids) showed that LRRK2 kinase activity increases DRP1 activation through phosphorylation activity (Esteves *et al.*, 2015). Cybrids were created by depleting the endogenous mtDNA of NT2 (NT2 rho0) cells with long term exposure to ethidium bromide, a chemical which inhibits mitochondrial DNA replication. PD patient or control platelet mitochondria were then isolated from blood and introduced into the mitochondria-depleted NT2 rho0 cells. Ultimately, these hybrid cells contained nuclear genes from the NT2 rho0 cells and mitochondrial genes from PD patients or controls. It has also been shown that *LRRK2* G2019S cybrids exhibit an increase in kinase activity, similar to previous studies, which the researchers believe is a compensatory response to already dysfunctional mitochondria (Cardoso and Esteves, 2015). When the kinase activity of LRRK2 was inhibited in these cells by LRRK2-IN-1, a potent inhibitor of LRRK2 activity, mitochondrial elongation was promoted and the level of phospho-DRP1 decreased. This triggered a reduction in DRP1-dependent mitochondrial fission which resulted in decreased mitophagy, ultimately causing accumulation of dysfunctional mitochondria. However, Luerman and co-workers showed LRRK2-IN-1 to be non-specific and to have off-target effects and thus highlights

the need to validate previous results on LRRK2 inhibition and to identify novel, and more specific inhibitors of LRRK2 (Luerman *et al.*, 2014).

The impaired mitochondrial function and morphology caused by *LRRK2* G2019S in patient derived fibroblasts further supports the idea of mitochondrial fission/fusion dynamics underlying the distinct phenotypic presentations of mutant *LRRK2*-affected PD patients (Mortiboys *et al.*, 2010; Wang *et al.*, 2012b), possibly in a PINK1/Parkin/LRRK2-associated manner. Stafa and colleagues subsequently proposed that the widespread distribution and multifunctional nature of LRRK2 could suggest a general housekeeping function in the regulation of membrane biogenesis and dynamics within neurons (Stafa *et al.*, 2014).

1.7 LRRK2's involvement in mitochondrial respiration and mitochondrial membrane potential

Oxidative phosphorylation within mitochondria results in the movement of protons and ions across the IMM, creating a voltage difference/gradient (Gottlieb *et al.*, 2003). The difference in electrical potential between inner and outer membranes is defined as membrane potential and MMP is essential for mitochondrial processes including the production of ATP, Ca^{2+} uptake, detoxification of ROS and general mitochondria functionality (Nicholls, 2004). Essentially, MMP is responsible for ATP synthesis since it is the driving force behind protons being pumped through the ATP synthase complex (complex V) (Figure 1.9). When MMP is decreased or disrupted, both ATP production and cellular integrity is compromised, whereas the total loss of MMP will cause mitochondrial permeabilization and ultimately lead to cell death.

Several studies have implicated LRRK2, and more specifically its kinase activity, in MMP disruption. For example, overexpression of *LRRK2* G2019S in a human neuroblastoma cell line (SHSY5Y) causes mitochondrial uncoupling leading to reduced MMP and increased O_2 consumption (Papkovskaia *et al.*, 2012). Similarly, MMP is reduced in cells expressing *LRRK2* WT and more significantly in cells expressing *LRRK2* G2019S and R1441C compared to control or vector cells (Wang *et al.*, 2012b).

Interestingly, MMP remained unchanged in cells expressing kinase dead forms of *LRRK2* (K1347A and D1994A) (Wang *et al.*, 2012b). An increase in intracellular ROS levels was also detected for *LRRK2* WT and more so for G2019S and R1441C mutant cells compared to non-transfected or empty-vector transfected control cells. The loss of MMP caused by either WT or mutant *LRRK2* overexpression has been reported in primary mouse cortical neurons, various cell lines as well as in fibroblasts from PD patients and is believed to play an essential role in the development of neurodegeneration

(Papkovskaia *et al.*, 2012; Wang *et al.*, 2012b; Cherra *et al.*, 2013). Furthermore, *ex vivo* models in the form of skin fibroblasts derived from PD patients showed that *LRRK2* G2019S exhibit markedly decreased MMP and total ATP production (Mortiboys *et al.*, 2010).

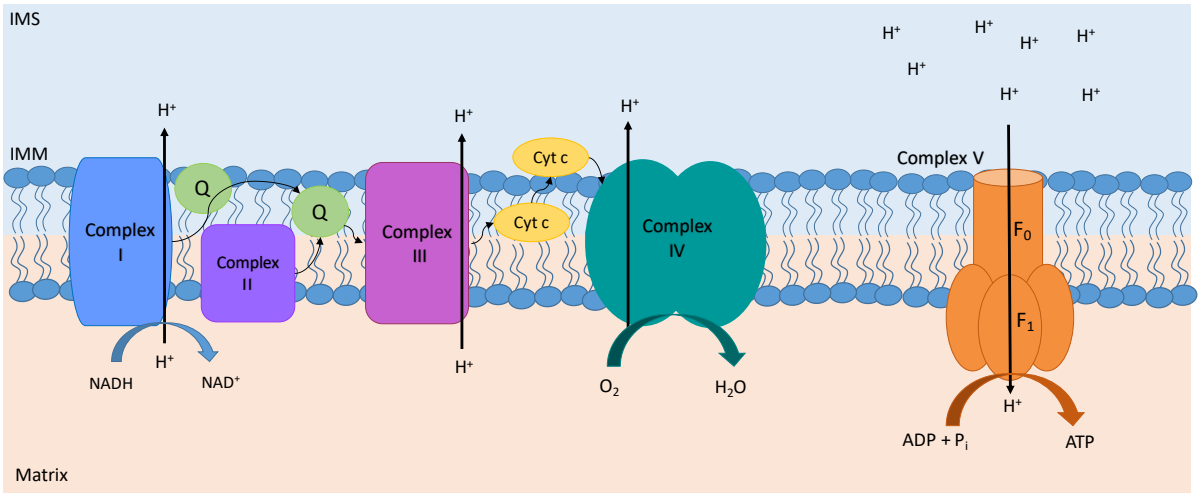

Figure 1.9 The mitochondrial electron transport chain (ETC). The mammalian ETC includes the NADH-ubiquinone oxidoreductase (complex I) and cytochrome bc_1 (complex III) enzymes responsible for proton-pumping and cytochrome c oxidase (complex IV) responsible for generating proton force required to drive F_1F_O-ATP synthase (complex V). Ubiquinone (Q), embedded in the Inner mitochondrial membrane (IMM), and soluble cytochrome *c* (Cyt c) in the Intermembrane space (IMS), mediates the electron transport between these complexes. Electrons from NADH enters complex I and are then passed through complex III and IV where molecular oxygen (O_2) is used to produce water (H_2O). As the electrons move from complex to complex, protons (H^+) are pumped from the mitochondrial matrix to the IMS. A proton gradient is generated across IMM to drive the protons back to the matrix through complex V (). These protons are used to generate adenosine triphosphate (ATP) from adenosine diphosphate (ADP) and inorganic phosphate (P_i).

Mitochondria are the main producers of ROS in mammalian cells and when mitochondria are dysfunctional, oxidative stress is increased through ROS production, subsequently leading to continuous fission and subsequently cell death (Lin and Beal, 2006). Mitochondrial dysfunction includes dysfunctional ATP production and increased oxidative stress as a results of an imbalance between ROS production and antioxidant activity (Hwang, 2013). ROS form part of a group of molecules that have a shortage of electrons in their outer orbital known as free radicals (Brand and Nicholls, 2011). O_2 is one of these molecules and contains two unpaired electrons in its outer orbital. ROS will scavenge these unpaired electrons in order to find stability, which leads to oxidation of these O_2 molecules. During oxidative phosphorylation and subsequent ATP production, hydrogen peroxide (H_2O_2) and superoxide (O_2^-) radicals are produced in the mitochondria. When mitochondrial dysfunction is induced, for example through mtDNA mutations or complex I inhibition, the production

of ROS is dramatically increased and leads to unwanted oxidation of lipids and proteins and subsequently causes cellular damage. Antioxidant mechanisms are not able to manage this rapid increase in ROS which later causes cytochrome *c* to be released into the cytosol, ultimately leading to cell death via apoptosis.

Oxidative stress and mitochondrial complex I inhibition were first found to be associated with PD when complex I deficiency was found to be present in the substantia nigra of PD patients (Parker *et al.*, 1989; Schapira *et al.*, 1989). Since then, many studies have focused on the involvement of mitochondrial function and ETC activity in PD development. Mitochondrial alterations were also observed when expressing *LRRK2* G2019S in transgenic mice (Ramonet *et al.*, 2011).

LRRK2 is known to bind to one of the most well-known H_2O_2 scavengers in the mitochondria known as peroxiredoxin 3 (PRDX3) (Angeles *et al.*, 2011). Mutant *LRRK2* enhances PRDX3 phosphorylation in cell cultures, consequently decreasing peroxidase activity and increasing cytotoxicity. This was later confirmed in a *Drosophila* model of PD (Angeles *et al.*, 2014). It was subsequently hypothesized that the enhanced phosphorylation and inhibition of PRDX3 antioxidant activity could be a mechanism involved in oxidative stress induced by the LRRK2 kinase mutant since the co-expression of PRDX3 and G2019S ameliorated G2019S induced peroxidase activity, neuronal cell death, shortened lifespan and mitochondrial defects. Oxidative stress may cause mutations in mtDNA and upregulate the apoptotic pathway in DA neurons. Previously, when *LRRK2* (WT and G2019S) was expressed in DA cells (SN4741) and treated with H_2O_2 to mimic oxidative stress, neurotoxicity as well as intracellular ROS (to a lesser extent) were increased in both instances, although G2019S presented a more severe phenotype (Heo *et al.*, 2010b). Similarly, it was shown that the overexpression of *LRRK2* WT and *LRRK2* G2019S significantly increase ROS levels in HEK293 cells (Niu *et al.*, 2012). The kinase dead form of *LRRK2* did not have any effect on ROS levels, indicating that the induction of oxidative stress via LRRK2 is dependent on kinase activity in this cell model. Additionally, iPSCs carrying G2019S show increased sensitivity to H_2O_2 exposure leading to an increase in the apoptotic marker, caspase 3 (Nguyen *et al.*, 2011). In contrast, Greggio and colleagues previously showed cellular toxicity in the absence of oxidative stress when over-expressing *LRRK2* G2019S in neuronal cell lines (Greggio *et al.*, 2006). Taken together, the evidence suggests that LRRK2 and its kinase activity are implicated in mitochondrial function leading to cellular toxicity however, its exact involvement in oxidative stress related pathways remains vague and in some cases, controversial.

Mitochondrial dysfunction also occurs as a result of alterations in the rate of mitochondrial respiration (Brand and Nicholls, 2011). Cells generally operate at basal respiration (which is controlled by ATP turnover and substrate oxidation) but when cellular stress is induced, the demand for cellular energy

is increased, requiring cells to function at maximal respiratory capacity. The difference between ATP production via oxidative phosphorylation at basal capacity and ATP production at maximal activity is known as the spare respiratory capacity (Desler *et al.*, 2012). Under normal physiological conditions, the spare respiratory capacity will provide cells with extra energy to manage cellular stress. However, when reserve respiratory capacity is not sufficient or able to provide the required energy, affected cells could be destined for cell death. Previously, the exhaustion of spare respiratory capacity has been linked to neurodegeneration in models of PD (Nicholls, 2008). Mitochondria are responsible for ATP production, to isolate excess Ca^{2+} from the cytoplasm, and to both produce and detoxify superoxide free radicals. When sodium (Na^{2+}), Ca^{2+} and other positively charged ions enter the *N*-methyl-d-aspartate receptor (NMDA receptor) on the membranes of nerve cells, a large energetic load is exerted on cells, sometimes utilizing the entire respiratory capacity of the mitochondria. Thus, even the slightest disruption in mitochondrial capacity for example caused by low concentrations of ETC inhibitors such as rotenone in models of PD, will exacerbate neuronal toxicity.

1.8 LRRK2's involvement in autophagy and mitophagy

Autophagy-related genes and their associated enzymes are responsible for mediating the three pathways involved in autophagy; macroautophagy, microautophagy and chaperone-mediated autophagy (CMA). The main pathway, macroautophagy (and typically referred to as autophagy), is an essential process which removes damaged cell organelles as well as unused or unwanted proteins (Klionsky and Emr, 2000; Glick *et al.*, 2010). Induced autophagy is essential in the initial stages of cellular stress but later becomes detrimental to the cell (Hayat, 2016). Macroautophagy is characterized by the formation of autophagosomes (Saito and Sadoshima, 2015). The formation of the autophagosome is induced by the autophagy-related gene (*Atg*6) also known as Beclin-1 (Bcl-1), ubiquitin-like conjugation reactions and interaction with the class III phosphoionositide-3-kinases (PI3KC3)/Vps34 (Kang *et al.*, 2011). This double membrane vesicle forms around the targeted cytoplasmic organelles or proteins and transports the engulfed material through the cytoplasm to the lysosome (Figure 1.10). The autophagosomes and lysosomes fuse together to form an autolysosome, causing the contents of the autolysosome to be degraded by the acidic lysosomal hydrolases. Mitophagy is a type of macroautophagy (Cheung and Ip, 2009; Saito and Sadoshima, 2015). Microautophagy comprises the direct engulfment of parts of damaged organelles or unused or unwanted proteins into the lysosome which is then followed by degradation of the cytoplasmic material.

The third pathway, CMA, is complex and specific and includes the recognition by the heat shock conjugate protein of 70 kDa (hsc70)-containing complexes. Therefore, in order for the CMA-substrate/chaperone complex to be formed, it is essential that the target protein contains the recognition site for hsc70 complex which will allow it to bind to the chaperone. The CMA substrate/chaperone complex translocates to the lysosomal membrane bound protein, which will recognize and bind with the CMA receptor (lysosomal-associated membrane protein 2A; LAMP-2A), allowing it to enter the organelle. Once recognized, the targeted substrate protein unfolds and translocates across the lysosomal membrane via the lysosomal hsc70 chaperone. This is a particularly selective pathway and is strictly regulated.

Two of the autophagy pathways, namely macroautophagy (including mitophagy) and CMA, have been implicated in PD (Zhu *et al.*, 2003; Martinez-Vicente *et al.*, 2008; Ashrafi and Schwarz, 2013). Zhu and colleagues suggested a link between mitochondrial dysfunction, autophagy and the MAP kinase/ERK signaling pathway. Although SNCA can be degraded via CMA, mutant SNCA blocks the lysosomal translocation and thus disrupts SNCA degradation via the CMA pathway (Zhu *et al.*, 2003; Martinez-Vicente *et al.*, 2008). Several other studies have implicated LRRK2 in the macroautophagy pathway showing LRRK2 localizing to lysosomal compartments and membranous structures (Biskup *et al.*, 2006; Alegre-Abarrategui *et al.*, 2009; Gómez-Suaga *et al.*, 2012). It has also been noted that the large protein structure of LRRK2 contains several putative CMA motifs and that LRRK2 may potentially be a substrate for CMA, similar to that of SNCA (Orenstein *et al.*, 2013). Upon further investigation it was shown that not only could *LRRK2* WT and *LRRK2* G2019S be degraded via CMA, but that high levels of WT *LRRK2* were able to inhibit CMA. An increase in the translocation complex component, LAMP-2A, was observed as a response to CMA blockage via LRRK2. This increase in LAMP-2A levels was also detected in brains of *LRRK2* transgenic mice and *LRRK2* G2019S mutant patients. Orenstein and co-workers confirmed that SNCA and LRRK2 function in similar pathways, working together to inhibit the typical degradation of dysfunctional proteins via CMA. The inhibition of degradation subsequently leads to the accumulation of unwanted proteins such as SNCA which has previously been suspected to underlie the development of PD.

The majority of evidence has associated autophagy with a cytoprotective role in cells such as neurons. Autophagy has been shown to play a preventative role in Alzheimer's disease, Huntington's disease, spinocerebellar ataxia and some forms of familial PD and is essential for neuronal homeostasis (Komatsu *et al.*, 2006; Zhang *et al.*, 2013) where the removal of dysfunctional proteins and organelles are believed to aid in cell survival. However, others believe that autophagy is an essential promoter of non-apoptotic programmed cell death (Anglade *et al.*, 1997; Tsujimoto and Shimizu, 2005; Ghavami

et al., 2014). More recent studies showed that LRRK2 and autophagy is directly associated with neurodegeneration (Scott *et al.*, 2007; Plowey *et al.*, 2008; Manzoni *et al.*, 2013a, 2013b; Saha *et al.*, 2015). Therefore, it is likely that cell damage and cell death can occur either due to an increase or a decrease in autophagic flux, which can be defined as the rate of autophagic degradation (Nelson and Shacka, 2013; Loos *et al.*, 2014). Although there is a lot of controversy surrounding the role of autophagy in cellular health, the maintenance of normal autophagic function and balance is crucial for all cells, especially non-dividing neuronal cells since the dysregulation of autophagy can significantly contribute to neurodegeneration (Nixon *et al.*, 2005; Wang *et al.*, 2006; Janda *et al.*, 2012).

Mutations in the functional domains of LRRK2 lead to alterations in markers for autophagy-lysosomal functions when compared to WT *LRRK2* cells (Plowey *et al.*, 2008; Alegre-Abarrategui *et al.*, 2009; Ramonet *et al.*, 2011; Bravo-San Pedro *et al.*, 2013). LRRK2's regulatory role in autophagy response was investigated using human neuroglioma cells (H4), SHSY5Y as well as HEK293 cells that were exposed to the well-known LRRK2 inhibitor, LRRK2-IN-1 (Manzoni *et al.*, 2013a). An increase in the autophagic marker light chain type 3 (LC3 II) was observed, and was later ascribed to autophagy induction, thus providing more evidence for the involvement of LRRK2 kinase activity in autophagy. When autophagy is induced, the cytosolic from of LC3 (LC3 I) is converted to LC3 II. LC3 II is then integrated into the lipid membrane of the autophagosomes, after which it is subsequently degraded with the autophagolysosome (Figure 1.10). Therefore, the amount of LC3 II present in the samples corresponds to the number of autophagosomes present (Mizushima and Yoshimori, 2007).

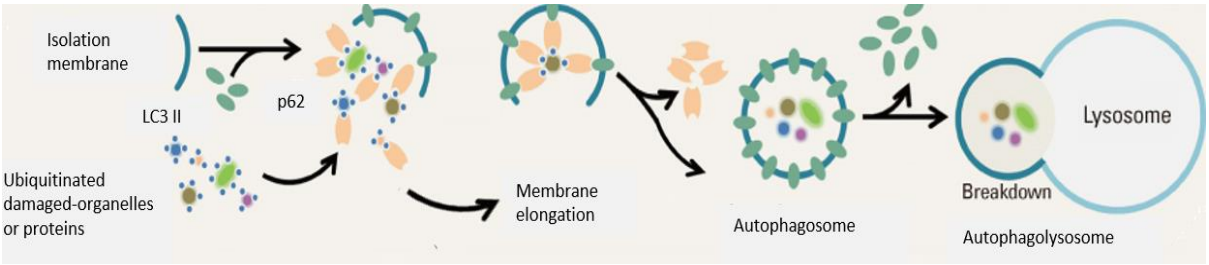

Figure 1.10 Schematic diagram of macroautophagy. Autophagy is initiated by the formation of an isolation membrane. P62 molecules binds ubiquitinylated proteins which are transported to the autophagosome through the interaction between p62 and LC3 II. The autophagosome fuse to the lysosome to form an autophagolysosome. Reproduced with permission from (Choi and Kim, 2013).

Previously, Manzoni and co-workers investigated whether autophagy is involved in a PD model (Manzoni *et al.*, 2013b). PD patient derived fibroblasts carrying the G2019S, R1441G and Y1699C mutations were collected and results confirmed that these mutations in the kinase, ROC and COR domains of LRRK2 caused a significant disruption in autophagic response to starvation, supporting a

pathogenic mechanism in the autophagic-lysosomal pathway. Similar results were reported by others (Sánchez-Danés *et al.*, 2012; Bravo-San Pedro *et al.*, 2013). These studies used patient fibroblasts and neurons derived from iPSCs of patients carrying the G2019S mutation which supported the hypothesis that a causal link exists between impaired autophagy and the development of PD.

Interestingly, Esteves and co-workers recently considered the impact of inhibiting LRRK2's kinase activity in PD cellular function and showed that the inhibition of LRRK2 decreased normal fission dynamics (Esteves *et al.*, 2015). This resulted in elongation of the mitochondrial networks which contributed to the inadequate degradation of dysfunctional mitochondria. Furthermore, the inhibition of LRRK2 stimulated the clustering of lysosomes around the nucleus through Rab7 which is said to impede autophagosome degradation. The Rab family proteins, only active in the GTP-bound form, are responsible for regulating the transport and fusion of autophagosomes and recently a study revealed that LRRK2 regulates a subset of Rab GTPases *in vivo* and *in vitro* (Bento *et al.*, 2013; Toyofuku *et al.*, 2015; Steger *et al.*, 2016). Although the exact mechanism by which LRRK2 interacts with Rab7 remains unclear (Esteves and Cardoso, 2016), it has been shown that LRRK2 acts as a negative regulator of Rab7 (Beilina *et al.*, 2014) and that this protein is mainly responsible for the perinuclear localization of lysosomes (Bucci *et al.*, 2000; Dodson *et al.*, 2012). The inhibition of LRRK2 kinase activity was also shown to reduce autophagic degradation, highlighting the importance of this domain in autophagy regulation (Schapansky *et al.*, 2014). Schapansky and others also demonstrated that silencing endogenous LRRK2 gives rise to autophagy induction deficits via the stimulation of toll-like receptor 4 (TLR4) in macrophages. This study, along with others, demonstrates the importance of LRRK2 in the regulation and control of autophagy (Anglade *et al.*, 1997; Plowey *et al.*, 2008; Alegre-Abarrategui *et al.*, 2009; Ramonet *et al.*, 2011; Tong *et al.*, 2012; Manzoni *et al.*, 2013b)

In summary, LRRK2's involvement in autophagy has long been an intriguing area of study, especially with respect to neurodegeneration and neurodegenerative diseases. Numerous studies have implicated WT and mutant forms of *LRRK2* in this highly dynamic and coordinated cellular process, providing support for the premise that LRRK2 contributes to the pathophysiology of PD by functioning in an autophagy-dependent pathway.

1.9 The present study

Evidence provided in the preceding sections supports the link between LRRK2 and mitochondrial function. Although LRRK2 has been the focus of many studies, more research is required to elucidate additional functions and roles of this multifaceted protein. Given the overlapping evidence of LRRK2, PINK1 and Parkin's involvement in mitochondrial (dys)function, mitochondrial clearance and general

mitochondrial homeostasis we believe that LRRK2 could function in pathways similar to those of Parkin and PINK1. Furthermore, since Parkin and PINK1 are known to associate with the TOM complex (Bertolin *et al.*, 2013; Kato *et al.*, 2013) and to interact with LRRK2 (Venderova *et al.*, 2009), we hypothesize that LRRK2 could possibly also associate with the TOM protein complex similar to PINK1 and Parkin.

Recently, members of our group identified a novel variant (Q2089R) in *LRRK2*. This variant is located in the kinase domain of LRRK2, the same domain as G2019S, and warrants further investigation. It was therefore hypothesized that Q2089R would affect kinase activity and that mutations in *LRRK2* will influence metabolic activity, mitochondrial function and autophagy. Additionally, we postulated that LRRK2 may also interact with subunits of the TOM protein complex, which could suggest a mechanistic link between this protein complex, mitochondrial dysfunction and PD development.

Therefore, the aim of the present study was to functionally characterize WT and mutant LRRK2 (Q2089R and G2019S) using a variety of techniques and approaches, such as basal and stress-induced growth conditions using DMSO and CCCP (a potent mitochondrial uncoupler) respectively, in different cellular models. Also, we aimed to investigate the potential association between WT LRRK2 and the TOM protein complex. The aim was achieved through the following objectives:

1. To determine the frequency of the *LRRK2* Q2089R variant in South African PD patients and controls using TaqMan™ allelic discrimination.
2. To use *in silico* tools including SIFT, Polyphen, Mutation Taster, Combined Annotation Dependent Depletion (CADD) scores, Project Hope, SWISS-MODEL and Modeller to predict the effect of Q2089R on protein folding and function.
3. To determine whether the kinase activity of LRRK2 is affected by Q2089R using autophosphorylation (as an indicator of kinase activity) in HEK293 cells overexpressing Q2089R.
4. To investigate the effect of the common G2019S mutation and the Q2089R variant on cellular metabolic activity in transfected HEK293 cells and patient-derived fibroblasts using an MTT assay.
5. To investigate the effect of G2019S and Q2089R on mitochondrial membrane potential in transfected HEK293 cells and patient-derived fibroblasts under both normal and stressed-induced conditions (CCCP-treated) using the JC-1 assay.
6. To study the effect of G2019S and Q2089R on mitochondrial respiration and glycolysis in transfected HEK293 cells and patient-derived fibroblasts using the Seahorse extracellular flux analyzer.

7. To determine the effect of G2019S and Q2089R on autophagy in transfected HEK293 cells and patient-derived fibroblasts using autophagic markers, LC3 II and P62, and Western blot analysis.
8. To determine if WT LRRK2 co-localizes and interacts with specific subunits of the TOM protein complex using
    a. Confocal microscopy in transfected COS7 cells.
    b. Super Resolution Structured Illumination Microscopy (SR-SIM) in transfected HEK293 cells under normal and stress-induced conditions.
    c. Co-immunoprecipitation (Co-IP) analysis in transfected HEK293 cells under normal and stressed-induced conditions.

Chapter 2: Materials and Methods

Contents

2.1 Summary of Methodology

A broad outline of the methodology used in the present study is shown in figure 2.1.

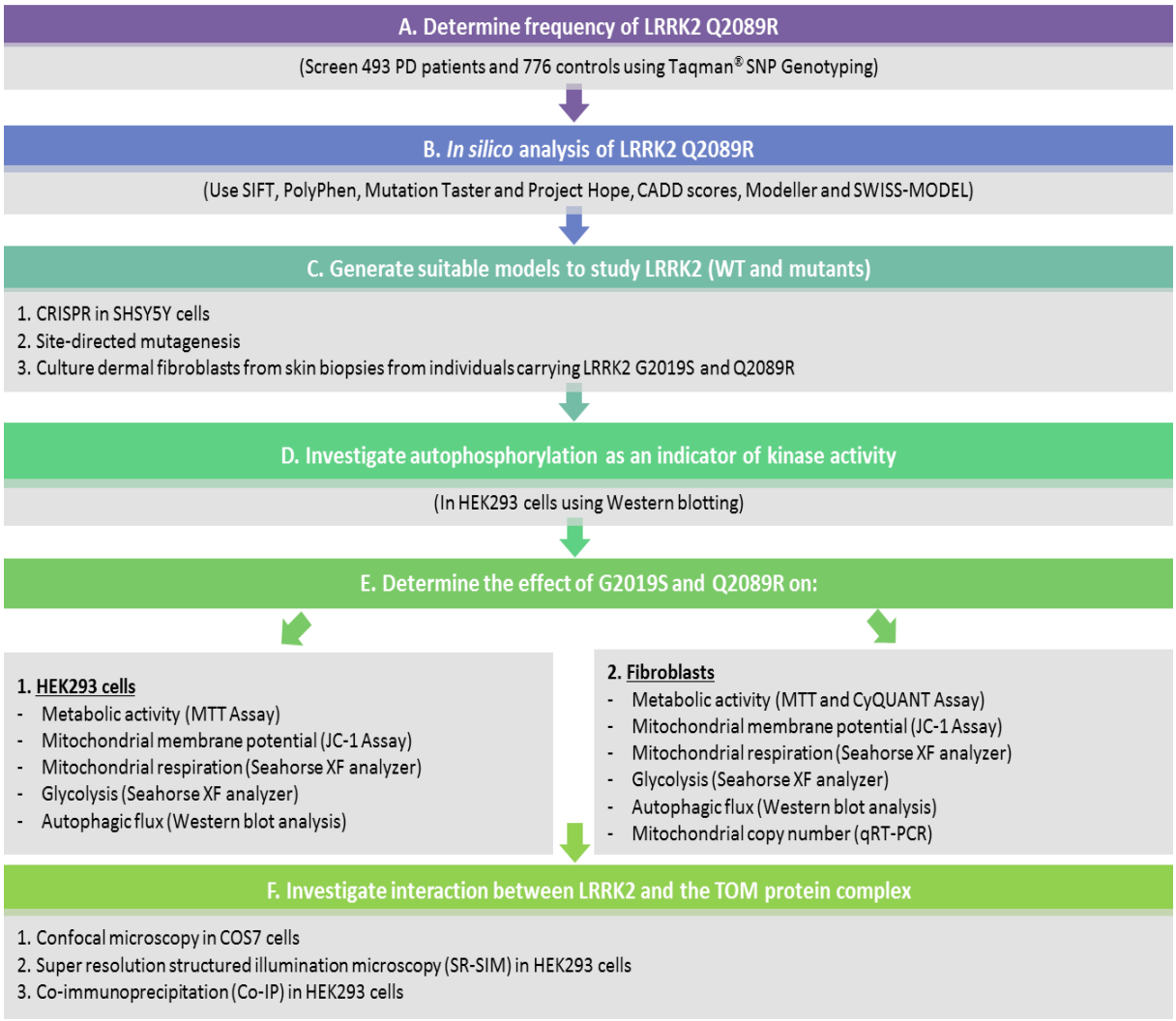

Figure 2.1 A schematic outline of the techniques and approaches used in the present study

2.2 Constructs, bacterial strains, cell lines and primary cells

2.2.1 Constructs

2.2.1.1 Commercially available constructs

Two commercially available constructs cloned into the pcDNA-DEST53 vector (Appendix I), a kind gift from Dr. Mark Cookson (Addgene, www.addgene.org, United States) were used for overexpression studies. One contains the full length wild type (WT) sequence of *LRRK2* (pDEST53 *LRRK2* WT, Addgene plasmid #25044) and the other contains the full length sequence of *LRRK2* G2019S in the pcDNA-DEST53 vector backbone (*LRRK2* G2019S, Addgene plasmid #25045). Additionally, a reporter gene, β-glucuronidase (*GUS*), was cloned in-frame into the pcDNA-DEST53 vector and used as the control plasmid in transfection experiments. LRRK2 as well as GUS was tagged to the GFP.

2.2.1.2 Generation of construct using site-directed mutagenesis

The Q5® Site-Directed Mutagenesis Kit (New England Biolabs® Inc., United States) was used to generate pDEST53 *LRRK2* Q2089R according to the manufacturer's instructions. In brief, the pDEST53 *LRRK2* WT plasmid (Addgene plasmid #25044) was used as template DNA in a PCR reaction with a mutagenic forward primer, containing the single base pair change that leads to the generation of the Q to R substitution, and back-to-back reverse primer (Figure 2.2 and Table 2.1)

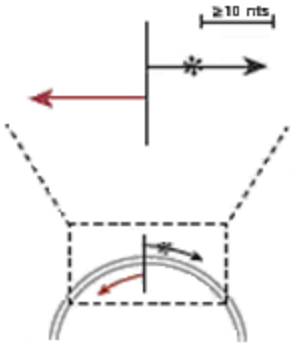

Figure 2.2 Q5® site-directed mutagenesis primer design. In order to generate a single base pair change, a mutagenic forward (black arrow) and a back-to-back reverse (red arrow) was designed. Taken from https://www.neb.com/products/e0554-q5-site-directed-mutagenesis-kit

Table 2.1 Primer sequences used to generate the novel *LRRK2* Q2089R construct

Primer	Sequence (5'-3')	Tm (°C)	Ta (°C)
Q5 Q2089R Forward	5'- TAG AAA TAC GAG GAA AAT TAC CTG ATC C -3'	54.6	57
Q5 Q2089R Reverse	5'-ATT CAT CAA ACT CAT TTG GAA ACT TCA AAC -3'	55.4	

The blue G indicates the variant base pair that will be introduced during site-directed mutagenesis. Abbreviations: A, adenine; C, cytosine; G, guanine; T, thymine; Ta, annealing temperature; ˚C, degrees Celsius.

Following the PCR reaction according to cycling conditions in Table 2.2, the kinase, ligase and DpnI enzyme mixture was added to the PCR product and incubated at room temperature for five minutes. This mixture is used to efficiently phosphorylate, ligate and circularize the new construct and remove the template construct. After the incubation period, 5µl of reaction mixture was used for bacterial transformation.

Table 2.2 PCR cycling conditions for generation of Q5® site-directed mutagenesis construct

Step	Temperature	Time
Initial denaturation	98°C	30 seconds
25 cycles	98°C 57°C 72°C	10 seconds 30 seconds 7 minutes
Final extension	72°C	2 minutes
Hold	4°C	∞

Abbreviations: °C, Degrees Celsius.

2.2.2 Bacterial strains

In order to propagate the desired constructs, the *Escherichia coli* (*E.coli*) DH5α bacterial strain was transformed. Transformed bacterial colonies were selected based on their ability to grow on LB agar plates (Appendix II) containing appropriate antibiotics. When selecting for the pDEST53 vector, Ampicillin (Amp) was used as selection antibiotic. Colonies containing the correct plasmids were identified by bacterial colony PCR using gel electrophoresis and sequencing with the appropriate exonic primers (Table 2.4).

2.2.3 Cell lines

The human neuroblastoma SHSY5Y cell line was purchased from the European Collection of Cell Cultures (ECACC, United Kingdom) and used for CRISPR-Cas9 genome editing. The SHSY5Y cell line is routinely used as a model of neuronal function as they are adrenergic in phenotype but also express dopaminergic markers. The human embryonic kidney 293 (HEK293) cell line was used for all overexpression studies, functional assays, super resolution structured illumination microscopy (SR-SIM) and co-immunoprecipitation (Co-IP) analysis since they are more amenable to transfection than SHSY5Y cells. HEK293 cells were purchased from American Type Culture Collection (ATCC, United States). The COS7 cells were a kind gift from Dr. Olga Corti and were used to study subcellular co-localization using confocal microscopy since mitochondria are easily visible in these cells.

2.2.4 Generation of CRISPR-Cas9 cell line

In order to generate a cell line endogenously expressing either *LRRK2* G2019S or *LRRK2* Q2089R, the GeneArt® CRISPR Nuclease Vector Kit was purchased from Invitrogen™ (United States) and used according to the manufacturer's instructions. This kit facilitates the generation of constructs that express non-coding guide RNA (gRNA) including Clustered Regularly Interspaced Short Palindromic Repeats (CRISPR) RNA, a target complementary CRISPR RNA (crRNA), an auxiliary trans-activating crRNA (tracrRNA) and the Cas9 nuclease to be used in CRISPR mediated gene editing in mammalian cells. The crRNA and tracrRNA acts as short guide RNAs to target the Cas9 nuclease to specific genomic loci. GeneArt® CRISPR Nuclease Vectors with Orange Fluorescent Protein (OFP) allows for Fluorescence-activated cell sorting (FACS) of Cas9 and CRISPR RNA expressing cell populations using flow cytometry. The linearized GeneArt® CRISPR Nuclease Vectors provide a rapid and efficient way to clone double-stranded oligonucleotides encoding a desired CRISPR RNA target into an expression cassette that allows targeting of the Cas9 nuclease in a sequence specific manner.

Genome editing involves the use of engineered nucleases in conjunction with endogenous repair mechanisms to insert, delete, or replace DNA sequences from a specific location in genomic DNA (gDNA). Engineered nucleases induce a double stranded break (DSB) at a specific location in the genome, after which endogenous repair mechanisms repair the break via non-homologous end joining (NHEJ) or homology directed repair (HDR) (Appendix III, Figure 1). Imprecise NHEJ-mediated repair can produce insertion and/or deletion mutations of variable length at the site of the DSB. HDR-mediated repair can introduce precise point mutations or insertions from a single-stranded or double-stranded DNA donor template. Essential for cleavage is a sequence motif immediately downstream on the 3' end of the target region, known as the protospacer-adjacent motif (PAM). The PAM is present in the target DNA, but not the crRNA that targets it. The PAM sites selected in exon 41 and 42 of *LRRK2* are shown in Appendix III, figure 3.

In brief, a target sequence ranging from 19 to 20 nucleotides in length adjacent to a PAM sequence on the 3' end of the target sequence was selected. Thereafter, the crRNA specific oligonucleotide primers were designed with the top strand oligonucleotide containing the specific top stand 3' overhang (Appendix III, Figure 2A and Table 1) and the bottom strand in the reverse complement containing the specific bottom stand 3' overhang (Appendix III, Figure 2B and Table 1). Annealing the two single-stranded oligonucleotides results in a double-stranded oligonucleotide with compatible ends for cloning into the GeneArt ® CRISPR Nuclease OFP Vector (Appendix III, Figure 2C). Following annealing and ligation reactions, the GeneArt ® CRISPR Nuclease OFP Vectors were transformed into *E.coli* (DH5α). Successfully transformed colonies were cultured, plasmid DNA extracted and sequenced

for sequence verification. These vectors could then be used to transfect the mammalian cell line of choice (SHSY5Y in this study) along with specifically designed mutant donor DNA templates for CRISPR genome editing (Appendix III, Table 1).

2.2.5 Primary cell lines

Primary cell lines derived from diseased and healthy control individuals are widely used as a cellular model, especially in PD. The use of *ex vivo* models is minimally invasive and serves as a useful tool to study disease-related cellular phenotypes, creating a model system with the desired mutation/variant and age-accumulated cellular changes (Auburger *et al.*, 2012). In the present study skin biopsies were obtained from individuals carrying either *LRRK2* G2019S or *LRRK2* Q2089R (Table 2.3). Primary dermal fibroblasts were derived from these skin biopsies. Five WT control individual fibroblast samples were also collected through the course of this study (Table 2.3). The control individuals had no history of neurological disease and were confirmed to not harbor G2019S or Q2089R. It should be noted that not all WT fibroblast samples were available for all functional assays (Table 2.3, last column).

2.3 Culturing of cells

2.3.1 Isolation of dermal fibroblasts from skin biopsies

Dermal fibroblasts were isolated by means of skin punch biopsies taken from individuals carrying either WT or mutant/variant *LRRK2*. Skin punch biopsies were performed by a registered nurse at Tygerberg Hospital (Cape Town, South Africa), after which dermal fibroblast cell lines were established by Unistel Medical Laboratories (Pty) Ltd. (Cape Town, South Africa). The 2mm x 2mm skin punch biopsies were taken from the inner lower arm and cultured in a sterile tissue culture environment. A volume of 300µl collagenase (Sigma-Aldrich, United States) per 1ml culture media of was added to the biopsy and incubated for one hour at 37°C with manual agitation in a 15ml polypropylene tube. The suspension was centrifuged at 160 x g (1200rpm) for 10 minutes in a Sorvall® GLC-6 general laboratory centrifuge (Separations, South Africa). The supernatant was discarded and the pellet resuspended in 5ml fibroblast isolation media (Appendix II), and the suspension transferred to a CellBind® T25 tissue culture flask (Corning Inc., United States). Culture flasks were incubation at 37°C in in a Farma thermosteri-cycle 5% CO_2 humidified incubator (Farma International, United States).

Table 2.3 List of fibroblast samples used in the present study

Lab ID	Ethnicity	Male/Female	AAO (years)	DOB	AAB	Mutation/ Variant	Assay
***LRRK2* WT**							
WT4	White	Female	unaffected	2013	54	n/a	• JC-1 Assay • Metabolic activity • Autophagic flux
WT525	Mixed ancestry	Male	unaffected	2016	77	n/a	• Autophagic flux • Mitochondrial respiration
WT5	White	Male	unaffected	2014	67	n/a	• Mitochondrial respiration
WT251	Mixed ancestry	Female	unaffected	2015	53	n/a	• Mitochondrial respiration
WT260	Mixed ancestry	Female	unaffected	2015	57	n/a	• Mitochondrial respiration
***LRRK2* mutant/variant**							
G2019S	White	Female	42	2014	75	*LRRK2* G2019S	• JC-1 Assay • Metabolic activity • Autophagic flux • Mitochondrial respiration
Q2089R	Afrikaner	Male	unaffected*	2015	47	*LRRK2* Q2089R	• JC-1 Assay • Metabolic activity • Autophagic flux • Mitochondrial respiration

Abbreviations: AAO, age at onset; DOB, date of biopsy; AAB, age at biopsy; n/a, not applicable; *skin biopsy collected from the son of the proband who was unaffected at the time.

2.3.2 Culture of cells from frozen stocks

Frozen cells (commercial cell lines or human derived fibroblasts) were rapidly thawed by immersing the cryovial in a waterbath at 37°C for 3 to 5 minutes. The vial was then sterilized with 70% ethanol and placed in the Esco Airstream® Class II Biohazard Safety cabinet (Esco Technologies Inc., United States) to be cultured.

2.4 Transformation and transfection of plasmids into prokaryotic and eukaryotic cells

2.4.1 Bacterial plasmid transformations

Prior to transforming plasmids of interest into the bacteria, tubes containing 200µl aliquots of *E.coli* DH5α cells were removed from the -80°C freezer and thawed on ice for 20 minutes. Once the cells had thawed, 5µl of plasmid preparation was added to the tube and the mixture was incubated on ice for an additional 20 minutes.

Following this incubation step, the samples were heat-shocked for exactly 45 seconds at 42°C in a heating block (Dry Block Heater HB2) (Hägar designs, South Africa). The samples were removed and incubated at room temperature for two minutes. Following this, 1ml of LB media (Appendix II) was added to each sample and incubated at 37°C for one to two hours shaking at 200rpm in a YIH DER model LM-530 (Scilab Instrument Co., Ltd., Taiwan) shaking incubator. The samples were subsequently centrifuged for four minutes in a bench top centrifuge (Labnet International Inc., United States). Next, 200µl of the supernatant was drawn off with a pipette and the rest discarded. The 200µl supernatant was used to resuspend the pellet and plate the sample on LB agar plates (Appendix II) containing the appropriate antibiotic. The plates were inverted and incubated for 16 hours at 37°C in a model 329 stationary CO_2 incubator (Former Scientific, United States).

2.4.2 Transfection of cell lines

COS7 and HEK293 cells were seeded at optimized densities in specific sterile cell culture plates (Appendix IV, Table 1) and transfected using either Lipofectamine2000 (Invitrogen™, United States) or DMRIE-C transfection reagent (Invitrogen™, United States). Several experiments were performed to optimize transfection efficiency including using different transfection reagents (NanoJuice® Merck Milipore, TransIT® Mirus Bio and Amaxa® Nucleofector™ Lonza) at different concentrations with various DNA concentrations. The HEK293 cells were subsequently transiently transfected using the Lipofectamine2000 transfection reagent at optimized conditions which can be seen in Appendix IV, Table 2. In brief, depending of the volume of the culture plate, optimized concentrations of plasmid

DNA and volumes of Lipofectamine2000 were separately incubated with a pre-determined volume of serum free media (SFM) for five minutes at room temperature (Appendix IV, Table 2). Thereafter, the two volumes were combined, gently mixed and incubated for 20 minutes at room temperature. Subsequently, a volume equal to the transfection volume was removed from each well and the transfection mixture added dropwise to each well and plates incubated at 37°C, 5% CO_2. After six hours the media was removed and replaced with pre-warmed complete media. Cells were further incubated overnight. The transfection efficiency was determined by staining the transfected cells with a GFP antibody (Appendix IV, Table 7, ab290) and the nucleic acid stain (Hoechst H-33342). Three replicate transfections were used and the GFP-positive cells and nuclei in a minimum of five fields in three different wells were counted. The efficiency was determined by reporting the percentage GFP-positive cells to the total amount of cells counted.

The COS7 cells were transiently transfected using the DMRIE-C transfection reagent at optimized conditions which can be seen in Appendix IV, Table 3. In brief, 1µg of plasmid DNA and 0.7µl of DMRIE-C transfection reagent were separately incubated with 75µl of SFM for 30 minutes at room temperature (Appendix IV, Table 3). Thereafter, the two volumes were combined, gently mixed and incubated for another 30 minutes at room temperature. Subsequently, all of the media was removed from the 24-well culture plates and replaced with 150µl transfection mixture and plates incubated at 37°C, 5% CO_2. After four to five hours the transfection media was removed and replaced with pre-warmed complete media followed by overnight incubation at 37°C, 5% CO_2.

2.5 DNA extraction

2.5.1 Bacterial plasmid purification using PureYield™ Plasmid Miniprep System

The specific *E.coli* colonies containing the plasmids of interest were inoculated in 50ml polypropylene tubes containing 10ml of LB media (Appendix II) as well as the appropriate antibiotic. The cultures were incubated at 37°C shaking in a YIH DER model LM-530 (Scilab Instrument Co., Ltd., Taiwan) incubator at 250rpm overnight. The following day the cultures were centrifuged for 10 minutes at 1250 x g (2500rpm) in an Eppendorf model 5810/5810R centrifuge (Eppendorf, United States) and the supernatant discarded. The plasmid DNA was extracted from the pellets using the PureYield™ Plasmid Miniprep system (Gene Tech Co., Ltd., Hong Kong) as indicated by the manufacturer's instructions. After purification, 2µl of the plasmid preparation was used to determine the purity and concentration of the sample by using a Nanodrop Spectrophotometer (Thermo Fisher Scientific, United States) and the 260/280 (>1.8) and 260/230 (>2.0) ratios. The remainder of the product used for transfection into the HEK293, SHSY5Y or COS7 cell line.

2.5.2 Bacterial plasmid purification using NucleoBond® PC 100 Xtra Midiprep system

In order to isolate endotoxin free plasmids from bacterial culture for transfection into the desired cell lines, the NucleoBond® PC100 Xtra Midiprep kit was used (MACHEREY-NAGEL GmbH and Co., Germany). A 10ml LB culture containing 100µl of the bacterial glycerol stock was incubated at 37°C shaking in a YIH DER model LM-530 (Scilab Instrument Co., Ltd., Taiwan) incubator at 250rpm overnight. The following day, 100µl of the start-up culture was inoculated in 200ml LB media containing the appropriate selection antibiotic. This 200ml culture was then incubated overnight shaking at 37°C in a YIH DER model LM-530 (Scilab Instrument Co., Ltd., Taiwan) incubator at 250rpm.

The 200ml culture was subsequently centrifuged for 10 minutes at 1250 x g (2500rpm) in an Eppendorf model 5810/5810R centrifuge (Eppendorf, United States) and the supernatant discarded. The plasmid was extracted from the bacterial pellet using the NucleoBond® PC100 Xtra Midiprep kit according to the manufacturer's instructions. The DNA was resuspended in 100-150µl ddH_2O and the concentration and plasmid purity was determined by a Nanodrop Spectrophotometer (Thermo Fisher Scientific, United States) and the 260/280 (>1.8) and 260/230 (>2.0) ratios. The remainder of the product was used for transfection into the SHSY5Y, HEK293 or COS7 cell line.

2.5.3 Genomic DNA extraction from biological samples

2.5.3.1 DNA from blood

Peripheral blood samples were collected from control and PD-affected individuals and gDNA was extracted using the NucleoSpin® Blood XL kit (MACHEREY-NAGEL GmbH and Co., Germany), following the manufacturer's recommendations.

2.5.3.2 DNA from fibroblasts

Fibroblasts were cultured in a T25 culture flasks until the confluency of cells reached 80-100%. Cells were detached from the growth surface with trypsin (Appendix VII) and transferred to 2ml microfuge tubes. Thereafter, the Quick-gDNA™ MiniPrep kit (Zymo Research Corp., United States) was used according to the manufacturer's instructions to isolate gDNA from cultured fibroblasts. The gDNA was eluted in ddH_2O and the concentration and DNA integrity was determined by the Nanodrop Spectrophotometer (Thermo Fisher Scientific, United States).

2.6 RNA extraction and cDNA synthesis

Dermal fibroblasts were cultured in a T25 culture flasks until the confluency of cells reached 80-100%. Cells were trypsinized (Appendix VII) and transferred to 2ml microfuge tubes. Thereafter, the RNeasy

Mini kit (Qiagen, Germany) was used according to the manufacturer's instructions to isolate and purify intracellular RNA from cultured fibroblasts.

RNA conversion into cDNA was subsequently carried out using the Quantitect Reverse Transcription Kit (Qiagen, Germany). This kit provides a convenient procedure for effective reverse transcription as well as effective gDNA removal. The first reaction allows the elimination of gDNA by the gDNA wipeout buffer, and the second step consist of a reverse transcription reaction prepared by the addition of reverse transcriptase, RT buffer and RT primer mix (Qiagen, Germany). The resulting cDNA templates were used in subsequent verification PCR reactions.

2.7 Polymerase chain reaction (PCR)

2.7.1 Oligonucleotide primer design and synthesis

All gene reference sequences for which primers were designed were obtained from the National Centre for Biotechnology Information (NBCI) Entrez Nucleotides Database (http://www.ncbi.nlm.nih.gov/nucleotide/). Primers were designed using Integrated DNA Technologies Software, OligoAnalyzer (http://eu.idtdna.com/calc/analyzer) and Primer3 (http://bioinfo.ut.ee/primer3-0.4.0/). The NCBI Basic Local Alignment Search Tool (BLAST) (http://www.ncbi.nlm.nih.gov/Blast/) was used to examine primer specificity. Oligonucleotide primers were synthesized either by Inqaba Biotech (South Africa) or Whitehead Scientific Pty. Ltd. (South Africa).

2.7.1.1 Primers for sequencing constructs

In order to verify WT and G2019S sequences from plasmids (Addgene plasmids #25044 and #25045) as well as Q5® Site-directed mutagenesis generated vectors, sequencing primers were designed and used for sequencing analysis (Appendix IV, Table 4). Additionally, universal primers were used to confirm the correct open reading fame of plasmid sequences (Appendix IV, Table 5).

2.7.1.2 Primers for variant verification

Primers were designed and synthesized to PCR amplify selected exons of *LRRK2* from gDNA, cDNA and plasmid DNA (Table 2.4). These primers were used to verify the presence or absence of mutations (G2019S in exon 41) or variants (Q2089R in exon 42) in specified DNA samples. Exonic primers were used to amplify exons from cDNA and plasmid DNA samples. In brief, PCR was performed in 25µl reactions in a Mastercycler® ep PCR system (Eppendorf, United States), with each reaction mixture containing 10 - 200ng template DNA, 20pmol of each primer (Table 2.4), 1.5mM MgCl2, 75µM dNTPs

(Promega, United States), 1X NH_4 reaction buffer (Bioline, United Kingdom) and 0.5 U BIOTAQ DNA polymerase (Bioline, United Kingdom).

Table 2.4 Primers designed for SNP verification in the *LRRK2* gene

Exon	Sequence (5'-3')	Tm (°C)	Ta (°C)
41	Forward: GCA CAG AAT TTT TGA TGC TTG Reverse: GAG GTC AGT GGT TAT CCA TCC	51.1 54.7	55
41 (Exonic primers)	Froward: CCT CCA CTC AGC CAT GAT TAT ATA C Reverse: GTG TGC CCT CTG ATG TTT TT	54.7 53.5	60
42	Forward: GCC TCC TTG GAT GTA TGA GC Reverse: TGA AGC TGC TGA TAT TAA GAA AA	55.5 50.4	55
42 (Exonic primers)	Forward: GGT TTC GTG CAC CTG AAG Reverse: CAT ATT CTT TAA CTG GAT CAG GTA ATT TTC	54.0 52.9	57

Abbreviation: Tm, melting temperature; Ta, annealing temperature; °C, degree Celsius; A, adenine; C, cytosine; G, guanine; T, thymine

PCR cycling conditions were as follows: an initial denaturation step at 94°C for 5 minutes, 30 cycles consisting of denaturation at 94°C for 30 seconds, annealing at Ta (Table 2.4) for 30 seconds and extension at 72°C for 45 seconds, and a final extension at 72°C for 10 minutes.

2.8 Gel electrophoresis

2.8.1 Agarose gel electrophoresis

In the present study, agarose gel electrophoresis was used either to visualize fragments that have been amplified by PCR or for plasmid preparation integrity. Approximately 7µl of the PCR product or plasmid preparation were mixed with 3µl of cresol loading dye (Appendix II) before loading the total 10µl into a separate well of a 1% (w/v) agarose gel (Appendix II). All agarose gels contained 1µg/ml ethidium bromide (Sigma-Aldrich., United States) and 1X sodium borate (SB) buffer (Appendix II). To calculate the size of each fragment, 5µl Kapa Universal Ladder (Kapa Biosystems, United States) was subjected to electrophoresis simultaneously. The products were resolved for 30 minutes at 100V in 1X SB running buffer (Appendix II). Gels were subsequently viewed under UV light and photographed with the Multigenius Bio Imaging System (Syngene, United Kingdom).

2.8.2 Sodium dodecyl sulphate polyacrylamide gel electrophoresis (SDS-PAGE)

Proteins from co-immunoprecipitation (Co-IP) reactions as well as Western blot analyses were subjected to electrophoresis in Mini-PROTEAN® TGX™ precast polyacrylamide gels (Bio-Rad Laboratories Inc., United States), containing 1% Sodium dodecyl sulfate (SDS), ranging from 4% to 25%

depending on the size of the proteins. Typically, 10µl - 35µl SDS loading dye (Appendix II) was mixed with 150µg of Co-IP reaction product or 30-50µg whole cell lysate for Western blot analysis and incubated at 95°C for 10 minutes.

Five microliters of molecular weight marker (Precision Plus Protein™ Kaleidoscope™ Prestained Protein Standard, Bio-Rad Laboratories Inc., United States) was also subjected to electrophoresis with the protein products. The samples were loaded onto the vertical gel and subjected to electrophoresis at 120V for approximately one hour in 1x SDS-PAGE running buffer (Appendix II).

2.8.3 Transfer of proteins from SDS-PAGE gels to Polyvinylidene difluoride (PVDF) membrane

In order to visualize the protein bands separated on SDS-PAGE gels for Western blot and Co-IP experiments, proteins were transferred to PVDF membranes. SDS-PAGE gels were rinsed in TBST (Appendix II) and placed on the PVDF membrane which is attached to the bottom stack of the IBLOT® transfer pack (Invitrogen™, United States). The transfer stack was further assembled according to the manufacturer's instructions and the proteins were transferred to the PVDF membrane using the IBLOT® transfer system (Invitrogen™, United States) at program setting P3 (20V, 8-10 minutes).

2.9 Automated DNA sequencing

A volume of 8µl of each PCR product was transferred to a 0.2ml micro-centrifuge PCR epi (Sigma-Aldrich, United States), and this was purified with 5U of each of the following enzymes: Exonuclease I (USN Corporation, United States) and SAP (Shrimp Alkaline Phosphatase; Promega, United States). The samples were incubated at 37°C for 15 minutes followed by 80°C for 10 minutes to deactivate the enzymes. Each product was diluted to 20ng/µl for the sequencing reaction. The primers used for sequencing were the same primers used during the PCR amplification diluted to 1.1µM. Extracted plasmid DNA was sent for sequencing at a minimum concentration of 100ng/µl. All automated sequencing reactions of the PCR products and plasmid DNA were performed at the Central Analytical Facility (CAF) of Stellenbosch University using the BigDye terminator V3.1 Ready reaction kit on the ABI 3130xl® Genetic analyser (Applied Biosystems, United States). All sequenced data was analyzed using the BioEdit Sequence Alignment Editor Software system (Ibis Biosciences, United States) to verify the sequence integrity and identity of the fragments generated. The generated fragments were compared to their reference sequences obtained from the GenBank database (www.ncbi.nlm.nih.gov/Entrez).

2.10 *In silico* prediction and genetic analysis of Q2089R

In a previous study by our group, selected exons of *LRRK2* were screened for pathogenic mutations in South African patients (R Keyser, PhD thesis, 2011). Exon 42 was screened, as a putative pathogenic variant in this exon, Q2089R, had previously been identified in one Afrikaner PD patient using the exon 42 primer set in Table 2.4. Bioinformatics tools including SIFT (http://sift.jcvi.org/), Polyphen (http://genetics.bwh.harvard.edu/pph2/), Mutation Taster (http://www.mutationtaster.org/) and the Combined Annotation Dependent Depletion (CADD) score (http://cadd.gs.washington.edu/score) was determined for Q2089R by using a Variant Effect Predictor (VEP) algorithm (http://www.ensembl.org/Homo_sapiens/Tools/VEP). Project Hope (http://www.cmbi.ru.nl/hope/method) was used to predict the effect of Q2089R on protein folding and function. In order to assess the evolutionary conservation of Q2089, protein sequences of LRRK2 from a variety of species were selected from UniProt and aligned to each other using UniProt (http://www.uniprot.org/align/).

2.10.1 TaqMan® SNP genotyping

Genotyping was performed in patient and control samples in order to determine the frequency of candidate variants in both patients and controls. A total of 1269 individuals, 493 patients (all the PD probands available at the time of the study) and 776 controls were included for genotyping. The controls were ethnically matched and were divided into a total of 415 white individuals (of which 245 were Afrikaners), 181 mixed ancestry individuals and 180 black individuals (Table 2.5). White Afrikaners are Afrikaans speaking South African individuals mainly of Dutch decent, but may also contain German and French ancestry (Greeff, 2007).

Mixed ancestry refers to an admixed population or combination of different ethnic groups, including Western European and Indian as well as ethnic groups indigenous to South Africa such as the San and Khoi-Khoi (Patterson *et al.*, 2010).

Table 2.5 Study group selected for Q2089R Taqman® genotyping.

	Probands		**Controls**
Ancestry	Number of individuals	Ancestry	Number of individuals
Afrikaner	190	Afrikaner	245
Black	23	Black	180
Mixed ancestry	109	Mixed ancestry	181
White	171	White	170
TOTAL	**493**	**TOTAL**	**776**

The DNA samples were subjected to TaqMan® allelic discrimination technology using the ABI TaqMan® Custom SNP Genotyping Assay (Applied Biosystems, United States). The genotyping was outsourced to a commercial company, IKMB (Institut für Klinische Molekularbiologie – Institute for Clinical Molecular Biology) in Kiel, Germany.

Each ABI TaqMan® Custom SNP Genotyping Assay consists of two primers in order to amplify the sequence of interest, as well as two TaqMan® minor groove binding (MGB) probes for allele detection. Each probe contains a reporter dye at the 5' end of each allele specific probe (the first allele contains the VIC reporter dye and the second allele probe contains the FAM reporter dye). Each probe also contains the MGB as well as a non-fluorescent quencher (NQF) at the 3' end of the probe. The MGB will increase the probe's melting temperature (Tm) without increasing the length of the probe, thereby generating greater differences in Tm values between matched and mismatched probes, thus improving allelic discrimination.

2.10.2 Whole exome sequencing (WES) analysis

Whole exome sequencing (WES) was performed using gDNA from the affected proband (Figure 3.2, Individual II:1) and his unaffected sibling (Figure 3.2, Individual II:3) as a means to exclude all other known mutations as a cause of the disorder. WES was performed at Otogenetics Corporation (United States) using in-solution capturing (Agilent Human V5 (51Mb); Agilent Technologies, United States) and Illumina HiSeq2500, 100 paired-end sequencing. Reads were aligned to the human reference genome hg19 (build 37) using NovoAlign (Selangor, Malaysia) while GATK (Genome-Analysis-Toolkit) was used for the detection of indels. Data was filtered using an in-house custom designed bioinformatics pipeline.

2.11 Metabolic activity measured by MTT assay

The metabolic activity of WT and mutant fibroblasts as well as transfected HEK293 cells were investigated using a 3-(4,5-Dimethylthiazol-2-yl)-2,5-Diphenyltetrazolium Bromide (MTT) (Sigma-Aldrich, United States) assay according to the manufacturer's instructions. An MTT assay measures cell metabolic activity by measuring NADPH-dependent cellular oxidoreductase enzymes. During incubation of the cells in the MTT solution, the presence of these enzymes reduce the yellow tetrazolium MTT dye to its insoluble form formazan, which is purple. This is an indication of living and viable cells.

A total of 1 x 10^5 HEK293 cells were seeded in a 24-well plate in triplicate and transfected with the *LRRK2* WT, G2019S, Q2089R or empty vector plasmids for 24 hours. Supplemented medium was

removed, replaced with 200µl 10mg/ml MTT diluted in phosphate buffed saline (PBS) (Lonza, Switzerland) and incubated at 37°C for 4 hours in a Farma thermosteri-cycle 5% CO_2 humidified incubator (Farma International, United States). After four hours, an equal amount of acidified isopropanol (a 50:1 ration of 1% isopropanol: HCL) and 0.1% Triton-x solution was added to each well to dissolve the crystals. Absorbance was read at 595nm with background subtraction at 650nm using a microplate reader (BioTek, Synergy HT, United States) and the KC4™ software. All values were calculated from three independent experiments with each experiment containing three replicates.

Additionally, for *ex vivo* analysis, 1 x 10^4 WT, G2019S- and Q2089R-carrying fibroblasts were plated per well of a 96-well plate in quadruplicate and allowed to proliferate either for 24 hours, 48 hours, 72 hours, 96 hours or 120 hours. Culture media was subsequently removed, replaced with 100µl 10mg/ml MTT diluted in PBS and incubated at 37°C for four hours in a Farma thermosteri-cycle 5% CO_2 humidified incubator (Farma International, United States). Thereafter, an equal amount of acidified isopropanol and 0.1% Triton-x solution was added to each well to dissolve the crystals. Absorbance was read at 595nm with background subtraction at 650nm using a microplate reader (BioTek, Synergy HT, United States).

To quantify the number of fibroblast cells plated per sample, the CyQUANT® NF Cell Proliferation assay (Thermo Fisher Scientific, United States) was used according to the manufacturer's instructions. In brief, the culture media was removed from the cells and all wells gently rinsed with pre-warmed PBS. A volume of 100µl 1X dye binding solution was added to each well. The plate was incubated in the dark at 37°C in a Farma thermosteri-cycle 5% CO_2 humidified incubator for one hour. The subsequent fluorescence intensity was measured in a Synergy HT luminometer using KC4™ software, with excitation at 480nm and emission detection at 530nm.

2.12 Measuring mitochondrial membrane potential (MMP)

The MMP was determined by staining the cells with the tetraethyl benzimidazolyl carbocyanine iodide (JC-1) fluorochrome. The fluorescent signals were determined using flow cytometric analysis. JC-1 exhibits a potential-dependent accumulation of aggregates in mitochondria. The JC-1 dye is present in its monomeric form at low concentrations and emits a fluorescent signal at 525nm (green). At higher concentrations, i.e. upon accumulation of the J-aggregates which is a specific type of dye, the fluorescent signal shifts to 590nm (red). Thus, the loss of MMP is monitored by a decrease in the red:green fluorescence emission ratio (Reers *et al.*, 1995).

2.12.1 Staining cells with JC-1

HEK293 cells (*LRRK2* WT, G2019S, Q2089R and pDEST53-GUS), transfected in 6-well culture plates, were incubated for 24 hours at 37°C after which 5mg/ml stock solution of JC-1 (Appendix II) was diluted to 10µg/ml in 2ml complete media and added to the cells. A volume of 2ml clean culture media was added to the untransfected, unstained control and media containing DMSO was added to the negative (vehicle) control in each experimental run. Cells were incubated for 30 minutes at 37°C in a Farma thermosteri-cycle 5% CO_2 humidified incubator. Subsequently, cells were gently rinsed with pre-warmed PBS and removed from the growth surface of the culture plates using trypsin. The suspended cells were transferred to 15ml tubes and centrifuged for three minutes at 450 x g (1500rpm). The supernatant was discarded and the pellet resuspended in 500µl PBS to be analyzed using flow cytometry. Alternatively, to interrogate MMP under stress induced conditions, transfected HEK293 cells were treated with 10µM Carbonyl cyanide m-chlorophenyl hydrazone (CCCP), a potent mitochondrial uncoupler, or DMSO (vehicle control) or 50µM CCCP (positive control) and incubated at 37°C for 30 minutes in a Farma thermosteri-cycle 5% CO_2 humidified incubator before being stained with 10µg/ml JC-1 solution as described above.

Differences in MMP were also assessed for WT and patient-derived fibroblasts (G2019S and Q2089R) as follows: Fibroblasts were cultured in 6-well plates until 70-80% confluent. Two additional WT fibroblasts were cultured for use as positive and unstained controls. The culture media was removed and the monolayer stained with 1µg/ml JC-1 solution diluted in 2ml pre-warmed culture media. The positive control sample was treated with 50µM CCCP and 2ml of clean culture media containing only DMSO was added to the unstained control. Samples were incubated for one hour at 37°C in a Farma thermosteri-cycle 5% CO_2 humidified incubator. The staining solution was subsequently removed and the monolayer briefly rinsed with pre-warmed PBS. The cells were detached form the culture flasks using trypsin and transferred to 15ml tubes. The suspended cells were centrifuged for three minutes at 450 x g (1500rpm). The supernatant was discarded and the pellet resuspended in 500µl PBS to be analyzed using flow cytometry. Alternatively, to interrogate the MMP of fibroblasts under stress induced conditions, WT and mutant fibroblasts were treated with 10µM CCCP or DMSO (vehicle control) or 50µM CCCP (positive control) and incubated at 37°C for one hour in a Farma thermosteri-cycle 5% CO_2 humidified incubator before being stained with 1µg/ml JC-1 solution as described above.

2.12.2 Flow cytometric analysis

All flow cytometric analyses were performed on a FACSAria flow cytometer (Becton Dickinson Biosciences, United States) equipped with a 488nm Coherent Sapphire solid state laser (13-20mW), 633nm JDS Uniphase HeNe air-cooled laser (10-20mW) and 407nm Point Source Violet solid state laser

(1025mW). The FACSAria is able to sort a mixture of cells based on the fluorescent signal from each cells. Cells for this assay were sorted based on polarization. This was done at CAF at Stellenbosch University, with the help of Miss. Rozanne Adams.

Samples were analyzed on the flow cytometer and a minimum of 10 000 events were collected per sample. Fluorescence signal intensity was measured using the geometric mean on the intensity histogram. JC-1 aggregates in red, indicative of healthy mitochondria and a high MMP, were measured with the PE (Phycoerythrin) fluorochrome, whereas JC1 monomers in green, indicative of lowered MMP were measured with the FITC (Fluorescein isothiocyanate) fluorochrome. Thereafter, the PE/FITC ratio could be used as a measure of the ratio of healthy mitochondria to depolarized mitochondria.

2.13 Measuring mitochondrial and glycolytic respiration

Cellular metabolism and mitochondrial respiration of cells were measured using the XF^{e}96 Analyzer (Seahorse Bioscience, United States). This was achieved by measuring the oxygen consumption rate (OCR) of transfected HEK293 cells (WT and mutant) and fibroblasts (patient and control).

Additionally, glycolytic respiration was measured by recording lactic acid production through protons released into the media surrounding the cells. This was achieved by measuring extracellular acidification rate (ECAR). The XF^{e}96 Analyzer has a cartridge that enters each well of a 96-well plate. At the bottom of each cartridge two fluorophores are situated. The one is quenched by oxygen and thus measures the mitochondrial component of respiration (OCR) while the rate of extracellular acidification (ECAR), through the extrusion of protons, is proportional to glycolysis and quenches the other fluorophore. A change in fluorophore emission represents a change in the levels of oxygen or hydrogen in the cells.

All Seahorse cell culture plates that had been analyzed in sections 2.13.1 – 2.13.2, were normalized according to the DNA content per well in order to account for any differences in cell seeding density between wells using the CyQUANT Cell Proliferation Assay (Thermo Fisher Scientific, United States) according to the manufacturer's instructions. One plate was used for both the XF Mito Stress Test and XF Glycolysis Stress Test for the HEK293 cells (Appendix VI, Figure 1) whereas two separate plates were used for the fibroblasts (Appendix VI, Figure 2).

2.13.1 The XF Cell Mito Stress Test

Several measures of mitochondrial respiration were derived by the sequential addition of pharmacological agents to cells including basal respiration, ATP-linked respiration, proton leak respiration, maximal respiration and reserve capacity (Figure 2.3).

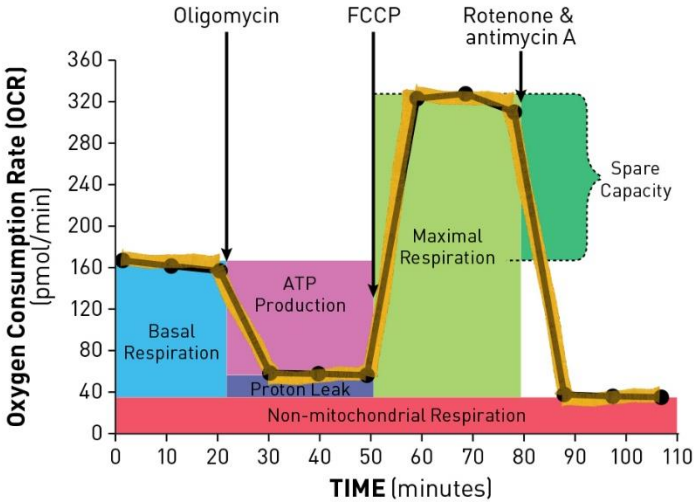

Figure 2.3 Mitochondria respiration as measured by the Mito Stress test. Oxygen consumption rate (OCR) is measured before and after the addition of inhibitors to derive several parameters of mitochondrial respiration including basal respiration, ATP-linked, proton leak respiration, maximal respiration and spare respiratory capacity. With permission from www.seahorsebio.com.

The kit includes three pharmacological agents that are injected into the media surrounding the cells. First, baseline cellular oxygen consumption is measured, from which basal respiration is derived. Next Oligomycin, a complex V inhibitor, is added and the resulting OCR is used to derive ATP-linked respiration (ATP production) and respiration due to proton leak across the inner membrane. The reduction in OCR after Oligomycin shows the OCR as a result of ATP synthesis.

The ratio of ATP-linked respiration to basal OCR is indicated as ATP coupling efficiency. Subsequently, carbonyl cyanide-p-trifluoromethoxyphenyl-hydrazon (FCCP), a protonophore, is added to collapse the inner membrane gradient, which causes the ETC to function at its maximal rate. Finally, Antimycin A, a complex III inhibitor, and Rotenone, a complex I inhibitor, are added to deplete ETC function and increase ECAR as the cells switch to glycolysis for energy production. This reveals the non-mitochondrial respiration and allows mitochondrial reserve capacity to be calculated (Table 2.6).

HEK293 cells were plated at a density of 12 500 cells per well of the 96-well XF Analyzer culture plate and underwent transfection for 24 hours as previously described. Fibroblasts were seeded at a density of 25 000 cells per well. Cells were counted using the Scepter Handheld Cell Sorter (Merck, Germany) and plate set-ups can be seen in Appendix VI, Figure 1 and Figure 2, respectively.

Table 2.6 Calculations of oxygen consumption rates

Measure	Calculation
Non-mitochondrial respiration	Minimum OCR measurement after Rotenone and Antimycin A injection.
Basal respiration	Last OCR measurement prior to Oligomycin injection – Non-mitochondrial respiration
ATP-linked respiration	Last OCR measurement prior to Oligomycin injection – Minimum OCR measurement after Oligomycin injection
Proton leak	Minimum OCR measurement after Oligomycin injection – Non-mitochondrial respiration
Maximal respiration	Maximum OCR measurement after FCCP injection – Non-mitochondrial respiration
Spare respiratory capacity	Maximal respiration – Basal respiration
ATP coupling efficiency (%)	$\frac{\text{ATP} - \text{linked respiration x } 100}{\text{Basal respiration}}$

Abbreviations: ATP, adenosine tri-phosphate; FCCP, carbonyl cyanide-p-trifluoromethoxyphenyl-hydrazon; OCR, Oxygen consumption rate; %, percentage.

The following day the culture media was removed and replaced with 175µl Seahorse assay media supplemented with 5mM glucose and 1mM pyruvate (pH7.4). The plates were subsequently incubated for one hour at 37˚C without CO_2. The final concentrations for each compounds for the HEK293 cells were as follows: 1µM Oligomycin, 0.5µM FCCP and 0.5µM Rotenone + Antimycin A. For the fibroblast run the concentrations were as follows: 1µM Oligomycin, 0.8µM FCCP and 0.5µM Rotenone + Antimycin A. The compounds were loaded in specific ports using the loading plate. Oligomycin was added to port A, FCCP to port B and Rotenone + Antimycin A to port C. The run was initiated and the XF^e Wave software (Seahorse Biosciences, United States) was used to analyze results.

2.13.2 The XF Glycolysis Stress Test

The XF Glycolysis Stress Test is used to measure glycolysis in real-time and identify selected parameters of glycolytic flux including glycolysis, glycolytic capacity and glycolytic reserve (Figure 2.4). ECAR is primarily a measure of lactate production and can be compared to the glycolytic rate (i.e., glycolysis). The conversion of glucose to pyruvate, and then to lactate, results in the production and release of protons to the extracellular medium. The increase in the release of protons results in an increase in the measurable ECAR, which indicates an increase in glycolytic activity.

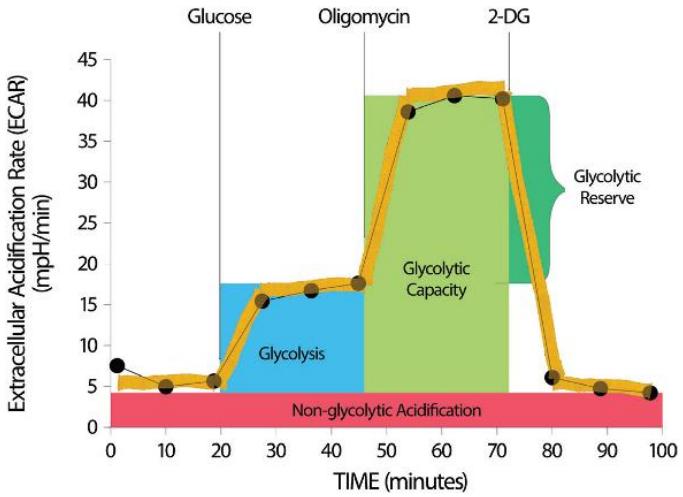

Figure 2.4 Glycolytic flux as measured by the Glycolysis Stress Test. Extracellular acidification rate is measured including glycolysis, glycolytic capacity and glycolytic reserve. With permission from www.seahorsebio.com.

The XF Glycolysis Stress Test makes use of three compounds that are injected into the media surrounding the cells through the injection ports. Following basal ECAR measurements in glucose-free medium, a saturating concentration of glucose is injected to the cells (Figure 2.4). This causes an increase in ECAR as glycolysis increase. Subsequently, Oligomycin is injected; inhibiting oxidative phosphorylation. This results in maximal cellular glycolytic capacity. Finally, 2-deoxy-glucose (2-DG), a glucose analogue, is injected to the cells and inhibits glycolysis. Calculations are shown in Table 2.7.

Table 2.7 Calculations of extracellular acidification rates

Measure	Calculation
Glycolysis	Maximum rate measurement **before** Oligomycin injection – Last rate measurement before Glucose injection.
Glycolytic capacity	Maximum rate measurement **after** Oligomycin injection – Last rate measurement before Glucose injection
Glycolytic reserve	Glycolytic capacity – Glycolysis
Non-glycolytic acidification	Last rate measurement before Glucose injection

Cells were plated and plates prepared as described in section 2.13.1. The following day the culture media was removed and replaced with 175µl Seahorse assay media and the plates incubated for one hour at 37˚C without CO_2. The final concentrations of compounds were as follows: 10mM Glucose, 1µM Oligomycin and 50mM 2-DG prepared in glycolysis assay medium. The compounds were loaded in specific ports using the loading plate. Glucose was added to port A, Oligomycin to port B and 2-DG to port C. The run was initiated and the XF^e Wave software (Seahorse Biosciences, United States) was used to analyze results.

2.14 Determination of Relative mtDNA Copy Number using real-time PCR

Fibroblasts (WTs and mutant/variant) were cultured for at least one week prior to mitochondrial and glycolytic respiration experiments (section 2.13) to a confluency of approximately 90%. Cells were detached from the culture flasks and plated in Seahorse culture plates. The remaining cells were pelleted and frozen at -20°C. Fibroblast passage numbers were matched, ranging from passage four to seven. DNA was extracted from the frozen pelleted cells from control and patient derived fibroblasts to determine the relative mtDNA copy number (RMCN) using real-time PCR 24 hours prior to the Seahorse experiments. This was achieved by quantifying the nuclear gene Hemoglobin subunit beta or *HBB* (β-globin) and the mtDNA gene, MT-ND2 (Mitochondrial encoded $NADH_2$), using real-time PCR and the $2^{-\Delta\Delta CT}$ method to calculate the RMCN. To obtain $\Delta\Delta C_T$ values, C_T values were acquired from the real-time PCR instrument (Applied Biosystems, United States). The average C_T values were calculated for both β-globin and MT-ND2, and the average C_T for β-globin was subtracted from the average C_T MT-ND2. These values then represented the $\Delta\Delta C_T$ value and could then be used to calculate the $2^{-\Delta\Delta CT}$ value. The final value represents the number of mtDNA molecules relative to the number of each nuclear DNA (nDNA) molecule and since two copies of nDNA exists in every human cell, the final values were multiplied by two (Ye *et al.*, 2014; Zandberg *et al.*, 2016).

TaqMan® Gene Expression Assays, containing the two primers (18µM per primer) and a 6-FAMTM dye-labelled TaqMan® MGB probe (5µM) were purchased from Thermo Fisher Scientific (United States) for the nuclear β-globin gene (Hs00758889_s1) and the mitochondrial ND2 gene (Hs02596874_g1). Each reaction mixture for the two genes was prepared separately as follows: 1x TaqMan® Gene Expression Assay, 1x TaqMan® Gene Expression Master Mix, 5µL PCR-grade H_2O and 4 µL DNA (2.5ng/µL). Samples were run in triplicate for each gene and analyzed in an ABI 7300 real-time PCR system. The CT values were acquired using version 1.4 of the 7300 System Sequence Detection Software (Applied Biosystems, United States). The PCR cycling conditions were as follow: 95°C for 10 minutes followed by 40 cycles of 95°C for 15 seconds and 60°C for one minute. The RMCN determination was executed by Ms. Hayley van Dyk.

2.15 Western blotting

2.15.1 Cell lysis

Cells needed to be lysed in order to be used for subsequent co-immunoprecipitation and Western blot analysis. Lysis of cells was achieved as follows: The growth media was removed and 3-5ml of trypsin was added to the flasks or culture plates. The cells with trypsin was incubated at 37°C for 10-15 minutes to facilitate the detachment of the cells after which a cell scraper was used to scrape the remaining cells off from the growth surface. The detached cells were transferred to a 15ml tube to

which a volume of 3-5ml of growth media was added to deactivate the enzyme activity of the trypsin. The tubes were centrifuged at 4°C for three minutes at 1250 x g (2500rpm)in a Beckman model TJ-6 centrifuge (Beckman Coulter, United Kingdom). The supernatant was discarded and the pellet resuspended in 1ml of PBS and the suspension transferred to 2ml microfuge tubes. The cells were re-pelleted at 7600 x g (9000rpm) for two minutes and the PBS removed with a pipette. Lysis buffer was prepared (Appendix II) and 50 to 250µl used to resuspend the pellet. The mixture was placed on ice for 30 minutes after which lysates were cleared by centrifugation at 20 000 x g (130 000rpm) at 4°C followed in a bench top centrifuge (Labnet International Inc., United States) for 30 minutes. The supernatant was subsequently transferred to fresh 1.5ml microfuge tubes and stored at -80°C until required.

2.15.2 Bradford protein concentration determination

Before storage of samples prepared in section 2.15.1, 1µl of each lysed sample was aliquoted and used to perform a Bradford assay in order to assess the protein concentration. This was done as follows: In order to calculate the standard curve, 10µl of serial diluted bovine serum albumin (BSA) ranging from 0-1000µg/µl and 1µl of the lysate samples in duplicate was loaded into the wells of a luminometer plate. Two hundred microliters of Bradford reagent were added to all of the standard as well as the lysate samples. The plates were read on a Synergy HT luminometer (BioTek Instruments Inc., United States) and were used to determine the protein concentration of each well. The KC4™ v 3.4 software (BioTek Instruments Inc., United States) was used to calculate and set up the standard curve, as well as each sample's protein concentration at an absorbance of 595nm.

2.15.3 Membrane blocking

Following SDS-PAGE, the proteins were transferred to a membrane using the IBLOT® transfer system (Invitrogen™, United States). The transfer was not controlled for however, we used GAPDH as a loading control when carrying out Western blot analysis. After complete transfer of the proteins onto the membrane, the membranes were removed from the transfer apparatus and washed in TBST for approximately two minutes. Afterwards, the membrane was placed in 5% fat free powder milk in TBST supplemented with 0.01% Tween-20 to ensure the blockage of all not specific binding sites. The membrane was incubated at room temperature for one hour shaking on a Stuart® orbital shaker SSL1 (Barloworld Scientific Ltd., United Kingdom).

2.15.4 Addition of primary antibody

After blocking of the membranes, the membranes were rinsed with TBST and the primary antibodies diluted in 5% fat free powder milk in TBST or 5% BSA in TBST supplemented with 0.01% Tween-20

(Appendix IV, Table 6). The membranes were placed in a container along with the appropriate primary antibody and incubated overnight shaking at 4°C on an Orbit 300 shaker (Labnet International Inc., United States).

2.15.5 Addition of secondary antibody

The membranes were washed in TBST (Appendix II) for approximately 15 minutes after which the membranes were placed in 5% fat free powder milk in TBST supplemented with 0.01% Tween-20 containing the appropriate horseradish peroxidase (HRP) conjugated secondary antibodies (Santa Cruz Biotechnology Inc., United States, Appendix IV, Table 6). The membranes were placed on a shaker for one hour shaking at room temperature on a Stuart® orbital shaker SSL1 (Barloworld Scientific Ltd., United Kingdom). Subsequently, the membranes were rinsed twice in TBST and then washed for 30 minutes in TBST (Appendix II).

2.15.6 Chemiluminescent visualization of membrane proteins

Following sections 2.15.1-2.15.5, the membranes were taken to a dark room where the two components of the Clarity™ Western ECL Blotting Substrate (Bio-Rad Laboratories, United States), were mixed in a ratio of 1:1 and used to label the membranes for five minutes. After removing the excess chemiluminescent reagent, the membranes were placed in an autoradiography cassette and covered with a transparent plastic sheet after which they were exposed to CL-Xposure™ autoradiography film (Thermo Fisher Scientific, United States). The exposure time varied between 10 seconds and 10 minutes, depending on the strength of the signal. Following adequate exposure, the film was developed in a Hyperprocessor™ automatic autoradiography film processor (Amersham Pharmacia Biotech Ltd., United Kingdom) and the protein bands visualized.

2.15.7 Autophosphorylation assay

Transfected HEK293 cells were lysed and subjected to Western blotting as described in section 2.15.1-2.15.6. To determine the autophosphorylation status of each sample, the membrane was probed with LRRK2 pSer^{1292} (ab203181) and GFP (ab290) (Appendix IV, Table 6) and quantified as described in section 2.15.8. These experiments were conducted in triplicate.

2.15.8 Quantification of Western blot

All Western blots were quantified using the Image J software (http://imagej.nih.gov/ij/). Image J is able to measure the pixel intensity of the band and obtain an arbitrary unit, which could be used as a measure of relative protein abundance on the Western blot. All blots were performed in biological and technical triplicates.

2.16 Co-localization

COS7 and HEK293 cells were plated on glass slides (Lasec Pty Ltd., South Africa) in 24-well plates and transfected with *LRRK2* WT constructs for 24 hours. The culture media was subsequently removed and replaced with media containing 10µM CCCP or DMSO (vehicle control) and incubated for six hours at 37°C in a Farma thermosteri-cycle 5% CO_2 humidified incubator. Co-localization was used to assess protein localization in a physical cellular environment. Overexpressed WT LRRK2 and the endogenously expressed subunits of the TOM protein complex were labelled with appropriate primary and secondary antibodies. For confocal co-localization using COS7 cells, single-plane images were acquired with an Olympus FluoView™ FV-1000 confocal microscope (Olympus Corp., Japan) driven by Olympus FV-1000 Software housed at the Brain and Spine Institute (ICM) (Paris, France). Super resolution structured illumination microscopy (SR-SIM) images of HEK293 cells were acquired using the Zeiss LSM 510 Meta confocal microscope housed at CAF at the Department of Anatomy imaging facility (University of Stellenbosch, South Africa). Optimized antibody concentrations are indicated in Appendix IV, Table 7.

2.16.1 Co-localization assay

Following transfection and treatment with either DMSO or CCCP, the media was removed and the cells briefly rinsed with pre-warmed sterile PBS. The cells were fixed for 20 minutes at 37°C in 4% Formaldehyde diluted in culture media (Appendix II). Subsequently, the cells were washed in PBS three times for 10 minutes. The cells were then incubated in 1% BSA for one hour at room temperature.

The 1% BSA solution acts as the blocking solution to ensure blockage of all non-specific binding sites. Following this incubation period, the cells were incubated with the appropriate pair of primary antibodies (Appendix IV, Table 7) diluted in 1% BSA (Blocking solution). The slides were transferred to a sealed container and incubated at 4°C overnight. The following day the cells were washed with PBS for 10 minutes, repeating the wash step three times. The cells were labelled with the appropriate secondary antibodies diluted in PBS (Appendix IV, Table 7) and incubated at room temperature for 90 minutes in the dark. With every experiment, negative controls were included that consisted of COS7 or HEK293 cells labelled with secondary antibodies only. This was necessary for constructing baseline values for each fluorochrome (secondary antibodies) before acquiring the single and z-stacks images. Cells were washed with PBS for 10 minutes, repeating the wash step three times. A 1:200 dilution of the nucleic acid stain Hoechst H-33342 (Sigma-Aldrich, United States) was made for staining the nuclear material. The cells were incubated with Hoechst at room temperature for 10 minutes after which a brief 10-minute wash step with PBS followed.

ProLong® Gold Antifade Mountant (Thermo Fisher Scientific, United States), was used to mount the cells onto glass slides. The slides were stored at 4°C in the dark until viewing. After viewing and acquisition of a minimum of three single images, three overlay images as well as three z-stacked images from the appropriately labelled cells, co-localization analysis followed.

Olympus images of COS7 cells were processed for co-localization using ImageJ software (http://imagej.nih.gov/ij/) and SR-SIM images of HEK293 cells were processed using the ZEN 2009 light edition software package (http://www.zeiss.com/microscopy/en_de/downloads/zen.html) in combination with co-localization coefficients in Appendix IV, Table 8.

For SR-SIM images, scatter diagrams were generated using the ZEN 2009 light edition software. For each pair the signal intensity of pixels from the red channel (TV2-T2-SR) were interpreted as x-axis coordinates and the signal intensity of pixels from the green channel (TV2-T1-SR) as y-axis coordinates. The crosshair in each diagram corresponds to the threshold values determined by the pixel intensity of the single images acquired for LRRK2 (TV2-T1-SR, green) and the subunits of the TOM complex; TOM20 (TV2-T2-SR), TOM22 (TV2-T2-SR), TOM40 (TV2-T2-SR) and TOM70 (TV2-T2-SR). Z-stack images (11 slices) were acquired from three to four cells per condition. The z-stacks were processed by combining slice 1 and 2, slice 3-5, slice 6-8 and slice 9-11 and creating maximum intensity projections from these images for each cell. These images were then used to generate the desired coefficients and to interpret the data.

2.17 Co-immunoprecipitation (Co-IP)

HEK293 cells were seeded in 6-well culture plates and transfected with *LRRK2* WT constructs for 24 hours as previously described. Subsequently, culture media was removed and replaced with media containing 10µM CCCP or DMSO and incubated for six hours at 37°C in a Farma thermosteri-cycle 5% CO_2 humidified incubator. Cells were then harvested, lysed and the protein concentration determined by a Bradford assay. A final concentration of 150µg protein lysate was pre-cleared by adding 30µl Protein G agarose beads (KPL Inc., United States) to each sample and incubating it at 4°C on a rotating wheel for 30 minutes. Following incubation, the samples were centrifuged at 7600 x g (9000rpm) for 30 seconds in a bench top centrifuge (Labnet International Inc., United States) and the supernatant transferred to fresh 1.5ml microfuge tubes. One microgram of the appropriate primary antibody was added to each lysate samples and the volume made up to 100µl by adding lysis buffer (Appendix II). Negative controls included a sample incubated with only Protein G agarose and a sample incubated with the negative control antibody, anti-Hemaglutinin (anti-HA antibody) which is a synthetic peptide. This mixture was incubated overnight at 4°C on a rotating wheel.

The following morning, 60µl of Protein G agarose was added to each sample after which an incubation period of one hour followed at 4°C rotating. Afterwards, the beads were collected by centrifugation at 7600 x g (9000rpm) for 30 seconds in a bench top centrifuge (Labnet International Inc., United States). The beads were washed four times with ice cold prepared lysis buffer (Appendix II) by mixing it and collecting it again by means of centrifugation at 9000rpm for 30 seconds in a bench top centrifuge (Labnet International Inc., United States). After completion of all the wash steps, 35µl of SDS loading dye (Appendix II) was added to each sample and denatured at 95°C for 10 minutes after which the beads were pelleted again and the supernatant loaded onto SDS-PAGE gel. Co-immunoprecipitation (Co-IP) analysis was performed in order to verify the association of LRRK2 and the selected TOM proteins within the same complex.

2.18 Autophagic flux measurement and calculation

For analysis of cellular autophagy, the detection of autophagic proteins through Western blot analysis were achieved with the P62 and LC3 II antibodies. The LC3 II antibody was used to measure both lipidated and unlipidated LC3 II proteins. These proteins are incorporated within the inner and outer membrane of the autophagic vacuole (AV), and therefore detection of LC3 II is an indicator for the presence of autophagosomes (Figure 2.5). Additionally, p62 is also used to measure autophagic flux, as it binds to LC3 II in the autophagosome and is rapidly degraded during autophagy. Autophagic flux was calculated by measuring both LC3 II and p62 after activation of basal autophagy in a starvation state, as well as after the addition of Bafilomycin A1 (BafA1), which acts as an autophagosome-lysosome fusion inhibitor (Figure 2.5). The difference in protein levels before and after BafA1 treatment was used to define autophagic flux. A 20µg/ml stock solution of BafA1 was made up in ethanol (Appendix II) and stored at -20°C for future use.

HEK293 cells were plated in 6-well plates and transfected with WT, G2019S and Q2089R constructs in duplicate for 24 hours. Additionally, WT and mutant/variant fibroblasts were plated in 6-well plates in duplicate and allowed to proliferate to a confluency of 70-80%. The media was removed and one duplicate well of each sample was replaced with 3ml HBSS media. HBSS is a saline solution that contains 1g/L glucose and no amino acids and is therefore capable of inducing nutrient starvation to the cells and a successive increase in autophagy. Alternatively, the second duplicate well was treated with 3ml HBSS media containing 100nM BafA1 (9.7µl BafA1 in 3ml HBSS media). Both groups were incubated at 37°C for two hours.

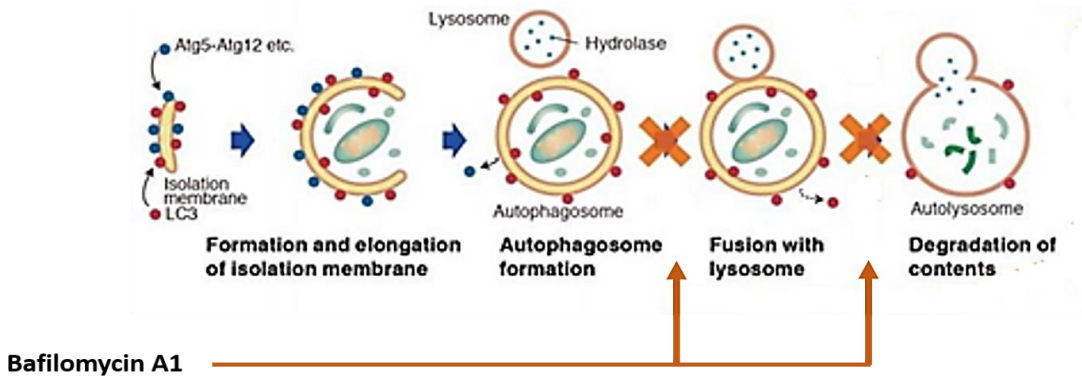

Figure 2.5 The effect of Bafilomycin A1 on autophagy. Bafilomycin A1 inhibits vacuolar-ATPase and prevents lysosomal fusion with the autophagosomes. Bafilomycin A1 ultimately inhibits the degradation of autophagosome content. Reprinted with permission by MBL http://www.caltagmedsystems.co.uk/information/autophagy-watch/

Following incubation, the cells were lysed and protein concentration was determined by the Bradford assay. Both groups of samples (HBSS-BafA1 and HBSS+BafA1) were simultaneously run on gels and detected by Western blot analysis. Antibodies for LC3 II, p62 and GAPDH (the loading control) were used at optimal concentrations (Appendix IV, Table 6). Intensity of the bands for each protein was quantified by Image J software (http://imagej.nih.gov/ij/), and band intensities of LC3 II and p62 were each normalized to the corresponding band intensities of LRRK2 and GAPDH. Autophagic flux was then calculated by comparing the normalized LC3 II and p62 in BafA1 treated versus untreated samples. These results were technically repeated three times, and replicated in three independent experiments.

2.19 Statistical analysis

All statistical analyses were performed using GraphPad Prism Software V5 (http://www.graphpad.com/scientific-software/prism/). Column and line graphs were generated indicating the mean with standard error of the mean (SEM). Either one-way analysis of variance (ANOVA) with Bonferroni's posttest, two-way ANOVA with Bonferroni's posttest or unpaired t-tests were performed to determine p-values. P-values of < 0.05 were considered statistically significant. Statistical analyses were conducted with the assistance of Ms. Tonya Esterhuizen (Centre for Evidence Based Health Care, Biostatistics Unit, Stellenbosch University, South Africa) and Ms. Hayley van Dyk (North West University, Potchefstroom, South Africa).

Chapter 3: Results

Contents

3.1 LRRK2 p.Q2089R identification, verification and frequency determination

This study was approved by the Health Research Ethics Committee at Stellenbosch University (Protocol number: S14/03/072). Renewed ethics approval was obtained annually. All study participants were recruited with written informed consent.

In a previous study in our laboratory, 13 exons encoding the functional domains of *LRRK2* were selected and screened in 30 unrelated patients diagnosed with autosomal dominant (AD) PD using Sanger sequencing. These exons included exons 29-31 (Roc domain), exon 35 (COR domain), exons 38-44 (kinase domain) and exons 45-46 (WD40 domain). A novel variant, p.Q2089R, (on chromosome 12: 40346909; c.A6267G) was identified in one of the 30 PD probands (Dr. R Keyser, PhD thesis 2011) and later in one control individual out of 132 controls screened (B Glanzmann, MSc thesis 2013). In the present study, these findings were independently confirmed by Sanger sequencing (Figure 3.1).

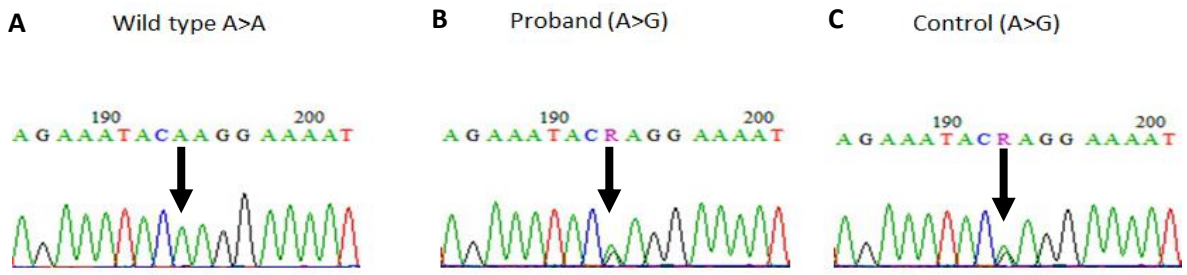

Figure 3.1 Sequence chromatogram indicating the position of LRRK2 Q2089R. The variant is absent in the wild type (**A**) and present in a proband (**B**) as well as one Afrikaner control (**C**). Abbreviations: A, Adenine; C, Cytosine; G, Guanine; R, either A or G; T, Thymine.

3.1.1 Pedigree of p.Q2089R-positive proband

The Q2089R variant is in the kinase domain of LRRK2 and is located in exon 42. This variant was found in a single PD patient of white Afrikaner ancestry with an AAO of 50 years and an AD family history of the disorder (individual II:1; Figure 3.2 A). The patient had, at age 64, developed marked motor fluctuations with dyskinesia, and subsequently underwent bilateral globus pallidus internus (GPi) deep brain stimulation (DBS) with excellent results, at which time he was cognitively normal. The father of the proband (individual I:1, Figure 3.2 A) had also been diagnosed with definite PD prior to his demise.

The family members of the proband were screened in order to possibly identify additional carriers of the variant. Q2089R was found to be present in both of his asymptomatic children (individuals III:1 and III:2, aged 47 and 50, respectively; Figure 3.2 A) and was absent in his unaffected 79-year old sibling (individual II:3). In addition, we performed WES on the proband which excluded the presence of any other known PD-causing mutations or any other possibly pathogenic mutations in *LRRK2*.

Protein alignment results showed that the Q2089 amino acid is evolutionarily well-conserved across various species from zebrafish to human (Figure 3.2 C).

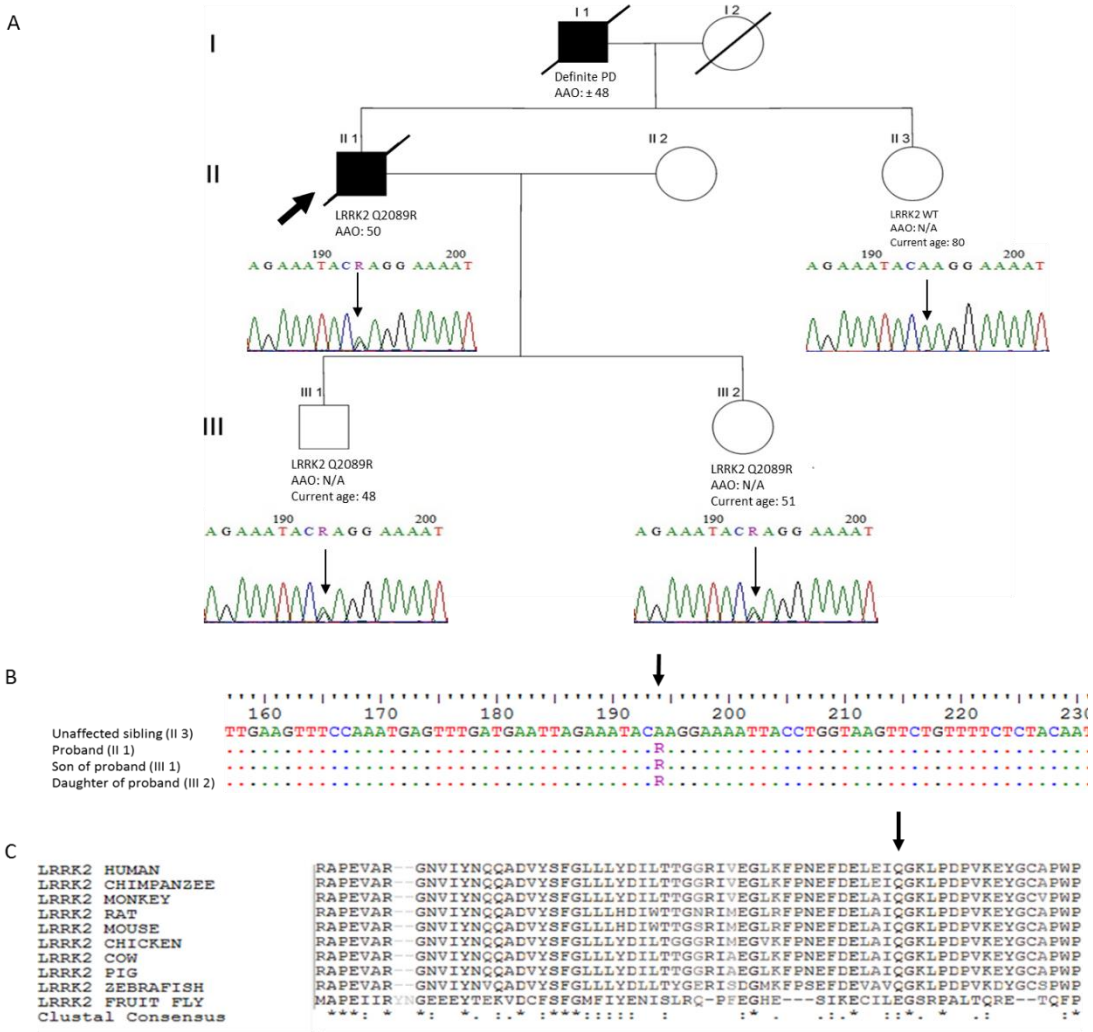

Figure 3.2 Sequencing results and pedigree of the family with the LRRK2 Q2089R variant. **A)** Q2089R is present in both children (III:1 and III:2) of the proband, but it is absent in his unaffected sibling (II:3). The small black arrow indicates the proband and the large downward pointing arrows shows the position where the Q2089R variant is present or absent in the sequence chromatograms. **B)** The sequence alignment of *LRRK2* exon 42 indicating the absence and presence of the variant is indicated by the back arrow. **C)** UniProt protein sequence alignments show the evolutionarily well-conserved LRRK2 Q2089 amino acid indicated by the black arrow at the top of the figure. The conserved regions (where there are no amino acid changes) have been indicated with asterisks at the bottom of the figure. Abbreviations: AAO, age at onset; A, adenine; C, cytosine; G, guanine; N/A, not applicable; T, thymine.

3.1.2 Frequency of Q2089R

To our knowledge, Q2089R has not previously been reported in the literature and it is not present in any of the online databases searched on 17 October 2016. These databases include dbSNP

(http://www.ncbi.nlm.nih.gov/projects/SNP/), Ensembl http://www.ensembl.org/), NHLBI Grand Opportunity Exome Sequencing Project (ESP, https://esp.gs.washington.edu/drupal/), 1000 Genomes project (http://www.1000genomes.org/), PDmutDB (http://www.molgen.vib-ua.be/PDMutDB/), as well as the Exome Aggregation Consortium database (*ExAC,* http://exac.broadinstitute.org/).

In order to determine the frequency in the South African PD patients and controls, a total of 1,269 individuals were screened using TaqMan SNP genotyping. These included 493 unrelated SA PD probands and 776 controls of various ethnicities including 245 white Afrikaners, 170 white individuals, 181 mixed ancestry individuals and 180 black individuals (Table 2.5). Figure 3.3 shows the genotyping results as a representation of the allelic discrimination plots obtained with the Sequence Detection System (SDS) software package.

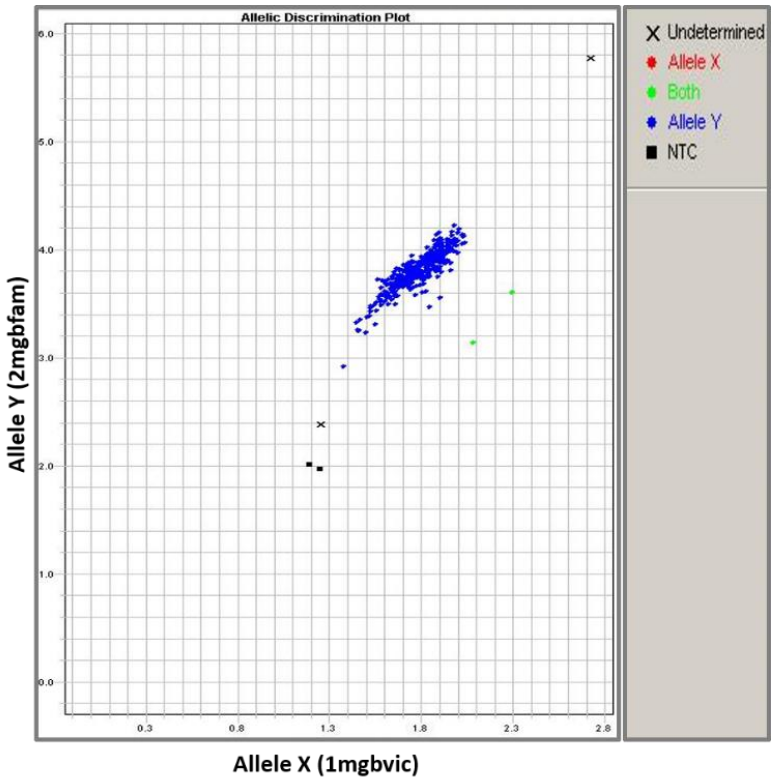

Figure 3.3 Representative results for Taqman® allelic discrimination. Genotyping results for the Q2089R variant as a representation of the allelic discrimination plots obtained with the SDS software during analysis. Allele X = G (variant); Allele Y = A (WT). WT, wild-type; NTC, non-template control.

The wild type allele (A) was plotted on the y-axis and the variant allele (G) was plotted on the x-axis. No amplification was observed in the non-template control samples which indicated that there was no contamination. All samples of 'undetermined genotyping status' and samples that were labelled as heterozygote mutants were selected for Sanger sequencing to confirm their genotype. Genotyping of the Q2089R variant in PD patients and controls revealed that it was absent in all of the other PD

probands and controls screened. Therefore, in South African patients and controls, this variant is present at an overall frequency of 0.2% (1/493) in PD patients and 0.1% (1/776) in controls.

The control individual in whom the Q2089R variant was present is also of white Afrikaner ancestry and she had been recruited from the Geriatric Clinic at Tygerberg Hospital in Cape Town. She was 82 years old at recruitment and at the time of her death at the age of 83 years, she had apparently not exhibited any signs of PD. There was no information available on her family history of PD.

3.2 In-silico analysis

3.2.1 Functional predictions

Bioinformatics tools including SIFT, Polyphen, Mutation Taster and the Combined Annotation Dependent Depletion (CADD) score were employed to predict the effect of the Q2089R variant on protein function. SIFT predicted that the Q to R substitution was 'deleterious' (score = 0.02) and that it would affect likely protein function. Polyphen predicted the variant to be 'possibly damaging' with a score of 0.689 (1.0 being the highest possible score) and Mutation Taster predicted the variant to be disease-causing with a score of 0.95; 1.0 being the highest possible score. A CADD score of 24.1 was predicted for Q2089R providing further evidence of the deleteriousness of this variant, while G2019S has a CADD score of 35 (CADD scores range from 1 – 99 with 1 being the lowest and 99 the highest score of deleteriousness) (Kircher *et al.*, 2014). Scores of >20 indicate that the substitution is in the upper 1% of substitutions least likely to be observed, thus indicating that the variant could have functional implications.

3.2.2 Protein modeling

Project Hope reported that the 2089R amino acid has different properties to the WT allele, which could affect and possibly abolish the protein function (Venselaar *et al.*, 2010). Although the exact crystal structure of the LRRK2 protein is still unknown, a model of LRRK2 was generated based on the Mixed-lineage kinase 1 (MLK1) kinase domain (PDB ID: 4UY9)(West *et al.*, 2007) using SWISS-MODEL (https://**swissmodel**.expasy.org*)* and Modeller (https://salilab.org/**modeller/***)*. The sequence identity of MLK1 with LRRK2 was 35.10% and the coverage was 100%. However, it is important to bear in mind that Q2089 is on a large loop in the protein structure, and disordered structures like loops are extremely difficult to model with any degree of accuracy. This is due to the fact that they do not have definite conformations like helices or sheets and are also very flexible, with the component residues being able to move more easily relative to each other as well as to the rest of the protein. Figure 3.4

shows the amino acid structures of the glutamine (Q) (left) and Arginine (R) (right) amino acids. The backbone, which is the same for all amino acids, is colored red, and the side chain, unique for each amino acid, is shown in black.

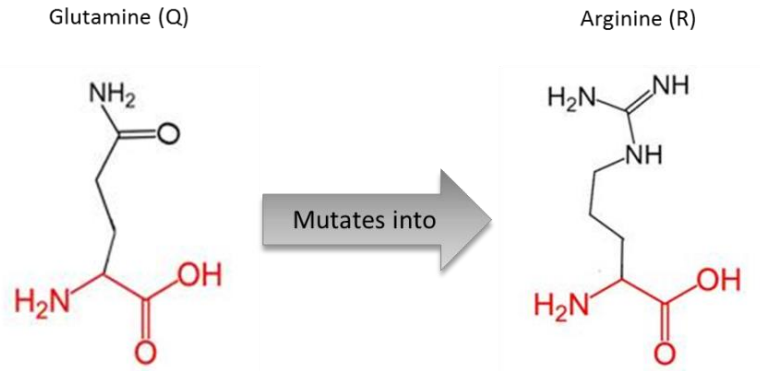

Figure 3.4 Residue change from LRRK2 WT to LRRK2 Q2089R. The illustration shows the change in the residue side chain when the Glutamine (Q) at position 2089 in LRRK2 changes to an Arginine (R). (Venselaar *et al.*, 2010).

The variant residue is much larger than the WT residue (Figure 3.4). Also, the WT (Q) residue is a neutral polar amino acid while the variant introduces a charged aliphatic amino acid which could cause repulsion between variant and neighboring residues. Additionally, this residue is located on the surface of the protein (Figure 3.5) and is located in the central catalytic core of LRRK2, and this region is speculated to be important for binding of other proteins or molecules (Cookson, 2010). We therefore hypothesize that when Q is mutated to R in LRRK2, possible protein-protein interactions could be disturbed and that this substitution could possibly affect the function and activity of the protein.

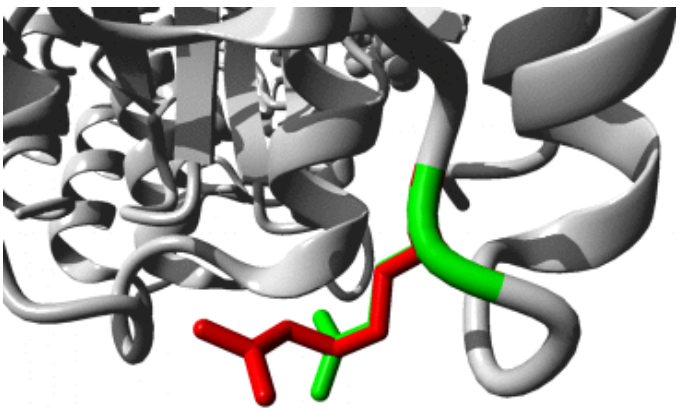

Figure 3.5 Visual representation of the substitution from Glutamine to Arginine at position 2089 in a model of LRRK2's kinase domain. Homology model of the LRRK2 kinase domain with the wild type (WT) residue, Glutamine (Q), shown in green and the mutant residue, Arginine (R), shown in red. The variant results in a significant change in the protein structure as seen in this representation (Venselaar *et al.*, 2010).

3.3 Generation of cellular models to study LRRK2 Q2089R

We attempted to study the functional effect of Q2089R in comparison to WT and the common G2019S mutation using various cellular models. In order to generate these models, we used different approaches including the Clustered Regularly Interspaced Short Palindromic Repeat (CRISPR)-Cas9 system, site-directed mutagenesis and collection of patient-derived dermal fibroblasts. In all experiments, G2019S was used as a control for comparison purposes as the effect of this mutation has been well-studied in previous studies.

3.3.1 CRISPR-Cas9

Firstly, in order to generate a suitable model to study LRRK2 WT and mutants, the (CRISPR)-Cas9 system was considered. This is an RNA-guided gene-editing platform derived from *Streptococcus pyogenes* that makes use of an endonuclease (Cas9) and a synthetic guide RNA to introduce a double strand break at a specific location within the genome. The human neuroblastoma cell line, SHSY5Y, was selected for these experiments as they are adrenergic in phenotype but also express dopaminergic markers and have previously been used to study PD (Lopes *et al.*, 2010; Xie *et al.*, 2010). Target sequences were carefully selected based on GeneArt® CRISPR Nuclease Vector Kit guidelines directly upstream of proto-spacer adjacent motif (PAM) sequences (Appendix III, Figure 3).

Two single-stranded DNA oligonucleotides with overhangs complementing the linearized GeneArt® CRISPR Nuclease Vector were designed (Appendix III, Table 1). The top strand targets the CRISPR RNA (crRNA) and the bottom strand is its complement. Also, long DNA templates, carrying the mutated sequences, were designed to be co-transfected into SHSY5Y cells and to serve as the template to be incorporated into the cellular genome during DNA repair (Appendix III, Table 1). The strands were annealed and ligated into the linearized Orange Fluorescent Protein (OFP) reporter vector. Sanger sequencing of the resulting plasmids show that the guide sequences were successfully ligated into the reporter vectors (Figure 3.6).

However, it was then discovered that the SHSY5Y cell line is not compatible with the CRISPR-Cas9 system, since the CRISPR-Cas9 system requires that cells are able to generate a new cell line from *a single cell*, which SHSY5Y cells are not able to do (personal communication, Dr Sally Cowley, James Martin Stem Cell Facility, Sir William Dunn School of Pathology, United Kingdom and Ms. Liesl Brand, Sales Specialist, Sigma-Aldrich (Pty) LTD, South Africa).

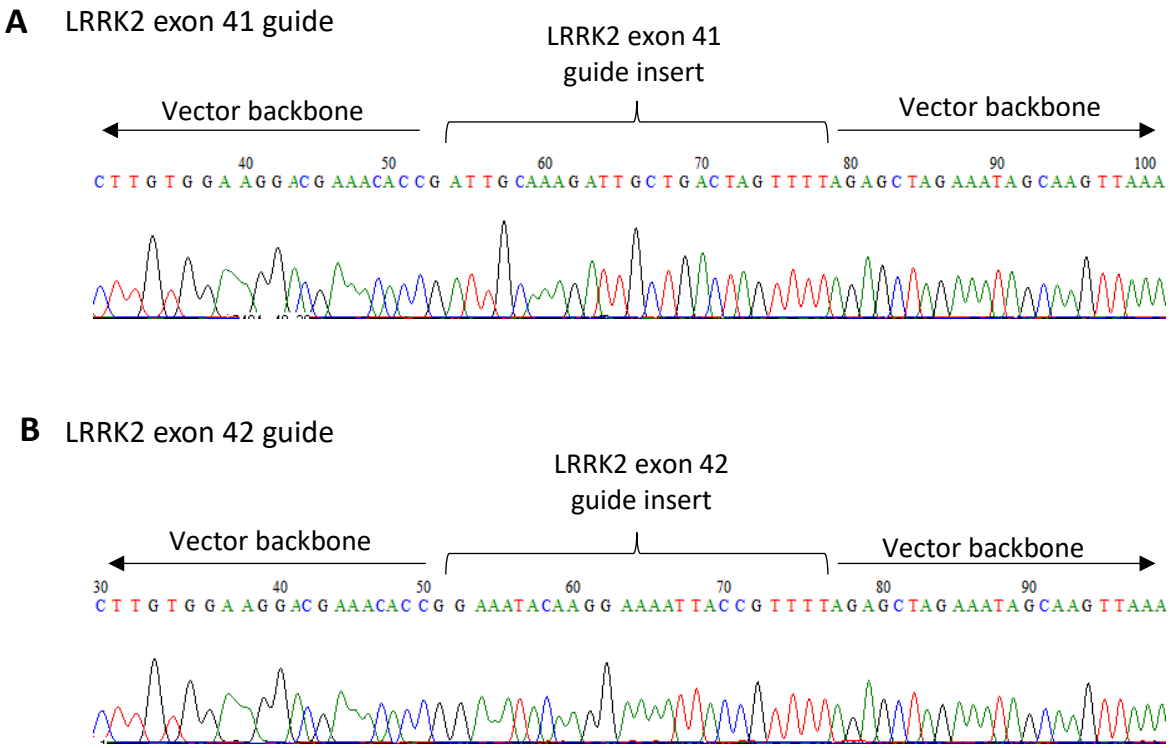

Figure 3.6 Sanger sequencing of CRISPR reporter vectors. A) The guide sequence of *LRRK2* exon 41 was successfully ligated into the GeneArt® CRISPR Nuclease OFP reporter vector. **B)** The guide sequence of *LRRK2* exon 42 was successfully ligated into the GeneArt® CRISPR Nuclease OFP reporter vector.

This is a requirement of this system because CRISPR theoretically randomly mutates every allele differently, and because the pool of positively transfected/edited cells will always contain a percentage of WT background. Subsequently, we also learnt that off-target effects are a major problem of the CRISPR genome editing system especially with the system that we were using. These off-target effects can be difficult to identify and require whole genome sequencing to determine whether mutations have been introduced at sites with sequence similarity to that of the gRNA target sequence. Furthermore, DNA repair through non-homologous end joining (NHEJ) can also produce different mutations from the same targeting constructs, thus also creating the need for whole genome sequencing before conducting any downstream laboratory experiments. This makes the CRISPR-Cas9 technique rather labor intensive, time-consuming and expensive. Therefore, the CRISPR-Cas9 genome editing approach was abandoned and we considered alternative techniques to create cellular models to study the effect of Q2089R.

3.3.2 LRRK2 Q2089R construct generated using site-directed mutagenesis

Two commercially available plasmids namely pDEST53 *LRRK2* WT and (LRRK2 WT) and pDEST53 *LRRK2* G2019S (LRRK2 G2019S) (Appendix I) which encode N-terminally tagged GFP-LRRK2 fusion proteins

were used for transfections. The WT plasmid was used to generate a LRRK2 Q2089R construct. These plasmids were purified from *E. coli* and sequenced using specific primer sets (Table 2.7) to confirm the absence and presence of the G2019S mutation in the LRRK2 WT sample (WT codon GGC) and LRRK2 G2019S plasmid sample (G2019S codon AGC), respectively (Figure 3.7). Additionally, the GUS insert (a gift from Mr. J Gallant, Stellenbosch University, South Africa) was cloned into the pDEST53 empty vector, and used as a negative control in subsequent experiments.

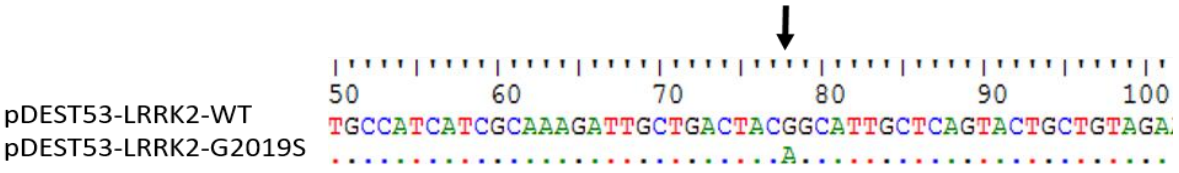

Figure 3.7 Sequence alignments of LRRK2 WT and LRRK2 G2019S plasmid sequences. The black arrow indicates the position of the G2019S mutation which was present in the LRRK2 G2019S plasmid sequence (AGC) and absent in the LRRK2 WT plasmid sequence (GGC). Abbreviations: A, adenine; C, cytosine; G, guanine; T, thymine.

The Q5® Site-Directed Mutagenesis Kit was used to generate a pDEST53 LRRK2 Q2089R plasmid using the pDEST53 LRRK2 WT construct as a template. Specific primers were designed to synthesize the full-length plasmid (Table 2.1) and these plasmids were transformed into *E. coli* and purified for sequencing. The purified plasmid was sequenced using specific exonic primers (Table 2.4) to confirm the presence of the Q2089R variant in the correct position, to confirm the open reading frame and to verify the absence of any other variants that might have been introduced during site-directed mutagenesis.

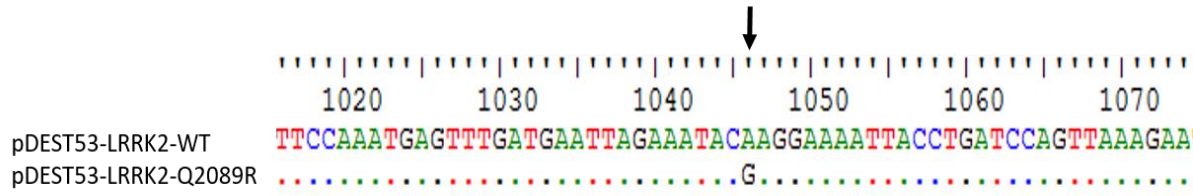

Figure 3.8 Sequence alignments of LRRK2 WT and LRRK2 Q2089R sequences. Sequencing results validated the presence of the Q2089R variant at the correct position in the newly generated LRRK2 Q2089R construct. The LRRK2 WT codon, CAA, was successfully mutated to CGA with no other SNPs being introduced into the sequence. The black arrow indicates the position of the Q2089R variant present in the LRRK2 Q2089R sequence (CGA) and absent in the LRRK2 WT sequence (CAA).

Figure 3.8 shows the alignment between the LRRK2 WT construct (CAA) and the LRRK2 Q2089R construct (CGA). Therefore, we had successfully generated a construct containing Q2089R.

3.3.3 Patient-derived fibroblasts

Skin biopsies were obtained from individuals with WT, G2019S or Q2089R *LRRK2* genotypes to study the functional effects of the variants in an *ex vivo* model. These individuals included five with no mutations in *LRRK2*, one individual carrying the G2019S mutation [Appendix V, Figure 1, individual III:2), (Bardien *et al.*, 2010)], and one individual carrying the Q2089R variant (Figure 3.2 A, individual III:1) (Table 2.3). We were not able to obtain a skin biopsy from the Q2089R-positive proband as he was deceased at the time of biopsy sampling.

The dermal fibroblasts were successfully cultured from all of these biopsies. RNA was extracted from the patient fibroblasts, converted to cDNA and exons 41 and 42 were PCR-amplified. The resulting fragments were sequenced to confirm the presence of the G2019S mutation and the Q2089R variant in the respective exons (Figure 3.9).

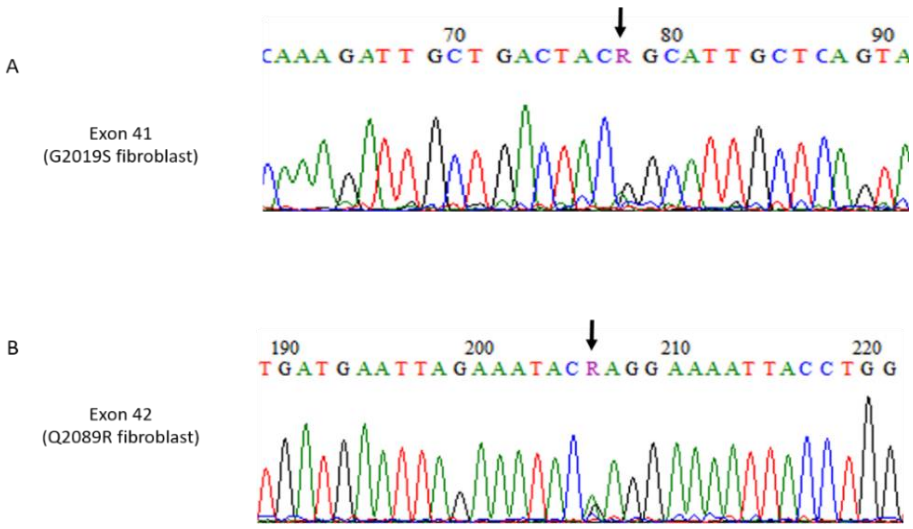

Figure 3.9 Sequence chromatograms of exons 41 and 42 of patient derived fibroblasts A) Sequence of exon 41 of cDNA extracted from fibroblasts carrying the G2019S mutation (as indicated by the black arrow). **B)** Sequence of exon 42 of cDNA from fibroblasts carrying the Q2089R variant (as indicated by the black arrow) Abbreviations: A, adenine; C, cytosine; G, guanine; R, purine (either a G or an A); T, thymine.

Therefore, in summary we had successfully generated two cellular models to study the effect of Q2089R in comparison to WT and G2019S. The WT, G2019S and Q2089R constructs were used to transfect either HEK293 or COS7 cells, and this represented the 'overexpression' model in our study to investigate the functional effect of G2019S and Q2089R *in vitro*. The dermal fibroblasts served as an *ex vivo* model and were used to compare the findings from the overexpression model.

3.4 Q2089R exhibits reduced autophosphorylation

As Q2089R is located within the kinase domain of LRRK2, 70 amino acids downstream of G2019S, we postulated that is could affect the kinase activity of LRRK2. HEK293 cells were transfected with LRRK2 WT, G2019S, Q2089R or the pDEST53-GUS control vector. Western blot analysis was performed using the anti-LRRK2 phospho-Ser^{1292} autophosphorylation antibody as an indirect indicator of kinase activity. Results from three biological replicate experiments indicated that HEK293 cells transfected with G2019S exhibited a significant increase in autophosphorylation (p=0.019) (Figure 3.10).

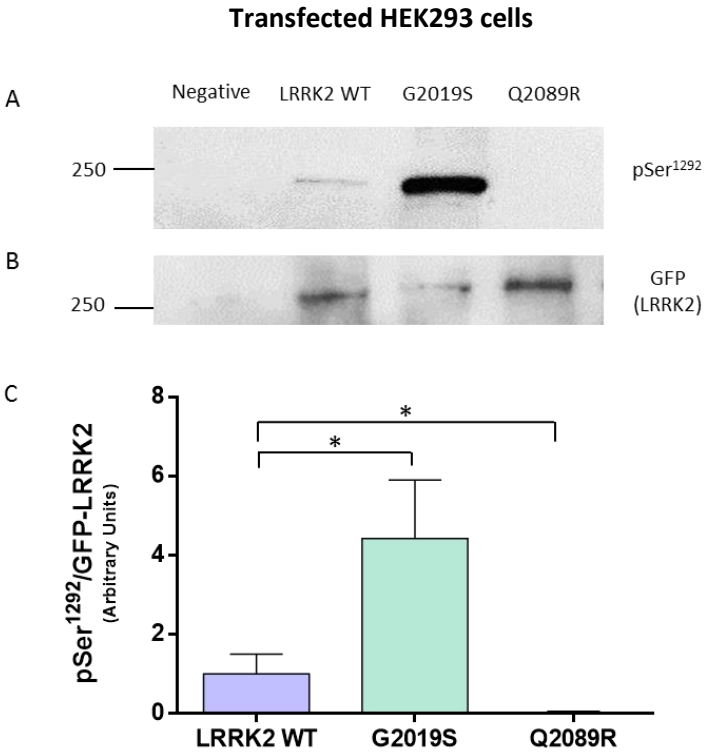

Figure 3.10 Phospho-Ser^{1292} autophosphorylation of LRRK2 in transfected HEK293 cells. A) A representative western blot probed with anti-LRRK2 (pSer^{1292}) antibody which was used to determine the autophosphorylation status of untransfected (Negative), LRRK2 WT, G2019S and Q2089R. **B)** A representative western blot probed with anti-GFP antibody. This value approximates total LRRK2 since levels of endogenous LRRK2 was negligible relative to the levels of the GFP-fusion proteins. **C)** Three independent western blots were quantified to indicate LRRK2 (pSer^{1292}) autophosphorylation relative to GFP-LRRK2 levels. LRRK2 G2019S showed significant higher levels of autophosphorylation while LRRK2 Q2089R exhibited nearly undetectable autophosphorylation levels (Unpaired t-test, *p<0.05).

Notably, Q2089R exhibited almost completely abolished autophosphorylation activity (p=0.026), (Figure 3.10). These results suggest that the novel variant may eliminate the kinase activity of LRRK2 and this finding correlates with *in silico* protein prediction results which indicated that Q2089R could affect protein function.

3.5 Q2089R decreases metabolic activity

Next, we decided to investigate whether Q2089R affects the cells' metabolic activity. HEK293 cells were transfected with plasmids expressing WT, G2019S or Q2089R, and the effect on metabolic activity was assessed using the MTT assay. A significant decrease in metabolic activity was observed in cells overexpressing G2019S (p=0.021) (Figure 3.11 A). Interestingly, Q2089R also significantly decreased the cellular metabolic activity (p=0.016) (Figure 3.11 A). The control vector did not have any effect on metabolic activity (p=0.078) and the transfection efficiencies were comparable between all samples (Figure 3.11 B).

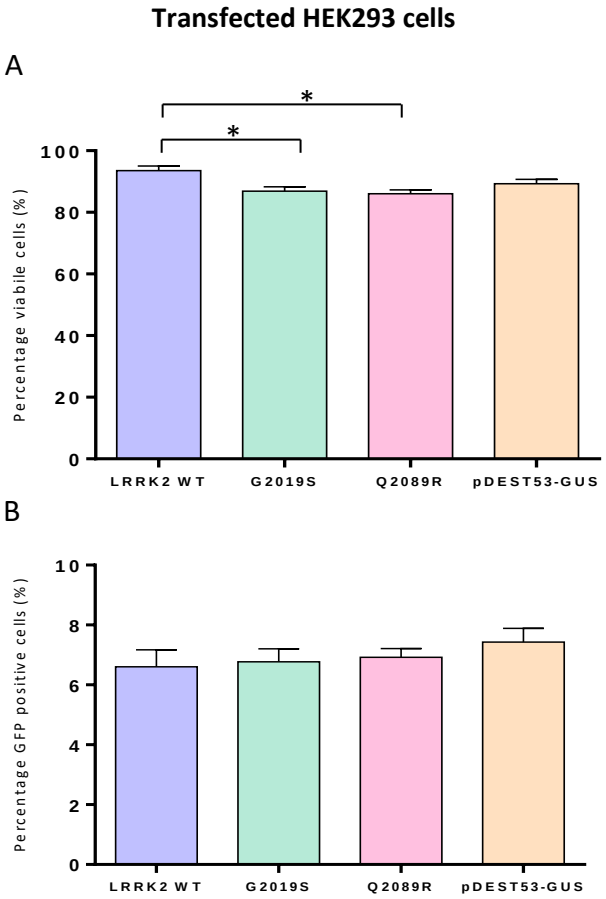

Figure 3.11 Metabolic activity of LRRK2 WT and mutants transfected into HEK293 cells. A) A decrease in metabolic activity was observed in HEK293 cells expressing LRRK2 G2019S and LRRK2 Q2089R compared to LRRK2 WT. The control vector did not have any effect on metabolic activity when compared to WT cells. Data is represented as percentage (%) cell viability. **B)** The transfection efficiencies were statistically comparable between constructs (One-way ANOVA, Bonferroni's posttest, *p<0.05). Data is represented as the % of cells expressing the GFP tagged LRRK2 (WT, G2019S or Q2089R) or GFP control constructs (pDEST53-GUS) after transfection.

To further investigate and validate these findings, the experiment was also conducted on dermal fibroblasts. The metabolic activity of the individual fibroblasts were investigated over a period of five days at 24 hourly intervals.

At 24 and 48 hours, no significant differences were observed between the WT and mutant fibroblasts however, after 72 hours the metabolic activity of Q2089R positive fibroblasts significantly declined (p=0.003) (Figure 3.12). This reduced metabolic activity continued through 96 hours (p=0.004) and 120 hours (p=0.001). The G2019S fibroblasts also showed a significant decline in metabolic activity rate at 72 hours (p=0.03), 96 hours (p=0.01) and 120 hours (p=0.001) (Figure 3.12).

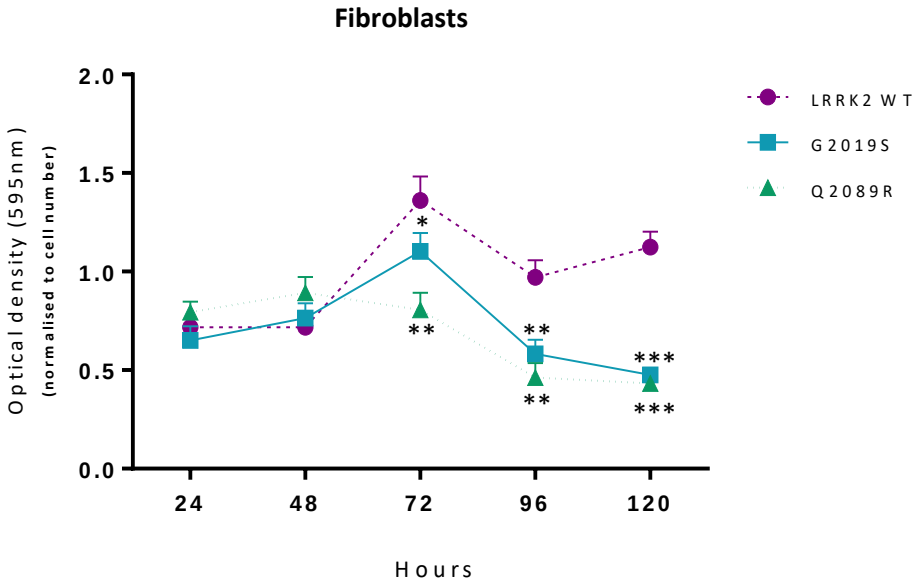

Figure 3.12 Metabolic activity of WT and mutant *LRRK2* fibroblasts. A decrease in metabolic activity was observed in G2019S and Q2089R-positive fibroblasts compared to WT fibroblasts. Values were calculated from four replicates per group and normalized using the CyQUANT® NF cell proliferation assay. Significant differences were observed between the mutant and WT cells at 72 hours, 96 hours and 120 hours (two-way ANOVA, Bonferroni's posttest, *p<0.05, **p<0.01 and ***p<0.001).

This indicates that mutant LRRK2 fibroblasts exhibit lower metabolic activity than cells containing WT LRRK2. At this stage, we are unsure of the reason(s) for these differences in metabolic activity for both HEK293 cells and primary cell lines since the reduction in metabolic activity may be due to a decrease in enzyme activity, cell viability or cytostatic activity which means that the cells shift from proliferation to quiescence.

3.6 Q2089R reduces mitochondrial membrane potential

Next, we evaluated the effect of WT and mutant LRRK2 on MMP in both transfected HEK293 cells as well as in patient derived fibroblasts using JC-1 dye. When MMP is maintained, JC-1 is able to permeabilize the mitochondrial membrane, aggregate inside mitochondria and emit a fluorescence signal in the red (PE) channel. When MMP is lost through the depolarization of cells, JC-1 diffuses into the cytoplasm and is converted into its monomeric form which emits fluorescence through the green (FITC) channel. Changes in MMP were determined by calculating the ratio of PE/FITC mean intensity values, and lower ratio values were associated with decreased MMP.

Results from the flow cytometric analysis in HEK293 cells indicated that transfected LRRK2 WT did not have any effect on MMP compared to untransfected cells (Figure 3.13, A). However, treatment with CCCP (a potent mitochondrial uncoupler) significantly lowered the MMP of treated cells (p=0.0065) (Figure 3.13 B).

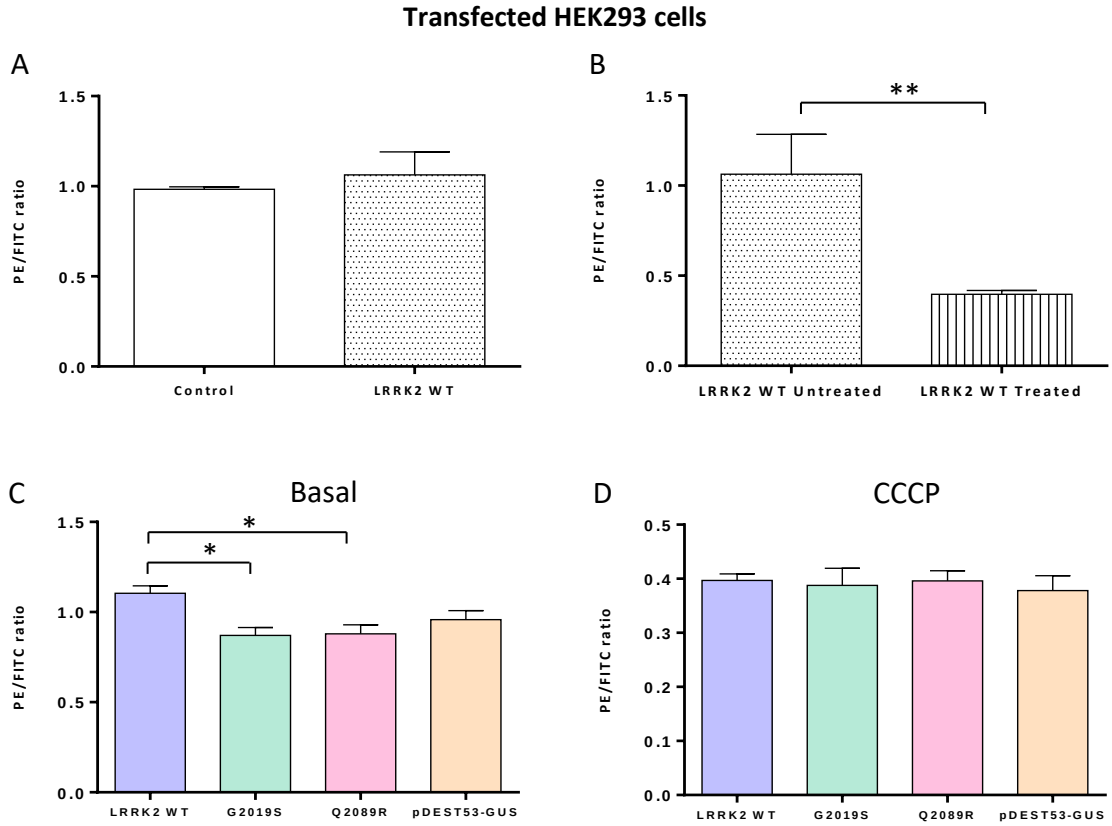

Figure 3.13 Mitochondrial membrane potential of transfected HEK293 cells. A) LRRK2 WT did not affect mitochondrial membrane potential (MMP) compared to untransfected (control) cells. **B)** Treatment with the mitochondrial uncoupler, CCCP, caused a significant decrease in MMP, as expected. **C)** Both G2019S and Q2089R showed significantly lower MMP compared to WT cells under basal conditions. Transfection with pDEST53-GUS (the negative control vector) did not have any effect on MMP. **D)** When cellular stress was induced by CCCP treatment (10µM) the MMP was comparable between all groups (One-way ANOVA, Bonferroni's posttest, *p<0.05).

Both G2019S and Q2089R, significantly reduced MMP compared to WT cells (p=0.038 and p=0.043, respectively; Figure 3.13 C). The negative control vector (pDEST53-GUS) did not have any effect on MMP. These findings suggested that both G2019S and Q2089R could induce mitochondrial dysfunction by depolarizing the mitochondrial membrane. Once MMP is lost, mitochondria cannot function normally which could lead to cell death. To interrogate the MMP of these cells under stress conditions, cells were treated with CCCP. However, interestingly, no significant changes were observed between the different groups under stress-induced conditions (Figure 3.13, D).

Next, the effect of MMP on patient derived fibroblasts was investigated. A notable difference between WT cells was detected when treating the cells with CCCP, significantly decreasing the MMP of the fibroblasts as expected (p<0.0001) (Figure 3.14 A). Interestingly, results showed that G2019S and Q2089R carrying fibroblasts did not display any difference in PE/FITC ratios compared to control fibroblasts under basal conditions (Figure 3.14 B). After treatment with CCCP, flow cytometric results revealed that the MMP of Q2089R fibroblasts were significantly reduced (p=0.009, Figure 3.14 C). G2019S fibroblasts also exhibited reduced MMP although it did not reach statistical significance (p=0.057, Figure 3.14 C).

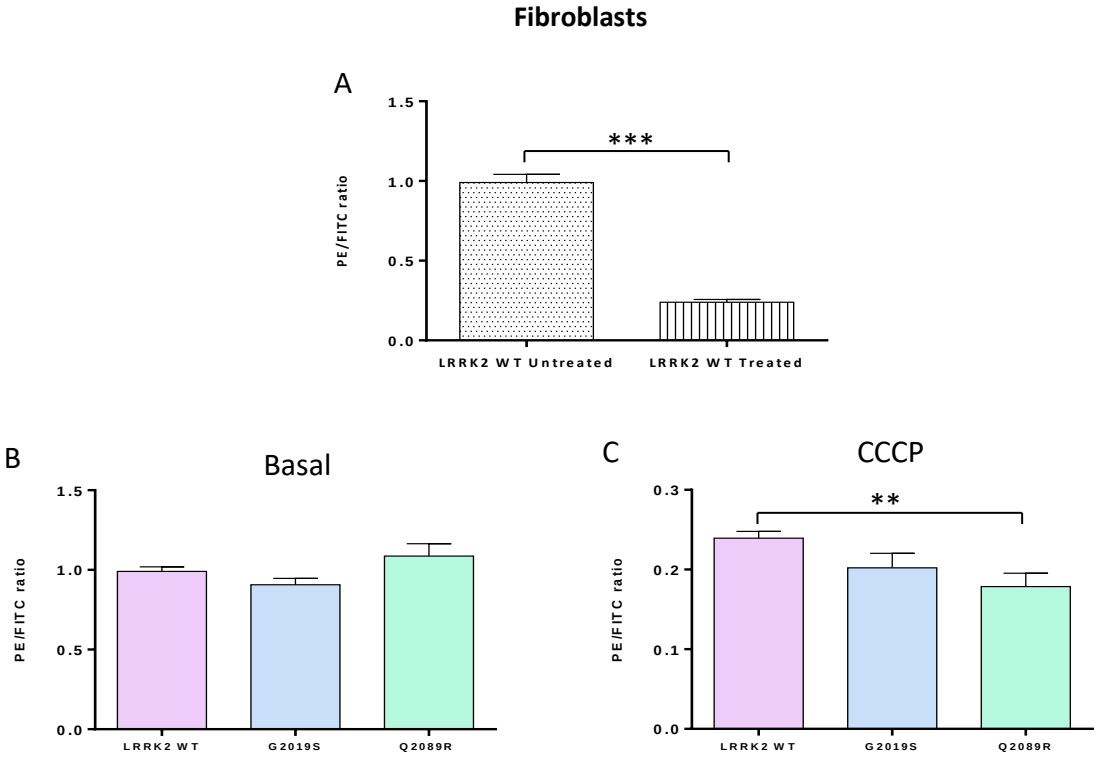

Figure 3.14 Mitochondrial membrane potential of patient derived fibroblasts. A) Treatment of WT LRRK2 fibroblasts with the mitochondrial uncoupler, CCCP, caused a significant decrease in mitochondrial membrane potential (MMP), as expected. **B)** Under basal conditions G2019S and Q2089R carrying fibroblast did not affect MMP. **C)** Induction of cellular stress using CCCP treatment (10µM) caused Q2089R cells to display significantly lower MMP compared to WT cells (Unpaired t-test, **p<0.01, ****p<0.0001).

These findings suggest that the G2019S fibroblasts in our study are less susceptible to extracellular stress and can maintain their MMP even under stressed conditions. Our results also indicate that fibroblasts carrying Q2089R are more vulnerable to extracellular stressors which could indicate that mitochondria in Q2089R carrying fibroblasts are not functioning optimally.

3.7 Q2089R affects mitochondrial and glycolytic respiration

The fact that Q2089R cells exhibit reduced MMP was interesting, and we therefore investigated whether Q2089R could affect mitochondrial respiration and glycolysis. These experiments were done in both transfected HEK293 cells and patient derived fibroblasts, on the Seahorse XF Analyzer. This instrument measures oxygen consumption rates (OCR) as well as the protons released during glycolysis, also known as extracellular acidification rate (ECAR) of the media surrounding the cells. This was used to determine the bioenergetic status of cells. For the HEK293 cells an average of 20 replicate measurements for each group (n=20) was performed, and for the fibroblasts there were an average of 10 replicate measurements for each patient and control sample (n=10). The results from four control fibroblasts were grouped together for analysis of OCR and ECAR.

3.7.1 Mitochondrial Stress Test

A series of OCR measurements were taken for each group. Respiration was first measured at baseline (basal respiration) followed by three measurements after the addition of Oligomycin, a potent complex V inhibitor of the ETC, which causes inhibition of ATP synthesis.

The ATP-linked respiration was calculated by measuring the difference between basal respiration and the minimum OCR measurement after Oligomycin injection. OCR measured here was due to the proton leak across the IMM. Carbonyl cyanide-p-trifluoromethoxyphenyl-hydrazon (FCCP) was subsequently added to uncouple the mitochondria in order to measure the maximum rate at which mitochondria respire, known as maximal respiration. This also allows for the calculation of spare respiratory capacity (taken as the difference between OCR of maximal respiration and basal respiration). Finally, Rotenone and Antimycin A, the complex I and III inhibitors, respectively were added to completely deplete mitochondrial respiration. This was necessary to measure non-mitochondrial OCR. The ratio of ATP-linked respiration over basal OCR was used in order to calculate the ATP-coupling efficiency.

The point-by-point data of OCR, indicative of oxidative phosphorylation, for transfected HEK293 cells and the fibroblasts are shown in Figure 3.15 A and B, respectively. After analysis of the data, the values were plotted as bar graphs for the various parameters measured to facilitate statistical comparisons between the groups (Figure 3.16 and 3.17).

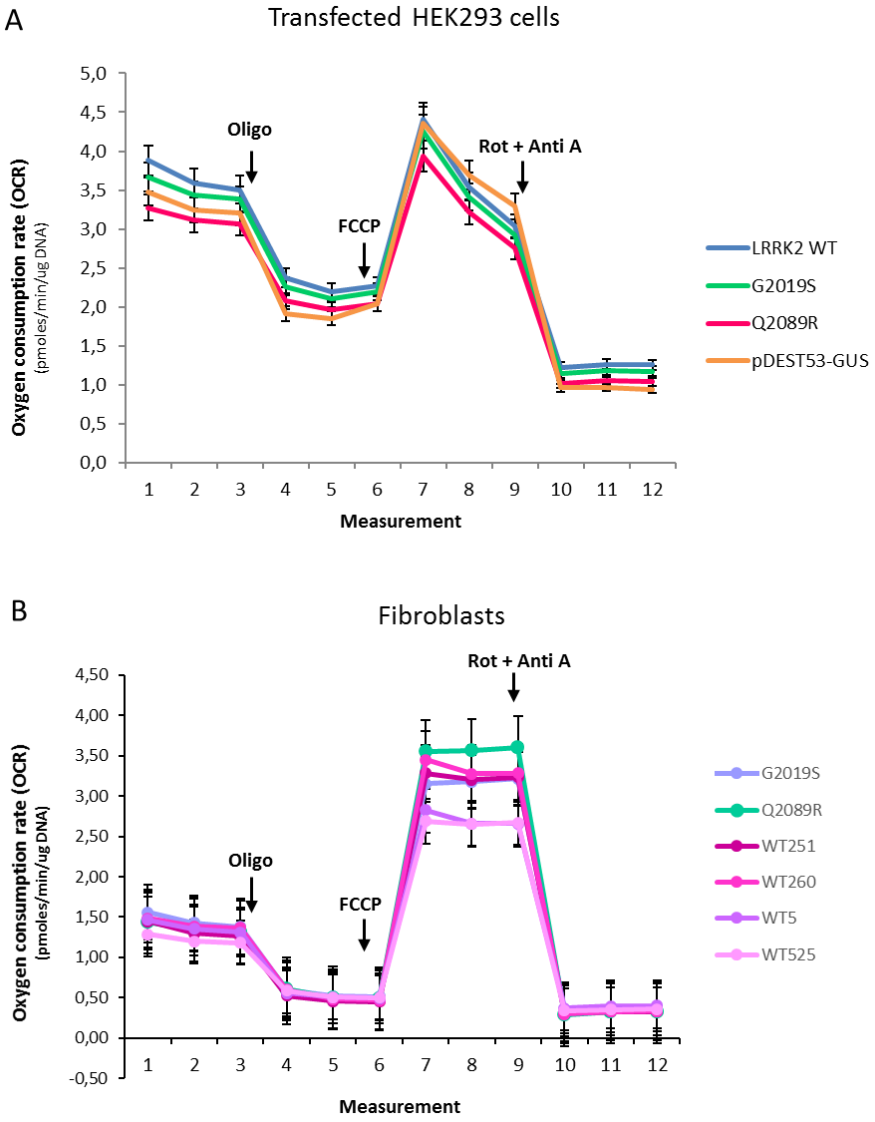

Figure 3.15 Oxygen consumption rate (OCR) profiles of transfected HEK293 cells and patient derived fibroblasts. The graphs represent the OCR for each group of the transfected HEK293 cells **(A)** and patient derived fibroblasts **(B)** after the addition of drug compounds**.** Abbreviations: Oligo, Oligomycin; FCCP, carbonyl cyanide-p-trifluoromethoxyphenyl-hydrazon; Rot, Rotenone; Anti A, Antimycin A.

As shown in Figure 3.16, in transfected HEK293 cells, the only difference observed was that Q2089R had significantly reduced mitochondrial respiration under basal conditions compared to WT cells (Figure 3.16 A, p=0.044). Q2089R did not exhibit any additional changes in OCR (Figure 3.16 B-F).

G2019S and the negative control vector (pDEST53-GUS) did not show significant differences for any of the OCR parameters investigated (Figure 3.16 A-F).

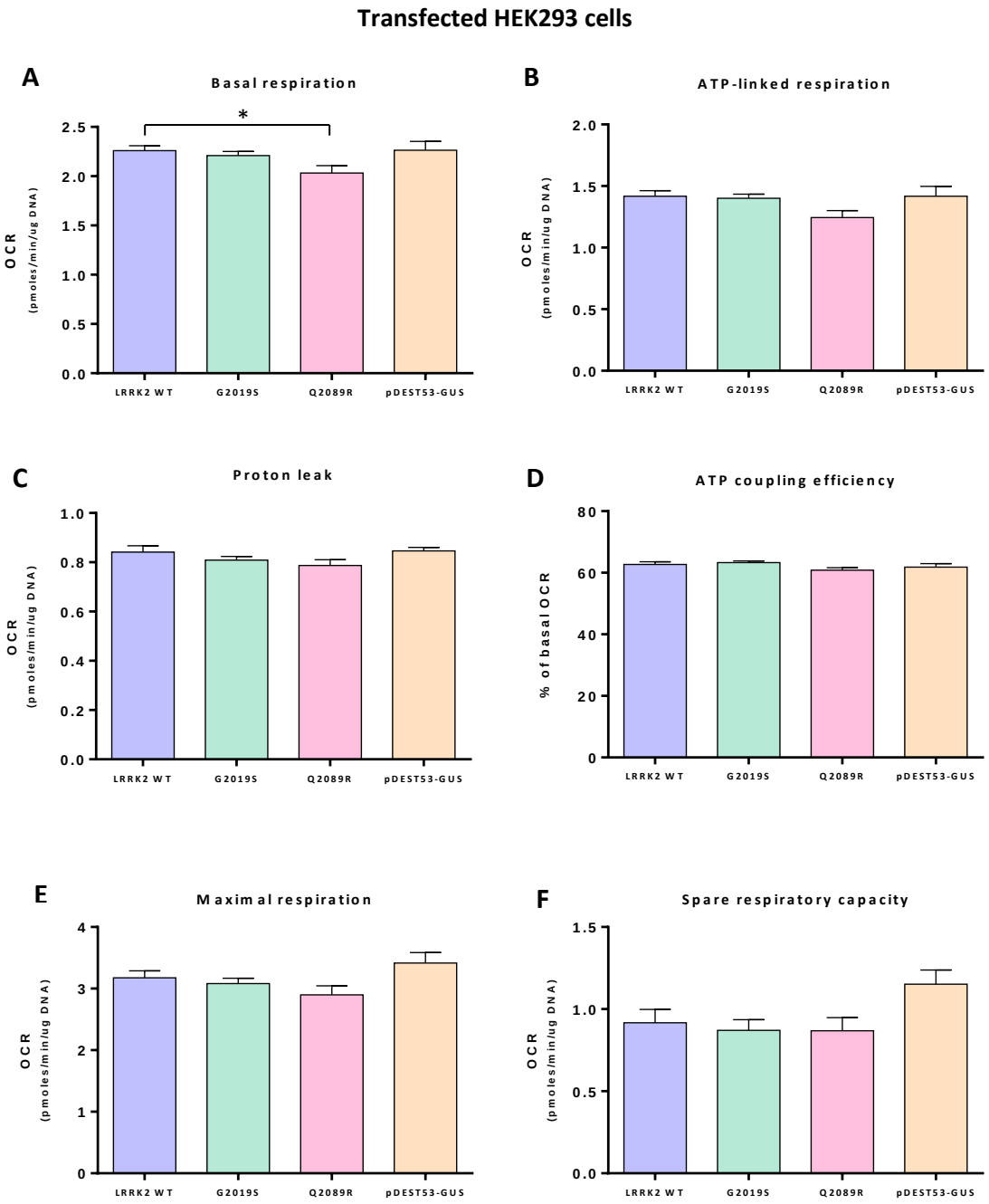

Figure 3.16 Parameters of mitochondrial respiration in transfected HEK293 cells. Q2089R reduced basal respiration **(A)** but did not affect ATP production **(B)**, Proton leak **(C)**, ATP coupling efficiency **(D)**, Maximal respiration **(E)** or Spare respiratory capacity **(F)** in HEK293 cells. G2019S and pDEST53-GUS did not result in any changes of OCR compared to WT cells **(A-F)** (One-way ANOVA, Bonferroni's posttest, *p<0.05).

Next, we determined the OCR of the fibroblasts. Raw data showed that, at basal respiration, the Seahorse profiles were near identical for each of the control fibroblasts (Figure 3.15 B, measurement

one to three). It was subsequently decided to conduct grouped analysis with these cell lines. Interestingly, the basal respiration of both G2019S and Q2089R fibroblasts were significantly increased when compared to WT cells (p=0.029 and p=0.012, Figure 3.17 A) but only G2019S fibroblasts exhibited increased ATP-linked respiration (p=0.029, Figure 3.17 B).

Furthermore, Q2089R showed a pronounced increase in proton leak (p=0.0001, Figure 3.17 C) and significantly reduced ATP coupling efficiency compared to WT fibroblasts (p=0.0014, Figure 3.17 D). Maximal respiration was induced by the addition of FCCP, causing the direct transport of protons across the IMM instead of through the ATP synthase proton channel which results in rapid oxygen consumption without the generation of ATP.

The difference between maximal respiration and basal respiration represents spare respiratory capacity which is a feature indicative of cellular health and survival during times of high energy demand in the cell. In our study, Q2089R fibroblasts exhibited a considerably higher rate of maximal respiration and spare respiratory capacity compared to healthy control cells (p<0.001 and p<0.001, Figure 3.17 E and F). G2019S fibroblasts did not exhibit any effect on proton leak, ATP coupling efficiency, maximal respiration or spare respiratory capacity (Figure 3.17 D-F).

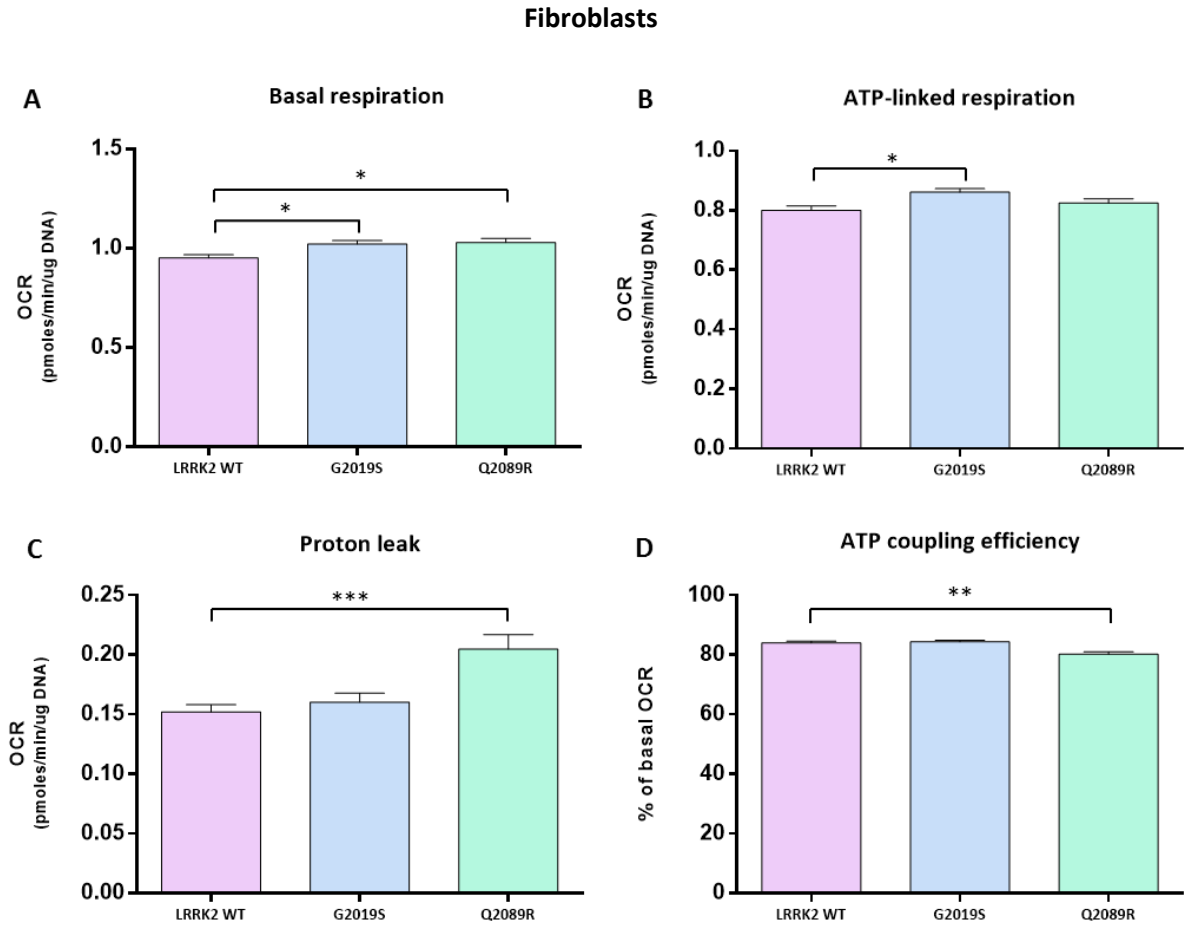

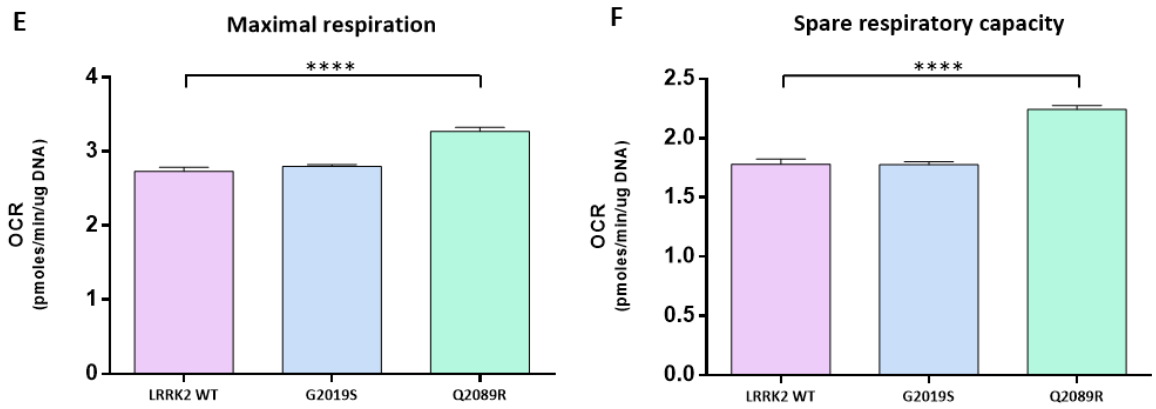

Figure 3.17 Parameters of mitochondrial respiration in control and patient derived fibroblasts. A) G2019S and Q2089R exhibit increased basal mitochondrial OCR. **B)** G2019S shows increased ATP-linked respiration while Q2089R did not have any effect. Q2089R increased OCR due to increased proton leak respiration **(C)** and decreased ATP coupling efficiency **(D)**. Q2089R increased Maximal respiration **(E)** and Spare respiratory capacity **(F)**. (Unpaired t-test, *p<0.05, **p<0.01 and ***p<0.001).

Taken together, our findings indicate that the G2019S fibroblasts used in our study do not exhibit major mitochondrial deficits whereas the Q2089R fibroblasts show clear signs of mitochondrial dysfunction. Thus, although maximal respiration and spare respiratory capacity was significantly increased for Q2089R fibroblasts, the concurrent increase in 'proton leak respiration' and the reduced ATP-coupling efficiency leads us to speculate that the mitochondria in Q2089R fibroblasts cannot fulfil the energy requirements of the cells. Additionally, the marked increase in maximal respiration and spare respiratory capacity could be ascribed to a possible compensatory mechanism exhibited by these cells.

3.7.2 Glycolysis Stress Test

When the oxidative phosphorylation system becomes damaged or is inhibited, glycolysis can become the main producer of ATP in the cell. Therefore, it is essential to investigate glycolytic function to understand the complete effect of mutations or variants on cellular function and energy demands. The point-by-point data of ECAR, indicative of glycolysis, for transfected HEK293 cells and fibroblasts are shown in Figure 3.18 A and B, respectively. Individual reagents were sequentially added to the cells to investigate the glycolytic function for each group.

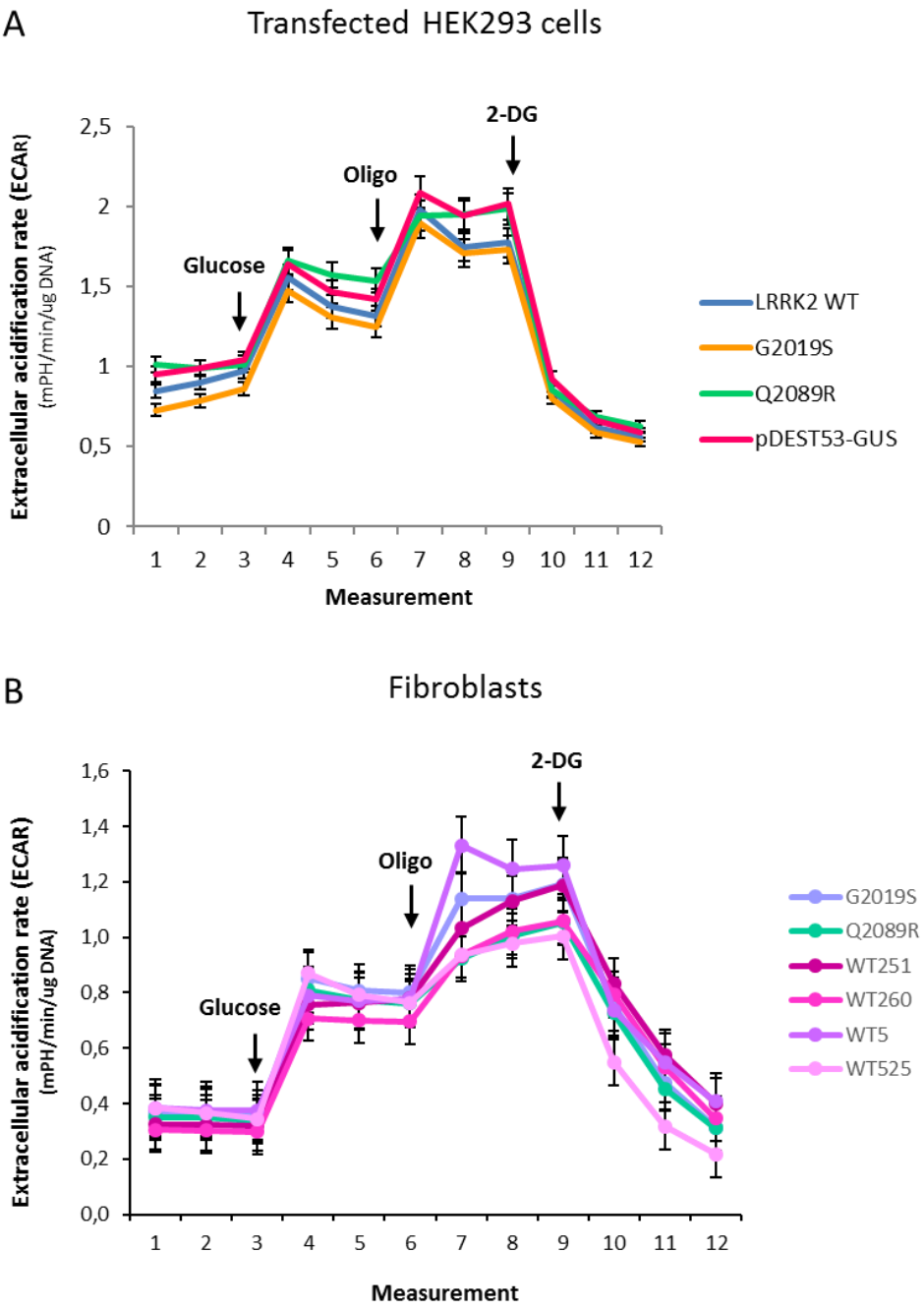

Figure 3.18 Extracellular acidification rate (ECAR) profiles of transfected HEK293 cells and patient derived fibroblasts. The graphs represent the ECAR for each group of the transfected HEK293 cells **(A)** and patient derived fibroblasts **(B)** in glucose-free medium after the addition of compounds**.** Abbreviations: Oligo, Oligomycin; 2-DG, 2-deoxy-D-glucose.

The ECAR of basal (non-glycolytic acidification) rate was determined in glucose-free medium. Subsequently, a saturating concentration of glucose was added to the medium to measure the rate of glycolysis. Thereafter, the ATP synthase inhibitor Oligomycin was added to determine the glycolytic capacity of cells. This was calculated by the difference between ECAR at basal levels and after the

addition of Oligomycin. Lastly, 2-DG which inhibits glycolysis was added to the medium. Glycolytic reserve was determined by the difference between ECAR of glycolytic capacity and ECAR of glycolysis. Again, the individual data are plotted as bar graphs in Figures 3.19 and 3.20.

Results for transfected HEK293 cells revealed that G2019S and the negative control vector did not have any effect on the parameters of ECAR (Figure 3.19, A-D). However, Q2089R showed significantly reduced glycolytic reserve ECAR when compared to WT cells (p=0.012, Figure 3.19, D).

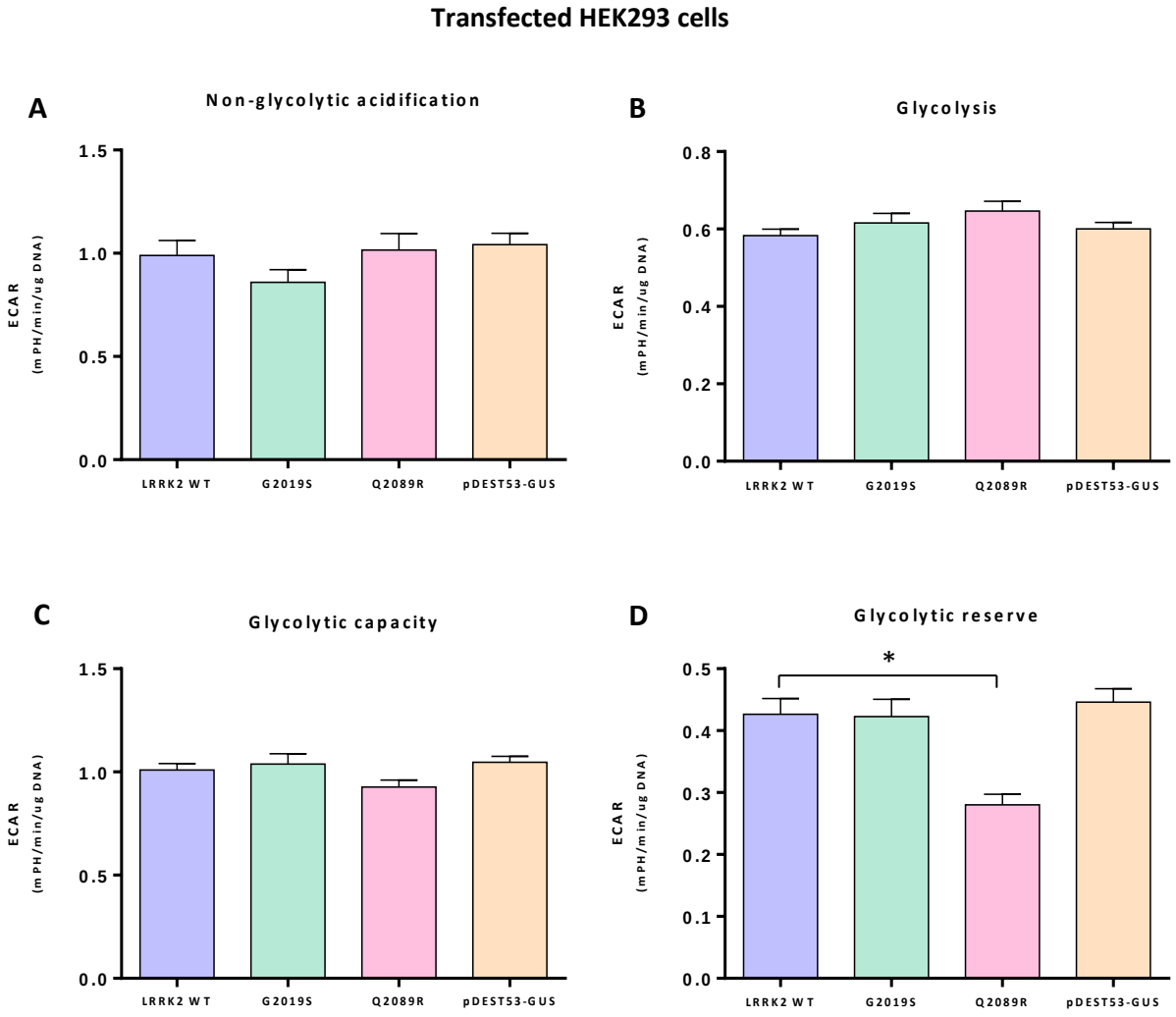

Figure 3.19 Parameters of glycolysis measured in transfected HEK293 cells. Cells transfected with Q2089R and G2019S did not have any effect on Basal respiration **(A)**, Glycolysis **(B)** or Glycolytic capacity rates **(C)**. Q2089R significantly reduced ECAR of Glycolytic reserve, while G2019S showed no changes **(D)** (One-way ANOVA, Bonferroni's posttest, *p<0.05). The negative control (pDEST53-GUS) did not affect any of the parameters measured.

Subsequently, glycolysis was investigated in control and patient derived fibroblasts. Again, at basal levels, virtually indistinguishable glycolysis profiles were recorded for the control fibroblasts cell lines (Figure 3.18 B, measurement four to six) and grouped analyses were performed. In this model, G2019S fibroblasts displayed an increase in ECAR of glycolysis, (p=0.001, Figure 3.20, B), but did not have any effect on non-glycolytic acidification (basal), glycolytic capacity or glycolytic reserve when compared to control fibroblasts (Figure 3.20 A, C, and D).

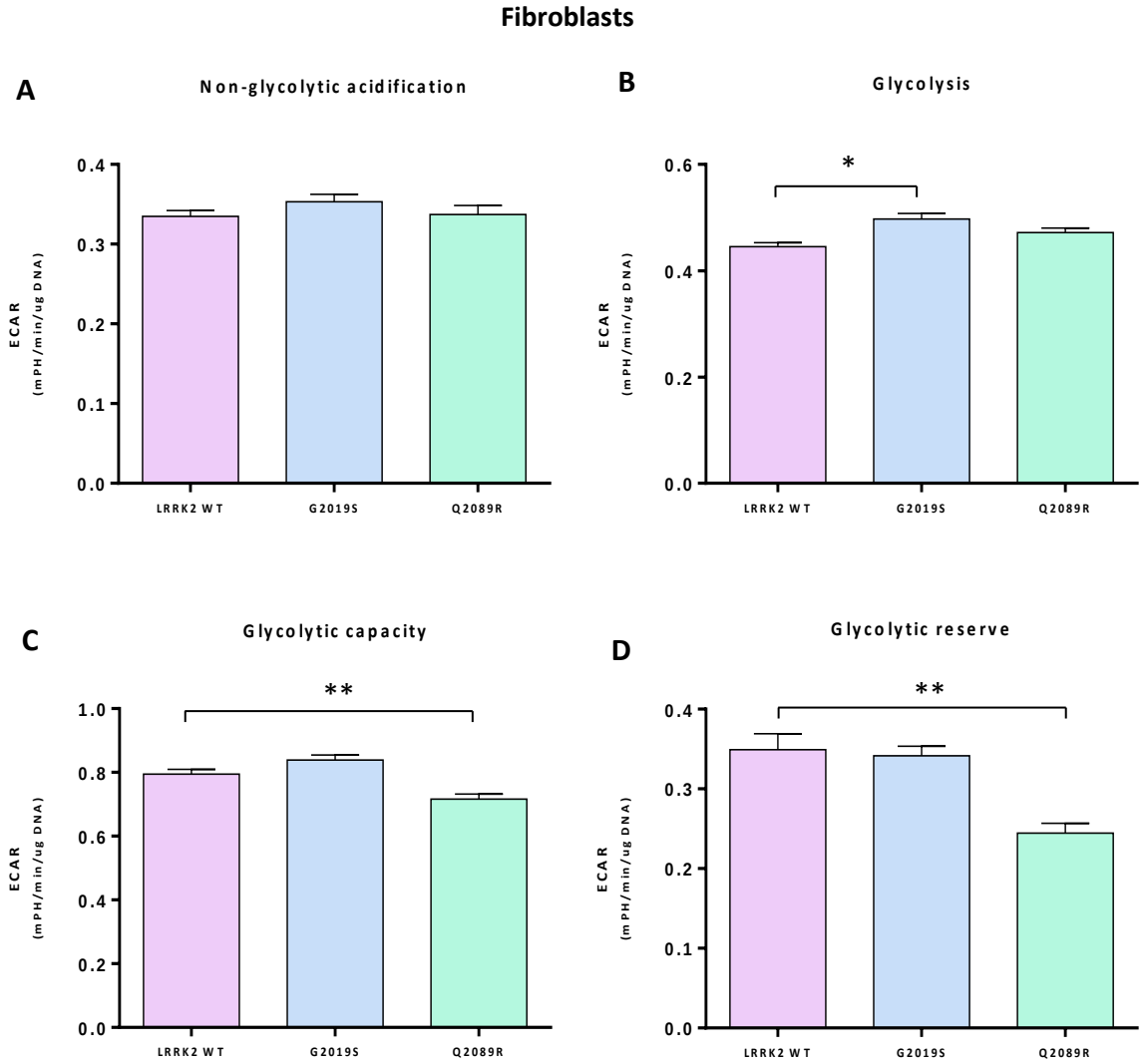

Figure 3.20 Parameters of glycolysis measured in control and patient derived fibroblasts. A) G2019S and Q2089R did not affect Basal ECAR. **B)** G2019S increased Glycolysis while Q2089R did not have any affect. Q2089R decreased ECAR of Glycolytic capacity **(C)** and Glycolytic reserve **(D)** however G2019S did not have any effect (Unpaired t-test, *p<0.05 and **p<0.01).

Similarly, Q2089R did not cause any changes in non-glycolytic acidification (Figure 3.20 A) or glycolysis, although a trend for an increase was observed in the latter but this was not significant (p=0.051, Figure 3.20 B). Interestingly, however, Q2089R markedly reduced the ECAR of glycolytic capacity (p=0.007)

and the glycolytic reserve (p=0.006, Figure 3.20 C and D). This decrease (in both HEK293 cells and fibroblasts) implies that Q2089R containing cells are not able to supply sufficient energy when it is required. Thus, although compensatory mechanisms are at work to a certain extent, these results indicate that Q2089R cells exhibit significant energy demand deficiencies.

3.8 Q2089R exhibits increased mitochondrial DNA (mtDNA) copy number

Increased mitochondrial biogenesis has previously been implicated as a compensatory response of patient fibroblasts (Grünewald *et al.*, 2010; Pacelli *et al.*, 2011) and to investigate this possibility, we determined the relative mtDNA copy number (RMCN) of each patient and control fibroblast sample. DNA was isolated from the fibroblasts and used to determine the RMCN using real-time PCR. Triplicate $\Delta\Delta C_T$ values were obtained for the nuclear gene, β-globin and the mtDNA gene, MT-ND2, and the $2^{-\Delta\Delta C_T}$ formula was used to calculate RMCN. The WT and mutant/variant cell lines remained in culture for at least one week before isolating DNA for RMCN determination in order to allow stabilization of the mitochondrial load. Additionally, passage numbers were matched between individuals (passage five to seven). When comparing the RMCN between individual WT cell lines, no differences were detected (One-way ANOVA, Bonferroni's posttest, p>0.05, data not shown). Subsequently, grouped analysis revealed that fibroblasts carrying Q2089R had a significantly higher number of mitochondrial copies compared to control fibroblasts (p=0.0006, Figure 3.21) and that there was no difference between G2019S and WT cells.

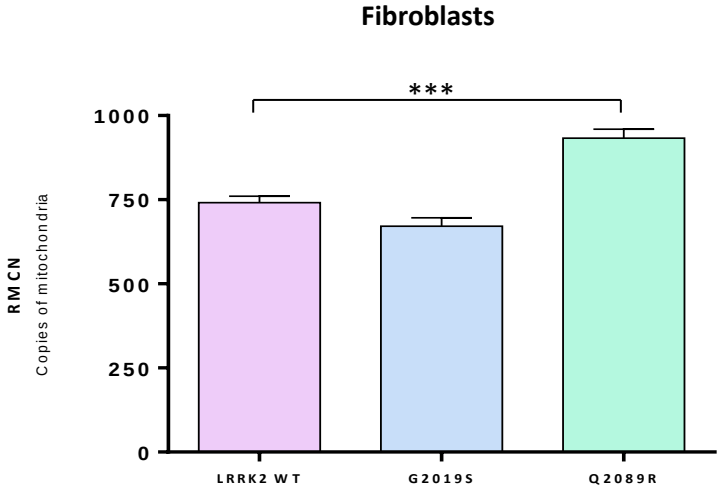

Figure 3.21 Relative mtDNA copy number of control and patient derived fibroblasts. Q2089R positive fibroblasts contained significantly more copies of mitochondria when compared to control fibroblasts (Unpaired t-test, ***p<0.001). Abbreviations: RMCN, Relative mtDNA Copy Number.

We believe that the increase in mitochondrial biogenesis could possibly be due to compensatory mechanisms previously described (Grünewald *et al.*, 2010).

3.9 Q2089R enhances autophagic flux

Furthermore, we sought to investigate the effect of Q2089R on autophagic flux. Autophagic markers LC3 II and P62 were employed to investigate the effect of WT and mutant LRRK2 on the rate of protein degradation through macro-autophagy i.e. autophagic flux. For these experiments, both LC3 II and P62 were measured after activation of basal autophagy under starvation conditions, in the presence and absence of a autophagosome-lysosome fusion inhibitor, Bafilomycin A 1 (BafA1). BafA1 prevents the degradation of the autophagosome-lysosome by inhibiting acidification. This inhibition blocks the degradation of LC3 II and P62, resulting in the accumulation or increase in LC3 II and P62 expression (since LC3 II proteins are incorporated within the inner and outer membrane of the autophagic vacuoles (AVs) and P62 binds to LC3 II in the autophagosomal membrane) (Klionsky *et al.*, 2008; Barth *et al.*, 2010).

Transfected HEK293 cells were starved (in amino acid-free media) in the absence or presence of BafA1 and LC3 II and P62 (Figure 3.22 A) levels were determined with and without BafA1 treatment. When LC3 II and P62 levels are increased after BafA1 treatment, this indicates that an accumulation of autophagosomes has occurred; indicating an increase in autophagic flux and increased clearance rates through autophagy. Conversely, when these levels are decreased after BafA1 treatment, the opposite is true.

In our study, we showed the expected elevation in LC3 II after BafA1 treatment in all sample groups, indicating that the mechanism of autophagy was not defective and functioning correctly (Mizushima and Yoshimori, 2007) (Figure 3.22 A). Our analysis showed that in transfected HEK293 cells, G2019S did not have any significant effect on either LC3 II ($p=0.322$) or P62 ($p=0.206$) levels when compared to WT cells (Figure 3.22 B and C). Interestingly, however, a significant increase in LC3 II ($p=0.004$) and in P62 ($p=0.018$) levels were observed for Q2089R compared to WT LRRK2 (Figure 3.22 B and C). The increase in the autophagic markers suggests that the pool size of autophagosomes in Q2089R cells significantly increased. This suggested that in Q2089R cells, an accumulation of (AVs) had occurred. This could suggest that autophagy increases or perhaps that the degradation of AVs decreases (Manzoni *et al.*, 2013a; Schapansky *et al.*, 2014).

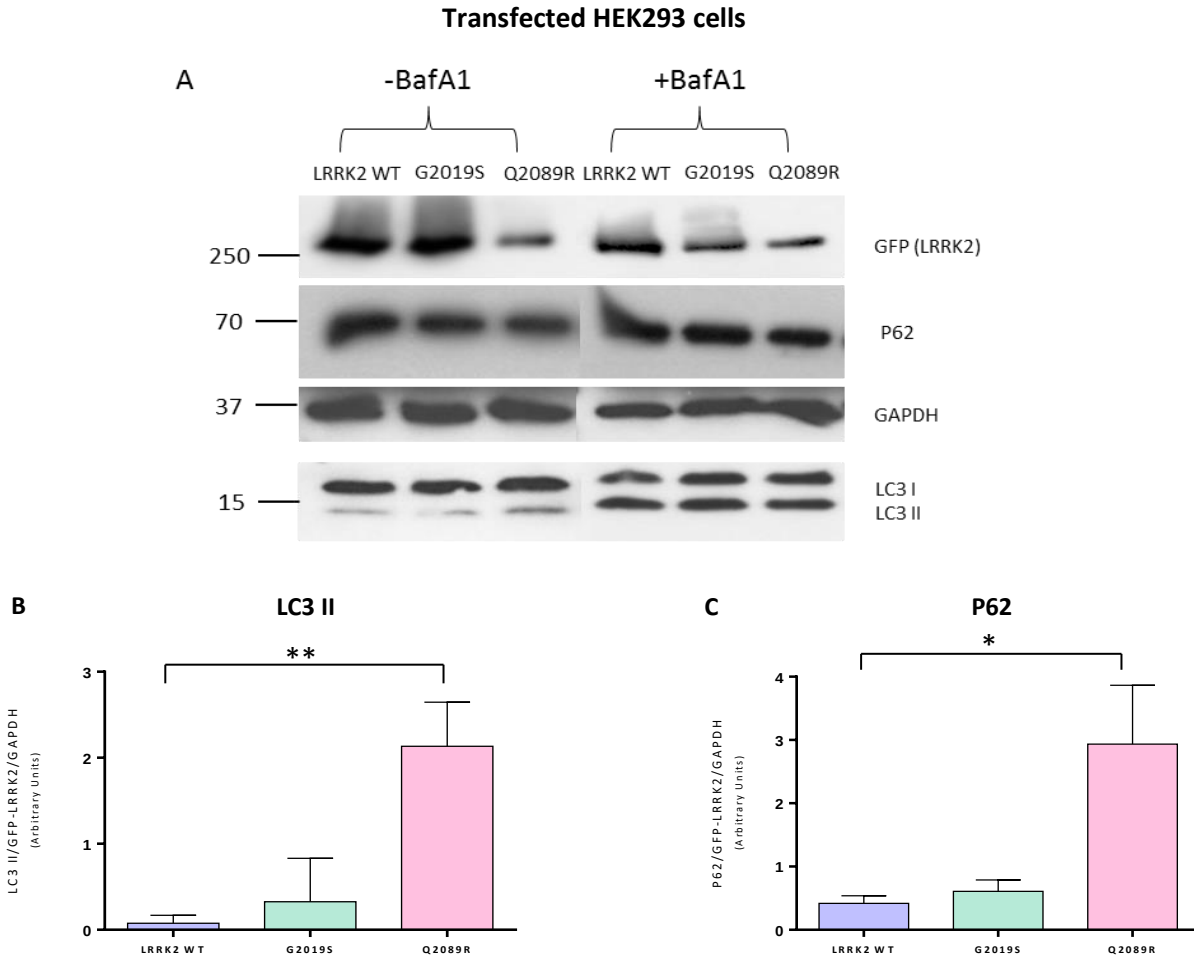

Figure 3.22 Detection and quantification of autophagic markers LC3 II and P62 for transfected HEK293 cells. A) Representative Western blot images of HEK293 cells transfected with LRRK2 WT, G2019S and Q2089R in the absence (-BafA1) and presence (+BafA1) of BafA1 (n=3). Western blots were quantified and the difference in LC3 II and P62 before (-BafA1) and after (+BafA1) treatment was calculated and standardized to GFP-LRRK2 and GAPDH. Q2089R exhibited increased LC3 II **(B)** and increased P62 levels **(C)** when compared to LRRK2 WT. No significant differences in LC3 II **(B)** and P62 levels **(C)** were observed for G2019S (Unpaired t-test, *p<0.05, **p<0.01). The experiments were done in three independent experiments (i.e. three biological replicate experiments).

Additionally, this experiment was conducted on the fibroblasts (Figure 3.23 A) which also showed autophagy working correctly (an increase in LC3 II following BafA1 treatment) in all groups.

Furthermore, we detected significantly increased LC3 II levels in both G2019S and Q2089R carrying fibroblasts (p=0.022 and p=0.031, Figure 3.23 B). Interestingly, when quantifying P62 levels, both G2019S and Q2089R indicated an enhanced autophagosomal pool size, although only Q2089R reached statistical significance (p=0.131 and p=0.006, respectively, Figure 3.23 C).

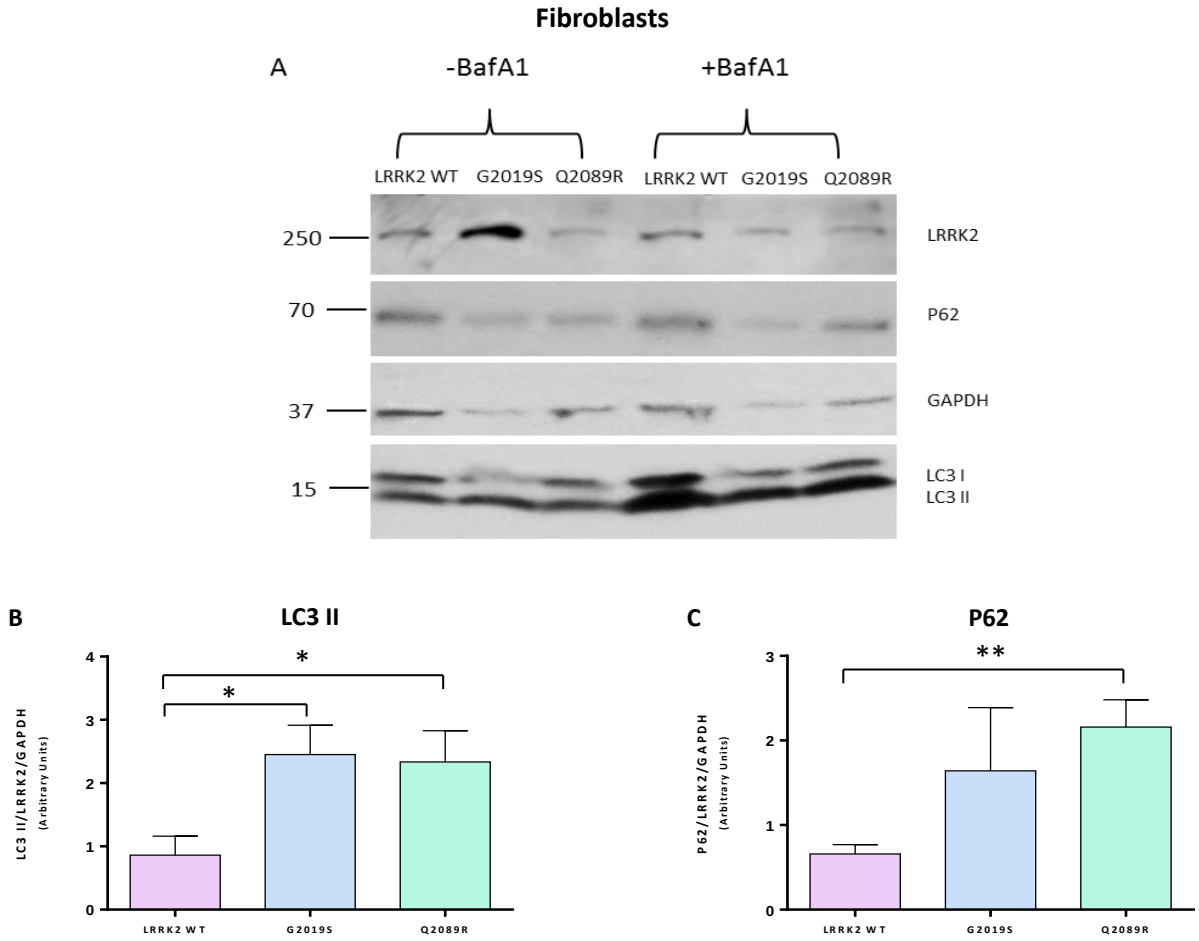

Figure 3.23 Detection and quantification of autophagic markers LC3 II and P62 in control and patient derived fibroblasts. A) Representative Western blot images of individual fibroblasts in the absence (-BafA1) and presence (+BafA1) of BafA1 (n=3). Western blots were quantified and the difference in LC3 II and P62 before (-BafA1) and after (+BafA1) treatment was calculated and standardized to total LRRK2 and GAPDH. Q2089R exhibited increased LC3 II **(B)** and P62 levels **(C)**. G2019S fibroblasts showed an increase LC3 II signal **(B)**. The increase in P62 levels were not significant **(C)** (Unpaired t-test, *p<0.05, **p<0.01).

In conclusion, we observed an increase in autophagic flux in both transfected HEK293 cells and fibroblasts carrying Q2089R when compared to control cells. Therefore, we speculate that the increased autophagy observed in Q2089R cells could indicate that toxic products (such as dysfunctional mitochondria) are accumulating in the cell, triggering the upregulation of autophagy.

3.10 Wild type LRRK2 interacts with the translocase of outer mitochondrial membrane (TOM) complex

In our final experiment, as LRRK2 has previously been associated with the OMM and with evidence implicating the TOM complex in PD (Bender *et al.*, 2013; Bertolin *et al.*, 2013), we investigated the

possible co-localization of WT LRRK2 and essential subunits of the TOM protein complex using confocal imaging and co-localization analysis. The co-localization experiments were performed on two commercial cell lines, COS7 cells and HEK293 cells. The confocal imaging was done on COS7 cells as these cells are large and therefore it is easier to visualize the cellular structures. Also, many previous co-localization experiments on LRRK2 had been done in these cells (Gloeckner *et al.*, 2006; Greggio *et al.*, 2006; Bertolin *et al.*, 2013). The super-resolution imaging was done on HEK293 cells as the work on the COS7 cells had been done in Dr. Corti's laboratory in France and were not available in our laboratory in South Africa.

3.10.1 Co-localization of LRRK2 and TOM subunits using confocal microscopy

Intracellular localization of LRRK2 and the subunits of the TOM complex (TOM20, TOM22, TOM40 and TOM70) in transfected COS7 cells showed co-localization between LRRK2 and all of subunits under normal physiological conditions (Figure 3.24). Visually, the co-localization output indicated that LRRK2 occupies the same three-dimensional subcellular space as the proteins of the TOM complex (Figure 3.24, D, H, L and P).

Images were corrected for background noise by including negative control images with every experiment and image acquisition. The images were analyzed using ImageJ software (https://imagej.nih.gov/ij/) and the JaCoP plugin analysis. Both Mander's coefficient and the overlap coefficient algorithms were used for the quantification of confocal co-localization images (Appendix IV, Table 8).

According to Mander's coefficients, approximately 20% of the total overexpressed LRRK2 (M1) co-localizes with the proteins of the TOM complex (Table 3.1). Furthermore, roughly 25-60% of each individual TOM subunit (column labelled M2 in Table 3.1) co-localizes with LRRK2. In each co-localization experiment, the overlap coefficient was equal to or higher than 0.9, i.e. close to 1, indicating a high degree of overlap between green and red pixels.

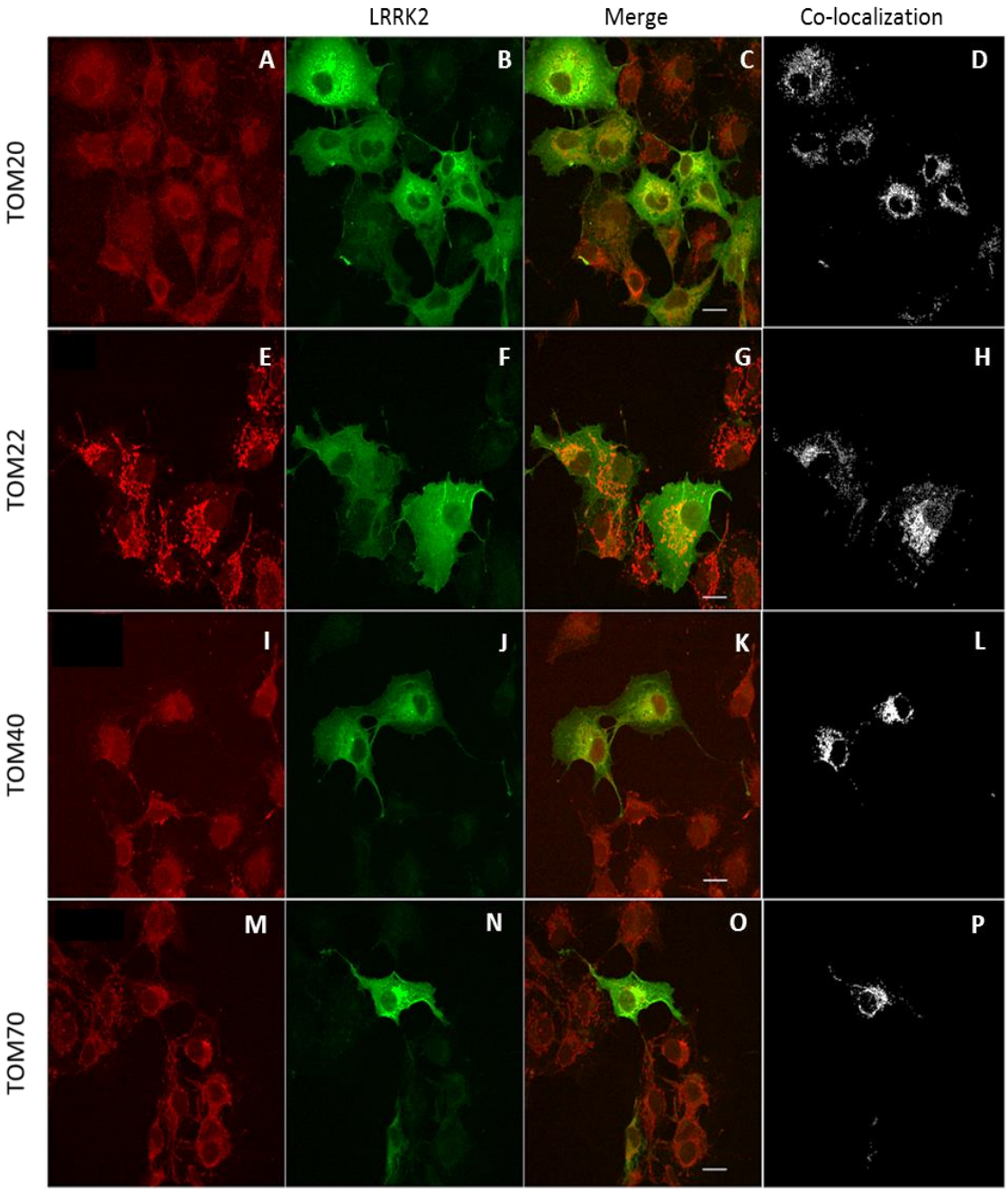

Figure 3.24 Fluorescent confocal imaging and co-localization analysis of LRRK2 and the subunits of the TOM complex in transfected COS7 cells. The fluorescent images of endogenous TOM proteins (Red): TOM20 labelled with donkey anti-mouse cy3 **(A),** TOM22 labelled with donkey anti-mouse cy3 **(E),** TOM40 labelled with donkey anti-rabbit cy3 **(I)** and TOM70 labelled with donkey anti-mouse cy3 **(M)** co-localized with exogenous LRRK2 (Green) labelled with donkey anti-rabbit Alexa 488 **(B, F and N)** and exogenous LRRK2 (Green) labelled with donkey anti-mouse Alexa 488 **(J)**. Images **C, G, K** and **O** show the overlay of LRRK2 and the respective TOM proteins. Figures **D, H, L** and **P** represent the red and green pixels that co-localize (White). Scale bar 20µm.

Table 3.1 Quantification of co-localization between LRRK2 and the TOM protein complex in COS7 cells

Subunit	Mander's Coefficient		Overlap coefficient
	M1	M2	
TOM20	0.253	0.632	0.90
TOM22	0.240	0.547	0.93
TOM40	0.190	0.520	0.92
TOM70	0.170	0.250	0.93

Abbreviations: M1, Mander's coefficient for the green channel; M2, Mander's coefficient for the red channel.

Taken together, in each of the co-localization experiments the visual outputs as well as the co-localization coefficients, indicate that LRRK2 positively co-localizes with the subunits of the TOM complex.

3.10.2 Co-localization of LRRK2 and TOM subunits using super-resolution microscopy

To confirm the co-localization of LRRK2 with the TOM complex subunits, HEK293 cells were transfected with LRRK2 and investigated using super resolution microscopy (SR-SIM). SR-SIM allows the detection of co-localizing pixels with a resolution of 100-200nm, thus providing a more accurate measure of protein co-localization. The co-localization results for LRRK2 and TOM20 (Figure 3.25), TOM22 (Figure 3.26), TOM40 (Figure 3.27) and TOM70 (Figure 3.28) are shown.

In each figure, panels A and E are overlay images of LRRK2 (green) and the respective TOM subunits (red), B and F show zoomed images to focus on specific pixels in A and E, respectively, and C and G represents scatter diagrams. These scatterplots are important as they provide a qualitative indication of the degree of co-localization in the third quadrant (Dunn *et al.*, 2011). Panels D and H show the overlap of pixels from B and F, respectively, occupying the exact same subcellular space and thus signifies the co-localized pixels.

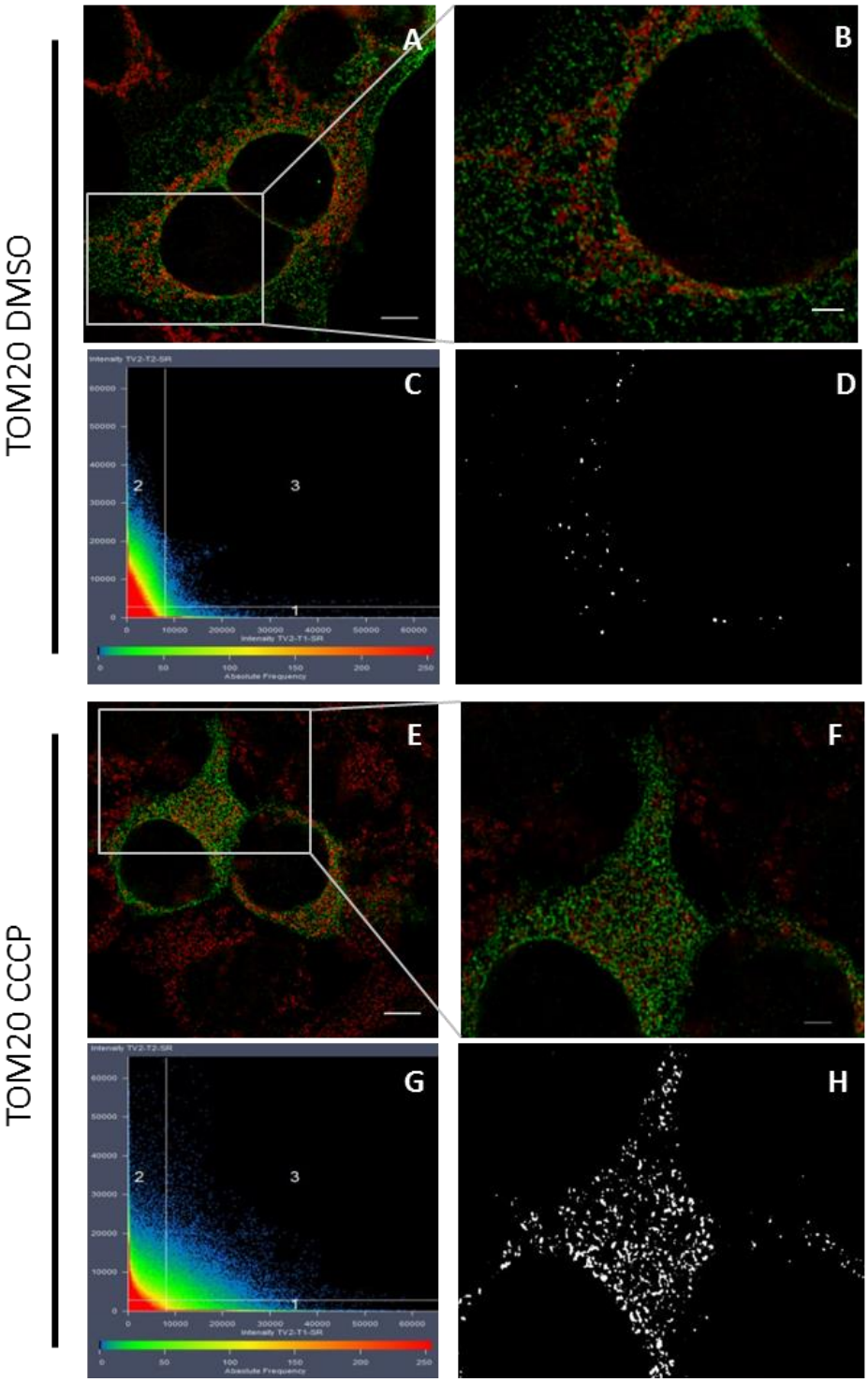

Figure 3.25 Super resolution images and co-localization analysis of LRRK2 and TOM20 under basal (DMSO) and stress conditions (CCCP) in transfected HEK293 cells. Overlay of LRRK2 labelled with donkey anti-rabbit Alexa 488 secondary antibody (Green) and TOM20 labelled with donkey anti-mouse cy3 secondary antibody (Red) treated with DMSO **(A)** and CCCP **(E)**. Enlarged images of overlays **(B and F)** and co-localized pixels (**D and H)**. Scatter diagram generated by co-localization analysis of LRRK2 and TOM20 with DMSO **(C)** or CCCP **(G)** treatment. Scale bar: 5µm **(A and E)**, 2 µm (**B and F**).

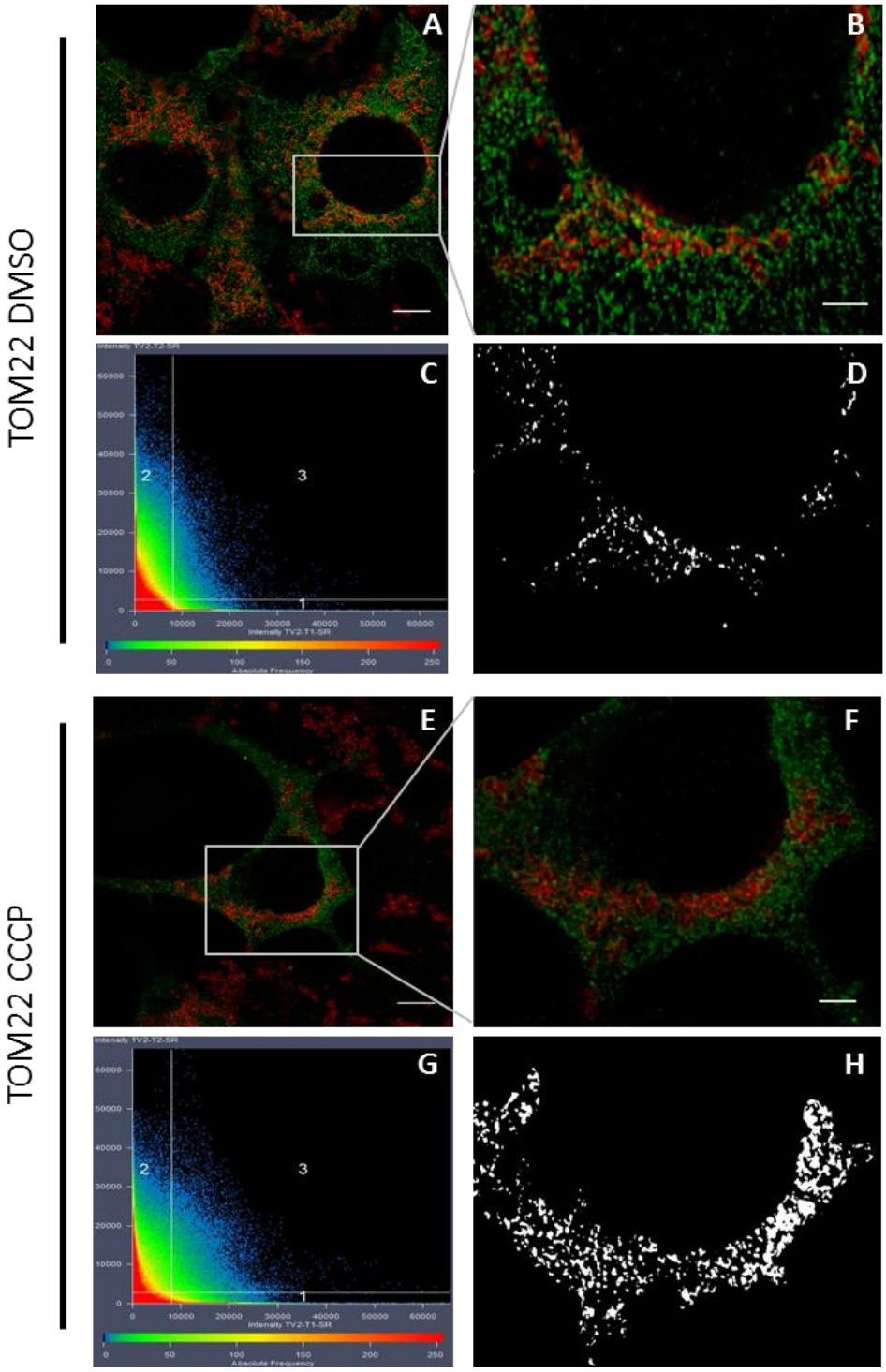

Figure 3.26 Super resolution images and co-localization analysis of LRRK2 and TOM22 under basal (DMSO) and stress conditions (CCCP) in transfected HEK293 cells. Overlay of LRRK2 labelled with donkey anti-rabbit Alexa 488 secondary antibody (Green) and TOM22 labelled with donkey anti-mouse cy3 secondary antibody (Red) treated with DMSO **(A)** and CCCP **(E)**. Enlarged images of overlays **(B and F)** and co-localized pixels (**D and H)**. Scatter diagram generated by co-localization analysis of LRRK2 and TOM22 with DMSO **(C)** or CCCP **(G)** treatment. Scale bar: 5µm **(A and E)**, 2 µm (**B and F**).

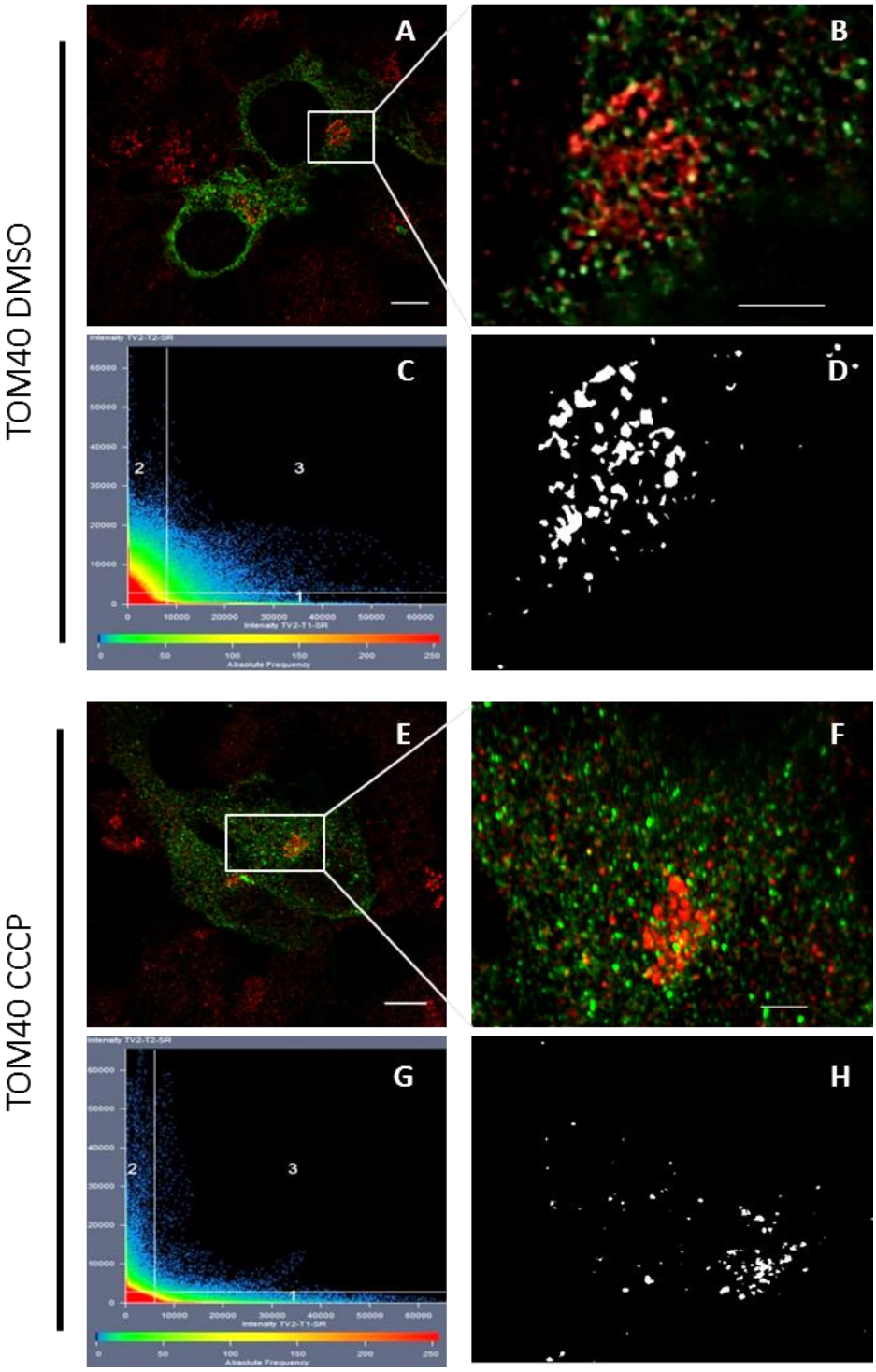

Figure 3.27 Super resolution images and co-localization analysis of LRRK2 and TOM40 under basal (DMSO) and stress conditions (CCCP) in transfected HEK293 cells. Overlay of LRRK2 labelled with donkey anti-mouse Alexa 488 secondary antibody (Green) and TOM40 labelled with donkey anti-rabbit cy3 secondary antibody (Red) treated with DMSO **(A)** and CCCP **(E)**. Enlarged images of overlays **(B and F)** and co-localized pixels (**D and H)**. Scatter diagram generated by co-localization analysis of LRRK2 and TOM40 with DMSO **(C)** or CCCP **(G)** treatment. Scale bar: 5µm **(A and E)**, 2 µm (**B and F**).

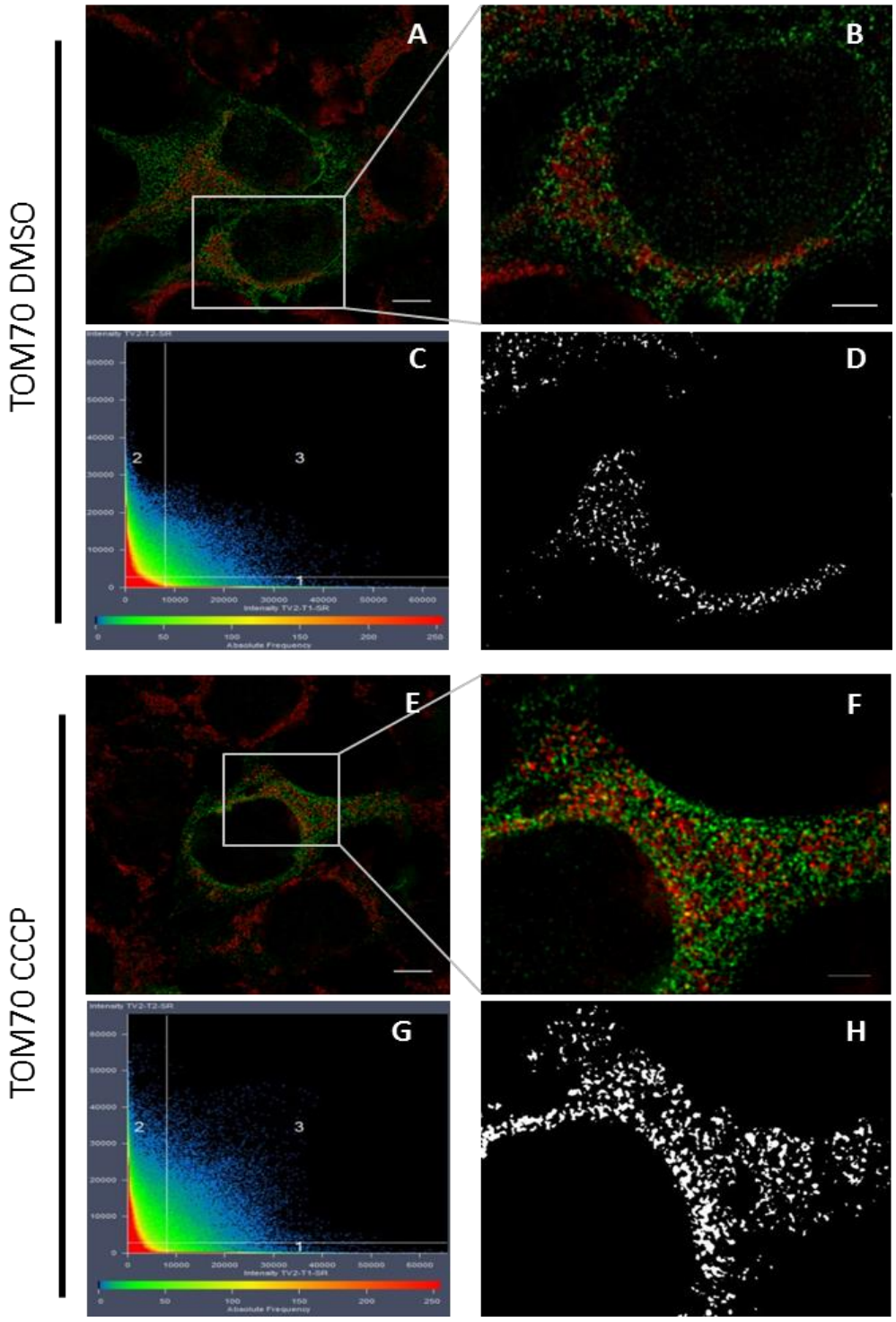

Figure 3.28 Super resolution images and co-localization analysis of LRRK2 and TOM70 under basal (DMSO) and stress conditions (CCCP) in transfected HEK293 cells. Overlay of LRRK2 labelled with donkey anti-rabbit Alexa 488 secondary antibody (Green) and TOM70 labelled with donkey anti-mouse cy3 secondary antibody (Red) treated with DMSO **(A)** and CCCP **(E)**. Enlarged images of overlays **(B and F)** and co-localized pixels (**D and H)**. Scatter diagram generated by co-localization analysis of LRRK2 and TOM70 with DMSO **(C)** or CCCP **(G)** treatment. Scale bar: 5µm **(A and E)**, 2 µm **(B and F)**.

Quantitative analysis of overlapping pixels and intensities using the Zeiss Zen black edition software package showed that LRRK2 did not co-localize with TOM20 under basal conditions (Figure 3.25 A-D). However, co-localization was confirmed between LRRK2 and the other subunits under these conditions (TOM22, Figure 3.26 A-D; TOM40, Figure 3.27 A-D; and TOM70, Figure 3.28 A-D).

Next, we investigated the co-localization of LRRK2 and the TOM complex under stress induced conditions (using CCCP to induce damage to mitochondria) based on previous studies showing the accumulation of PINK1 on the OMM and the subsequent translocation of Parkin to the OMM during mitochondrial stress (Geisler *et al.*, 2010; Narendra *et al.*, 2010; Vives-Bauza *et al.*, 2010; Kondapalli *et al.*, 2012; Bertolin *et al.*, 2013). Interestingly, we now observed co-localization between LRRK2 and TOM20 (Figure 3.25 E-H) and a marked increase in the co-localization between LRRK2 and TOM22 (Figure 3.26 E-H) based on the coefficients (Table 3.2), the scatter diagrams as well as the visual outputs. However, the induction of cellular stress, marginally reduced the co-localization between LRRK2 and TOM40 (Figure 3.27, E-H) while the co-localization between LRRK2 and TOM70 remained unchanged (Figure 3.28 E-H). For all of the co-localization experiments the weighted co-localization coefficients, the overlap coefficients and the Pearson's correlation coefficients were calculated and are shown in Table 3.2).

Table 3.2 Quantification of co-localization parameters for the association between LRRK2 and the TOM complex under normal (DMSO) and stress induced (CCCP) growth conditions in HEK293 cells

	DMSO				CCCP			
TOM subunit	Weighted (TV2-T1-SR)	Weighted (TV2-T2-SR)	Overlap	Pearson's Correlation	Weighted (TV2-T1-SR)	Weighted (TV2-T2-SR)	Overlap	Pearson's Correlation
TOM20	0.170	0.007	0.5	-0.03	0.299	0.093	0.51	-0.02
TOM22	0.255	0.049	0.49	-0.03	0.308	0.09	0.52	-0.06
TOM40	0.192	0.09	0.54	-0.02	0.053	0.101	0.32	-0.19
TOM70	0.203	0.052	0.54	-0.0	0.373	0.084	0.56	0.03

In summary, our findings indicate that co-localization between LRRK2 and TOM20 occurred under stress conditions only, whereas the co-localization between LRRK2 and TOM22, TOM40 and TOM70 occurred under both basal and stress conditions. Interestingly, the co-localization with TOM22 was increased when stress was induced whereas for TOM40 the co-localization was increased under basal conditions.

3.10.3 Co-immunoprecipitation of LRRK2 and TOM subunits

Although, co-localization is a powerful tool to identify subcellular location of proteins at a specific time and under specific conditions it does not provide proof of an actual association between proteins within a complex. Therefore, co-immunoprecipitation (Co-IP) was used in our study to validate the confocal and SR-SIM findings.

The Co-IP results for the association between LRRK2 and TOM subunits (Figure 3.29 A, C, E and G) and the reciprocal experiments (Figure 3.29 B, D, F and H) are shown. All negative controls (protein G agarose control and immunoprecipitation with the anti-HA negative control antibody), except the one for TOM40, did not produce any bands. Non-specific bands were present in the Co-IP assays with TOM40 (Figure 3.29 E) which were at the predicted size for antibody light chains (approximately 35kDa), however these were observed in all the samples and could therefore be excluded from the analysis. It should also be noted that these Co-IP assays were completed in the context of whole protein lysate from a given cell population.

As suggested by SR-SIM experiments, LRRK2 and TOM20 did not associate under basal conditions however, when stress was induced using CCCP, an association was detected (Figure 3.29 A). Reciprocal assays also corroborated the SR-SIM and initial Co-IP results, showing both LRRK2 and TOM20 within the same protein complex exclusively under CCCP conditions, and not under basal conditions (Figure 3.29 B). These results confirm the co-localization findings (Figure 3.25). Furthermore, LRRK2 and TOM22 were moderately associated with the complex under basal conditions but this association increased during cellular stress (Figure 3.29 C). Reciprocal Co-IP analysis verified this increased association between LRRK2 and TOM22 upon CCCP treatment (Figure 3.29 D). This trend was also observed in SR-SIM co-localization analysis (Figure 3.26 A-H).

Our results further showed that LRRK2 could immunoprecipitate with the protein complex containing both TOM40 (Figure 3.29 E) and TOM70 (Figure 3.29 G) under both DMSO and CCCP conditions. This was also confirmed by reciprocal immunoprecipitations, although to a lesser extent with TOM40 under stress conditions (Figure 3.29 F and H). Again, these findings corroborated the SR-SIM results (Figure 3.27 E-H and Figure 3.28).

We consequently propose that LRRK2 associates with several subunits of the TOM complex, possibly through the multiple potential protein-protein interaction domains surrounding the central core of LRRK2 or through its phosphorylation activity.

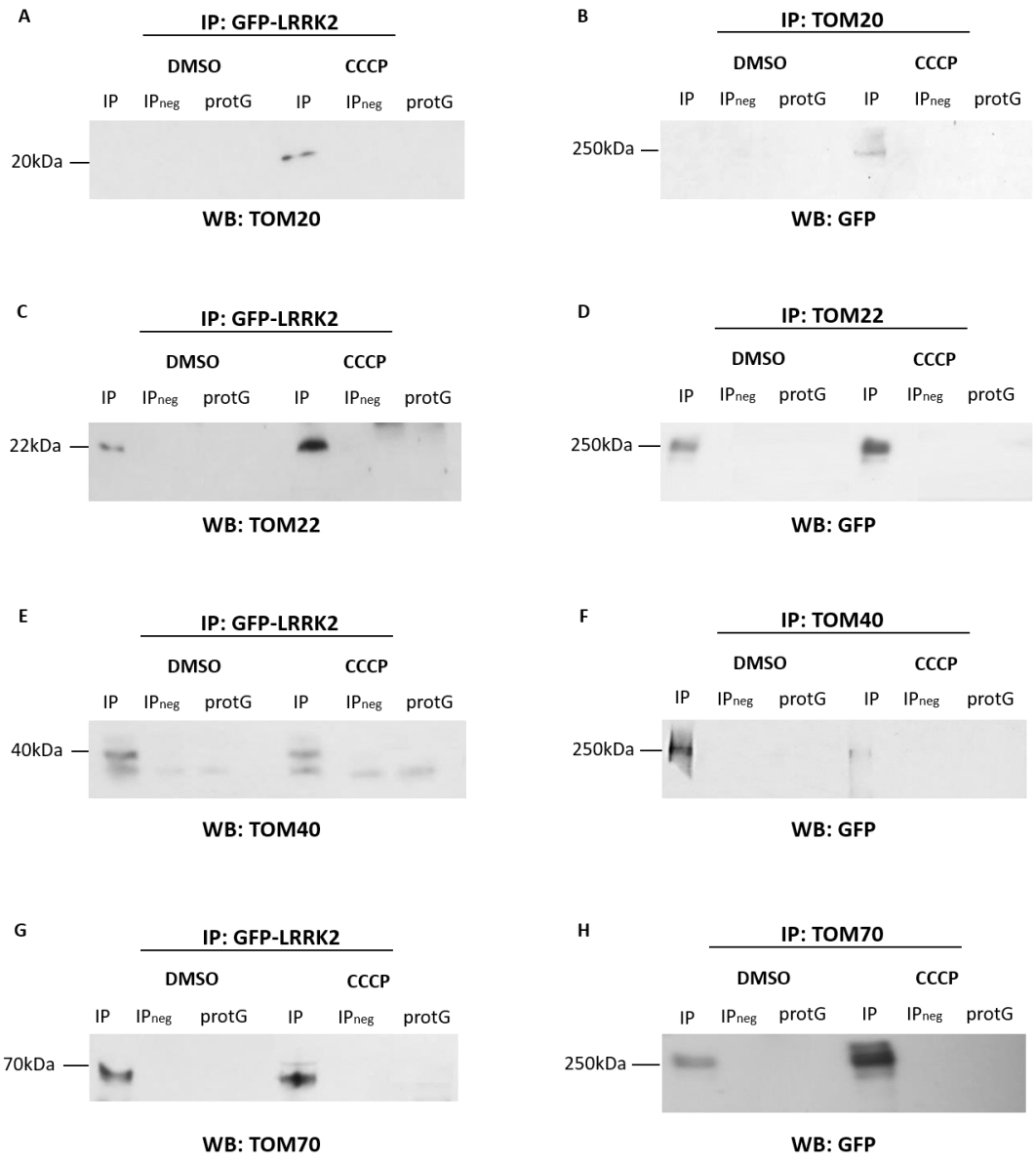

Figure 3.29 Western blots of co-immunoprecipitation analysis of LRRK2 with the subunits of the TOM complex under basal (DMSO) and stress induced (CCCP) conditions in transfected HEK293 cells. Reciprocal reactions were performed for each experiment. Abbreviations: CCCP, Carbonyl cyanide m-chlorophenyl hydrazone; DMSO, Dimethyl sulfoxide; GFP, green fluorescent protein; IP, immunoprecipitation; IPneg, immunoprecipitation using a "non-relevant" antibody as negative control; kDa, kilo dalton; WB, Western blot; protG, protein G agarose control.

In conclusion, both co-localization and Co-IP analysis revealed and confirmed that LRRK2 associates with a protein complex containing the subunits of the TOM complex. These associations were identified under both basal and stress conditions, and differing levels of associations were identified for the different subunits. Reasons for this are unclear at present and further validation studies are required.

Chapter 4: Discussion

Contents

4.1 Summary of the main findings

The present study aimed to functionally characterize the novel Q2089R variant which is located in the kinase domain of LRRK2. To our knowledge, we are the first group to ever report on Q2089R, which was found in the unique South African population. G2019S was included in the functional analyses for comparison purposes. The presence of any other known PD-causing mutations or any other possibly pathogenic mutations in *LRRK2* in the Q2089R-positive proband was excluded by WES analysis. Bioinformatics analysis indicated that the variant may significantly disrupt the structure and function of the protein and therefore may be pathogenic. Interestingly, Q2089R was found to significantly decrease autophosphorylation of LRRK2 *in vitro* and showed a reduction in metabolic activity and MMP when overexpressed in HEK293 cells. A decrease in glycolytic reserve and in basal respiration was detected when measuring extracellular acidification rate (ECAR) and oxygen consumption rate (OCR). Q2089R-positive fibroblasts showed significantly reduced cellular metabolic activity and MMP (under cellular stress) when compared to WT cells. Additionally, an increase in basal respiration, proton leak, maximal respiration and spare respiratory capacity was observed while ATP-coupling efficiency was significantly reduced. A non-significant trend for an increase in glycolysis was observed whereas both glycolytic reserve and glycolytic capacity were significantly reduced. In both models used in this study, Q2089R significantly increased the pool size of autophagosomes.

In comparison, in the G2019S overexpression model a significant increase in autophosphorylation, reduced metabolic activity and reduced MMP was observed. However, no changes were detected in mitochondrial respiration and glycolysis. In the *ex vivo* model, G2019S-positive cells showed reduced cellular metabolic activity and increased basal respiration, ATP-linked respiration and autophagic flux. The MMP of these cells were not affected under basal conditions although a non-significant trend for a decrease was observed under stress conditions.

Finally, we showed that WT LRRK2 co-localizes and associates with a protein complex containing TOM22, TOM40 and TOM70. Surprisingly, LRRK2 and TOM20 associated with the complex only when cells were stressed with CCCP. This induction of cellular stress also resulted in an increased association of LRRK2, TOM22 and TOM70 while the association of TOM40 with this complex was decreased.

Our findings in comparison to the literature is summarized in Table 4.1. We found that the G2019S models in our study, for the most part, agreed with previous literature. Interestingly, however, we showed that Q2089R had a more severe effect on various cellular phenotypes. For example, Q2089R exhibited increased proton leak respiration and decreased ATP-coupling efficiency, glycolytic reserve, glycolytic capacity and MMP when compared to WT cells.

Table 4.1 Summary of findings from functional experiments for LRRK2 G2019S and Q2089R

Assay		Previous studies						Present study	
		G2019S						G2019S	Q2089R
Autophosphorylation using pSer1292		Increase (Sheng *et al.*, 2012)	Increase (Reynolds *et al.*, 2014)	Increase (Henry *et al.*, 2015)	Increase (Alcalay *et al.*, 2015)	Increase (Fraser *et al.*, 2016)	-	Increase (HEK293)	Decrease (HEK293)
Cell viability (Commercial cell line)		Decrease (Smith *et al.*, 2006)	Decrease (West *et al.*, 2007)	Decrease (Liou *et al.*, 2008)	Decrease (Heo *et al.*, 2010b)	Decrease (Kondo *et al.*, 2011)	Decrease (Wang *et al.*, 2012b)	Decrease (HEK293)	Decrease (HEK293)
Cell viability (Neurite morphology)		Decrease (MacLeod *et al.*, 2006)	Decrease (Plowey *et al.*, 2008)	Decrease (Parisiadou *et al.*, 2009)	Decrease (Heo *et al.*, 2010a)	Decrease (Lavalley *et al.*, 2016)	-	ND	ND
Cell proliferation (Primary cells)		Unchanged (Decrease with MPP^+) (Yakhine-Diop *et al.*, 2014)	-	-	-	-	-	Decrease (Fibroblasts)	Decrease (Fibroblasts)
Mitochondrial membrane potential	**Commercial cell line**	Decrease (Wang *et al.*, 2012b)	Decrease (Papkovskaia *et al.*, 2012)	Decrease (Cherra *et al.*, 2013)	-	-	-	Decrease (HEK293)	Decrease (HEK293)
	Primary cells	Decrease (Basal) (Mortiboys *et al.*, 2010)	Decrease (Basal) (Papkovskaia *et al.*, 2012)	Decrease (Basal) (Grünewald *et al.*, 2014)	Decrease (Basal) (Su *et al.*, 2015)	-	-	No change with DMSO (Fibroblasts) No change with CCCP (Fibroblasts)	No change with DMSO (Fibroblasts) Decrease with CCCP (Fibroblasts)
Mitochondrial respiration	**Commercial cell line**	Increase basal resp. (Papkovskaia *et al.*, 2012)	-	-	-	-	-	No change (HEK293)	Decrease in basal respiration (HEK293)
	Primary cells	Decrease ATP production (Mortiboys *et al.*, 2010)	Increase basal resp. Increase proton leak Decrease ATP production (Papkovskaia *et al.*, 2012)	Decrease basal resp. Decrease maximal resp. (Cooper *et al.*, 2012)	Increase proton leak (Grünewald *et al.*, 2014)	Decrease basal resp. Decrease maximal resp. Decrease ATP-coupling (Mortiboys *et al.*, 2015)	-	Increase in basal resp. Increase in ATP-linked resp. (Fibroblasts)	Increase in basal resp. Increase in proton leak Decrease in ATP-coupling Increase in maximal resp. Increase in spare resp. capacity (Fibroblasts)

Mitochondrial DNA copy number (Primary cells)		Increase (G2019S carriers) Decrease (G2019S affected) (Grünewald *et al.*, 2014)	No change (Sanders *et al.*, 2014)	Decrease (Su *et al.*, 2015)	-	-	-	No change (Fibroblasts)	Increase (Fibroblasts)
Glycolysis	**Commercial cell line**	Upregulation of glycolysis (Nikonova *et al.*, 2012)	-	-	-	-	-	No change (HEK293)	Decrease in glycolytic reserve (HEK293)
	Primary cells	-	-	-	-	-	-	Increase in glycolysis (Fibroblasts)	Decrease in glycolytic reserve Decrease in glycolytic capacity (Fibroblasts)
Autophagic flux	**Commercial cell line**	Increase (Plowey *et al.*, 2008)	Increase (Su and Qi, 2013)	No change in LC3 (Orenstein *et al.*, 2013)	-	-	-	No change in LC3 II No change in P62 (HEK293)	Increase in LC3 II Increase in P62 (HEK293)
	Primary cells	Increase in LC3 II Increase in P62 (Sánchez-Danés *et al.*, 2012)	Increase in LC3 II No change in P62 (Manzoni *et al.*, 2013b)	Increase (Bravo-San Pedro *et al.*, 2013)	Increase (Yakhine-Diop *et al.*, 2014)	Increase in LC3 II and P62 (Su *et al.*, 2015)	-	Increase in LC3 II No change in P62 (Fibroblasts)	Increase in LC3 II Increase in P62 (Fibroblasts)

resp., respiration; LC3 II, Microtubule Associated Protein 1 Light Chain 3; P62, Sequestosome 1; ND, not done

4.2 Identification of Q2089R

LRRK2 Q2089R was present in only one of 493 PD patients and in one of the 776 controls screened. The Q2089R-positive patient had an age at onset (AAO) of 50 years and presented with typical features of PD. He developed marked motor fluctuations with dyskinesia including shaking of the legs and feet as well as speech impediments. He had undergone bilateral globus pallidus internus (GPi) deep brain stimulation (DBS) surgery with excellent results at the age of 64, and was cognitively normal. He passed away of pneumonia at the age of 74 years. *LRRK2*-associated PD patients typically present with features of motor symptoms including resting tremor and postural instability (Trinh *et al.*, 1993), and while the AAO varies widely, individuals usually present with the first symptoms after the age of 60 years (Paisán-Ruíz *et al.*, 2005; Kay *et al.*, 2006b; Trinh *et al.*, 2014). These patients respond well to treatment (Schüpbach *et al.*, 2007), have lower rates of developing dementia (Srivatsal *et al.*, 2015) and mainly present with an AD family history of disease. Our patient presented with many of these features except that his AAO was younger (but again this is not uncommon) (Kay *et al.*, 2006b).

It is well-established that the penetrance of pathogenic PD-causing variants, especially *LRRK2* mutations, are variable and have been shown to be dependent on age, ethnicity as well as environmental factors (Trinh *et al.*, 1993; Klein and Westenberger, 2012). In fact, the penetrance of G2019S in certain populations has been shown to be as low as 30% (Clark *et al.*, 2006b; Ozelius *et al.*, 2006; Ferreira *et al.*, 2007; Hentati *et al.*, 2014). Also, G2019S has been found in numerous unaffected control individuals in various studies (Bonifati, 2006; Kay *et al.*, 2006a; Change *et al.*, 2008). Therefore, the finding of Q2089R in one unaffected female control individual cannot rule it out as being 'disease-causing'. The control had been recruited from the Geriatric clinic at Tygerberg Hospital (South Africa) and apparently did not exhibit any signs of PD at the time of her demise at 83 years of age. It is possible however that subtle clinical symptoms might have been overlooked, as she had not been assessed by a neurologist. She had already died by the time we identified that she harbored Q2089R. No family history of PD was reported by this individual.

Modelling and *in silico* functional predictions of the 2089R amino acid, showed that its side chain introduces a significant difference which likely affects protein folding and function. Each amino acid has its own specific size, charge, and hydrophobicity value (Biro, 2006), and the WT (Q) and mutant (R) residues have distinct properties. For example, R is much larger than Q, and as Q is predicted to be buried in the core of the protein, the introduction of this larger, charged residue will most likely not fit into the core which could lead to a change in protein structure. Also, as this amino acid position is located in a loop structure that is predicted to be involved in protein-protein interactions, disruption of the loop by the R residue is likely to alter these interactions (Regad *et al.*, 2010). Although, it is

acknowledged that the template used to model the kinase domain of LRRK2 only has an approximately 30% sequence homology with LRRK2, it does provide a reasonable estimate of how the amino acid change will affect protein function/folding in that specific domain. However, it would be interesting to investigate the protein modelling and folding using a structure with closer similarity to LRRK2, which is currently unavailable, or ideally to have the crystal structure of full-length LRRK2 available for modelling purposes.

4.3 Overexpression of Q2089R reduces metabolic activity

In the present study, our results revealed that the overexpression of Q2089R and G2019S substantially decreased the metabolic activity of the cells (Figure 3.11). The increase in cytotoxicity, attributed to the overexpression of G2019S, was in accordance with previous studies using similar techniques (Liou *et al.*, 2008; Kondo *et al.*, 2011).

Commercial cell lines and mouse primary cortical neurons transfected with either R1441C or G2019S constructs only or co-transfected with both G2019S and kinase dead constructs (D1994N and K1906A), exhibited decrease cell viability (Smith *et al.*, 2006; Wang *et al.*, 2012b). Similarly, West and co-workers showed that the overexpression of G2019S, Y1699C, and I2020T reduce cell viability of transfected mouse cortical neurons compared to control cells (West *et al.*, 2007). Likewise, the overexpression of the PD risk variant, G2385R, also significantly reduced the cell viability compared to control cells. In a recent study, five *LRRK2* variants (L1165P, T1410M, M1646T, L2063X and Y2189) of unknown pathogenicity were analyzed for their possible involvement in PD using an overexpression model in HEK293 cells and cell viability assays (Refai *et al.*, 2015). All of these variants significantly reduced cell viability. Interestingly, all variants also exhibited increased kinase activity, except L2063X which is located in the kinase domain of LRRK2.

When investigating the viability of patient-derived fibroblasts in the present study, we did not detect any differences between WT and mutant (G2019S or Q2089R) cells after 24 hours of growth (Figure 3.12). This was in agreement with a previous study showing similar cellular viability between control and G2019S carrying cells after 24 hours of growth under basal conditions (Yakhine-Diop *et al.*, 2014). Furthermore, fibroblasts from patients carrying *Parkin* mutations were shown to have similar growth rates when compared to healthy control cells (Mortiboys *et al.*, 2008). However, inconsistencies have been reported regarding the growth rate of *Parkin* mutant fibroblasts, with literature showing both increased and decreased cellular growth rates (Pacelli *et al.*, 2011; Haylett *et al.*, 2016). Interestingly, in the present study, we noted a significant decline in metabolic activity for both G2019S- and Q2089R-carrying cells compared to control cells after three days of incubation. To our knowledge, this is the

first study to investigate the metabolic activity of human fibroblasts carrying *LRRK2* mutations/variants over an extended period (i.e. five days). Our findings thus highlight the advantages of investigating metabolic activity over time since important differences might be missed with short-term growth assays.

Although additional studies are required to further interrogate the effect of Q2089R on cytotoxicity, possibly by investigating neurite morphology, our findings suggest that Q2089R could have functional implications. Previous studies showed G2019S to reduce neurite length, branching and general complexity (MacLeod *et al.*, 2006; Ramonet *et al.*, 2011; Schwab and Ebert, 2015). However, it should be noted that neither the inhibition of LRRK2 kinase activity nor the expression of WT or G2019S *LRRK2* in human fibroblasts or transgenic mouse brains affected neurite complexity in a recent study (Garcia-Miralles *et al.*, 2015). Thus, we suggest that assays on neurite complexity in combination with alternative toxicity tests, for example the Image-iT® DEAD™ Green cytotoxicity assay (Smith *et al.*, 2015), should be used in future studies to determine the effect of mutations/variants on cell viability and metabolic activity over an extended period.

4.4 Could decreased LRRK2 kinase activity be linked to PD?

Increased kinase activity of LRRK2 is widely acknowledged to be implicated in PD pathogenesis (Cookson et al. 2007; Gloeckner et al. 2006; Greggio 2012; Henry et al. 2015; Smith et al. 2006). In the present study we used pSer^{1292} autophosphorylation as a measure of WT and mutant (G2019S and Q2089R) LRRK2 kinase activity *in vitro*. In earlier studies, autophosphorylation had been detected using radioactivity (Luzón-Toro *et al.*, 2007; Webber *et al.*, 2011; Lewis, 2012) or other kinase assays using purified protein (Nichols *et al.*, 2009; Liu *et al.*, 2014). But more recent advances made it possible to use a single autophosphorylation site (Ser^{1292}) and Western blot analysis to measure the kinase activity of LRRK2.

The use of the pSer^{1292} autophosphorylation method has been validated as an indicator of kinase activity *in vitro* as well as a potential biomarker for *ex vivo* studies (Sheng *et al.*, 2012; Reynolds *et al.*, 2014; Alcalay *et al.*, 2015; Fraser *et al.*, 2016). Reynolds and colleagues showed that G2019S and R1441C augment autophosphorylation of the serine residue at position 1292 when compared to WT *LRRK2* protein (Reynolds *et al.*, 2014). Additionally, the kinase-dead mutant, D1994A, showed no autophosphorylation activity.

In another study, abundant LRRK2 protein levels were found in urinary exosomes of PD patients (Fraser *et al.*, 2013). Alcalay and colleagues subsequently proposed to measure pSer^{1292} LRRK2 levels in the exosomes of *LRRK2* G2019S carriers with PD, non-carriers with PD and healthy individuals

without PD (Alcalay *et al.*, 2015). They found that it was possible to distinguish between *LRRK2* G2019S carriers (with PD) and non-carriers with and without PD using pSer^{1292}. G2019S carriers with PD also had higher ratios of pSer^{1292} LRRK2 over total LRRK2 protein when compared to asymptomatic G2019S carriers (Fraser *et al.*, 2016). Therefore, the G2019S mutation is not necessarily sufficient to cause PD. Finally, LRRK2 autophosphorylation and phosphorylation of LRRKtide, the proposed synthetic substrate of LRRK2, were found to be comparable (Reynolds *et al.*, 2014). Thus, researchers identified autophosphorylation as a true biochemical readout of LRRK2 kinase activity *in vitro* (Reynolds *et al.*, 2014). Therefore, we believe that the use of pSer^{1292} autophosphorylation is a reliable and robust indicator of kinase activity for LRRK2.

Unexpectedly, we observed a marked reduction in the autophosphorylation activity for Q2089R when compared to WT and G2019S, indicating that Q2089R almost totally abolishes autophosphorylation of LRRK2 (Figure 3.10). G2019S, in agreement with previous studies (West *et al.*, 2005; Smith *et al.*, 2006; Sheng *et al.*, 2012; Reynolds *et al.*, 2014; Fraser *et al.*, 2016), exhibited significantly increased autophosphorylation activity (Figure 3.10). There have been many previous studies investigating the effect of other PD-causing mutations on the kinase activity of LRRK2, but they have produced conflicting findings. Some studies show that I2020T decreases kinase activity (Jaleel *et al.*, 2007; Anand *et al.*, 2009), while others show an increased or unchanged kinase activity for this mutation (Gloeckner *et al.*, 2006; Sheng *et al.*, 2012). G2385R (the PD risk factor), has been shown to decrease GTPase and kinase activity and was identified as a partial loss-of-function mutation (Rudenko *et al.*, 2012b; Rudenko and Cookson, 2014; Ho *et al.*, 2016). A variant of unknown pathogenicity (L2063X), also located in the kinase domain of LRRK2, was recently shown to decrease autophosphorylation activity although these findings were not statistically significant (Refai *et al.*, 2015). These findings highlight the limitations of regarding *increased kinase activity* as the sole disease mechanism underlying *LRRK2* mutations.

Kinase activity is an essential process involved in numerous pathways including cell signaling, protein regulation, mitochondrial homeostasis and autophagy (Manzoni *et al.*, 2013a). PINK1 is a protein kinase that is known to be involved in PD development. PINK1 has been shown to be autophosphorylated on specific serine residues (Ser^{228} and Ser^{402}) (Okatsu *et al.*, 2012; Aerts *et al.*, 2015), which occurs upon cellular stress and was shown to be essential for the recruitment of Parkin to defective mitochondria (Okatsu *et al.*, 2012; Song *et al.*, 2013). Mutations in the kinase domain of PINK1 (such as L347P) effectively destabilize the protein and reduce its kinase activity (Beilina *et al.*, 2005). For LRRK2, increased kinase activity leads to altered phosphorylation of its substrates and enlargement of lysosomes (Greggio, 2012; Henry *et al.*, 2015) whereas the inhibition of LRRK2's kinase

activity has been shown to alter binding of proteins and to result in the dephosphorylation of its serine residues (Dzamko *et al.*, 2010). Furthermore, this inhibition also altered the cytoplasmic localization of LRRK2. Another study showed that DRP1 recruitment for mitochondrial homeostasis (fission/fusion) is dependent on LRRK2's kinase activity, thus highlighting its importance in cellular health (Su and Qi, 2013). Very recently, Lobbestael and co-workers also showed that the inhibition of LRRK2's kinase activity destabilizes the protein and reduces LRRK2 protein levels (Lobbestael *et al.*, 2016). It is therefore crucial to consider all consequences of LRRK2 kinase inhibition on cellular function since it is anticipated that a decrease or loss of kinase activity could also be detrimental to cells (Greggio *et al.*, 2006), and that both increased and decreased LRRK2 kinase activity could be linked to the development of PD (Anand *et al.*, 2009; Rudenko *et al.*, 2012a).

In our study we show that Q2089R reduces LRRK2's kinase activity and we speculate that this could have further detrimental effects on cellular functions for which LRRK2 is responsible. Consequently, from the findings of our study and the evidence provided by many previous studies, we propose that decreased kinase activity of LRRK2 could be implicated in PD pathogenesis.

4.5 Q2089R has a more damaging effect on glycolytic and mitochondrial respiration than G2019S

The maintenance of high MMP is essential for mitochondrial health. When the MMP is lost or decreased, the import of mitochondrial proteins and oxidative phosphorylation activities are disrupted, thus causing mitochondria to become dysfunctional. In the present study, we found that Q2089R overexpression resulted in significantly reduced MMP. This decrease in mitochondrial polarization was observed under basal conditions while the MMP of cells were not affected by an external mitochondrial stressor (CCCP) (Figure 3.13). When investigating the MMP of endogenous LRRK2 in patient-derived fibroblasts under basal conditions, we did not observe any differences between Q2089R-positive and WT and cells (Figure 3.14 B). However, when we compared cellular phenotypes of WT and mutant fibroblasts after treatment with CCCP, we found that Q2089R mitochondria were markedly more depolarized than mitochondria in control cells (Figure 3.14 C).

Additionally, we showed that G2019S decreased MMP when overexpressed in HEK293 cells (Figure 3.13) which is in agreement with previous studies showing decreased MMP in G2019S overexpression models (Papkovskaia *et al.*, 2012; Wang *et al.*, 2012b; Cherra *et al.*, 2013). However, when we investigated the MMP of G2019S-carrying fibroblasts, under both basal and CCCP-treatment conditions, we could not detect any significant differences compared to control cells although a trend towards a decrease in MMP was observed when these cells were stressed (Figure 3.14 C). These results were unexpected since previous studies, specifically focusing on LRRK2 fibroblasts, showed

G2019S to have significantly depolarized mitochondria (Mortiboys *et al.*, 2010; Papkovskaia *et al.*, 2012; Grünewald *et al.*, 2014; Su *et al.*, 2015). Grünewald et al. (2014) reported that even asymptomatic G2019S carriers exhibit reduced MMP under basal conditions (Grünewald *et al.*, 2014). Notably, contradictory findings have previously been reported for *Parkin* mutant fibroblasts where Zanellati et al. reported significantly lower MMP for mutant fibroblasts (Zanellati *et al.*, 2015), while others showed comparable MMP between mutant and WT *Parkin* fibroblasts (Grünewald *et al.*, 2010; Haylett *et al.*, 2016).

Somewhat similar to our results, Smith and colleagues could not detected any difference in MMP between WT and G2019S fibroblast lines at baseline (Smith *et al.*, 2015). However, upon exposure to Valinomycin, a potent antibiotic which acts as a potassium (K^+) ionophore, the MMP was reduced. They concluded that fibroblasts derived from PD patients carrying *LRRK2* mutations exhibit disease-relevant mitochondrial phenotypes, that were aggravated under conditions of pharmacological stress. Even though the results are widely variable between studies, we believe that these discrepancies could possibly be explained by the variable penetrance and phenotypic expression of *LRRK2* mutations (Nuytemans *et al.*, 2010; Wider *et al.*, 2010) as well as the diverse genetic backgrounds of patients used in the various studies.

Next, we investigated the effect of WT and mutant/variant *LRRK2* on mitochondrial respiration (as measured by OCR) and glycolysis (as measured by ECAR). HEK293 cells overexpressing Q2089R exhibited significantly lower basal respiration and severely decreased glycolytic reserve (Figure 3.16 A and 3.19 D, respectively). The decreased basal respiration was indicative of defective mitochondrial respiration and ETC function. This dysfunction was reflected by the major decrease in glycolytic reserve which signifies the inability of Q2089R expressing cells to produce adequate 'fuel' for glycolysis.

Overexpression of G2019S, conversely, did not show any differences in either OCR (Figure 3.16) or ECAR (Figure 3.19). This was surprising since a previous report, albeit using a Clark-type oxygen electrode, showed that G2019S-expressing SHSY5Y cells exhibit increased basal respiration (Papkovskaia *et al.*, 2012). It should be noted however that the transfection efficiency of constructs was relatively low, between 6% and 8% (Figure 3.11 B), which we believe may have contributed to the lack of differences recorded in the overexpression model in our study. To overcome this limitation and to determine the effect of *LRRK2* mutations *ex vivo*, we also studied the OCR and ECAR in patient-derived fibroblasts.

Some of our observations in the fibroblasts led us to speculate that the findings of the Q2089R model could be as a result of *compensatory mechanisms*. Protons are typically pumped through the ETC to the IMS to create a gradient across the IMM. This gradient is used to drive protons back through complex V (ATP synthase) to generate ATP. However, here we observed a major increase in proton leak for Q2089R-carrying fibroblasts (Figure 3.17 C), showing that protons leaked back across the membrane to the mitochondrial matrix which coincided with a reduced ATP-coupling efficiency (Figure 3.17 D). This increase in proton leak could also suggest an increase in membrane permeability (Porter *et al.*, 1999). Thus, we speculate that an increase in proton leakage and decreased ATP-coupling efficiency could signify an underlying mitochondrial deficit in these fibroblasts. However, it has been suggested that an increase in proton leakage could be a compensatory mechanism used to decrease ROS production (Brand, 2000; Lee *et al.*, 2000; Hayat, 2016). In support of this compensatory mechanisms theme, we observed striking increases in both maximal respiration and spare respiratory capacity (Figure 3.17 E and F). Maximal respiration is the maximum rate at which the mitochondria can respire while spare respiratory capacity is defined as the amount of additional ATP that can be produced in case of a sudden energy demand emergency (Nicholls, 2009; Desler *et al.*, 2012). We believe that the marked increase in maximal respiration and spare respiratory capacity contributes to the compensation of Q2089R fibroblasts to cellular stress and that these cells are attempting to enhance ATP production perhaps via increased glycolysis or mitochondrial biogenesis. This mechanism was, however, insufficient since basal respiration was only modestly increased and ATP-linked respiration was not increased at all (Figure 3.17 A and B).

When cells were forced to shift from oxidative phosphorylation to glycolytic metabolism to produce ATP, Q2089R fibroblasts did not show any significant changes in glycolysis (Figure 3.20 B) but exhibited severely reduced glycolytic capacity and glycolytic reserve ECAR (Figure 3.20 C and D). This suggest that Q2089R could result in serious cellular damage or even death due to energy demand deficiencies in fibroblasts and that the proposed mechanisms could not compensate for the deficit in glycolytic metabolism (Das, 2013).

Cells with high energy demand, such as neurons, rely on oxidative phosphorylation for ATP production and are dependent on mitochondrial biogenesis (Uittenbogaard and Chiaramello, 2014). Previous studies have implicated increased mitochondrial biogenesis as a compensatory mechanism in muscle cells and fibroblasts to improve aging phenotypes and compensate for mitochondrial deficits (Lee *et al.*, 2000; Dillon *et al.*, 2012). An increase in mitochondrial biogenesis was found to be directly correlated with the increase in expression of the master co-activator peroxisome proliferator-activated receptor γ co-activator-1α (PGC-1α) (Dillon *et al.*, 2012). Subsequently, the degradation of

PGC-1α was shown to cause inhibition of mitochondrial biogenesis which ultimately induced neurodegeneration (Xu *et al.*, 2014).

Interesting to note was the fact that mitochondrial biogenesis was shown to be induced by the cell cycle-dependent activation of the TOM protein complex and that this complex is essential for adequate mitochondrial biogenesis which increases due to fission of existing mitochondria (Harbauer *et al.*, 2014; Uittenbogaard and Chiaramello, 2014; Shiota *et al.*, 2015). Since LRRK2 has been implicated in mitochondrial fission/fusion dynamics (Wang *et al.*, 2012b) and showed altered mitochondrial respiration in our study, we were interested to determine whether differences in mitochondrial copy number between WT and mutant fibroblasts exists. We observed that Q2089R fibroblasts had a significantly increased mtDNA copy number, and therefore a possible increase in mitochondrial biogenesis, compared to WT and G2019S fibroblasts (Figure 3.21). Taken together, we believe that Q2089R-carrying fibroblasts are attempting to overcome their mitochondrial deficiencies through compensatory mechanisms such as increases in proton leak, maximal respiration, spare respiratory capacity and mitochondrial biogenesis. However, these mechanisms appear to be inadequate since mitochondrial ATP-coupling efficiency in these cells was significantly reduced. It should be noted however that the compensatory alterations proposed here would differ dramatically between different cell types and therefore the effects that we observe in the present study should not be directly extrapolated to adaptations or alterations that would occur in neuronal cells.

Next, we examined G2019S-carrying fibroblasts and found that these cells exhibited an increase in basal respiration and ATP-linked respiration (Figure 3.17 A and B, respectively). However, no difference in any of the other OCR parameters were detected when compared to control cells (Figure 3.17 C-F). This was unexpected since previous studies showed G2019S carriers to have decreased basal respiration (Cooper *et al.*, 2012; Mortiboys *et al.*, 2015), decreased maximal respiration (Cooper *et al.*, 2012; Mortiboys *et al.*, 2015), increased proton leak (Grünewald *et al.*, 2014) and decreased ATP-linked respiration (Mortiboys *et al.*, 2015) using OCR as a measure of mitochondrial respiration. Motriboys et al. (2015) specifically showed complex III and complex IV to be defective and not complex II as previously reported by their group (Mortiboys *et al.*, 2010, 2015). In the previous study mitochondrial ATP synthesis was decreased in G2019S patients (Mortiboys *et al.*, 2010). In another study using the Clark-type oxygen electrode, cellular ATP content and spare respiratory capacity was decreased whereas proton leak and basal oxygen consumption was increased in G2019S fibroblasts (Papkovskaia *et al.*, 2012). These results confirm the uncoupling of mitochondrial oxidative phosphorylation and ETC activity.

In our study, when G2019S fibroblasts were forced to use glycolytic metabolism, we observed an increase in glycolysis (Figure 3.20 B). This suggested that, together with increased basal respiration and ATP-linked respiration, G2019S fibroblasts did not display major mitochondrial deficits and that mitochondria of G2019S-carrying fibroblasts in our study were able to function relatively well under conditions of stress. We speculate that this could possibly be due to a compensatory mechanism which remains to be identified. This observation corresponds to our results on MMP of G2019S fibroblasts where no depolarization was seen under basal conditions and a non-significant decrease in MMP was observed under stress-induced culture conditions (Figure 3.14 C). Cells were stressed for one hour only during MMP assays and the pharmacological stressors added during mitochondrial respiration tests only measured the fibroblast response over a few minutes. Therefore, an increase in stress duration in both MMP and Seahorse experiments might reveal additional underlying information regarding mitochondrial respiration or glycolysis that may well have been overlooked.

It is interesting to postulate that the G2019S fibroblasts used in our study are genetically different from G2019S carriers from previous studies and could account for the contradictory results. Also, the G2019S-positive individual in our study has been taking numerous prescription medications which may influence the cells; the effect of specific medications (and combination of medications) on epigenetic changes and long-term cellular function such as mitochondrial respiration and glycolytic metabolism, in culture, remains to be elucidated.

4.6 Q2089R increases autophagic flux

Many previous studies have implicated LRRK2 as a key player in mitochondrial fission/fusion dynamics and have associated LRRK2 with the tightly regulated autophagic pathway (Plowey *et al.*, 2008; Wang *et al.*, 2012b; Esteves and Cardoso, 2016). In our study, when we examined Q2089R overexpression in HEK293 cells, a significant increase in both LC3 II and P62 levels, and therefore an increase in the autophagosome pool size, was observed (Figure 3.22 B and C). Similarly, Q2089R-carrying fibroblasts also exhibited significantly increased levels of both autophagic markers (Figure 3.23 B and C, respectively). Interestingly, the inhibition of LRRK2 kinase activity was previously shown to stimulate macroautophagy, leading to a striking increase in LC3 II levels (Manzoni *et al.*, 2013a). Another study subsequently showed that silencing of LRRK2 and the inhibition of LRRK2 kinase activity resulted in inadequate autophagy clearance and reduced autophagic degradation, thus highlighting the importance of LRRK2 kinase activity in autophagy regulation (Schapansky *et al.*, 2014). Similarly, Tong and colleagues reported that the absence of LRRK2 impaired the autophagic pathway, evident by the increase in LC3 II and P62 levels (Tong *et al.*, 2010, 2012). Since we showed that Q2089R almost completely abolished autophosphorylation (kinase activity) of LRRK2 *in vitro* (Figure 3.10), the

observed increase in autophagosome pool size for Q2089R (in both HEK293 and fibroblasts cells) supports the notion that the inhibition of LRRK2's kinase activity leads to an increase in autophagy (Manzoni *et al.*, 2013a; Schapansky *et al.*, 2014; Esteves and Cardoso, 2016).

The overexpression of G2019S in HEK293 cells in the present study did not result in any significant changes in LC3 II or P62 levels, although a trend for an increase in P62 was observed (Figure 3.22). This is contradictory to previous studies indicating a significant increase in autophagic vacuoles (AVs) in SHSY5Y cells (Plowey *et al.*, 2008) and increased LC3 II in HEK293 cells expressing LRRK2 G2019S (Su and Qi, 2013). However, our results were similar to one study indicating that HEK293 cells stably expressing G2019S showed no difference in LC3 flux (Orenstein *et al.*, 2013). When examining G2019S fibroblasts, we found increased levels of both LC3 II and P62. However, the increase in P62 levels did not reach statistical significance (Figure 3.23 C). Consistent with this discovery, results from a previous study showed that G2019S patient fibroblasts significantly increased autophagic flux (Su *et al.*, 2015). This was also observed in numerous other studies (Sánchez-Danés *et al.*, 2012; Bravo-San Pedro *et al.*, 2013; Manzoni *et al.*, 2013b; Yakhine-Diop *et al.*, 2014). Likewise, the loss of neurons in transgenic mice expressing G2019S also resulted in enhanced autophagy and accumulated AVs (Ramonet *et al.*, 2011). Although P62 levels were not significantly increased in G2019S fibroblasts in our study, we believe that this could be attributed to the fact that the detection of autophagic markers via Western blot analysis is less reliable than the detection via microscopy techniques and therefore small changes in the levels of these marker proteins could have been obscured.

Although increased autophagy is commonly associated with cell survival through the removal of damaged cellular material, some researchers believe that autophagy plays a key role in the promotion of non-apoptotic programmed cell death via the engulfment of the cytoplasm (Nelson and Shacka, 2013). Thus, it is speculated that cell death can occur from dysregulation of autophagy i.e. it being either too active or too inactive.

4.7 LRRK2 associates with and possibly binds to TOM subunits

Considering the abovementioned evidence, we hypothesized that, LRRK2 could associate with the OMM through interaction with the TOM complex. In the present study, we overexpressed WT LRRK2 in COS7 and HEK293 cells and found that LRRK2 significantly co-localized with the TOM complex using both confocal microscopy (Figure 3.24) and SR-SIM (Figure 3.25 – 3.28) under normal and stress induced culture conditions. Upon further investigation, we showed that LRRK2, overexpressed in HEK293 cells, associated with the TOM complex (Figure 3.29) and proposed that this association could be mediated by the potential protein-protein interaction domains surround the central core of LRRK2.

Under normal physiological conditions LRRK2 associated with a complex containing TOM22, TOM40 and TOM70. Interestingly, an association between LRRK2 and TOM20 was only observed when cells were stressed using CCCP. The association between LRRK2 and TOM22 and TOM70 markedly increased under these conditions while the relationship between TOM40 and this complex diminished. We could speculate that these results indicate that more LRRK2 is recruited specifically to TOM20 and TOM22 to aid in the phosphorylation of as-yet-unknown proteins that are essential for mitochondrial function and biogenesis under conditions of stress and high energy demand. Alternatively, we could postulate that TOM20 and more of TOM22 and TOM70 is recruited to this complex of proteins with which LRRK2 is associated. TOM20 and TOM22 are responsible for the recognition and movement of mitochondrial pre-proteins to TOM40 for import. When we considered additional explanations for these interactions, we found that TOM22 contains an F-x-T-x-K (FETEK) protein motif. This could imply that TOM22 is likely phosphorylated by LRRK2 (with LRRK2's consensus phosphorylation sequence being F/Y-x-T-x-R/K) (Pungaliya *et al.*, 2010). Additionally, we hypothesize that TOM70 could interact with LRRK2 through its tetratricopeptide repeat (TPR) motifs which is known to mediate protein-protein interactions and is involved in the assembly of multiprotein complexes (Chan *et al.*, 2006). In a previous study it was shown that molecular chaperones, heat shock protein 90 (Hsp90) and heat shock protein 70 (Hsp70), deliver pre-proteins to the OMM and more specifically to the TPR domains of TOM70 for mitochondrial import (Young *et al.*, 2003). This could subsequently explain another possible mechanism of interaction between LRRK2 and the TOM complex since LRRK2 has been shown to form a complex with Hsp90 (Wang *et al.*, 2008a; Ko *et al.*, 2009).

Although LRRK2 readily associates with a complex containing TOM22, TOM40 and TOM70, whether LRRK2 is imported into mitochondria or phosphorylates proteins required for mitochondrial import remains to be elucidated. Cui and colleagues previously found that LRRK2 interacts with an OMM protein known to be involved in mitochondrial permeability namely, voltage-dependent anion channel (VDAC), as well as the ubiquitous mitochondrial creatine kinase (uMtCK) which contains an mitochondrial targeting sequence (MTS) and is involved in cellular energy homeostasis (Schlattner *et al.*, 2006; Cui *et al.*, 2011). It was further shown that LRRK2, especially G2019S *LRRK2*, inhibits the uMtCK pre-protein from entering into the mitochondria and thereby negatively affects mitochondrial energy homeostasis (Cui *et al.*, 2011). Interestingly, TOM40 recognizes and interacts with proteins containing MTS which could include uMtCK.

Furthermore, Harbauer et al. (2014) showed that phosphorylation of Tom6 (in a yeast system) is necessary for the assembly of Tom40 which serves as the main protein import channel (Harbauer *et*

al., 2014). The phosphorylation of Tom6 was also shown to aid the import of fusion proteins, to activate mitochondrial respiration and to regulate mitochondrial biogenesis in a cell cycle-dependent manner. Increased levels of Tom6 resulted in increased TOM complex assembly which in turn led to increased mitochondrial biogenesis (Harbauer *et al.*, 2014; Shiota *et al.*, 2015). In our study, we did not investigate the interaction between or phosphorylation of TOM6 by LRRK2 as our attention was only drawn to TOM6 through the comprehensive literature research when writing the discussion of this dissertation. It would, however, be interesting to determine since phosphorylation of Tom6 (in yeast) is mediated by cyclin-dependent kinase (CDK1) which is a master regulator of the cell cycle (Harbauer *et al.*, 2014).

Notably, various studies have also implicated other PD-causing genes, such as *PINK1*, *Parkin* and *SNCA*, in the interaction with the TOM complex (Bender *et al.*, 2013; Bertolin *et al.*, 2013; Kato *et al.*, 2013; Okatsu *et al.*, 2015). For example, the overexpression of both WT and mutant (A53T) *SNCA* caused a reduction in TOM40 levels (Bender *et al.*, 2013) while mutations in *Parkin* disrupted the interaction between Parkin and the TOM complex (Bertolin *et al.*, 2013). Recently, SNCA was also shown to bind to TOM20 and inhibit mitochondrial protein import (Maio *et al.*, 2016). PINK1 plays a major role in distinguishing between functional and dysfunctional mitochondria and depends on TOM70 for its import into mitochondria (Kato *et al.*, 2013) whereas TOM7 has been shown to be essential for stabilizing PINK1 on the OMM following mitochondrial damage (Hasson *et al.*, 2013). Also, PINK1 protects the cell by targeting damaged mitochondria with the assistance of Parkin and forms a complex with TOM20, TOM22 and TOM40 (Lazarou *et al.*, 2012; Okatsu *et al.*, 2015). Taken together, these studies provide insight into novel mechanisms, via the TOM complex, by which PD-causing mutations alter mitochondrial integrity and functioning. In the present study we provided convincing evidence for WT LRRK2's association with the TOM complex. Therefore, it would be of interest to investigate whether and the extent to which mutant LRRK2 affects the association with subunits of the TOM complex.

4.8 Proposed model for WT and Q2089R LRRK2

Although we acknowledge that our findings are preliminary and that we did not observe all of the phenotypes in both cellular models, with the evidence gathered from our study as well as from previous studies, we propose a model for LRRK2's cellular functions. This model encompasses LRRK2's involvement in mitochondrial (dys)function, mitochondrial biogenesis and the autophagy/lysosomal pathway (Figure 4.1).

Under basal conditions, WT LRRK2 is involved in mitochondrial fission, fusion and biogenesis by recruiting the necessary proteins, such as DRP1 via phosphorylation, from the cytosol to the mitochondrial outer membrane (Figure 4.1 A). The recruitment of DRP1 for mitochondrial fission is dependent on LRRK2's kinase activity. LRRK2 also interacts with VDAC which plays a role in membrane permeability, possibly to aid in the maintenance of MMP and normal oxidative phosphorylation activity (Figure 4.1 A). Earlier evidence show LRRK2 to form a complex with Hsp90 protein, which is known to have chaperone activity (Wang *et al.*, 2008a; Ko *et al.*, 2009) and it was found that LRRK2 controls the trafficking of organelles and proteins (Migheli *et al.*, 2013; Hunn *et al.*, 2015; Manzoni *et al.*, 2015; Esteves and Cardoso, 2016). Also, as previously mentioned, the phosphorylation of Tom6 has been shown to aid in TOM complex assembly and mitochondrial biogenesis and that the PINK1 protein is imported for degradation into healthy mitochondria via TOM70. In the present study, we identified a novel association between LRRK2 and the TOM complex (via subunits TOM22, TOM40 and TOM70) (Figure 4.1 A), which we believe could explain additional functions of LRRK2 in mitochondrial homeostasis since the TOM complex is essential for mitochondrial protein import and overall mitochondrial health.

Under stress-induced conditions (e.g. mitochondrial depolarization), PINK1 is known to accumulate on the OMM and recruit Parkin for the ubiquitination of several OMM proteins, subsequently leading to the removal of defective mitochondria via mitophagy. Normally, mitochondrial precursor proteins are initially recognized by TOM20 or TOM70 (depending on their mitochondrial target sequences) after which they are translocated to TOM22 and then finally to TOM40 for mitochondrial import. We speculate that the relationship between LRRK2 and the complex containing the TOM proteins lead to increased phosphorylation (possibly of the subunits of the TOM complex) for increased complex assembly or alternatively, it acts to target defective mitochondria for degradation by accumulating on the OMM at the TOM complex. The latter hypothesis is substantiated by the fact that we saw increased association (and thus possible accumulation) of LRRK2 with the complex containing TOM20, TOM22 and TOM70 while less TOM40 was associated with this complex under stress. Taken together, we believe WT LRRK2 plays an important role in the cell by binding to the TOM complex where it is involved in regulating mitochondrial biogenesis and the removal of damaged mitochondria.

Furthermore, we speculate that the severely decreased autophosphorylation activity of LRRK2 Q2089R will have major effects on cellular functions (Figure 4.1 B). For example, we showed that Q2089R cells exhibit decreased MMP. And since the ATP generation was less efficient in Q2089R cells, we believe that the increase in maximal respiration and spare respiratory capacity are indicative of a compensatory mechanism(s). This hypothesis is supported by the increase in mtDNA copy number of

Q2089R-carrying cells and possible upregulation of mitochondrial biogenesis as part of the cell's compensatory mechanism(s) (Figure 4.1 B).

A. LRRK2 WT

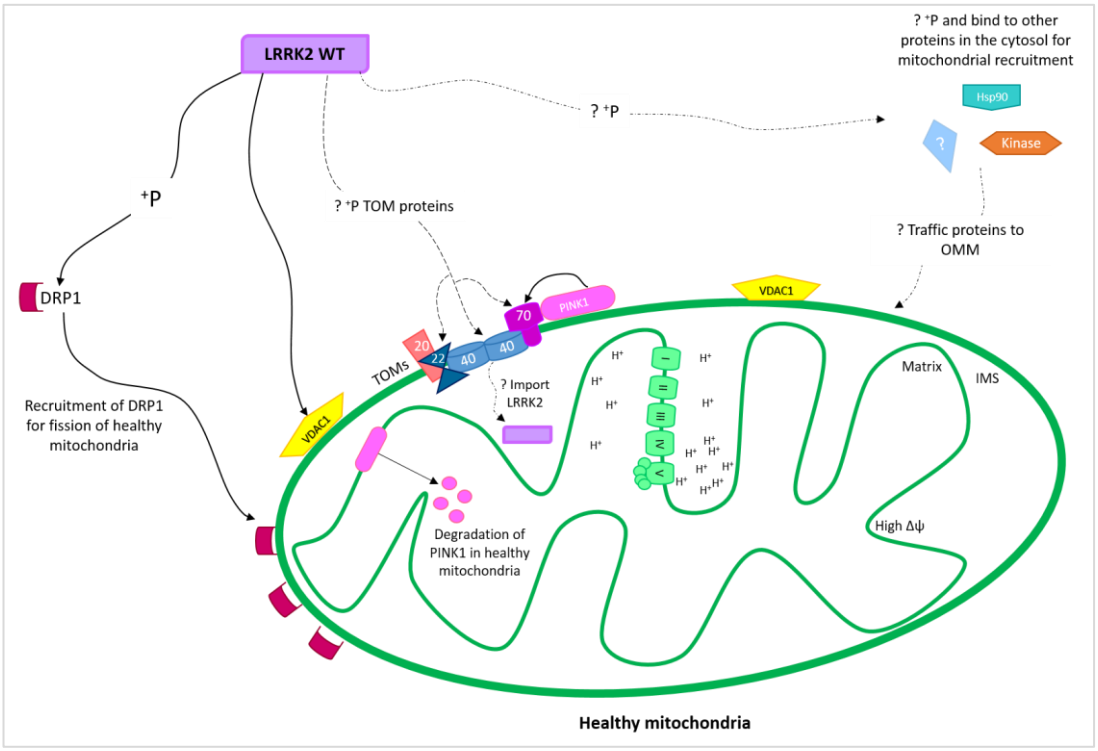

B. LRRK2 Q2089R

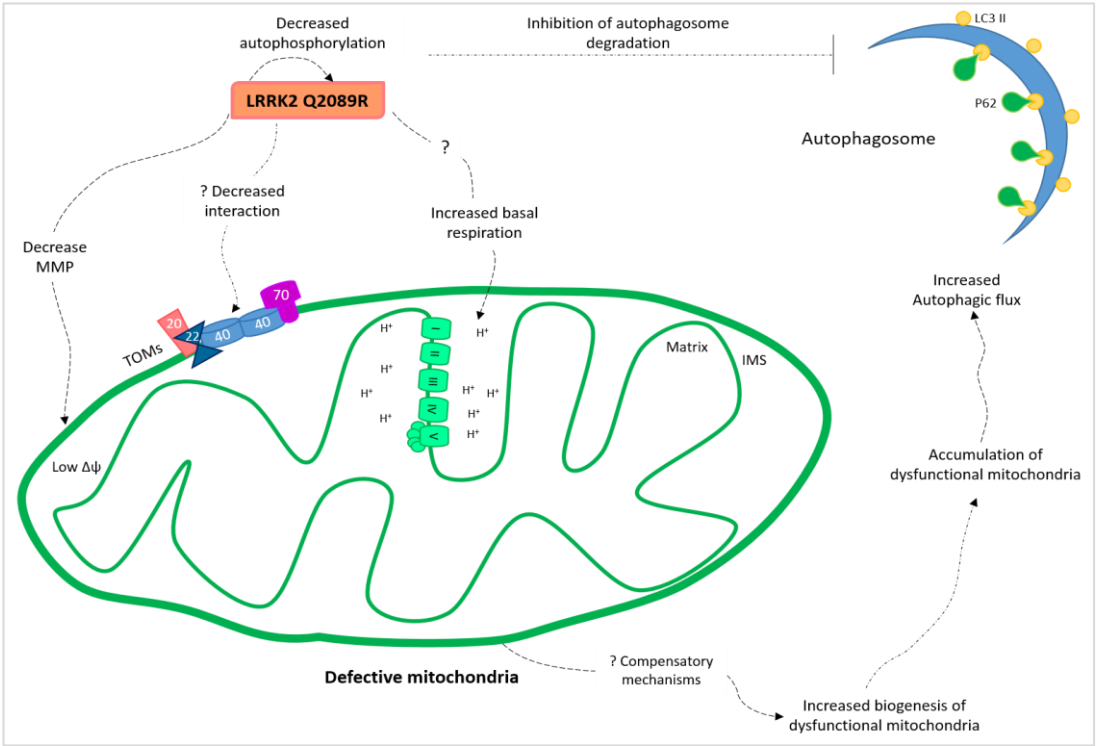

Figure 4.1 Schematic illustration of the proposed model for the functions of WT and Q2089R LRRK2. The solid lines in the figure shows evidence from previously published studies while the dotted lines represent interactions and processes proposed by findings from the present study.

However, because mitochondria of Q2089R-carrying cells are depolarized and not functioning optimally, the upregulation of mitochondrial biogenesis will lead to an accumulation of defective mitochondria since new mitochondria are generated from existing ones. This accumulation of dysfunctional mitochondria could result in the upregulation of autophagy (mitophagy). Thereafter, due to defective autophagosome clearance seen in Q2089R cells (possibly due to the diminished kinase activity), defective mitochondria would accumulate in the cytoplasm and lead to major cellular damage or even cellular death. It could be speculated that the decrease in LRRK2's kinase activity may also possibly lead to the decrease in TOM complex association or assembly, thereby exacerbating mitochondrial dysfunction.

Although a modest increase in basal respiration was observed (Figure 4.1 B), the decrease in MMP was linked to an increase in proton leak and the concomitant reduction of ATP-coupling efficiency when Q2089R cells were stressed for a short period (< 30 minutes). When these cells shift to glycolysis for energy production, a striking reduction in glycolytic capacity and glycolytic reserve is apparent which indicates that Q2089R affect the cells' ability to supply the necessary energy required for optimal functioning under high energy demand conditions. Finally, we postulate that increased stress (such as CCCP treatment for longer periods) will aggravate the already dysfunctional pathways described above, leading to a more severe phenotype and possibly accelerate autophagic death in Q2089R cells.

Since many of the proposed pathways or interactions can either be a cause or effect or can occur simultaneously, it is difficult at this stage to define the step-by-step sequence of events for this model. Therefore, we propose that these events all form part of an ongoing process(es) that together may contribute to disease pathogenesis.

4.9 Study limitations

Some of the major limitations of this study are drawbacks with the two cellular models used. Initially, we wanted to create a suitable model to study LRRK2 (WT and mutant) using the CRISPR-Cas9 genome editing system in combination with the SHSY5Y neuroblastoma cell line. Unfortunately, we could not overcome the many technical drawbacks with this system and were not able to generate the appropriate 'genome-edited' cultures. Consequently, we used HEK293 cells transfected with WT and mutant constructs which is a well-established model system to study functional differences. However, although these overexpression models provide valuable information and are widely used to study neurodegenerative and other diseases, it does represent an 'artificial' disease model and results obtained from such studies should always be interpreted with caution. Also, we determined that the

transfection efficiency of our constructs was rather low between 6% and 8% of our cell population. This could produce false negative findings and therefore the transfection efficiency should be optimized in future overexpression studies.

Because of these limitations, we also used patient-derived dermal fibroblasts which have been established by others as a reliable, minimally invasive model to study PD (Auburger *et al.*, 2012; Smith *et al.*, 2015). It should be cautioned however that dermal fibroblasts are known to have many different properties to neuronal cells and therefore results obtained from this cellular model should not be directly extrapolated to the molecular mechanisms of neuronal cells or tissues. Also, sample size of the fibroblasts was limited (only one individual per mutant and) but this is due to the rarity of these variants in our patient group. Another major limitation was the fact that we could not obtain fibroblasts from the PD patient harboring Q2089R. At the time of biopsy collection, he had already passed away and we could only obtain a skin biopsy from his son, who harbors Q2089R but is apparently unaffected (Figure 3.2 A, Individual III:1). We could speculate that this could possibly explain some of the proposed compensatory mechanisms observed for this individual's fibroblasts in the mitochondrial respiration and glycolysis results. The control fibroblast cell lines were negative for both G2019S and Q2089R however, we did not screen for any other known PD-causing mutations. Although this was a limitation of our pilot studyand future work will include extensive mutation screening on control cell lines. We will also investigate the additional known mutations of LRRK2 including R1441C/H/G, I2020T and Y1699C. Another limitation was the lack of age and gender matched controls available for these cell lines which will be addressed in future studies.

Also, when we investigated mitochondrial and glycolytic respiration of these primary cell lines, we grouped the WT fibroblasts. This was based on the raw data showing nearly indistinguishable basal respiration profiles for each of the control cell lines and on previous studies showing grouped analyses of control and patient groups (Grünewald *et al.*, 2014; Haylett *et al.*, 2016; Zandberg *et al.*, 2016). However, we recognize the limitations of this since inter-individual variability could have been overlooked. Future studies will to take this into account and will aim to recruit additional control and G2019S-positive individuals (both affected and unaffected if possible) and possibly additional Q2089R carriers. It would also be beneficial to investigate additional LRRK2 mutations including R1441C/H/G, I2020T and Y1699C.

Technical limitations of our study include the measure of autophosphorylation as an indirect indicator of kinase activity as opposed to a kinetic kinase assay with purified protein, even though this has been confirmed in previous and very recent studies (Sheng *et al.*, 2012; Reynolds *et al.*, 2014; Fraser *et al.*, 2016). Ribosomal protein s15 has been identified as a key substrate of LRRK2 and more recently a

study revealed that LRRK2 regulates a subset of Rab GTPases *in vivo* and *in vitro* thus identifying these as physiological substrates of LRRK2 (Martin *et al.*, 2014; Steger *et al.*, 2016). Therefore, future studies should include these substrates for investigation of LRRK2's kinase activity. Also, we were not able to detect autophosphorylation activity in fibroblast lysates using the pSer^{1292} antibody and this requires further optimization experiments.

We used an MTT assay (and CyQUANT®) to measure the metabolic activity of HEK293 cells and primary cells (fibroblasts) expressing G2019S and Q2089R. However, since this assay does not measure the viability of cells, we were unable to determine whether the mutation or variant is actually toxic to the cell. Therefore, this requires further attention.

When investigating autophagy in both PD models, we used LC3 II and P62 detection via Western blot analysis. Detection of these markers especially P62, is thought to be less reliable when using Western blotting rather than fluorescent microscopy techniques and thus small changes in autophagic marker levels might have been missed (Loos *et al.*, 2014). Additionally, we could have considered additional markers such as Bcl-1 for further verification of autophagy induction. Therefore, alternative techniques such as flow cytometry should be considered for future studies.

To identify an association between LRRK2 and the subunits of the TOM complex, we made use of co-immunoprecipitation. Although this method allows for the detection of proteins within a specific complex, whether there is a physical or direct interaction between LRRK2 and specific subunits of the TOM complex cannot be determined. Future studies should make use of Proximity Ligation assays to confirm such direct interactions (Trifilieff *et al.*, 2011; Gauthier *et al.*, 2015).

And finally, some experiments were only performed in biological and technical triplicates. Although this is standard and acceptable practice in experimental protocols, more replicates could have increased the statistical power of our experiments.

4.10 Future work

Further experiments, on the optimization of the CRISPR-Cas9 genome editing system to create an appropriate model to study PD, are necessary. Additionally, since we have low passage (< three) fibroblast cultures these could be used to culture iPSC-derived neural cells from PD patients and healthy individuals that could be used for the genome editing experiments. We should also attempt to obtain fibroblasts from other G2019S-positive individuals (both affected and unaffected) to increase our sample size for future studies. We would also suggest that future studies include

genotyping with microsatellite markers to determine whether the Q2089R-positive control individual and the Q2089R-positive proband are related.

Another important consideration should be to further analyze the WES data and search for mitochondrial-related gene variants in the Q2089R proband. This could possibly identify other candidate mutations/variants which might explain the functional phenotypes observed in this study.

Optimization of transfection efficiency and subsequent LRRK2 protein purification should be conducted in order to perform a kinetic kinase assay with purified WT, G2019S and Q2089R LRRK2, in order to verify the autophosphorylation results. Additionally, as mentioned previously, future experiments should verify the cytotoxicity results from this study with independent measures of neurite outgrowth in combination with other assays such as Image-iT® DEAD™ Green cytotoxicity assay or LIVE/DEAD® Viability/Cytotoxicity assays.

In addition, the measures of oxidative phosphorylation should be repeated using different equipment such as the Oxygraph-2K (Oroboros Instruments) to verify the findings obtained by the Seahorse XF analyzer. These experiments have already been planned and will be done in collaboration with Dr. Olga Corti at the Brain and Spine Institute, ICM, in Paris, France.

Furthermore, it would be interesting to investigate the association of LRRK2 with the TOM complex in more detail. For instance, future studies should include elucidating whether LRRK2 is imported into the mitochondria (using transmission electron microscopy), or if LRRK2 is accumulated at the TOM subunits on the OMM during cellular stress. Moreover, additional subunits of the TOM complex [including TOM5, TOM7 and in particular TOM6 based on previous studies (Harbauer *et al.*, 2014; Shiota *et al.*, 2015)] should be investigated as possible phosphorylation substrates or interactors of LRRK2. Importantly, the effect of G2019S and Q2089R on the interaction with the TOM complex should also be investigated. Lastly, experiments on mitochondrial fission/fusion should also be included in future studies of LRRK2 models since these processes are essential for mitochondrial adaptations to environmental changes and quality control.

4.11 Conclusion

Given the complexity and variability of mechanisms leading to neurodegenerative diseases such as PD, more research is needed to identify possible new therapeutic targets and pathways for effective disease treatment. The identification and characterization of Q2089R, a variant with functional implications, may shed some light on how variants in LRRK2 can influence a variety of cellular functions.

The identification of potential disease-causing mutations with the use of Next-Generation Sequencing is a powerful technique and is essential in developing our understanding of complex disorders such as PD, especially in the unique SSA populations. However, the identification of rare variants should always be accompanied by functional characterization as these variants cannot automatically be regarded as causal.

Q2089R exhibited decreased autophosphorylation activity, severe mitochondrial defects and significantly increased autophagic flux, providing preliminary evidence for its involvement in mitochondrial dysfunction and autophagic pathways which could possibly lead to neuronal cell death. If corroborated in follow-up studies, our findings challenge the idea that toxic gain-of-function mutations in the kinase domain of LRRK2 is the only pathological mechanism and we postulate that abolishment of kinase activity could also contribute to neurodegeneration and PD pathogenesis.

It is clear that this complex multi-domain protein is involved in many different cellular functions, however, further studies are needed to elucidate additional functions of LRRK2 and the effect of mutations on these functions. It is anticipated that this knowledge may be key to understanding the processes that lead to development of PD.

References

Electronic

Combined Annotation Dependent Depletion	http://cadd.gs.washington.edu/score
dbSNP	http://www.ncbi.nlm.nih.gov/projects/SNP/
Ensembl	http://www.ensembl.org/
Exome Aggregation Consortium database	http://exac.broadinstitute.org/
Exome Sequencing Project	https://esp.gs.washington.edu/drupal/
Graphpad	http://www.graphpad.com/scientific-software/prism/
ImageJ	http://imagej.nih.gov/ij/
Just Another Co-localization Plugin (JaCoP)	https://rsb.info.nih.gov/ij/plugins/track/jacop2.html
Modeller	https://salilab.org/modeller/
Mutation Taster	http://www.mutationtaster.org/
PDMap	http://minerva.uni.lu/MapViewer/
PDmutDB	http://www.molgen.vib-ua.be/PDMutDB/
Polyphen	http://genetics.bwh.harvard.edu/pph2/
Project Hope	http://www.cmbi.ru.nl/hope/method
SIFT	http://sift.jcvi.org/
Swiss Model	https://swissmodel.expasy.org
UniProt	http://www.uniprot.org/align/
Variant Effect Predictor (VEP)	http://www.ensembl.org/Homo_sapiens/Tools/VEP
ZEN software	http://www.zeiss.com/microscopy/en_de/downloads/zen.html
1000 Genomes	http://www.1000genomes.org/

Journals and Books

Abeliovich H, Dengjel J. 2016. Mitophagy as a stress response in mammalian cells and in respiring S. cerevisiae. *Biochemical Society Transactions* **44**: 541–545.

Adler T. 2009. Pesticides and Parkinson's Disease: The legacy of contaminated well water. *Environmental Health Perspectives* **117**: A553.

Aerts L, Craessaerts K, De Strooper B, Morais VA. 2015. PINK1 kinase catalytic activity is regulated by phosphorylation on serines 228 and 402. *The Journal of Biological Chemistry* **290**: 2798–2811.

Akinyemi RO. 2012. Epidemiology of Parkinsonism and Parkinson's disease in Sub-Saharan Africa: Nigerian profile. *Journal of Neurosciences in Rural Practice* **3**: 233–234.

Alcalay R, Fraser K, West A. 2015. Phosphorylated pS1292 LRRK2 to total LRRK2 concentration ratio in urine exosomes distinguishes LRRK2-PD and idiopathic PD. *Neurology* **84**.

Alcalay RN, Mirelman A, Saunders-Pullman R, Tang M-X, Mejia Santana H, Raymond D, Roos E, Orbe-Reilly M, Gurevich T, Bar Shira A, et al. 2013. Parkinson disease phenotype in Ashkenazi Jews with and without LRRK2 G2019S mutations. *Movement Disorders: Official Journal of the Movement Disorder Society* **28**: 1966–1971.

Alegre-Abarrategui J, Christian H, Lufino MMP, Mutihac R, Venda LL, Ansorge O, Wade-Martins R. 2009. LRRK2 regulates autophagic activity and localizes to specific membrane microdomains in a novel human genomic reporter cellular model. *Human Molecular Genetics* **18**: 4022–4034.

Anand VS, Reichling LJ, Lipinski K, Stochaj W, Duan W, Kelleher K, Pungaliya P, Brown EL, Reinhart PH, Somberg R, et al. 2009. Investigation of leucine-rich repeat kinase 2 : enzymological properties and novel assays. *The FEBS journal* **276**: 466–478.

Angeles DC, Gan B-H, Onstead L, Zhao Y, Lim K-L, Dachsel J, Melrose H, Farrer M, Wszolek ZK, Dickson DW, et al. 2011. Mutations in LRRK2 increase phosphorylation of peroxiredoxin 3 exacerbating oxidative stress-induced neuronal death. *Human Mutation* **32**: 1390–1397.

Angeles DC, Ho P, Chua LL, Wang C, Yap YW, Ng C, Zhou ZD, Lim K-L, Wszolek ZK, Wang HY, et al. 2014. Thiol-peroxidases ameliorate LRRK2 mutant-induced mitochondrial and dopaminergic neuronal degeneration in Drosophila. *Human molecular genetics*.

Anglade P, Vyas S, Javoy-Agid F, Herrero MT, Michel PP, Marquez J, Mouatt-Prigent A, Ruberg M, Hirsch EC, Agid Y. 1997. Apoptosis and autophagy in nigral neurons of patients with Parkinson's disease.

Ashrafi G, Schwarz TL. 2013. The pathways of mitophagy for quality control and clearance of mitochondria. *Cell Death and Differentiation* **20**: 31–42.

Auburger G, Klinkenberg M, Drost J, Marcus K, Morales-Gordo B, Kunz WS, Brandt U, Broccoli V, Reichmann H, Gispert S, et al. 2012. Primary skin fibroblasts as a model of Parkinson's disease. *Molecular Neurobiology* **46**: 20–27.

Bach J-P, Ziegler U, Deuschl G, Dodel R, Doblhammer-Reiter G. 2011. Projected numbers of people with movement disorders in the years 2030 and 2050. *Movement disorders: official journal of the Movement Disorder Society* **26**: 2286–2290.

Bardien S, Marsberg A, Keyser R, Lombard D, Lesage S, Brice A, Carr J. 2010. LRRK2 G2019S mutation: frequency and haplotype data in South African Parkinson's disease patients. *Journal of Neural Transmission* **117**: 847–853.

Barth S, Glick D, Macleod KF. 2010. Autophagy: assays and artifacts. *The Journal of pathology* **221**: 117–124.

Beal MF. 1998. Mitochondrial dysfunction in neurodegenerative diseases. *Biochimica et Biophysica Acta - Bioenergetics* **1366**: 211–223.

Beilina A, Van Der Brug M, Ahmad R, Kesavapany S, Miller DW, Petsko GA, Cookson MR. 2005. Mutations in PTEN-induced putative kinase 1 associated with recessive parkinsonism have differential effects on protein stability. *Proceedings of the National Academy of Sciences of the United States of America* **102**: 5703–5708.

Beilina A, Rudenko IN, Kaganovich A, Civiero L, Chau H, Kalia SK, Kalia LV, Lobbestael E, Chia R, Ndukwe K, et al. 2014. Unbiased screen for interactors of leucine-rich repeat kinase 2 supports a common pathway for sporadic and familial Parkinson disease. *Proceedings of the National Academy of Sciences of the United States of America* **111**: 2626–2631.

Bender A, Desplats P, Spencer B, Rockenstein E, Adame A, Elstner M, Laub C, Mueller S, Koob AO, Mante M, et al. 2013. TOM40 mediates mitochondrial dysfunction induced by α-synuclein accumulation in Parkinson's disease. *PloS one* **8**: e62277.

Bento CF, Puri C, Moreau K, Rubinsztein DC. 2013. The role of membrane-trafficking small GTPases in the regulation of autophagy. *J Cell Sci* **126**: 1059–1069.

Berg JM, Tymoczko JL, Stryer L, Berg JM, Tymoczko JL, Stryer L. 2002. *Biochemistry*. W H Freeman.

Bertolin G, Ferrando-Miguel R, Jacoupy M, Traver S, Grenier K, Greene AW, Dauphin A, Waharte F, Bayot A, Salamero J, et al. 2013. The TOMM machinery is a molecular switch in PINK1 and PARK2/PARKIN-dependent mitochondrial clearance. *Autophagy* **9**: 1801–1817.

Biro J. 2006. Amino acid size, charge, hydropathy indices and matrices for protein structure analysis. *Theoretical Biology & Medical Modelling* **3**: 15.

Biskup S, Moore DJ, Celsi F, Higashi S, West AB, Andrabi SA, Kurkinen K, Yu S-W, Savitt JM, Waldvogel HJ, et al. 2006. Localization of LRRK2 to membranous and vesicular structures in mammalian brain. *Annals of Neurology* **60**: 557–569.

Blanckenberg J, Bardien S, Glanzmann B, Okubadejo NU, Carr JA. 2013. The prevalence and genetics of Parkinson's disease in sub-Saharan Africans. *Journal of the Neurological Sciences* **335**: 22–25.

Bliek AM van der, Shen Q, Kawajiri S. 2013. Mechanisms of Mitochondrial Fission and Fusion. *Cold Spring Harbor Perspectives in Biology* **5**: a011072.

Bolender N, Sickmann A, Wagner R, Meisinger C, Pfanner N. 2008. Multiple pathways for sorting mitochondrial precursor proteins. *EMBO reports* **9**: 42–49.

Bonifati V. 2006. Parkinson's Disease: The LRRK2-G2019S mutation: opening a novel era in Parkinson's disease genetics. *European Journal of Human Genetics* **14**: 1061–1062.

Bonifati V, Rizzu P, van Baren MJ, Schaap O, Breedveld GJ, Krieger E, Dekker MCJ, Squitieri F, Ibanez P, Joosse M, et al. 2003. Mutations in the DJ-1 gene associated with autosomal recessive early-onset parkinsonism. *Science (New York, N.Y.)* **299**: 256–259.

Bosgraaf L, Van Haastert PJM. 2003. Roc, a Ras/GTPase domain in complex proteins. *Biochimica et Biophysica Acta (BBA) - Molecular Cell Research* **1643**: 5–10.

Brand MD. 2000. Uncoupling to survive? The role of mitochondrial inefficiency in ageing. *Experimental Gerontology* **35**: 811–820.

Brand MD, Nicholls DG. 2011. Assessing mitochondrial dysfunction in cells. *Biochemical Journal* **435**: 297–312.

Bravo-San Pedro JM, Niso-Santano M, Gómez-Sánchez R, Pizarro-Estrella E, Aiastui-Pujana A, Gorostidi A, Climent V, López de Maturana R, Sanchez-Pernaute R, López de Munain A, et al. 2013. The LRRK2 G2019S mutant exacerbates basal autophagy through activation of the MEK/ERK pathway. *Cellular and molecular life sciences: CMLS* **70**: 121–136.

Bucci C, Thomsen P, Nicoziani P, McCarthy J, van Deurs B. 2000. Rab7: a key to lysosome biogenesis. *Molecular Biology of the Cell* **11**: 467–480.

Cardoso SM, Esteves AR. 2015. LRRK2 a pivotal player in mitochondrial dynamics and lysosomal clustering: highlights to sporadic Parkinson's disease. *Therapeutic Targets for Neurological Diseases* **2**: 10–14800/ttnd.629.

Carr J, Coller R van. 2014. A putative founder effect for Parkinson's disease in South African Afrikaners. *South African Medical Journal* **104**: 411–412.

Chacinska A, Koehler CM, Milenkovic D, Lithgow T, Pfanner N. 2009. Importing mitochondrial proteins: machineries and mechanisms. *Cell* **138**: 628–644.

Chan DC. 2006. Mitochondria: dynamic organelles in disease, aging, and development. *Cell* **125**: 1241–1252.

Chan NC, Likić VA, Waller RF, Mulhern TD, Lithgow T. 2006. The C-terminal TPR domain of Tom70 defines a family of mitochondrial protein import receptors found only in animals and fungi. *Journal of Molecular Biology* **358**: 1010–1022.

Chan NC, Salazar AM, Pham AH, Sweredoski MJ, Kolawa NJ, Graham RLJ, Hess S, Chan DC. 2011. Broad activation of the ubiquitin–proteasome system by Parkin is critical for mitophagy. *Human Molecular Genetics* **20**: 1726–1737.

Change N, Mercier G, Lucotte G. 2008. Genetic screening of the G2019S mutation of the LRRK2 gene in Southwest European, North African, and Sephardic Jewish subjects. *Genetic Testing* **12**: 333–339.

Chartier-Harlin M-C, Dachsel JC, Vilariño-Güell C, Lincoln SJ, Leprêtre F, Hulihan MM, Kachergus J, Milnerwood AJ, Tapia L, Song M-S, et al. 2011. Translation initiator EIF4G1 mutations in familial Parkinson disease. *American Journal of Human Genetics* **89**: 398–406.

Chen H, Chan DC. 2009. Mitochondrial dynamics-fusion, fission, movement, and mitophagy-in neurodegenerative diseases. *Human Molecular Genetics* **18**: R169–R176.

Cherra SJ 3rd, Steer E, Gusdon AM, Kiselyov K, Chu CT. 2013. Mutant LRRK2 elicits calcium imbalance and depletion of dendritic mitochondria in neurons. *The American journal of pathology* **182**: 474–484.

Cheung ZH, Ip NY. 2009. The emerging role of autophagy in Parkinson's disease. *Molecular Brain* **2**: 29.

Chiong M, Cartes-Saavedra B, Norambuena-Soto I, Mondaca-Ruff D, Morales PE, García-Miguel M, Mellado R. 2014. Mitochondrial metabolism and the control of vascular smooth muscle cell proliferation. *Molecular Medicine* **2**: 72.

Choi TG, Kim SS. 2013. Autophagy in Redox Signalling. *Hanyang Medical Reviews* **33**: 83.

Clark IE, Dodson MW, Jiang C, Cao JH, Huh JR, Seol JH, Yoo SJ, Hay BA, Guo M. 2006a. Drosophila pink1 is required for mitochondrial function and interacts genetically with parkin. *Nature* **441**: 1162–1166.

Clark LN, Wang Y, Karlins E, Saito L, Mejia-Santana H, Harris J, Louis ED, Cote LJ, Andrews H, Fahn S, et al. 2006b. Frequency of LRRK2 mutations in early- and late-onset Parkinson disease. *Neurology* **67**: 1786–1791.

Cohen P. 2001. The role of protein phosphorylation in human health and disease. The Sir Hans Krebs Medal Lecture. *European journal of biochemistry / FEBS* **268**: 5001–5010.

Cookson MR. 2010. The role of leucine-rich repeat kinase 2 (LRRK2) in Parkinson's disease. *Nature reviews. Neuroscience* **11**: 791–797.

Cookson MR, Bandmann O. 2010. Parkinson's disease: insights from pathways. *Human Molecular Genetics* **19**: R21–R27.

Cookson MR, Dauer W, Dawson T, Fon EA, Guo M, Shen J. 2007. The roles of kinases in familial Parkinson's disease. *Journal of Neuroscience* **27**: 11865–11868.

Cooper AA, Gitler AD, Cashikar A, Haynes CM, Hill KJ, Bhullar B, Liu K, Xu K, Strathearn KE, Liu F, et al. 2006. Alpha-synuclein blocks ER-Golgi traffic and Rab1 rescues neuron loss in Parkinson's models. *Science (New York, N.Y.)* **313**: 324–328.

Cooper O, Seo H, Andrabi S, Guardia-Laguarta C, Graziotto J, Sundberg M, McLean JR, Carrillo-Reid L, Xie Z, Osborn T, et al. 2012. Familial Parkinson's disease iPSCs show cellular deficits in mitochondrial responses that can be pharmacologically rescued. *Science translational medicine* **4**: 141ra90.

Cui J, Yu M, Niu J, Yue Z, Xu Z. 2011. Expression of leucine-rich repeat kinase 2 (LRRK2) inhibits the processing of uMtCK to induce cell death in a cell culture model system. *Bioscience Reports* **31**: 429–437.

Dächsel JC, Mata IF, Ross OA, Taylor JP, Lincoln SJ, Hinkle KM, Huerta C, Ribacoba R, Blazquez M, Alvarez V, et al. 2006. Digenic parkinsonism: investigation of the synergistic effects of PRKN and LRRK2. *Neuroscience Letters* **410**: 80–84.

Dachsel JC, Nishioka K, Vilariño-Güell C, Lincoln SJ, Soto-Ortolaza AI, Kachergus J, Hinkle KM, Heckman MG, Jasinska-Myga B, Taylor JP, et al. 2010. Heterodimerization of Lrrk1-Lrrk2: Implications for LRRK2-associated Parkinson disease. *Mechanisms of ageing and development* **131**: 210–214.

Das KC. 2013. Hyperoxia decreases glycolytic capacity, glycolytic reserve and oxidative phosphorylation in MLE-12 cells and inhibits complex I and II function, but not complex IV in isolated mouse lung mitochondria. *PLOS ONE* **8**: e73358.

Dawson TM. 2003. Molecular pathways of neurodegeneration in Parkinson's disease. *Science* **302**: 819–822.

Deng H-X, Shi Y, Yang Y, Ahmeti KB, Miller N, Huang C, Cheng L, Zhai H, Deng S, Nuytemans K, et al. 2016. Identification of TMEM230 mutations in familial Parkinson's disease. *Nature Genetics* **48**: 733–739.

Desler C, Hansen TL, Frederiksen JB, Marcker ML, Singh KK, Juel Rasmussen L, Desler C, Hansen TL, Frederiksen JB, Marcker ML, et al. 2012. Is there a link between mitochondrial reserve respiratory capacity and aging? *Journal of Aging Research, Journal of Aging Research* **2012**, **2012**: e192503.

Di Fonzo, Rohé CF, Ferreira J, Chien HF, Vacca L, Stocchi F, Guedes L, Fabrizio E, Manfredi M, Vanacore N, et al. 2005. A frequent LRRK2 gene mutation associated with autosomal dominant Parkinson's disease. *Lancet (London, England)* **365**: 412–415.

Di Fonzo A, Dekker MCJ, Montagna P, Baruzzi A, Yonova EH, Correia Guedes L, Szczerbinska A, Zhao T, Dubbel-Hulsman LOM, Wouters CH, et al. 2009. FBXO7 mutations cause autosomal recessive, early-onset parkinsonian-pyramidal syndrome. *Neurology* **72**: 240–245.

Dias V, Junn E, Mouradian MM. 2013. The role of oxidative stress in Parkinson's disease. *Journal of Parkinson's disease* **3**: 461–491.

Dillon LM, Williams SL, Hida A, Peacock JD, Prolla TA, Lincoln J, Moraes CT. 2012. Increased mitochondrial biogenesis in muscle improves aging phenotypes in the mtDNA mutator mouse. *Human Molecular Genetics* **21**: 2288–2297.

Dodson MW, Zhang T, Jiang C, Chen S, Guo M. 2012. Roles of the Drosophila LRRK2 homolog in Rab7-dependent lysosomal positioning. *Human Molecular Genetics* **21**: 1350–1363.

Doggett EA, Zhao J, Mork CN, Hu D, Nichols RJ. 2012. Phosphorylation of LRRK2 serines 955 and 973 is disrupted by Parkinson's disease mutations and LRRK2 pharmacological inhibition. *Journal of Neurochemistry* **120**: 37–45.

Dorsey ER, Constantinescu R, Thompson JP, Biglan KM, Holloway RG, Kieburtz K, Marshall FJ, Ravina BM, Schifitto G, Siderowf A, et al. 2007. Projected number of people with Parkinson disease in the most populous nations, 2005 through 2030. *Neurology* **68**: 384–386.

Dotchin C, Msuya O, Kissima J, Massawe J, Mhina A, Moshy A, Aris E, Jusabani A, Whiting D, Masuki G, et al. 2008. The prevalence of Parkinson's disease in rural Tanzania. *Movement Disorders* **23**: 1567–1672.

Dotchin CL, Akinyemi RO, Gray WK, Walker RW. 2012. Geriatric medicine: services and training in Africa. *Age and Ageing*: afs119.

Dudek J, Rehling P, van der Laan M. 2013. Mitochondrial protein import: Common principles and physiological networks. *Biochimica et Biophysica Acta (BBA) - Molecular Cell Research* **1833**: 274–285.

Dunn KW, Kamocka MM, McDonald JH. 2011. A practical guide to evaluating colocalization in biological microscopy. *American Journal of Physiology - Cell Physiology* **300**: C723–C742.

Dzamko N, Deak M, Hentati F, Reith AD, Prescott AR, Alessi DR, Nichols RJ. 2010. Inhibition of LRRK2 kinase activity leads to dephosphorylation of Ser(910)/Ser(935), disruption of 14-3-3 binding and altered cytoplasmic localization. *The Biochemical Journal* **430**: 405–413.

Edvardson S, Cinnamon Y, Ta-Shma A, Shaag A, Yim Y-I, Zenvirt S, Jalas C, Lesage S, Brice A, Taraboulos A, et al. 2012. A deleterious mutation in DNAJC6 encoding the neuronal-specific clathrin-uncoating co-chaperone auxilin, is associated with juvenile parkinsonism. *PloS One* **7**: e36458.

Eliyahu E, Pnueli L, Melamed D, Scherrer T, Gerber AP, Pines O, Rapaport D, Arava Y. 2010. Tom20 mediates localization of mRNAs to mitochondria in a translation-dependent manner. *Molecular and Cellular Biology* **30**: 284–294.

Esteves AR, Cardoso SM. 2016. LRRK2 at the crossroad between autophagy and microtubule trafficking: insights into Parkinson's disease. *The Neuroscientist: A Review Journal Bringing Neurobiology, Neurology and Psychiatry*.

Esteves AR, G-Fernandes M, Santos D, Januário C, Cardoso SM. 2015. The upshot of LRRK2 inhibition to Parkinson's disease paradigm. *Molecular Neurobiology* **52**: 1804–1820.

Exner N, Treske B, Paquet D, Holmström K, Schiesling C, Gispert S, Carballo-Carbajal I, Berg D, Hoepken H-H, Gasser T, et al. 2007. Loss-of-function of human PINK1 results in mitochondrial pathology and can be rescued by parkin. *The Journal of Neuroscience: The Official Journal of the Society for Neuroscience* **27**: 12413–12418.

Exner N, Lutz AK, Haass C, Winklhofer KF. 2012. Mitochondrial dysfunction in Parkinson's disease: molecular mechanisms and pathophysiological consequences: Mitochondrial dysfunction in Parkinson's disease. *The EMBO Journal* **31**: 3038–3062.

Ferreira JJ, Guedes LC, Rosa MM, Coelho M, van Doeselaar M, Schweiger D, Di Fonzo A, Oostra BA, Sampaio C, Bonifati V. 2007. High prevalence of LRRK2 mutations in familial and sporadic Parkinson's disease in Portugal. *Movement Disorders: Official Journal of the Movement Disorder Society* **22**: 1194–1201.

Foroud T. 2005. LRRK2: both a cause and a risk factor for Parkinson disease? *Neurology* **65**: 664–665.

Fraser KB, Moehle MS, Daher JPL, Webber PJ, Williams JY, Stewart CA, Yacoubian TA, Cowell RM, Dokland T, Ye T, et al. 2013. LRRK2 secretion in exosomes is regulated by 14-3-3. *Human Molecular Genetics* **22**: 4988–5000.

Fraser KB, Moehle MS, Alcalay RN, West AB, LRRK2 Cohort Consortium. 2016. Urinary LRRK2 phosphorylation predicts parkinsonian phenotypes in G2019S LRRK2 carriers. *Neurology* **86**: 994–999.

Fu C, Wehr DR, Edwards J, Hauge B. 2008. Rapid one-step recombinational cloning. *Nucleic Acids Research* **36**: e54.

Funayama M, Hasegawa K, Kowa H, Saito M, Tsuji S, Obata F. 2002. A new locus for Parkinson's disease (PARK8) maps to chromosome 12p11.2-q13.1. *Annals of Neurology* **51**: 296–301.

Funayama M, Hasegawa K, Ohta E, Kawashima N, Komiyama M, Kowa H, Tsuji S, Obata F. 2005. An LRRK2 mutation as a cause for the parkinsonism in the original PARK8 family. *Annals of Neurology* **57**: 918–921.

Funayama M, Ohe K, Amo T, Furuya N, Yamaguchi J, Saiki S, Li Y, Ogaki K, Ando M, Yoshino H, et al. 2015. CHCHD2 mutations in autosomal dominant late-onset Parkinson's disease: a genome-wide linkage and sequencing study. *The Lancet Neurology* **14**: 274–282.

Gadir N, Haim-Vilmovsky L, Kraut-Cohen J, Gerst JE. 2011. Localization of mRNAs coding for mitochondrial proteins in the yeast Saccharomyces cerevisiae. *RNA (New York, N.Y.)* **17**: 1551–1565.

Garcia-Miralles M, Coomaraswamy J, Häbig K, Herzig MC, Funk N, Gillardon F, Maisel M, Jucker M, Gasser T, Galter D, et al. 2015. No dopamine cell loss or changes in cytoskeleton function in transgenic mice expressing physiological levels of wild type or G2019S mutant LRRK2 and in human fibroblasts. *PLoS ONE* **10**.

Gauthier T, Claude-Taupin A, Delage-Mourroux R, Boyer-Guittaut M, Hervouet E. 2015. Proximity Ligation In situ Assay is a Powerful Tool to Monitor Specific ATG Protein Interactions following Autophagy Induction. *PLOS ONE* **10**: e0128701.

Geisler S, Holmström KM, Skujat D, Fiesel FC, Rothfuss OC, Kahle PJ, Springer W. 2010. PINK1/Parkin-mediated mitophagy is dependent on VDAC1 and p62/SQSTM1. *Nature Cell Biology* **12**: 119–131.

Ghavami S, Shojaei S, Yeganeh B, Ande SR, Jangamreddy JR, Mehrpour M, Christoffersson J, Chaabane W, Moghadam AR, Kashani HH, et al. 2014. Autophagy and apoptosis dysfunction in neurodegenerative disorders. *Progress in Neurobiology* **112**: 24–49.

Gilsbach BK, Kortholt A. 2014. Structural biology of the LRRK2 GTPase and kinase domains: implications for regulation. *Frontiers in Molecular Neuroscience* **7**: 32.

Glick D, Barth S, Macleod KF. 2010. Autophagy: cellular and molecular mechanisms. *The Journal of pathology* **221**: 3–12.

Gloeckner CJ, Kinkl N, Schumacher A, Braun RJ, O'Neill E, Meitinger T, Kolch W, Prokisch H, Ueffing M. 2006. The Parkinson disease causing LRRK2 mutation I2020T is associated with increased kinase activity. *Human Molecular Genetics* **15**: 223–232.

Godena VK, Brookes-Hocking N, Moller A, Shaw G, Oswald M, Sancho RM, Miller CCJ, Whitworth AJ, De Vos KJ. 2014. Increasing microtubule acetylation rescues axonal transport and locomotor deficits caused by LRRK2 Roc-COR domain mutations. *Nature Communications* **5**.

Gómez-Suaga P, Luzón-Toro B, Churamani D, Zhang L, Bloor-Young D, Patel S, Woodman PG, Churchill GC, Hilfiker S. 2012. Leucine-rich repeat kinase 2 regulates autophagy through a calcium-dependent pathway involving NAADP. *Human Molecular Genetics* **21**: 511–525.

Gottlieb E, Armour SM, Harris MH, Thompson CB. 2003. Mitochondrial membrane potential regulates matrix configuration and cytochrome c release during apoptosis. *Cell Death and Differentiation* **10**: 709–717.

Greeff JM. 2007. Deconstructing Jaco: genetic heritage of an Afrikaner. *Annals of Human Genetics* **71**: 674–688.

Greenamyre JT, Hastings TG. 2004. Biomedicine. Parkinson's--divergent causes, convergent mechanisms. *Science (New York, N.Y.)* **304**: 1120–1122.

Greene AW, Grenier K, Aguileta MA, Muise S, Farazifard R, Haque ME, McBride HM, Park DS, Fon EA. 2012. Mitochondrial processing peptidase regulates PINK1 processing, import and Parkin recruitment. *EMBO reports* **13**: 378–385.

Greggio E. 2012. Role of LRRK2 kinase activity in the pathogenesis of Parkinson's disease. *Biochemical Society Transactions* **40**: 1058–1062.

Greggio E, Jain S, Kingsbury A, Bandopadhyay R, Lewis P, Kaganovich A, van der Brug MP, Beilina A, Blackinton J, Thomas KJ, et al. 2006. Kinase activity is required for the toxic effects of mutant LRRK2/dardarin. *Neurobiology of disease* **23**: 329–341.

Grünewald A, Voges L, Rakovic A, Kasten M, Vandebona H, Hemmelmann C, Lohmann K, Orolicki S, Ramirez A, Schapira AHV, et al. 2010. Mutant parkin impairs mitochondrial function and morphology in human fibroblasts. *PLOS ONE* **5**: e12962.

Grünewald A, Arns B, Meier B, Brockmann K, Tadic V, Klein C. 2014. Does uncoupling protein 2 expression qualify as marker of disease status in LRRK2-associated Parkinson's disease? *Antioxidants & Redox Signaling* **20**: 1955–1960.

Guo L, Wang W, Chen SG. 2006. Leucine-rich repeat kinase 2: Relevance to Parkinson's disease. *The International Journal of Biochemistry & Cell Biology* **38**: 1469–1475.

Guo L, Gandhi PN, Wang W, Petersen RB, Wilson-Delfosse AL, Chen SG. 2007. The Parkinson's disease-associated protein, leucine-rich repeat kinase 2 (LRRK2), is an authentic GTPase thatstimulates kinase activity. *Experimental Cell Research* **313**: 3658–3670.

Gwinn-Hardy K, Mehta ND, Farrer M, Maraganore D, Muenter M, Yen SH, Hardy J, Dickson DW. 2000. Distinctive neuropathology revealed by alpha-synuclein antibodies in hereditary parkinsonism and dementia linked to chromosome 4p. *Acta Neuropathologica* **99**: 663–672.

Gwinn-Hardy K, Singleton A, O'Suilleabhain P, Boss M, Nicholl D, Adam A, Hussey J, Critchley P, Hardy J, Farrer M. 2001. Spinocerebellar ataxia type 3 phenotypically resembling parkinson disease in a black family. *Archives of Neurology* **58**: 296–299.

Harbauer AB, Opalińska M, Gerbeth C, Herman JS, Rao S, Schönfisch B, Guiard B, Schmidt O, Pfanner N, Meisinger C. 2014. Cell cycle–dependent regulation of mitochondrial preprotein translocase. *Science* **346**: 1109–1113.

Hasson SA, Kane LA, Yamano K, Huang C-H, Sliter DA, Buehler E, Wang C, Heman-Ackah SM, Hessa T, Guha R, et al. 2013. High-content genome-wide RNAi screens identify regulators of parkin upstream of mitophagy. *Nature* **504**: 291–295.

Hayat MA. 2016. *Autophagy: Cancer, Other Pathologies, Inflammation, Immunity, Infection, and Aging: Volume 9: Human Diseases and Autophagosome*. Academic Press.

Haylett W, Swart C, van der Westhuizen F, van Dyk H, van der Merwe L, van der Merwe C, Loos B, Carr J, Kinnear C, Bardien S, et al. 2016. Altered mitochondrial respiration and other features of mitochondrial function in Parkin-mutant fibroblasts from Parkinson's disease patients. *Parkinson's Disease, Parkinson's Disease* **2016**, **2016**: e1819209.

Henry AG, Aghamohammadzadeh S, Samaroo H, Chen Y, Mou K, Needle E, Hirst WD. 2015. Pathogenic LRRK2 mutations, through increased kinase activity, produce enlarged lysosomes with reduced degradative capacity and increase ATP13A2 expression. *Human Molecular Genetics*: ddv314.

Hentati F, Trinh J, Thompson C, Nosova E, Farrer MJ, Aasly JO. 2014. LRRK2 parkinsonism in Tunisia and Norway: A comparative analysis of disease penetrance. *Neurology* **83**: 568–569.

Heo HY, Kim K-S, Seol W. 2010a. Coordinate Regulation of Neurite Outgrowth by LRRK2 and Its Interactor, Rab5. *Experimental Neurobiology* **19**: 97–105.

Heo HY, Park J-M, Kim C-H, Han BS, Kim K-S, Seol W. 2010b. LRRK2 enhances oxidative stress-induced neurotoxicity via its kinase activity. *Experimental Cell Research* **316**: 649–656.

Hirsch L, Jette N, Frolkis A, Steeves T, Pringsheim T. 2016. The incidence of Parkinson's disease: A systematic review and meta-analysis. *Neuroepidemiology* **46**: 292–300.

Ho DH, Kim H, Kim J, Sim H, Ahn H, Kim J, Seo H, Chung KC, Park B-J, Son I, et al. 2015. Leucine-Rich Repeat Kinase 2 (LRRK2) phosphorylates p53 and induces p21WAF1/CIP1 expression. *Molecular Brain* **8**.

Ho DH, Jang J, Joe E, Son I, Seo H, Seol W. 2016. G2385R and I2020T Mutations Increase LRRK2 GTPase Activity. *BioMed Research International* **2016**: e7917128.

Hunn BHM, Cragg SJ, Bolam JP, Spillantini M-G, Wade-Martins R. 2015. Impaired intracellular trafficking defines early Parkinson's disease. *Trends in Neurosciences* **38**: 178–188.

Hwang O. 2013. Role of oxidative stress in Parkinson's disease. *Experimental Neurobiology* **22**: 11–17.

Isacson O. 2002. Models of repair mechanisms for future treatment modalities of Parkinson's disease. *Brain Research Bulletin* **57**: 839–846.

Jaleel M, Nichols RJ, Deak M, Campbell DG, Gillardon F, Knebel A, Alessi DR. 2007a. LRRK2 phosphorylates moesin at threonine-558: characterization of how Parkinson's disease mutants affect kinase activity. *The Biochemical Journal* **405**: 307–317.

Jaleel M, Nichols RJ, Deak M, Campbell DG, Gillardon F, Knebel A, Alessi DR. 2007b. LRRK2 phosphorylates moesin at threonine-558: characterization of how Parkinson's disease mutants affect kinase activity. *Biochemical Journal* **405**: 307.

Janda E, Isidoro C, Carresi C, Mollace V. 2012. Defective autophagy in Parkinson's disease: role of oxidative stress. *Molecular Neurobiology* **46**: 639–661.

Jin SM, Lazarou M, Wang C, Kane LA, Narendra DP, Youle RJ. 2010. Mitochondrial membrane potential regulates PINK1 import and proteolytic destabilization by PARL. *The Journal of Cell Biology* **191**: 933–942.

Kaddumukasa M, Kakooza A, Kaddumukasa MN, Ddumba E, Mugenyi L, Sajatovic M, Katabira E. 2015. Knowledge and Attitudes of Parkinson's Disease in Rural and Urban Mukono District, Uganda: A Cross-Sectional, Community-Based Study. *Parkinson's Disease* **2015**.

Kang R, Zeh HJ, Lotze MT, Tang D. 2011. The Beclin 1 network regulates autophagy and apoptosis. *Cell Death and Differentiation* **18**: 571–580.

Kato H, Lu Q, Rapaport D, Kozjak-Pavlovic V. 2013. Tom70 Is Essential for PINK1 Import into Mitochondria (OS Shirihai, Ed). *PLoS ONE* **8**: e58435.

Kay DM, Bird TD, Zabetian CP, Factor SA, Samii A, Higgins DS, Nutt J, Roberts JW, Griffith A, Leis BC, et al. 2006a. Validity and utility of a LRRK2 G2019S mutation test for the diagnosis of Parkinson's disease. *Genetic Testing* **10**: 221–227.

Kay DM, Zabetian CP, Factor SA, Nutt JG, Samii A, Griffith A, Bird TD, Kramer P, Higgins DS, Payami H. 2006b. Parkinson's disease and LRRK2: frequency of a common mutation in U.S. movement disorder clinics. *Movement Disorders: Official Journal of the Movement Disorder Society* **21**: 519–523.

Kircher M, Witten DM, Jain P, O'Roak BJ, Cooper GM, Shendure J. 2014. A general framework for estimating the relative pathogenicity of human genetic variants. *Nature Genetics* **46**: 310–315.

Kitada T, Asakawa S, Hattori N, Matsumine H, Yamamura Y, Minoshima S, Yokochi M, Mizuno Y, Shimizu N. 1998. Mutations in the parkin gene cause autosomal recessive juvenile parkinsonism. *Nature* **392**: 605–608.

Klein C, Westenberger A. 2012. Genetics of Parkinson's Disease. *Cold Spring Harbor Perspectives in Medicine* **2**.

Klionsky DJ, Emr SD. 2000. Autophagy as a Regulated Pathway of Cellular Degradation. *Science (New York, N.Y.)* **290**: 1717–1721.

Klionsky DJ, Abeliovich H, Agostinis P, Agrawal DK, Aliev G, Askew DS, Baba M, Baehrecke EH, Bahr BA, Ballabio A, et al. 2008. Guidelines for the use and interpretation of assays for monitoring autophagy in higher eukaryotes. *Autophagy* **4**: 151–175.

Ko HS, Bailey R, Smith WW, Liu Z, Shin J-H, Lee Y-I, Zhang Y-J, Jiang H, Ross CA, Moore DJ, et al. 2009. CHIP regulates leucine-rich repeat kinase-2 ubiquitination, degradation, and toxicity. *Proceedings of the National Academy of Sciences of the United States of America* **106**: 2897–2902.

Kobe B, Kajava AV. 2001. The leucine-rich repeat as a protein recognition motif. *Current Opinion in Structural Biology* **11**: 725–732.

Komatsu M, Waguri S, Chiba T, Murata S, Iwata J, Tanida I, Ueno T, Koike M, Uchiyama Y, Kominami E, et al. 2006. Loss of autophagy in the central nervous system causes neurodegeneration in mice. *Nature* **441**: 880–884.

Kondapalli C, Kazlauskaite A, Zhang N, Woodroof HI, Campbell DG, Gourlay R, Burchell L, Walden H, Macartney TJ, Deak M, et al. 2012. PINK1 is activated by mitochondrial membrane potential depolarization and stimulates Parkin E3 ligase activity by phosphorylating Serine 65. *Open Biology* **2**: 120080.

Kondo K, Obitsu S, Teshima R. 2011. α-Synuclein aggregation and transmission are enhanced by leucine-rich repeat kinase 2 in human neuroblastoma SH-SY5Y cells. *Biological & Pharmaceutical Bulletin* **34**: 1078–1083.

Krebs CE, Karkheiran S, Powell JC, Cao M, Makarov V, Darvish H, Di Paolo G, Walker RH, Shahidi GA, Buxbaum JD, et al. 2013. The Sac1 domain of SYNJ1 identified mutated in a family with early-onset progressive Parkinsonism with generalized seizures. *Human Mutation* **34**: 1200–1207.

Labrousse AM, Zappaterra MD, Rube DA, van der Bliek AM. 1999. C. elegans dynamin-related protein DRP-1 controls severing of the mitochondrial outer membrane. *Molecular Cell* **4**: 815–826.

Langston JW, Ballard P, Tetrud JW, Irwin I. 1983. Chronic Parkinsonism in humans due to a product of meperidine-analog synthesis. *Science* **219**: 979–980.

Lavalley NJ, Slone SR, Ding H, West AB, Yacoubian TA. 2016. 14-3-3 Proteins regulate mutant LRRK2 kinase activity and neurite shortening. *Human Molecular Genetics* **25**: 109–122.

Lazarou M, Jin SM, Kane LA, Youle RJ. 2012. Role of PINK1 binding to the TOM complex and alternate intracellular membranes in recruitment and activation of the E3 ligase Parkin. *Developmental Cell* **22**: 320–333.

Lee HC, Yin PH, Lu CY, Chi CW, Wei YH. 2000. Increase of mitochondria and mitochondrial DNA in response to oxidative stress in human cells. *Biochemical Journal* **348**: 425–432.

Lemasters JJ. 2005. Selective mitochondrial autophagy, or mitophagy, as a targeted defense against oxidative stress, mitochondrial dysfunction, and aging. *Rejuvenation Research* **8**: 3–5.

Lesage S, Brice A. 2009. Parkinson's disease: from monogenic forms to genetic susceptibility factors. *Human Molecular Genetics* **18**: R48-59.

Lesage S, Patin E, Condroyer C, Leutenegger AL, Lohmann E, Giladi N, Bar-Shira A, Belarbi S, Hecham N, Pollak P, et al. 2010. Parkinson's disease-related LRRK2 G2019S mutation results from independent mutational events in humans. *Human Molecular Genetics* **19**: 1998–2004.

Lewis PA. 2012. Assaying the kinase activity of LRRK2 in vitro. *Journal of visualized experiments: JoVE*.

Lewis PA, Greggio E, Beilina A, Jain S, Baker A, Cookson MR. 2007. The R1441C mutation of LRRK2 disrupts GTP hydrolysis. *Biochemical and biophysical research communications* **357**: 668–671.

Li J-Q, Tan L, Yu J-T. 2014. The role of the LRRK2 gene in Parkinsonism. *Molecular Neurodegeneration* **9**: 47.

Li L, Hu G. 2015. Pink1 protects cortical neurons from thapsigargin-induced oxidative stress and neuronal apoptosis. *Bioscience Reports* **35**: 1–8.

Lin MT, Beal MF. 2006. Mitochondrial dysfunction and oxidative stress in neurodegenerative diseases. *Nature* **443**: 787–795.

Liou AKF, Leak RK, Li L, Zigmond MJ. 2008. Wild-type LRRK2 but not its mutant attenuates stress-induced cell death via ERK pathway. *Neurobiology of Disease* **32**: 116–124.

Liu Z, Galemmo RA, Fraser KB, Moehle MS, Sen S, Volpicelli-Daley LA, DeLucas LJ, Ross LJ, Valiyaveettil J, Moukha-Chafiq O, et al. 2014. Unique Functional and Structural Properties of the LRRK2 Protein ATP-binding Pocket. *Journal of Biological Chemistry* **289**: 32937–32951.

Lobbestael E, Zhao J, Rudenko IN, Beylina A, Gao F, Wetter J, Beullens M, Bollen M, Cookson MR, Baekelandt V, et al. 2013. Identification of protein phosphatase 1 as a regulator of the LRRK2 phosphorylation cycle. *Biochemical Journal* **456**: 119–128.

Lobbestael E, Civiero L, De Wit T, Taymans J-M, Greggio E, Baekelandt V. 2016. Pharmacological LRRK2 kinase inhibition induces LRRK2 protein destabilization and proteasomal degradation. *Scientific Reports* **6**: 33897.

Loos B, du Toit A, Hofmeyr J-HS. 2014. Defining and measuring autophagosome flux—concept and reality. *Autophagy* **10**: 2087–2096.

Lopes FM, Schröder R, da Frota MLC, Zanotto-Filho A, Müller CB, Pires AS, Meurer RT, Colpo GD, Gelain DP, Kapczinski F, et al. 2010. Comparison between proliferative and neuron-like SH-SY5Y cells as an in vitro model for Parkinson disease studies. *Brain Research* **1337**: 85–94.

Lorenzo-Betancor O, Samaranch L, Ezquerra M, Tolosa E, Lorenzo E, Irigoyen J, Gaig C, Pastor MA, Soto-Ortolaza AI, Ross OA, et al. 2012. LRRK2 haplotype-sharing analysis in Parkinson's disease reveals a novel p.S1761R mutation. *Movement Disorders: Official Journal of the Movement Disorder Society* **27**: 146–151.

Luerman GC, Nguyen C, Samaroo H, Loos P, Xi H, Hurtado-Lorenzo A, Needle E, Stephen Noell G, Galatsis P, Dunlop J, et al. 2014. Phosphoproteomic evaluation of pharmacological inhibition of leucine-rich repeat kinase 2 reveals significant off-target effects of LRRK-2-IN-1. *Journal of Neurochemistry* **128**: 561–576.

Lutz AK, Exner N, Fett ME, Schlehe JS, Kloos K, Lammermann K, Brunner B, Kurz-Drexler A, Vogel F, Reichert AS, et al. 2009. Loss of Parkin or PINK1 function increases Drp1-dependent mitochondrial fragmentation. *Journal of Biological Chemistry* **284**: 22938–22951.

Luzón-Toro B, Torre ER de la, Delgado A, Pérez-Tur J, Hilfiker S. 2007. Mechanistic insight into the dominant mode of the Parkinson's disease-associated G2019S LRRK2 mutation. *Human Molecular Genetics* **16**: 2031–2039.

MacLeod D, Dowman J, Hammond R, Leete T, Inoue K, Abeliovich A. 2006. The familial Parkinsonism gene LRRK2 regulates neurite process morphology. *Neuron* **52**: 587–593.

Maio RD, Barrett PJ, Hoffman EK, Barrett CW, Zharikov A, Borah A, Hu X, McCoy J, Chu CT, Burton EA, et al. 2016. α-Synuclein binds to TOM20 and inhibits mitochondrial protein import in Parkinson's disease. *Science Translational Medicine* **8**: 342ra78-342ra78.

Malkus KA, Tsika E, Ischiropoulos H. 2009. Oxidative modifications, mitochondrial dysfunction, and impaired protein degradation in Parkinson's disease: how neurons are lost in the Bermuda triangle. *Molecular Neurodegeneration* **4**: 24.

Manzoni C, Mamais A, Dihanich S, Abeti R, Soutar MPM, Plun-Favreau H, Giunti P, Tooze SA, Bandopadhyay R, Lewis PA. 2013a. Inhibition of LRRK2 kinase activity stimulates macroautophagy. *Biochimica et Biophysica Acta (BBA) - Molecular Cell Research* **1833**: 2900–2910.

Manzoni C, Mamais A, Dihanich S, McGoldrick P, Devine MJ, Zerle J, Kara E, Taanman J-W, Healy DG, Marti-Masso J-F, et al. 2013b. Pathogenic Parkinson's disease mutations across the functional domains of

LRRK2 alter the autophagic/lysosomal response to starvation. *Biochemical and Biophysical Research Communications* **441**: 862–866.

Manzoni C, Denny P, Lovering RC, Lewis PA. 2015. Computational analysis of the LRRK2 interactome. *PeerJ* **3**: e778.

Marsden CD. 1982. Originally published as Volume 2, Issue 8308, Basal Ganglia disease. *The Lancet* **320**: 1141–1147.

Martin I, Kim JW, Lee BD, Kang HC, Xu J-C, Jia H, Stankowski J, Kim M-S, Zhong J, Kumar M, et al. 2014. Ribosomal protein s15 phosphorylation mediates LRRK2 neurodegeneration in Parkinson's disease. *Cell* **157**: 472–485.

Martin LJ, Pan Y, Price AC, Sterling W, Copeland NG, Jenkins NA, Price DL, Lee MK. 2006. Parkinson's disease alpha-synuclein transgenic mice develop neuronal mitochondrial degeneration and cell death. *The Journal of Neuroscience: The Official Journal of the Society for Neuroscience* **26**: 41–50.

Martinez-Vicente M, Talloczy Z, Kaushik S, Massey AC, Mazzulli J, Mosharov EV, Hodara R, Fredenburg R, Wu D-C, Follenzi A, et al. 2008. Dopamine-modified alpha-synuclein blocks chaperone-mediated autophagy. *The Journal of Clinical Investigation* **118**: 777–788.

Mata IF, Kachergus JM, Taylor JP, Lincoln S, Aasly J, Lynch T, Hulihan MM, Cobb SA, Wu R-M, Lu C-S, et al. 2005. Lrrk2 pathogenic substitutions in Parkinson's disease. *Neurogenetics* **6**: 171–177.

Mata IF, Alvarez V, Ribacoba R, Infante J, Sierra M, Gómez-Garre P, Mir P, Waldherr S, Yearout D, Zabetian CP. 2013. Novel Lrrk2-p.S1761R Mutation Is Not a Common Cause of Parkinson's Disease in Spain. *Movement disorders : official journal of the Movement Disorder Society* **28**: 248.

Mata IF, Davis MY, Lopez AN, Dorschner MO, Martinez E, Yearout D, Cholerton BA, Hu S-C, Edwards KL, Bird TD, et al. 2016. The discovery of LRRK2 p.R1441S, a novel mutation for Parkinson's disease, adds to the complexity of a mutational hotspot. *American Journal of Medical Genetics. Part B, Neuropsychiatric Genetics: The Official Publication of the International Society of Psychiatric Genetics* **171**: 925–930.

McLelland GL, Soubannier V, Chen CX, McBride HM, Fon EA. 2014. Parkin and PINK1 function in a vesicular trafficking pathway regulating mitochondrial quality control. *EMBO Journal* **33**: 282–295.

Merwe C van der, Haylett W, Harvey J, Lombard D, Bardien S, Carr J. 2012. Factors influencing the development of early- or late-onset Parkinson's disease in a cohort of South African patients. *South African Medical Journal* **102**: 848–851.

Migheli R, Del Giudice MG, Spissu Y, Sanna G, Xiong Y, Dawson TM, Dawson VL, Galioto M, Rocchitta G, Biosa A, et al. 2013. LRRK2 affects vesicle trafficking, neurotransmitter extracellular level and membrane receptor localization. *PLoS ONE* **8**: e77198.

Mizushima N, Yoshimori T. 2007. How to interpret LC3 immunoblotting. *Autophagy* **3**: 542–545.

Moore DJ, West AB, Dawson VL, Dawson TM. 2005. Molecular pathophysiology of Parkinson's disease. *Annual review of neuroscience* **28**: 57–87.

Mortiboys H, Thomas KJ, Koopman WJH, Klaffke S, Abou-Sleiman P, Olpin S, Wood NW, Willems PHGM, Smeitink JAM, Cookson MR, et al. 2008. Mitochondrial function and morphology are impaired in parkin-mutant fibroblasts. *Annals of Neurology* **64**: 555–565.

Mortiboys H, Johansen KK, Aasly JO, Bandmann O. 2010. Mitochondrial impairment in patients with Parkinson disease with the G2019S mutation in LRRK2. *Neurology* **75**: 2017–2020.

Mortiboys H, Furmston R, Bronstad G, Aasly J, Elliott C, Bandmann O. 2015. UDCA exerts beneficial effect on mitochondrial dysfunction in LRRK2(G2019S) carriers and in vivo. *Neurology* **85**: 846–852.

Narendra, Tanaka A, Suen D-F, Youle RJ. 2008. Parkin is recruited selectively to impaired mitochondria and promotes their autophagy. *The Journal of cell biology* **183**: 795–803.

Narendra, Walker JE, Youle R. 2012. Mitochondrial quality control mediated by PINK1 and Parkin: Links to Parkinsonism. *Cold Spring Harbor Perspectives in Biology* **4**: a011338.

Narendra DP, Jin SM, Tanaka A, Suen D-F, Gautier CA, Shen J, Cookson MR, Youle RJ. 2010. PINK1 Is Selectively Stabilized on Impaired Mitochondria to Activate Parkin. *PLoS Biol* **8**: e1000298.

Nelson MP, Shacka JJ. 2013. Autophagy Modulation in Disease Therapy: Where Do We Stand? *Current pathobiology reports* **1**: 239–245.

Nguyen HN, Byers B, Cord B, Shcheglovitov A, Byrne J, Gujar P, Kee K, Schüle B, Dolmetsch RE, Langston W, et al. 2011. LRRK2 mutant iPSC-derived DA neurons demonstrate increased susceptibility to oxidative stress. *Cell Stem Cell* **8**: 267–280.

Nicholls DG. 2004. Mitochondrial membrane potential and aging. *Aging Cell* **3**: 35–40.

Nicholls DG. 2008. Oxidative stress and energy crises in neuronal dysfunction. *Annals of the New York Academy of Sciences* **1147**: 53–60.

Nicholls DG. 2009. Spare respiratory capacity, oxidative stress and excitotoxicity. *Biochemical Society Transactions* **37**: 1385–1388.

Nichols RJ, Dzamko N, Hutti JE, Cantley LC, Deak M, Moran J, Bamborough P, Reith AD, Alessi DR. 2009. Substrate specificity and inhibitors of LRRK2, a protein kinase mutated in Parkinson's disease. *Biochemical Journal* **424**: 47–60.

Nikonova EV, Xiong Y, Tanis KQ, Dawson VL, Vogel RL, Finney EM, Stone DJ, Reynolds IJ, Kern JT, Dawson TM. 2012. Transcriptional responses to loss or gain of function of the leucine-rich repeat kinase 2 (LRRK2) gene uncover biological processes modulated by LRRK2 activity. *Human Molecular Genetics* **21**: 163–174.

Niu J, Yu M, Wang C, Xu Z. 2012. Leucine-rich repeat kinase 2 disturbs mitochondrial dynamics via Dynamin-like protein. *Journal of neurochemistry* **122**: 650–658.

Nixon RA, Wegiel J, Kumar A, Yu WH, Peterhoff C, Cataldo A, Cuervo AM. 2005. Extensive involvement of autophagy in Alzheimer disease: an immuno-electron microscopy study. *Journal of Neuropathology and Experimental Neurology* **64**: 113–122.

Nuytemans K, Theuns J, Cruts M, Van Broeckhoven C. 2010. Genetic etiology of Parkinson disease associated with mutations in the SNCA, PARK2, PINK1, PARK7, and LRRK2 genes: A mutation update. *Human Mutation* **31**: 763–780.

Okatsu K, Oka T, Iguchi M, Imamura K, Kosako H, Tani N, Kimura M, Go E, Koyano F, Funayama M, et al. 2012. PINK1 autophosphorylation upon membrane potential dissipation is essential for Parkin recruitment to damaged mitochondria. *Nature Communications* **3**: 1016.

Okatsu K, Kimura M, Oka T, Tanaka K, Matsuda N. 2015. Unconventional PINK1 localization to the outer membrane of depolarized mitochondria drives Parkin recruitment. *Journal of Cell Science* **128**: 964–978.

Okubadejo NU, Bower JH, Rocca WA, Maraganore DM. 2006. Parkinson's disease in Africa: A systematic review of epidemiologic and genetic studies. *Movement Disorders: Official Journal of the Movement Disorder Society* **21**: 2150–2156.

Orenstein SJ, Kuo S-H, Tasset I, Arias E, Koga H, Fernandez-Carasa I, Cortes E, Honig LS, Dauer W, Consiglio A, et al. 2013. Interplay of LRRK2 with chaperone-mediated autophagy. *Nature Neuroscience* **16**: 394–406.

Ozelius LJ, Senthil G, Saunders-Pullman R, Ohmann E, Deligtisch A, Tagliati M, Hunt AL, Klein C, Henick B, Hailpern SM, et al. 2006. LRRK2 G2019S as a cause of Parkinson's disease in Ashkenazi Jews. *The New England Journal of Medicine* **354**: 424–425.

Pacelli C, De Rasmo D, Signorile A, Grattagliano I, di Tullio G, D'Orazio A, Nico B, Comi GP, Ronchi D, Ferranini E, et al. 2011. Mitochondrial defect and PGC-1α dysfunction in parkin-associated familial Parkinson's disease. *Biochimica et Biophysica Acta (BBA) - Molecular Basis of Disease* **1812**: 1041–1053.

Paisán-Ruíz C, Lang AE, Kawarai T, Sato C, Salehi-Rad S, Fisman GK, Al-Khairallah T, George-Hyslop PS, Singleton A, Rogaeva E. 2005. LRRK2 gene in Parkinson disease Mutation analysis and case control association study. *Neurology* **65**: 696–700.

Paisan-Ruiz C, Bhatia KP, Li A, Hernandez D, Davis M, Wood NW, Hardy J, Houlden H, Singleton A, Schneider SA. 2009. Characterization of PLA2G6 as a locus for dystonia-parkinsonism. *Annals of Neurology* **65**: 19–23.

Paisán-Ruiz C, Lewis PA, Singleton AB. 2013. LRRK2: Cause, risk, and mechanism. *Journal of Parkinson's Disease* **3**: 85–103.

Paisán-Ruíz C, Jain S, Evans EW, Gilks WP, Simón J, van der Brug M, de Munain AL, Aparicio S, Gil AM, Khan N, et al. 2004. Cloning of the gene containing mutations that cause PARK8-linked Parkinson's disease. *Neuron* **44**: 595–600.

Papkovskaia TD, Chau K-Y, Inesta-Vaquera F, Papkovsky DB, Healy DG, Nishio K, Staddon J, Duchen MR, Hardy J, Schapira AHV, et al. 2012. G2019S leucine-rich repeat kinase 2 causes uncoupling protein-mediated mitochondrial depolarization. *Human molecular genetics* **21**: 4201–4213.

Parisiadou L, Xie C, Cho HJ, Lin X, Gu X-L, Long C-X, Lobbestael E, Baekelandt V, Taymans J-M, Sun L, et al. 2009. Phosphorylation of Ezrin/Radixin/Moesin proteins by LRRK2 promotes the rearrangement of actin cytoskeleton in neuronal morphogenesis. *The Journal of Neuroscience* **29**: 13971–13980.

Park J, Lee SB, Lee S, Kim Y, Song S, Kim S, Bae E, Kim J, Shong M, Kim J-M, et al. 2006. Mitochondrial dysfunction in Drosophila PINK1 mutants is complemented by parkin. *Nature* **441**: 1157–1161.

Parker WD, Boyson SJ, Parks JK. 1989. Abnormalities of the electron transport chain in idiopathic Parkinson's disease. *Annals of Neurology* **26**: 719–723.

Patterson N, Petersen DC, van der Ross RE, Sudoyo H, Glashoff RH, Marzuki S, Reich D, Hayes VM. 2010. Genetic structure of a unique admixed population: implications for medical research. *Human Molecular Genetics* **19**: 411–419.

Perier C, Vila M. 2012. Mitochondrial biology and Parkinson's disease. *Cold Spring Harbor Perspectives in Medicine* **2**.

Pfanner N, Chacinska A. 2002. The mitochondrial import machinery: preprotein-conducting channels with binding sites for presequences. *Biochimica et Biophysica Acta (BBA) - Molecular Cell Research* **1592**: 15–24.

Plowey ED, Cherra SJ, Liu Y-J, Chu CT. 2008. Role of autophagy in G2019S-LRRK2-associated neurite shortening in differentiated SH-SY5Y cells. *Journal of Neurochemistry* **105**: 1048–1056.

Polymeropoulos MH, Lavedan C, Leroy E, Ide SE, Dehejia A, Dutra A, Pike B, Root H, Rubenstein J, Boyer R, et al. 1997. Mutation in the alpha-synuclein gene identified in families with Parkinson's disease. *Science (New York, N.Y.)* **276**: 2045–2047.

Porter RK, Joyce OJ, Farmer MK, Heneghan R, Tipton KF, Andrews JF, McBennett SM, Lund MD, Jensen CH, Melia HP. 1999. Indirect measurement of mitochondrial proton leak and its application. *International Journal of Obesity and Related Metabolic Disorders: Journal of the International Association for the Study of Obesity* **23 Suppl 6**: S12-18.

Preux PM, Condet A, Anglade C, Druet-Cabanac M, Debrock C, Macharia W, Couratier P, Boutros-Toni F, Dumas M. 2000. Parkinson's disease and environmental factors. Matched case-control study in the Limousin region, France. *Neuroepidemiology* **19**: 333–337.

Pridgeon JW, Olzmann JA, Chin L-S, Li L. 2007. PINK1 protects against oxidative stress by phosphorylating mitochondrial chaperone TRAP1. *PLoS biology* **5**: e172.

Pringsheim T, Jette N, Frolkis A, Steeves TDL. 2014. The prevalence of Parkinson's disease: a systematic review and meta-analysis. *Movement Disorders: Official Journal of the Movement Disorder Society* **29**: 1583–1590.

Pungaliya PP, Bai Y, Lipinski K, Anand VS, Sen S, Brown EL, Bates B, Reinhart PH, West AB, Hirst WD, et al. 2010. Identification and Characterization of a Leucine-Rich Repeat Kinase 2 (LRRK2) Consensus Phosphorylation Motif. *PLOS ONE* **5**: e13672.

Quadri M, Fang M, Picillo M, Olgiati S, Breedveld GJ, Graafland J, Wu B, Xu F, Erro R, Amboni M, et al. 2013. Mutation in the SYNJ1 gene associated with autosomal recessive, early-onset Parkinsonism. *Human Mutation* **34**: 1208–1215.

Ramirez A, Heimbach A, Gründemann J, Stiller B, Hampshire D, Cid LP, Goebel I, Mubaidin AF, Wriekat A-L, Roeper J, et al. 2006. Hereditary parkinsonism with dementia is caused by mutations in ATP13A2, encoding a lysosomal type 5 P-type ATPase. *Nature Genetics* **38**: 1184–1191.

Ramonet D, Daher JPL, Lin BM, Stafa K, Kim J, Banerjee R, Westerlund M, Pletnikova O, Glauser L, Yang L, et al. 2011. Dopaminergic neuronal loss, reduced neurite complexity and autophagic abnormalities in transgenic mice expressing G2019S mutant LRRK2. *PloS One* **6**: e18568.

Ray S, Bender S, Kang S, Lin R, Glicksman MA, Liu M. 2014. The Parkinson disease-linked LRRK2 protein mutation I2020T stabilizes an active state conformation leading to increased kinase activity. *The Journal of Biological Chemistry* **289**: 13042–13053.

Reers M, Smiley ST, Mottola-Hartshorn C, Chen A, Lin M, Chen LB. 1995. Mitochondrial membrane potential monitored by JC-1 dye. *Methods in Enzymology* **260**: 406–417.

Reeve A, Simcox E, Turnbull D. 2014. Ageing and Parkinson's disease: Why is advancing age the biggest risk factor? *Ageing Research Reviews* **14**: 19–30.

Refai FS, Ng SH, Tan E-K. 2015. Evaluating LRRK2 genetic variants with unclear pathogenicity. *BioMed Research International* **2015**.

Regad L, Martin J, Nuel G, Camproux A-C. 2010. Mining protein loops using a structural alphabet and statistical exceptionality. *BMC Bioinformatics* **11**: 75.

Reynolds A, Doggett EA, Riddle SM, Lebakken CS, Nichols RJ. 2014. LRRK2 kinase activity and biology are not uniformly predicted by its autophosphorylation and cellular phosphorylation site status. *Frontiers in Molecular Neuroscience* **7**.

Roise D, Schatz G. 1988. Mitochondrial presequences. *Journal of Biological Chemistry* **263**: 4509–4511.

Rudenko IN, Cookson MR. 2014. Heterogeneity of Leucine-Rich Repeat Kinase 2 mutations: Genetics, mechanisms and therapeutic implications. *Neurotherapeutics: The Journal of the American Society for Experimental NeuroTherapeutics*.

Rudenko IN, Chia R, Cookson MR. 2012a. Is inhibition of kinase activity the only therapeutic strategy for LRRK2-associated Parkinson's disease? *BMC Medicine* **10**: 20.

Rudenko IN, Kaganovich A, Hauser DN, Beylina A, Chia R, Ding J, Maric D, Jaffe H, Cookson MR. 2012b. The G2385R variant of leucine-rich repeat kinase 2 associated with Parkinson's disease is a partial loss-of-function mutation. *The Biochemical Journal* **446**: 99–111.

Saha S, Ash PEA, Gowda V, Liu L, Shirihai O, Wolozin B. 2015. Mutations in LRRK2 potentiate age-related impairment of autophagic flux. *Molecular Neurodegeneration* **10**: 26.

Saito T, Sadoshima J. 2015. Molecular mechanisms of mitochondrial autophagy/mitophagy in the heart. *Circulation Research* **116**: 1477–1490.

Sánchez-Danés A, Richaud-Patin Y, Carballo-Carbajal I, Jiménez-Delgado S, Caig C, Mora S, Di Guglielmo C, Ezquerra M, Patel B, Giralt A, et al. 2012. Disease-specific phenotypes in dopamine neurons from human iPS-based models of genetic and sporadic Parkinson's disease. *EMBO Molecular Medicine* **4**: 380–395.

Sander JD, Joung JK. 2014. CRISPR-Cas systems for editing, regulating and targeting genomes. *Nature Biotechnology* **32**: 347–355.

Sanders LH, Laganière J, Cooper O, Mak SK, Vu BJ, Huang YA, Paschon DE, Vangipuram M, Sundararajan R, Urnov FD, et al. 2014. LRRK2 mutations cause mitochondrial DNA damage in iPSC-derived neural cells from Parkinson's disease patients: Reversal by gene correction. *Neurobiology of disease* **62**.

Sanna G, Del Giudice MG, Crosio C, Iaccarino C. 2012. LRRK2 and vesicle trafficking. *Biochemical Society transactions* **40**: 1117–1122.

Sarraf SA, Raman M, Guarani-Pereira V, Sowa ME, Huttlin EL, Gygi SP, Harper JW. 2013. Landscape of the PARKIN-dependent ubiquitylome in response to mitochondrial depolarization. *Nature* **496**: 372–376.

Schapansky J, Nardozzi JD, Felizia F, LaVoie MJ. 2014. Membrane recruitment of endogenous LRRK2 precedes its potent regulation of autophagy. *Human Molecular Genetics* **23**: 4201–4214.

Schapira AH, Jenner P. 2011. Etiology and pathogenesis of Parkinson's disease. *Movement Disorders* **26**: 1049–1055.

Schapira AH, Cooper JM, Dexter D, Jenner P, Clark JB, Marsden CD. 1989. Mitochondrial complex I deficiency in Parkinson's disease. *Lancet (London, England)* **1**: 1269.

Schapira AHV. 2008. Mitochondria in the aetiology and pathogenesis of Parkinson's disease. *The Lancet. Neurology* **7**: 97–109.

Scheffzek K, Ahmadian MR. 2005. GTPase activating proteins: structural and functional insights 18 years after discovery. *Cellular and Molecular Life Sciences CMLS* **62**: 3014–3038.

Schlattner U, Tokarska-Schlattner M, Wallimann T. 2006. Mitochondrial creatine kinase in human health and disease. *Biochimica et Biophysica Acta (BBA) - Molecular Basis of Disease* **1762**: 164–180.

Schon EA, Przedborski S. 2011. Mitochondria: The Next (Neurode)Generation. *Neuron* **70**: 1033–1053.

Schulte EC, Ellwanger DC, Dihanich S, Manzoni C, Stangl K, Schormair B, Graf E, Eck S, Mollenhauer B, Haubenberger D, et al. 2014. Rare variants in LRRK1 and Parkinson's disease. *Neurogenetics* **15**: 49–57.

Schüpbach M, Lohmann E, Anheim M, Lesage S, Czernecki V, Yaici S, Worbe Y, Charles P, Welter M-L, Pollak P, et al. 2007. Subthalamic nucleus stimulation is efficacious in patients with Parkinsonism and LRRK2 mutations. *Movement Disorders: Official Journal of the Movement Disorder Society* **22**: 119–122.

Schwab AJ, Ebert AD. 2015. Neurite Aggregation and Calcium Dysfunction in iPSC-Derived Sensory Neurons with Parkinson's Disease-Related LRRK2 G2019S Mutation. *Stem Cell Reports* **5**: 1039–1052.

Scott RC, Juhász G, Neufeld TP. 2007. Direct induction of autophagy by Atg1 inhibits cell growth and induces apoptotic cell death. *Current biology : CB* **17**: 1–11.

Sedgwick SG, Smerdon SJ. 1999. The ankyrin repeat: a diversity of interactions on a common structural framework. *Trends in Biochemical Sciences* **24**: 311–316.

Sen S, Webber PJ, West AB. 2009. Dependence of Leucine-rich Repeat Kinase 2 (LRRK2) kinase activity on dimerization. *Journal of Biological Chemistry* **284**: 36346–36356.

Shamoto-Nagai M, Maruyama W, Kato Y, Isobe K, Tanaka M, Naoi M, Osawa T. 2003. An inhibitor of mitochondrial complex I, rotenone, inactivates proteasome by oxidative modification and induces aggregation of oxidized proteins in SH-SY5Y cells. *Journal of Neuroscience Research* **74**: 589–597.

Sheng Z, Zhang S, Bustos D, Kleinheinz T, Le Pichon CE, Dominguez SL, Solanoy HO, Drummond J, Zhang X, Ding X, et al. 2012. Ser1292 autophosphorylation is an indicator of LRRK2 kinase activity and contributes to the cellular effects of PD mutations. *Science Translational Medicine* **4**: 164ra161.

Sherer TB, Betarbet R, Greenamyre JT. 2002. Environment, mitochondria, and Parkinson's disease. *The Neuroscientist: A Review Journal Bringing Neurobiology, Neurology and Psychiatry* **8**: 192–197.

Shiota T, Traven A, Lithgow T. 2015. Mitochondrial biogenesis: cell-cycle-dependent investment in making mitochondria. *Current biology: CB* **25**: R78-80.

Shojaee S, Sina F, Banihosseini SS, Kazemi MH, Kalhor R, Shahidi G-A, Fakhrai-Rad H, Ronaghi M, Elahi E. 2008. Genome-wide linkage analysis of a Parkinsonian-pyramidal syndrome pedigree by 500 K SNP arrays. *American Journal of Human Genetics* **82**: 1375–1384.

Silberberg D, Katabira E. 2006. Neurological Disorders. In *Disease and mortality in Sub-Saharan Africa*, Jamison DT, , Feachem RG, , Makgoba MW, , Bos ER, , Baingana FK, , Hofman KJ, , Rogo KO (eds). World Bank: Washington (DC);

Smirnova E, Griparic L, Shurland DL, van der Bliek AM. 2001. Dynamin-related protein Drp1 is required for mitochondrial division in mammalian cells. *Molecular Biology of the Cell* **12**: 2245–2256.

Smith GA, Jansson J, Rocha EM, Osborn T, Hallett PJ, Isacson O. 2015. Fibroblast biomarkers of sporadic Parkinson's disease and LRRK2 kinase inhibition. *Molecular Neurobiology*: 1–17.

Smith WW, Pei Z, Jiang H, Moore DJ, Liang Y, West AB, Dawson VL, Dawson TM, Ross CA. 2005. Leucine-rich repeat kinase 2 (LRRK2) interacts with parkin, and mutant LRRK2 induces neuronal degeneration. *Proceedings of the National Academy of Sciences of the United States of America* **102**: 18676–18681.

Smith WW, Pei Z, Jiang H, Dawson VL, Dawson TM, Ross CA. 2006. Kinase activity of mutant LRRK2 mediates neuronal toxicity. *Nature Neuroscience* **9**: 1231–1233.

Sokol AM, Sztolsztener ME, Wasilewski M, Heinz E, Chacinska A. 2014. Mitochondrial protein translocases for survival and wellbeing. *FEBS Letters* **588**: 2484–2495.

Song S, Jang S, Park J, Bang S, Choi S, Kwon K-Y, Zhuang X, Kim E, Chung J. 2013. Characterization of PINK1 (PTEN-induced putative kinase 1) mutations associated with Parkinson disease in mammalian cells and Drosophila. *The Journal of Biological Chemistry* **288**: 5660–5672.

Srivatsal S, Cholerton B, Leverenz JB, Wszolek ZK, Uitti RJ, Dickson DW, Weintraub D, Trojanowski JQ, Van Deerlin VM, Quinn JF, et al. 2015. Cognitive Profile of LRRK2-related Parkinson's Disease. *Movement disorders : official journal of the Movement Disorder Society* **30**: 728–733.

Stafa K, Tsika E, Moser R, Musso A, Glauser L, Jones A, Biskup S, Xiong Y, Bandopadhyay R, Dawson VL, et al. 2014. Functional interaction of Parkinson's disease-associated LRRK2 with members of the dynamin GTPase superfamily. *Human Molecular Genetics* **23**: 2055–2077.

Steger M, Tonelli F, Ito G, Davies P, Trost M, Vetter M, Wachter S, Lorentzen E, Duddy G, Wilson S, et al. 2016. Phosphoproteomics reveals that Parkinson's disease kinase LRRK2 regulates a subset of Rab GTPases. *eLife*: e12813.

Su Y-C, Qi X. 2013. Inhibition of excessive mitochondrial fission reduced aberrant autophagy and neuronal damage caused by LRRK2 G2019S mutation. *Human Molecular Genetics* **22**: 4545–4561.

Su Y-C, Guo X, Qi X. 2015. Threonine 56 phosphorylation of Bcl-2 is required for LRRK2 G2019S-induced mitochondrial depolarization and autophagy. *Biochimica Et Biophysica Acta* **1852**: 12–21.

Tayebi N, Walker J, Stubblefield B, Orvisky E, LaMarca ME, Wong K, Rosenbaum H, Schiffmann R, Bembi B, Sidransky E. 2003. Gaucher disease with parkinsonian manifestations: does glucocerebrosidase deficiency contribute to a vulnerability to parkinsonism? *Molecular Genetics and Metabolism* **79**: 104–109.

Tong Y, Yamaguchi H, Giaime E, Boyle S, Kopan R, Kelleher RJ, Shen J. 2010. Loss of leucine-rich repeat kinase 2 causes impairment of protein degradation pathways, accumulation of alpha-synuclein, and apoptotic cell death in aged mice. *Proceedings of the National Academy of Sciences of the United States of America* **107**: 9879–9884.

Tong Y, Giaime E, Yamaguchi H, Ichimura T, Liu Y, Si H, Cai H, Bonventre JV, Shen J. 2012. Loss of leucine-rich repeat kinase 2 causes age-dependent bi-phasic alterations of the autophagy pathway. *Molecular Neurodegeneration* **7**: 2.

Toyofuku T, Morimoto K, Sasawatari S, Kumanogoh A. 2015. Leucine-Rich Repeat Kinase 1 Regulates Autophagy through Turning On TBC1D2-Dependent Rab7 Inactivation. *Molecular and Cellular Biology* **35**: 3044–3058.

Trifilieff P, Rives M-L, Urizar E, Piskorowski RA, Vishwasrao HD, Castrillon J, Schmauss C, Slättman M, Gullberg M, Javitch JA. 2011. Detection of antigen interactions ex vivo by proximity ligation assay: endogenous dopamine D2-adenosine A2A receptor complexes in the striatum. *BioTechniques* **51**: 111–118.

Trinh J, Farrer M, Ross OA, Guella I. 1993. LRRK2-Related Parkinson Disease. In *GeneReviews(®)*, , Pagon RA, , Adam MP, , Ardinger HH, et al. (eds). University of Washington, Seattle: Seattle (WA);

Trinh J, Guella I, Farrer MJ. 2014. Disease penetrance of late-onset parkinsonism: a meta-analysis. *JAMA neurology* **71**: 1535–1539.

Tsujimoto Y, Shimizu S. 2005. Another way to die: autophagic programmed cell death. *Cell Death & Differentiation* **12**: 1528–1534.

Uittenbogaard M, Chiaramello A. 2014. Mitochondrial biogenesis: A therapeutic target for neurodevelopmental disorders and neurodegenerative diseases. *Current pharmaceutical design* **20**: 5574–5593.

Valente EM, Abou-Sleiman PM, Caputo V, Muqit MMK, Harvey K, Gispert S, Ali Z, Turco DD, Bentivoglio AR, Healy DG, et al. 2004. Hereditary early-onset Parkinson's disease caused by mutations in PINK1. *Science* **304**: 1158–1160.

Velkoff VA, Kowal PR. 2006. *Aging in Sub-Saharan Africa: The changing demography of the region*. National Academies Press (US).

Venderova K, Kabbach G, Abdel-Messih E, Zhang Y, Parks RJ, Imai Y, Gehrke S, Ngsee J, Lavoie MJ, Slack RS, et al. 2009. Leucine-Rich Repeat Kinase 2 interacts with Parkin, DJ-1 and PINK-1 in a Drosophila melanogaster model of Parkinson's disease. *Human Molecular Genetics* **18**: 4390–4404.

Venselaar H, Beek TA te, Kuipers RK, Hekkelman ML, Vriend G. 2010. Protein structure analysis of mutations causing inheritable diseases. An e-Science approach with life scientist friendly interfaces. *BMC Bioinformatics* **11**: 548.

Vilariño-Güell C, Wider C, Ross OA, Dachsel JC, Kachergus JM, Lincoln SJ, Soto-Ortolaza AI, Cobb SA, Wilhoite GJ, Bacon JA, et al. 2011. VPS35 mutations in Parkinson disease. *American Journal of Human Genetics* **89**: 162–167.

Vilariño-Güell C, Rajput A, Milnerwood AJ, Shah B, Szu-Tu C, Trinh J, Yu I, Encarnacion M, Munsie LN, Tapia L, et al. 2014. DNAJC13 mutations in Parkinson disease. *Human Molecular Genetics* **23**: 1794–1801.

Vives-Bauza C, Zhou C, Huang Y, Cui M, Vries RLA de, Kim J, May J, Tocilescu MA, Liu W, Ko HS, et al. 2010. PINK1-dependent recruitment of Parkin to mitochondria in mitophagy. *Proceedings of the National Academy of Sciences* **107**: 378–383.

Wallings R, Manzoni C, Bandopadhyay R. 2015. Cellular processes associated with LRRK2 function and dysfunction. *The FEBS journal* **282**: 2806–2826.

Wang L, Xie C, Greggio E, Parisiadou L, Shim H, Sun L, Chandran J, Lin X, Lai C, Yang W-J, et al. 2008a. The chaperone activity of heat shock protein 90 is critical for maintaining the stability of leucine-rich repeat kinase 2. *The Journal of Neuroscience: The Official Journal of the Society for Neuroscience* **28**: 3384–3391.

Wang QJ, Ding Y, Kohtz DS, Kohtz S, Mizushima N, Cristea IM, Rout MP, Chait BT, Zhong Y, Heintz N, et al. 2006. Induction of autophagy in axonal dystrophy and degeneration. *The Journal of Neuroscience: The Official Journal of the Society for Neuroscience* **26**: 8057–8068.

Wang X, Su B, Fujioka H, Zhu X. 2008b. Dynamin-Like Protein 1 reduction underlies mitochondrial morphology and distribution abnormalities in fibroblasts from sporadic Alzheimer's disease patients. *The American Journal of Pathology* **173**: 470–482.

Wang X, Su B, Liu W, He X, Gao Y, Castellani RJ, Perry G, Smith MA, Zhu X. 2011. DLP1-dependent mitochondrial fragmentation mediates 1-methyl-4-phenylpyridinium toxicity in neurons: implications for Parkinson's disease. *Aging Cell* **10**: 807–823.

Wang X, Petrie TG, Liu Y, Liu J, Fujioka H, Zhu X. 2012a. Parkinson's disease-associated DJ-1 mutations impair mitochondrial dynamics and cause mitochondrial dysfunction. *Journal of neurochemistry* **121**: 830–839.

Wang X, Yan MH, Fujioka H, Liu J, Wilson-Delfosse A, Chen SG, Perry G, Casadesus G, Zhu X. 2012b. LRRK2 regulates mitochondrial dynamics and function through direct interaction with DLP1. *Human molecular genetics* **21**: 1931–1944.

Webber PJ, Smith AD, Sen S, Renfrow MB, Mobley JA, West AB. 2011. Autophosphorylation in the leucine-rich repeat kinase 2 (LRRK2) GTPase domain modifies kinase and GTP-binding activities. *Journal of molecular biology* **412**: 94–110.

West AB, Moore DJ, Biskup S, Bugayenko A, Smith WW, Ross CA, Dawson VL, Dawson TM. 2005. Parkinson's disease-associated mutations in leucine-rich repeat kinase 2 augment kinase activity. *Proceedings of the National Academy of Sciences* **102**: 16842–16847.

West AB, Moore DJ, Choi C, Andrabi SA, Li X, Dikeman D, Biskup S, Zhang Z, Lim K-L, Dawson VL, et al. 2007. Parkinson's disease-associated mutations in LRRK2 link enhanced GTP-binding and kinase activities to neuronal toxicity. *Human Molecular Genetics* **16**: 223–232.

Wider C, Dickson DW, Wszolek ZK. 2010. Leucine-Rich Repeat Kinase 2 gene-associated disease: Redefining genotype-phenotype correlation. *Neuro-Degenerative Diseases* **7**: 175–179.

Wirdefeldt K, Adami H-O, Cole P, Trichopoulos D, Mandel J. 2011. Epidemiology and etiology of Parkinson's disease: a review of the evidence. *European Journal of Epidemiology* **26**: 1–58.

Xie H, Hu L, Li G. 2010. SH-SY5Y human neuroblastoma cell line: in vitro cell model of dopaminergic neurons in Parkinson's disease. *Chinese Medical Journal* **123**: 1086–1092.

Xiong N, Huang J, Zhang Z, Zhang Z, Xiong J, Liu X, Jia M, Wang F, Chen C, Cao X, et al. 2009. Stereotaxical infusion of Rotenone: A reliable rodent model for Parkinson's disease. *PLoS ONE* **4**.

Xu R, Hu Q, Ma Q, Liu C, Wang G. 2014. The protease Omi regulates mitochondrial biogenesis through the GSK3β/PGC-1α pathway. *Cell Death & Disease* **5**: e1373.

Yakhine-Diop SMS, Bravo-San Pedro JM, Gómez-Sánchez R, Pizarro-Estrella E, Rodríguez-Arribas M, Climent V, Aiastui A, de Munain AL, Fuentes JM, González-Polo RA. 2014. G2019S LRRK2 mutant fibroblasts from Parkinson's disease patients show increased sensitivity to neurotoxin 1-methyl-4-phenylpyridinium dependent of autophagy. *Toxicology* **324**: 1–9.

Ye K, Lu J, Ma F, Keinan A, Gu Z. 2014. Extensive pathogenicity of mitochondrial heteroplasmy in healthy human individuals. *Proceedings of the National Academy of Sciences* **111**: 10654–10659.

Young JC, Hoogenraad NJ, Hartl FU. 2003. Molecular Chaperones Hsp90 and Hsp70 Deliver Preproteins to the Mitochondrial Import Receptor Tom70. *Cell* **112**: 41–50.

Zandberg L, van Dyk HC, van der Westhuizen FH, van Dijk AA. 2016. A 3-methylcrotonyl-CoA carboxylase deficient human skin fibroblast transcriptome reveals underlying mitochondrial dysfunction and oxidative stress. *The International Journal of Biochemistry & Cell Biology* **78**: 116–129.

Zanellati MC, Monti V, Barzaghi C, Reale C, Nardocci N, Albanese A, Valente EM, Ghezzi D, Garavaglia B. 2015. Mitochondrial dysfunction in Parkinson disease: evidence in mutant PARK2 fibroblasts. *Frontiers in Genetics* **6**: 78.

Zhang X, Chen S, Huang K, Le W. 2013. Why should autophagic flux be assessed? *Acta Pharmacologica Sinica* **34**: 595–599.

Zhao J, Hermanson SB, Carlson CB, Riddle SM, Vogel KW, Bi K, Nichols RJ. 2012. Pharmacological inhibition of LRRK2 cellular phosphorylation sites provides insight into LRRK2 biology. *Biochemical Society Transactions* **40**: 1158–1162.

Zhu J, Chu CT. 2010. Mitochondrial dysfunction in Parkinson's disease. *Journal of Alzheimer's disease: JAD* **20 Suppl 2**: S325-334.

Zhu J-H, Guo F, Shelburne J, Watkins S, Chu CT. 2003. Localization of phosphorylated ERK/MAP kinases to mitochondria and autophagosomes in Lewy body diseases. *Brain Pathology (Zurich, Switzerland)* **13**: 473–481.

Zimprich A, Biskup S, Leitner P, Lichtner P, Farrer M, Lincoln S, Kachergus J, Hulihan M, Uitti RJ, Calne DB, et al. 2004. Mutations in LRRK2 Cause Autosomal-Dominant Parkinsonism with Pleomorphic Pathology. *Neuron* **44**: 601–607.

Zinchuk V, Zinchuk O, Okada T. 2007. Quantitative Colocalization Analysis of Multicolor Confocal Immunofluorescence Microscopy Images: Pushing Pixels to Explore Biological Phenomena. *Acta Histochemica et Cytochemica* **40**: 101–111.

Appendix I
Vector map

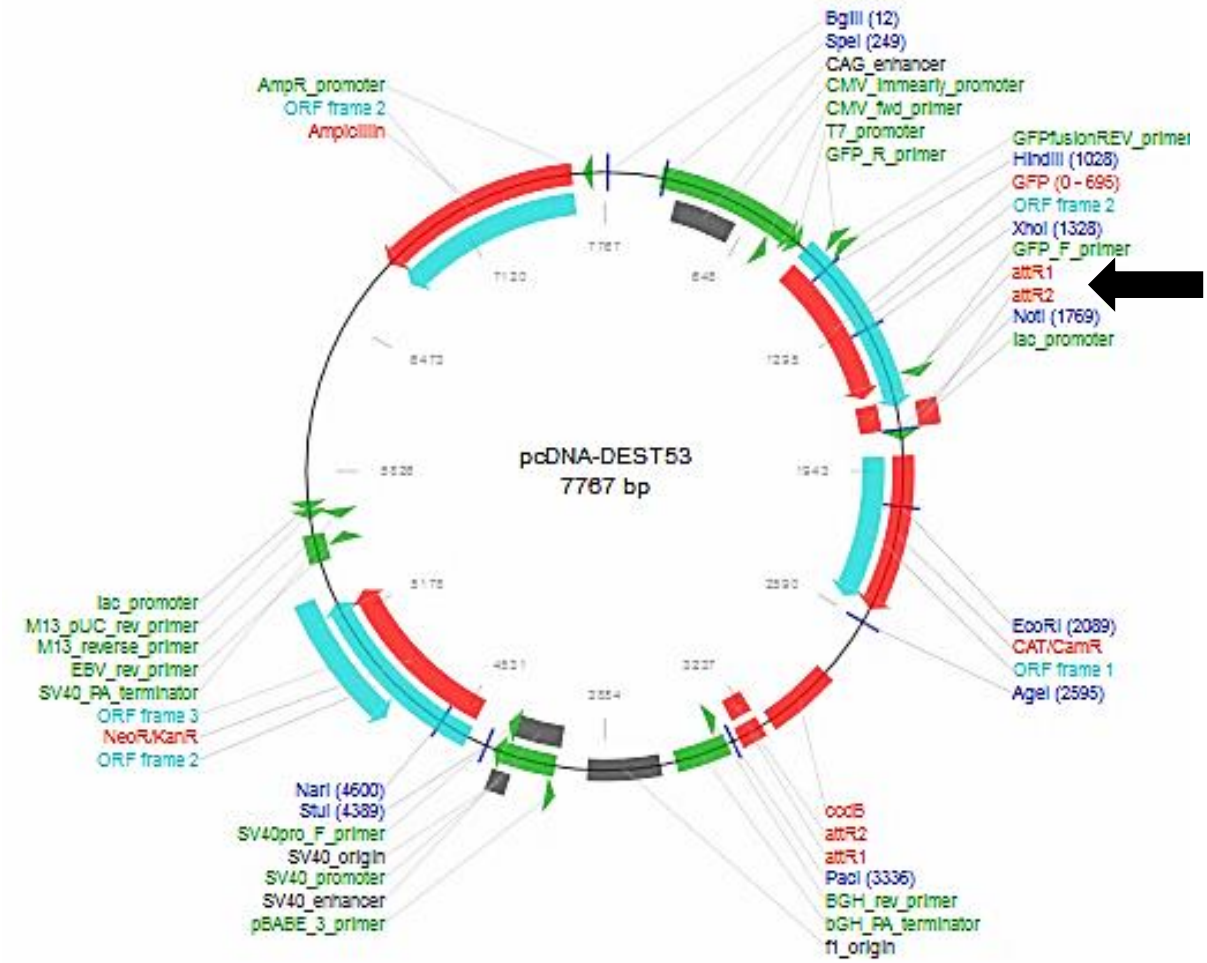

Restriction map and cloning site of the pcDNA-DEST53 vector. The positions of the resistance genes, Ampicillin (Amp) and Neomycin (Neo), various promotors such as CMV and T7, the GFP site and the attR1 and attR2 sites. Full length LRRK2 sequences were cloned into the vector using Gateway® cloning and recombination between the attR1 and attR2 cloning sites indicated by the black arrow. The GFP tag was fused to the N-terminal gene inserts. Taken from: https://www.addgene.org/browse/sequence_vdb/2088/ and (Fu *et al.*, 2008).

Appendix II
Reagents

1. Solution used in generation of competent cells

CAP buffer:

$CaCl_2$	2.21g
15% glycerol	37.5ml
PIPES	0.76g

ddH_2O up to 250ml. pH 7.0. Store at 4°C.

2. Bacterial media

Luria-Bertani (LB) Media

Bacto tryptone	5g
Yeast extract	2.5g
NaCl	5g

ddH_2O to final volume of 500ml

Autoclave for 20 minutes at 121°C

LB Agar Plates

Bacto tryptone	5g
Yeast extract	2.5g
NaCl	5g
Agar	8g

ddH_2O to final volume of 500ml

Autoclave for 20 minutes at 121°C and add appropriate antibiotic to media when the temperature has reached ±55°C, prior to pouring plates (Ampicillin, 50mg/ml).

3. Electrophoresis solutions

SB Buffer (20X stock)

Di-sodium tetraborate decahydrate	38.1g

ddH_2O to a final volume of 1L

SB Buffer (1X)

20X SB buffer	100ml
ddH_2O	2L

SDS-PAGE Running buffer (10X)

Tris base	30g
Glycine	144g
10% SDS	100ml

ddH_2O to a final volume of 1L

SDS-PAGE Running buffer (1X)

10x SDS Running Buffer	100ml
ddH_2O	900ml

4. Gels

1 % Agarose Gel

Agarose	1g

SB Buffer (1X)	100ml

Microwave for 2-3 minutes; add 5µl ethidium bromide (10mglml) when temperature reaches ± 55°C

5. Loading dyes

Ethidium bromide stock (10mg/ml)

Ethidium bromide (Sigma)	500mg
ddH_2O	50ml

Stir for 4 hours using magnetic stirrer and store in dark container at 4°C

Cresol Loading Dye

10mg/ml cresol stock solutiom	2% (v/v)
Sucrose	0.9933M

SDS Loading Dye

Laemmli sample buffer (Bio-Rad)	950µl
β-mercapto-ethanol	50µl

6. Co-IP reagents

Lysis buffer

1M Tris- HCl pH 7.4	5ml
5M NaCl	3ml
Triton-x	1%
1M $MgCl_2$	150µl
ddH_2O	150ml

Add fresh on day of lysis:

β-mercapto-ethanol	0.1%
Halt™ Protease and Phosphatase Inhibitor Cocktail 100x	1%

TBST (pH7.6)

5M NaCl	60ml
1M Tris base	40ml
0.1% Tween-20	2ml

ddH_2O to a final volume of 2L

Membrane blocking solution

Powder milk	7.5g
Tween-20	15µl
TBST solution	150ml

7. Co-localization reagents

4% Formaldehyde solution

16% Formaldehyde	10ml
ddH_2O	30ml

Dilute 4% Formaldehyde in culture media at a ratio of 1:1

1% Bovine Serum Albumin (BSA)

BSA	0.5g
PBS solution	50ml

8. Eukaryotic cell culture media

Growth Media

DMEM (4.5g/L glucose, with L-glutamine)	500ml
Foetal Bovine Serum	50ml
Penicillin/Streptomycin	5ml

Pre-warm to 37°C before use. Store at 4˚C.

Fibroblast isolation media

Amniochrome II complete media	95ml
Chang Medium® D	95ml
Non-essential amino acids (NEAA)	5ml
Penicillin/Streptomycin	5ml

Pre-warm to 37˚C before use. Store at 4˚C.

9. Solutions for functional assays

5mg/ml MTT stock solution

Thiazolyl blue tetrazolium bromide	10mg
PBS	2ml

40mM CCCP stock solution

Carbonyl cyanide m-chlorophenyl hydrazone	16.2mg
DMSO	2ml

Aliquot and store in the dark at -20˚C. Stable at 4˚C for up to two weeks.

10µM CCCP working solution

40mM CCCP stock solution	5µl
Fibroblast culture media	20ml

Make up fresh before each use

5mg/ml JC-1 stock solution

Tetraethyl benzimidazolyl carbocyanine iodide	5mg
DMSO	1ml

20µg/ml Bafilomycin A1 stock solution

Bafilomycin A1	100µg
Ethanol	5ml

Appendix III
Generation of CRISPR cell line

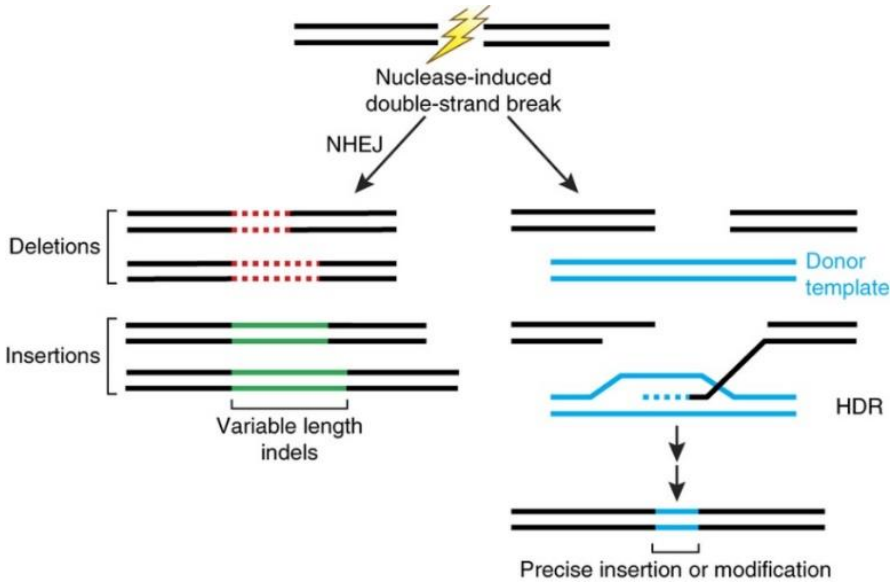

Figure 1 Repair mechanisms following nuclease-induced double-strand breaks (DSBs). DSBs can either be repaired by non-homologous end joining (NHEJ) or Homology-direct repair (HDR) pathways. Taken from (Sander and Joung, 2014).

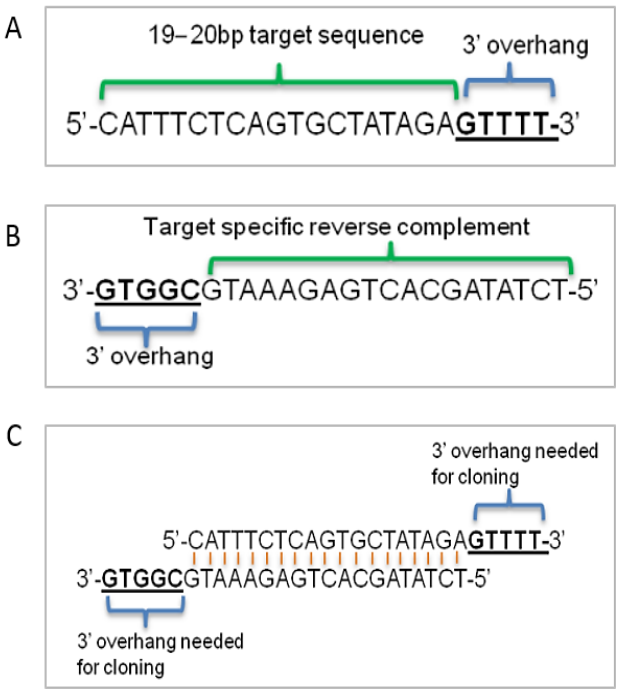

Figure 2 Guidelines for designing crRNA specific oligonucleotide primers for CRISPR target sequences. **A)** An example of a top strand of an oligonucleotide primer containing the GTTTT 3' overhang. **B)** An example of a bottom strand of an oligonucleotide primer containing the CGGTG 3' overhang. **C)** Annealing the top and bottom strands of the crRNA specific oligonucleotide primers for cloning into the GeneArt ® CRISPR Nuclease OFP Vector.

A **LRRK2 exon 41**

tttcctgtgcattttctggcagATACCTCCACTCAGCCATGATTATATACCGAGACCTGAAACCCCACAATGTGCTG
CTTTTCACACTGTATCCCAATGCTGCCATCATTGCAAAGATTGCTGACTACGGCATTGCTCAGTACTGCT
GTAGAATGGGGATAAAAACATCAGAGGGCACACCAGgtaggtgatcaggtctgtctcataatt

B **LRRK2 exon 42**

attttatctgcttactttcagGGTTTCGTGCACCTGAAGTTGCCAGAGGAAATGTCATTTATAACCAACAGGCTGA
TGTTTATTCATTTGGTTTACTACTCTATGACATTTTGACAACTGGAGGTAGAATAGTAGAGGGTTTGAAG
TTTCCAAATGAGTTTGATGAATTAGAAATACAAGGAAAATTACCTGgtaagttctgttttctctac

Figure 3 The sequences of Exon 41 and 42 of *LRRK2.* Small parts of the intronic sequences are shown in lower case and the capital text indicates the exonic regions of *LRRK2*. The underlined text shows the PAM sequences selected for each exon. **A)** The WT sequence of *LRRK2* exon 41 in which the most common PD-causing mutation (G2019S) is located. The WT codon is indicated in purple text (GGA). **B)** The WT sequence of *LRRK2* exon 42 in which the novel variant (Q2089R) is found. The WT codon is shown in green text (CAA).

Table 1 Oligonucleotides and templates designed for CRISPR-Cas9 genome editing

Oligonucleotides	Sequence (5'-3')	Number of bases
G2019S CRISPR top	ATTGCAAAGATTGCTGACTA*GTTTT*	25
G2019S CRISPR bottom	TAGTCAGCAATCTTTGCAAT*CGGTG*	25
G2019S template	AATGTGCTGCTTTTCACACTGTATCCCAATGCTGCCATCATTG CAAAGATTGCTGACTAC**AGC**ATTGCTCAGTACTGCTGTAGAA TGGGGATAAAAACATCAGAGGGCACACCAGGTAGGTGA	123
Q2089R CRISPR top	GAAATACAAGGAAAATTACC*GTTTT*	25
Q2089R CRISPR bottom	GGTAATTTTCCTTGTATTTC*CGGTG*	25
Q2089R template	GACATTTTGACAACTGGAGGTAGAATAGTAGAGGGTTTGAA GTTTCCAAATGAGTTTGATGAATTAGAAATA**CGA**GGAAAATT ACC**AGG**TAAGTTCTGTTTTCTCTACAATGAAGATTTTTTTTCT TAATATCAGCAGCTTCA	143

The **purple** text illustrates the introduction of the G2019S mutation (GGC>AGC). The underlined text indicates the simultaneous mutation of the PAM site (CGG>CAG). The **green** text represents the introduction of the Q2089R variant (CAA>CGA). The **blue** text shows the change of the PAM site (TGG>AGG). The *italic* text at the end of each top and bottom oligonucleotide is complementary to the overhang sequences in the linearized OFP reporter vector.

Appendix IV
Supplementary tables

Table 1 Optimized cell seeding densities for HEK293 and COS7 cells

Plate	HEK293	COS7
96-well	20 000 cells/well	
24-well	100 000 cells/well	50 000 cells/well
6-well	500 000 cells/well	

Table 2 Transfection of HEK293 cells with Lipofectamine 2000 transfection reagent

Plate	SFM	Lipo	SFM	Plasmid DNA	Transfection volume	Total well volume
96-well	20 µl	0,6 µl	20 µl	0,4 µg	40 µl	200 µl
24-well	25 µl	1 µl	25 µl	0,6 µg	50 µl	400 µl
6-well	200 µl	8 µl	200 µl	3 µg	400 µl	2 ml

Abbreviations: Lipo, Lipofectamine2000; SFM, Serum free media

Table 3 Transfection of COS7 cells with DMRIE-C transfection reagent

Plate	SFM	DMRIE-C	SFM	Plasmid DNA	Transfection volume	Total well volume
24-well	75 µl	0,70 µl	75 µl	1 µg	150 µl	150 µl

Abbreviations: SFM, Serum free media

Table 4 List of LRRK2 sequencing primers

Primer	Sequence (5'-3')	Tm (°C)
LSP 1	TAG GAT CCA TGG CTA GTG G	53.2
LSP 2	GTC CTC ATG AGT GGC AAT G	53.5
LSP 3	GCA GCA GTG GTC CCC AAA AT	58.5
LSP 4	GCA TCA TGG TTG AAT GCT TG	52.7
LSP 5	TCA GAT GAT TCA CTC AGG TCA	53.0
LSP 6	GCA TAT TTA TGG TCT AGA GTA GAG A	51.3
LSP 7	GAA TGC CAC CGA GGA ATC	53.4
LSP 8	GCC CAA ACA GAA TGT ATT GGC	54.8
LSP 10	GTC TGG TAC TCT CCT GGT C	53.8
LSP 11	GTC ATG CTG GTA TTG GGC	53.7
LSP 12	GTC CTC ATA TCT AGG AAA GAC AC	52.1

Abbreviations: LSP, LRRK2 sequencing primer; Tm, melting temperature; °C, degree Celsius

Table 5 List of universal primers

Primer	Sequence (5'-3')	Tm (°C)
U6 Forward	GGG CAG GAA GAG GGC CTA T	59.2
GFP Forward	GGT CCT TCT TGA GTT TGT AAC	51.1
CMV Forward	CGC AAA TGG GCG GTA GGC GTG	63.9
T7 Forward	TAA TAC GAC TCA CTA TAG GG	47.5

Abbreviations: Tm, melting temperature; °C, degree Celsius

Table 6 List of primary and secondary antibodies and their optimized concentrations used in Co-immunoprecipitation and Western blot assays

Antigen	Dilution	Primary antibody	Manufacturer	Blocking buffer	Secondary antibody*	Dilution
LRRK2	1:300	Rabbit Monoclonal [MJFF (c41-2)] LRRK2	Abcam ab133474	5% Milk	Donkey anti-rabbit	1:2000
LRRK2 pSer^{1292}	1:100	Rabbit Monoclonal [MJFR-19-7-8] LRRK2 (phosphor S1292)	Abcam ab203181	5% Milk	Donkey anti-rabbit	1:2000
GAPDH	1:10 000	Rabbit Polyclonal (FL-225) GAPDH	Santa Cruz Biotechnology sc-25779	5% Milk	Donkey anti-rabbit	1:2000
GFP	1:4000	Rabbit Polyclonal GFP-ChIP Grade	Abcam ab290	5% Milk	Donkey anti-rabbit	1:2000
TOM20	1:4000	Mouse Monoclonal TOMM20	Abcam ab56783	5% Milk	Donkey anti-mouse	1:2000
TOM22	1:4000	Mouse Monoclonal [1C9-2] TOMM22	Abcam ab10436	5% Milk	Donkey anti-mouse	1:2000
TOM40	1:2000	Rabbit Monoclonal [ERP6932(2)] TOMM40	Abcam ab185543	5% Milk	Donkey anti-rabbit	1:2000
TOM70	1:5000	Mouse Monoclonal [21] TOMM70A	Abcam ab106193	5% Milk	Donkey anti-mouse	1:2000
LC3 II	1:1000	Rabbit Polyclonal LC3B	Cell Signalling Technology CST-2775S	5% BSA	Donkey anti-rabbit	1:2000
P62	1:2000	Mouse Monoclonal SQSTM1/p62	Abcam ab56416	5% Milk	Donkey anti-mouse	1:2000

*, Santa Cruz Biotechnology Inc., United States.

Table 7 List of primary and secondary antibodies and their optimized concentrations used in co-localization assays

Antigen	Dilution	Primary antibody	Manufacturer	Secondary antibody*	Dilution
GFP	1:4000	Rabbit Polyclonal GFP-ChIP Grade	Abcam ab290	Donkey anti-rabbit Alexa 488 (Green)	1:500
GFP	1:2000	Mouse Monoclonal [9F9.F9] GFP	Abcam ab1218	Donkey anti-mouse Alexa 488 (Green)	1:500
TOM20	1:1000	Mouse Monoclonal TOMM20	Abcam ab56783	Donkey anti-mouse Cy3 (Red)	1:500
TOM22	1:1000	Mouse Monoclonal [1C9-2] TOMM22	Abcam ab10436	Donkey anti-mouse Cy3 (Red)	1:500
TOM40	1:100	Rabbit Monoclonal [ERP6932(2)] TOMM40	Abcam ab185543	Donkey anti-rabbit Cy3 (Red)	1:500
TOM70	1:2000	Mouse Monoclonal [21] TOMM70A	Abcam ab106193	Donkey anti-mouse Cy3 (Red)	1:500

*Jackson ImmunoResearch Laboratories, Inc., United States

Table 8 Co-localization coefficients

Coefficients	Meaning	Values
Weighted Co-localization Coefficient	Illustrates the contribution of each of the two channels to the pixels of interest	**0 – 1.0** If the red channel is 1.0 and the green channel is 0.2, it means that all (100%) red pixels co-localize with green, but only 20% of green pixels co-localize with red.
Mander's Coefficient	Illustrates the contribution of each channel regardless of the pixel intensity. A good indicator of the proportion of green channel signal coincident with a signal in the red channel.	**0 – 1.0** **M1** is the ratio of the summed intensities of pixels from the **green** channel for which the intensity in the red channel is above zero *to* the total green channel intensity. **M2** is defined conversely for the **red** channel. M1 and M2 can be expressed as % overlap between channels.
Overlap Coefficient	Signifies the actual overlap of signals and represents the true degree of co-localization	**0 – 1.0** Where 0.5 suggests that 50% of both selected channels co-localize.
Pearson's correlation coefficient (Correlation R)	The correlation of intensity distribution between channels	**-1.0 – 1.0** **0** indicates no significant correlation, **-1** indicates negative correlation and **1** indicates positive correlation.

Adapted from (Zinchuk *et al.*, 2007; Dunn *et al.*, 2011) and https://rsb.info.nih.gov/ij/plugins/track/jacop2.html.

Appendix V
Family pedigree

Family 85

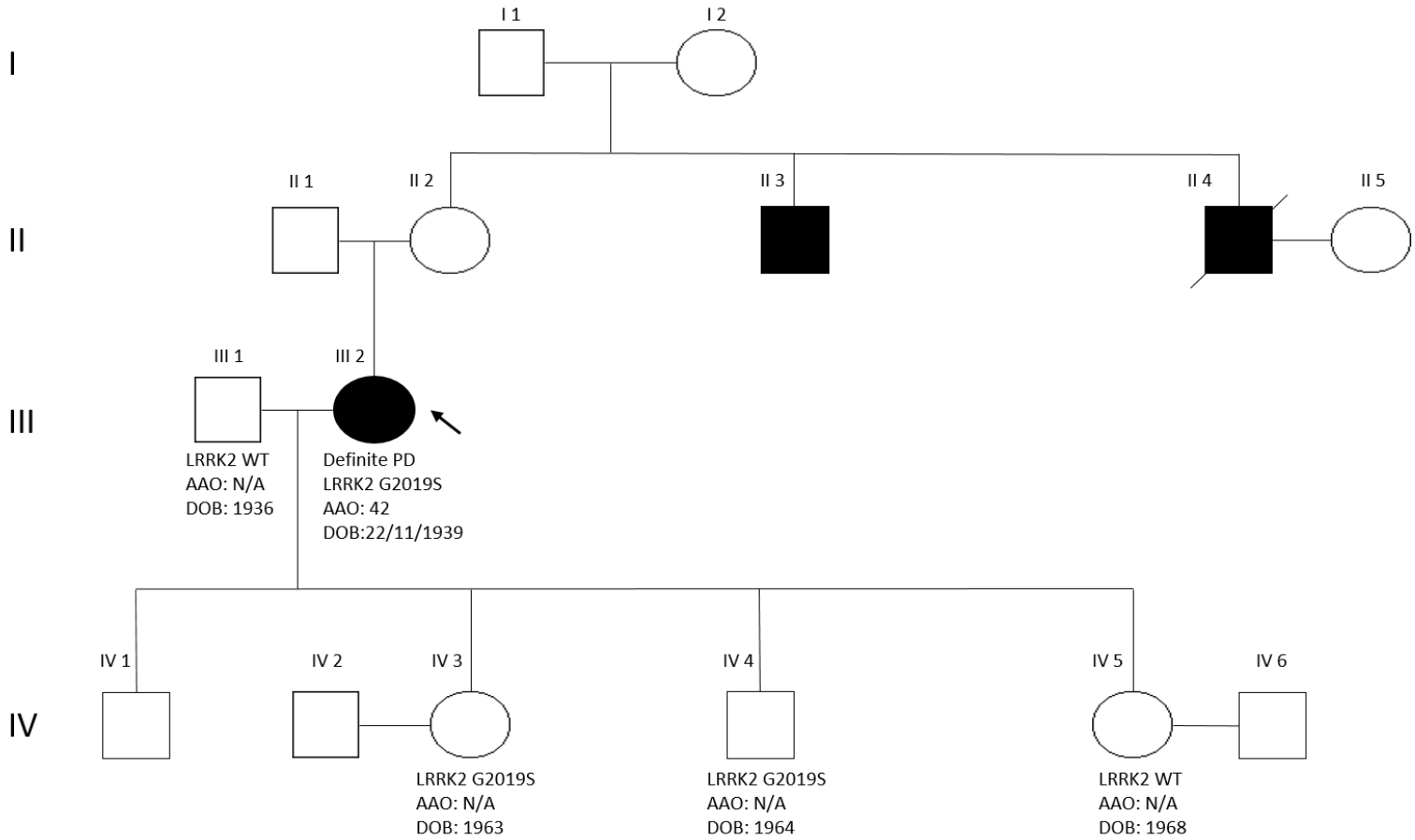

Figure 1 Pedigree of South African family with *LRRK2* G2019S

Appendix VI
Seahorse XF analyzer plate layouts

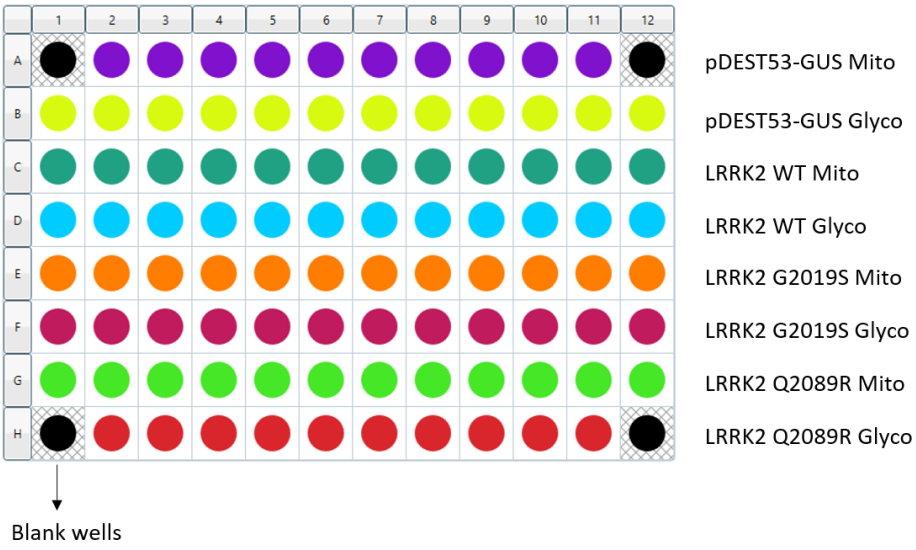

Figure 1 Design of 96-well plate layout for the XF Mito Stress Test and Glycolysis Stress Tests for transfected HEK293 cells. Rows A, C, E and G were used for the XF Mito Stress Test. Rows B, D, F and H were used for the XF Glycolysis Stress Test. The black corner wells indicate blank wells used for background corrections. Abbreviations: Mito, XF Mito Stress Test; Glyco, XF Glycolysis Stress Test.

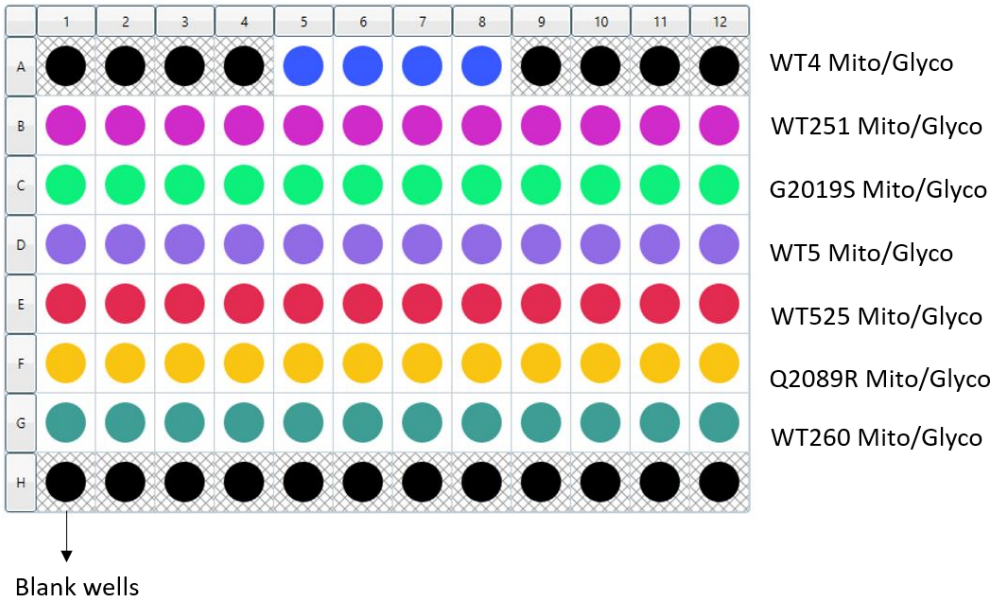

Figure 2 Design of 96-well plate layout for the XF Mito Stress Test and Glycolysis Stress Tests for control and patient-derived fibroblasts. The black corner wells indicate blank wells used for background corrections. Abbreviations: Mito, XF Mito Stress Test; Glyco, XF Glycolysis Stress Test.

Appendix VII
Supplementary methods

Removing DMSO from stocks and culturing cells

Cells were frozen with freezing media containing DMSO and in order to remove it from the cells, 1ml of pre-warmed culture media was added to 1ml of thawed cells. This mixture was transferred to a 15ml polypropylene tube containing 4ml of pre-warmed culture media. The suspension was centrifuged at 3000rpm for 3min in a Sorval® GLC-6 general laboratory centrifuge. The supernatant was discarded and the pellet resuspended in 5ml culture media, and the suspension transferred to a T25 tissue culture flask. The flasks were incubated at 37°C in in a Farma thermosteri-cycle 5% CO_2 humidified incubator until they were ready for sub-culturing, DNA extraction, RNA extraction or cell lysis.

Sub-culturing cell cultures

Cell cultures were passaged every 2 to 4 days (in the case of HEK293 and COS7) or 5 to 7 days (fibroblasts), at 70-80% confluency. The growth media was removed from the flasks and the adherent monolayer of cells gently rinsed with 3 to 5ml sterile phosphate-buffered saline (PBS) (Lonza, Switzerland). In order to facilitate the detachment of cells from the growth surface, 3 to 5 ml of trypsin (0.5g/L, Lonza, Switzerland) was added and flasks incubated at 37°C for 5 minutes. To deactivate the trypsin enzyme activity, an equal volume of culture media was added to the cells. The suspension was transferred to a 15 ml tube and centrifuged at 3000rpm for 3 minutes in a Sorval® GLC-6 general laboratory centrifuge. The supernatant was discarded and the pellet resuspended in 3ml culture media before the cells were evenly distributed into T75 or T125 tissue culture flasks (Corning Inc., United States) containing final volumes of 12ml or 20 ml complete growth media, respectively. Alternatively, cells were plated into 6-well, 24-well or 96-well plates at pre-determined seeding densities for desired downstream assays.